Quantification of the Longitudinal Relaxation Time for *in vivo* MRI - Influence of Magnetisation Transfer

Von der Fakultät für Mathematik, Informatik und Naturwissenschaften der RWTH Aachen University zur Erlangung des akademischen Grades einer Doktorin der Naturwissenschaften genehmigte Dissertation

vorgelegt von

Diplom Physikerin

Miriam Rabea Kubach

aus Rheinfelden

Berichter: Universitätsprofessor Dr. N. Jon Shah
Universitätsprofessor Dr. Achim Stahl

Tag der mündlichen Prüfung: 3.7.2012

Diese Dissertation ist auf den Internetseiten der Hochschulbibliothek online verfügbar.

Abstract

MRI contrast *in vivo* is influenced by biophysical and biochemical mechanisms, in particular by the exchange of the signal - creating protons between chemically different environments, termed magnetisation transfer (MT). These effects, though ubiquitous, are difficult to characterise due to their intrinsic complexity and strong dependence on sequence parameters and design.

Quantifying the longitudinal relaxation time, T_1, has been of particular interest in the realm of MRI. One motivating aspect behind this thesis was the aim of investigating the relationship between T_1 and MT. Thus, a careful and thorough investigation of the behaviour of T_1 quantification in the presence of MT was performed. A simulation framework for MRI was extended to consider MT. Simulations were complemented and confirmed by phantom and *in vivo* measurements. The framework was then employed to assess issues of T_1 quantification in the presence of MT, which are not amenable to measurement.

Tissue parameters influencing the observed longitudinal relaxation time were assessed based on the established two-pool model for MT. It was shown that estimation of the recovery time depends on almost all tissue parameters, e.g. the exchange rates, the pool sizes and the longitudinal relaxation times of the single pools. In the presence of MT, the observed T_1 values are generally shorter than the largest T_1 value of the single pools. This shortening arises from the exchange process. Common sequences used for T_1 estimations and changes in their signal equations arising from MT were derived analytically and calculated. The results were validated by simulations as well as by phantom measurements.

The consequences of neglecting MT effects on the estimated T_1 values were investigated. Three types of sequence were investigated with and without the MT effect, namely inversion recovery (IR), T_1 quantification by means of the Ernst equation, and Look-Locker type sequences. The simulations showed that IR-based methods give T_1 estimations with high accuracy (better than 2%) and precision (better than 5%), even in the presence of MT. However, this high accuracy can only be achieved if MT is considered by neglecting very short inversion times. Techniques employing the Ernst equation are usually less accurate and show worse precision than the inversion recovery methods, especially if only few sample points are considered in the former. Finally, the Look-Locker based method showed a strong dependence (in the presence of MT effects) of the estimated T_1 values on the sequence parameters used. It was demonstrated that a controlled variation of the inversion time gives rise to a novel method of MT quantification. Although this new method, the TAPIR TI approach, does not quantify all MT sample parameters, it offers the great advantage of fitting only three parameters to reveal some MT properties of the sample. The simulation results were successfully confirmed by *in vivo* measurements on 10 volunteers and thus the experimental feasibility of this method was proven.

The final part of this work investigates possible applications of T_1 quantification. An existing method for estimating the permeability of the blood-brain barrier, based on the Patlak model, was improved and a comparison with FET-PET measurements on tumour patients was obtained. A new approach to detect the linear part of a Patlak plot was developed and successfully implemented. It was demonstrated that the Patlak results give additional information about the tumour blood volume and the blood-brain barrier permeability.

Zusammenfassung

Biophysikalische und biochemische Mechanismen bestimmen den Bildkontrast von *in vivo* MRT-Bildern. Bei der konventionellen MRT wird das Signal von Protonen erzeugt. Protonen können sich chemisch austauschen, was bedeutet, dass sie sich zwischen chemisch verschiedenen Umgebungen bewegen und dabei ihre magnetischen Eigenschaften transferieren. Dieser Prozess genannt Magnetisierungstransfer (MT), ist komplex und wird von vielerlei Faktoren bestimmt, weshalb er sich nur schwer charakterisieren lässt. Die Ursachen dafür liegen sowohl in der intrinsischen Komplexität des MT-Mechanismus mit seinen vielen Parametern, als auch darin, dass der Effekt stark von den verwendeten MRT-Sequenzen und ihren Parametern abhängt.

Quantitative Messungen spielen in der MRT eine immer wichtigere Rolle. Insbesondere die Quantifizierung der longitudinalen Relaxationszeit, T_1, ist von Bedeutung. Die vorliegende Arbeit wurde vom Bestreben motiviert, die Zusammenhänge zwischen T_1 und MT zu erforschen. Das Verhalten der longitudinalen Relaxationszeit in Ab- und Anwesenheit von MT wurde sorgfältig studiert. Die Untersuchungen basieren zum Teil auf einer bestehenden Simulationsumgebung, die erweitert wurde, um eine Berücksichtigung des MT-Effekts zu ermöglichen. Die durchgeführten Simulationen wurden durch Messungen am Phantom und am Menschen validiert, ergänzt und bestätigt. Anschliessend wurden weitere Aspekte der T_1-Quantifizierung unter MT-Einfluss, die durch Messungen nicht zugänglich sind, mittels der Simulationssoftware untersucht.

Mit Hilfe des etablierten zwei-Pool-Modells für MT wurde untersucht, inwieweit die Gewebeeigenschaften die beobachtete longitudinale Relaxationszeit beeinflussen. Es konnte gezeigt werden, dass das effektive T_1 von fast allen Gewebeparametern abhängt, wie beispielsweise von der Austauschrate, den Poolgrössen und den T_1-Zeiten der einzelnen Pools. Zeigt ein Gewebe MT-Effekte, so ist das gemessene T_1 kürzer als das längste T_1 der einzelnen Austauschpools. Diese T_1-Verkürzung ist eine direkte Folge des Austauschprozesses.

Die Signalgleichungen weit verbreiteter Sequenzen zur T_1-Bestimmung sind unter Berücksichtigung von MT in der bekannten Form nicht mehr gültig. Analytische Neuberechnungen dieser Gleichungen unter Berücksichtigung der MT-Einflüsse wurden formuliert. Da sich die modifizierten Signalgleichungen jedoch durch viele freie Parameter auszeichnen, ist ein hohes Verhältnis von Signal zu Rauschen Voraussetzung für eine erfolgreiche T_1-Bestimmung. Aus diesem Grund eignet sich dieser Ansatz nur bedingt für *in vivo* Experimente.

Weitaus verbreiteter ist der Ansatz, bei der Bestimmung der longitudinalen Relaxationszeit sämtliche mögliche Effekte, die durch MT entstehen, zu vernachlässigen. Welche Konsequenzen sich daraus für die T_1-Bestimmung ergeben, wurde anhand von Simulationen mit und ohne MT untersucht. Drei Sequenzkategorien wurden dabei fokussiert: Inversion Recovery (IR)-Sequenzen, T_1-Bestimmung mittels der Ernst Gleichung, sowie Sequenzen des so genannten Look-Locker-Typs. Die Simulationen zeigten, dass T_1 auch bei MT mittels IR-Methoden mit hoher Präzision (besser als 5%) und Genauigkeit (besser als 2%) bestimmt werden kann. Unter MT-Einfluss setzt dies jedoch voraus, dass der Effekt auch berücksichtigt wird, beispielsweise durch das Nicht-Berücksichten der kurzen Inversionszeiten. Techniken, die auf der Ernst Gleichung basieren, sind normalerweise weniger genau und präzise als die IR-Methoden, insbesondere wenn man nur wenige Punkte misst. In diesem Fall sind Fehler, die durch die Vernachlässigung von MT-Effekten entstehen, kleiner als die Messgenauigkeit der Methode an sich.

Die untersuchte Look-Locker-Methode zeigte eine starke Abhängigkeit der gemessenen T_1-Werte von den Sequenzparametern, wenn bei der Signalsimulation MT berücksichtigt wurde. Es konnte jedoch gezeigt werden, dass diese Abhängigkeit genutzt werden kann, um MT zu quantifizieren. Diese neu entwickelte Methode basiert auf der kontrollierten Manipulation der Inversionszeit. Anschliessend wird die effektive T_1-Zeit für jede Inversionszeit bestimmt. Die änderung in der gefitteten T_1-Zeit hängt von den MT-Parametern ab und lässt Rückschlüsse auf MT-Vorgänge in der untersuchten Probe zu. Obwohl sich auf diese Art nicht alle MT-Parameter bestimmen lassen, bietet sie den Vorteil, dass nur drei freie Parameter gefittet werden müssen, während bei konventionellen Methoden sieben oder mehr freie Parameter zu bestimmen sind. Die Simulationsergebnisse wurden erfolgreich an zehn Probanden verifiziert, womit die experimentelle Machbarkeit bestätigt wurde.

Die Arbeit schliesst mit der Demonstration einer möglichen Anwendung von quantitativen T_1-Messungen ab. Mittels sukzessiven Messungen von T_1 vor und nach Kontrastmittelgabe lässt sich die Permeabilität der Blut-Hirnschranke messen. Grundlage dafür ist das Patlak-Modell, welches bereits erfolgreich für MRT-Messungen der Blut-Hirnschranke eingesetzt wurde. Diese Methode, insbesondere die notwendige Detektion des linearen Abschnitts des Patlak-Plots, wurde verbessert und an Tumorpatienten evaluiert. Die Ergebnisse wurden mit FET-PET-Messungen verglichen. Anhand des Vergleichs mit der etablierten FET-PET-Methode konnte gezeigt werden, dass die Patlak-Methode zusätzliche Informationen über das Tumorblutvolumen und die Hirnschrankenpermeabilität zur Verfügung stellt.

Contents

1. Introduction

Over the last decades, Magnetic Resonance Imaging (MRI) has proven to be a powerful tool for diagnostics as well as for follow-up studies, not only in medicine but also in other scientific pursuits. Its non-invasive nature, good availability and in particular the fact that MRI does not use ionising radiation has led to increasing interest during the last three decades. MRI benefits from a variety of different contrasts, especially in soft matter and tissue. Different contrasts arise not only from the tissue characteristics themselves but MR image contrast is a function of different sequences, different sequence parameters or different hardware, for example magnet field strength.

One of the strengths of MRI is the diversity of possible contrasts and the associated huge number of applications. However, the concomitant disadvantage is that radiological diagnostics is commonly based on qualitative information, namely weightings rather than quantitative results. Although qualitative images are sufficient for many routine applications, for some applications it would be most desirable to have comparable, and therefore, quantitative results.

Quantitative MRI (qMRI) allows one to obtain comparable data sets over large timescales or at different sites, largely independent of the scanner hardware (magnet strength notwithstanding) or particular sequence details. Moreover, by means of qMRI, potential tissue changes of interest can be monitored and related to the progress of particular diseases [1, 2], such as multiple sclerosis [3, 4], or hepatic encephalopathy [5]. Established quantitative MRI methods are water mapping [6, 7, 8] or relaxation time mapping (T_1, T_2, T_2^*) [9, 10, 11, 12]. Among the quantitative methods, mapping of longitudinal relaxation times, T_1, plays a prominent role within the established qMRI applications. It provides the basis for methods of Dynamic Contrast Enhanced imaging (DCE) [13, 2, 3, 14, 15] and neuronal tract tracing using manganese enhanced MRI [16]. Changes in T_1 values can be a sensitive indicator of pathological changes, such as tumours [17], hepatic encephalopathy [5] or the liver function [18].

Despite the many benefits of qMRI, there are a few difficulties that restrain the practical application of qMRI methods in clinical routine. One of the challenges that arise is, to find a balance between accuracy and precision of the measurement and an acceptable acquisition time. Using

larger accelerations or less sampling points and therefore shorter measurement times will give rise to lower SNR or larger fit errors, which propagate to the precision of the final quantitative map. Further, the accuracy of quantitative methods is known to be influenced by several factors, e.g. field inhomogeneities (B_0) [19, 20], transmitter as well as receiver sensitivities (B_1) [21, 22] and magnetisation transfer (MT) [23, 24]. Magnetisation transfer arises from dipolar cross-relaxation or chemical exchange between two distinct species, e.g. protons in free diffusing water and protons bound to macromolecules. For quantitative results of high fidelity, those factors have to be addressed and identified, ideally on an individual basis. All possible corrections need to be applied and an extensive postprocessing chain has to be executed.

In particular the issue of magnetisation transfer and its influence on T_1 estimation has been noted by several authors [25, 26, 27, 28]. However, the topic lacks elaborate discussion by means of theoretical and experimental analysis of quantitative results. This thesis aims to investigate several aspects of T_1 mapping in the presence of MT by means of the Bloch-McConnell equations. These empirical equations describe the dynamics of protons which are transferred back and forth between two magnetic environments by kinetic nuclear processes [29]. The Bloch-McConnell equations are extended to n exchanging pools (Chapter 6). Based on these equations, the existing signal equations for T_1 estimation (Chapter 4) are reassessed employing the Bloch-McConnell equations rather than the Bloch equations (Chapter 5). The Bloch-McConnell equations for n interacting pools are integrated into the existing simulation framework for MRI simulations, jemris [30] (Chapter 6), allowing for an in-depth investigation of the effect of MT on MRI signal generation and reception. The consequences of MT on the quantification of T_1 are then investigated thoroughly in Chapter 7 and 8, where the most important T_1 quantification methods were simulated with and without MT effects. An experimental *in vivo* validation was performed for Look-Locker type sequences.

Finally, Chapter 9 presents an application for quantitative T_1 mapping. The Patlak approach [31, 32, 2, 3] for estimations of the blood-brain barrier permeability and the cerebral blood volume is derived (Section 9.2), its applicability to MRI data is shown (Section 9.3) and improvements of an existing method [15] were achieved (cf. Section 9.4). Finally, the Patlak approach is employed to obtain the permeability of the blood-brain barrier as well as the cerebral blood volume in several patients suffering from brain tumours and the results are compared to FET-PET data (cf. Section 9.6).

2. Principles of Magnetic Resonance Imaging

The field of Nuclear Magnetic Resonance (NMR) and its application for imaging purposes, Magnetic Resonance Imaging (MRI) was pioneered by Felix Bloch and Edward Mills Purcell in the 1940s. When they discovered the phenomenon of nuclear induction, they were fascinated by the potential of this new method to observe specific quantum mechanical magnetic properties of the atomic nucleus. Since then, many scientific techniques have been developed to exploit NMR phenomena to study molecular physics, crystals, and non-crystalline materials through NMR spectroscopy.
Magnetic Resonance Imaging employs the phenomenon of NMR to obtain spatially encoded information, for example of a human body. The fundamentals to obtain images rather than spectroscopic data were discovered by Herman Carr, who reported on the creation of a one-dimensional MR image in the 1950s [33]. Carr's technique was expanded by Paul Lauterbur who developed a way to generate the first MRI images, in 2D and 3D, using gradients [34]. In 1973, Lauterbur published the first nuclear magnetic resonance image. Together with Raymond Damadian, who reported that tumours and normal tissue can be distinguished in vivo by NMR [35] the basics for modern MRI were provided.
This Chapter deals with the fundamentals of the NMR signal and provides the necessary background information about MRI to understand the physical background for this work.

2.1. From Proton to Signal

2.1.1. Nuclear Spin and Magnetic Moment

NMR predicates on the fact that some nuclei, in particular water protons, possess a spin angular momentum, $\vec{I}$, and therefore generate a dipolar magnetic moment, m, when placed in an external magnetic field.
According to Quantum Mechanics, the spin angular momentum is characterised by the magnetic

quantum number, m_I, and the following relations hold [36, p.357]:

$$|\vec{I}| = \sqrt{I \cdot (I+1)}\hbar, \tag{2.1}$$

$$I_z = \hbar \cdot m_I, \tag{2.2}$$

where the nuclear spin, $I = 0, \frac{1}{2}, 1, \frac{3}{2}, ...$, is scaled with Planck's constant,

$$\hbar = \frac{h}{2\pi} = 1,05457 \cdot 10^{-34}\text{Js}. \tag{2.3}$$

The dipolar magnetic moment, $\vec{\mu}$, is connected collinear with the angular momentum [36, p.357]:

$$\vec{\mu} = g_N \cdot \mu_N \cdot \frac{\vec{I}}{\hbar} = \gamma \cdot \vec{I}, \tag{2.4}$$

where g_N is the Lande g-factor of the nucleus. $\mu_N = 5,0508 \cdot 10^{-27}$ Am^2, is called nuclear magneton and $\gamma = \frac{|\vec{\mu}|}{I} \overset{\text{Proton}}{=} 2,6752 \cdot 10^8$ rad/Ts the gyromagnetic ratio.
Placed in a magnetic field, $\vec{B} = (0, 0, B_0)^\top$, one can observe a splitting of the nuclei's spectral lines (Zeeman-Effect, cf. Figure 2.1), where the energy difference is given by

$$E = -\vec{\mu} \cdot \vec{B} = -\hbar\gamma B m_I. \tag{2.5}$$

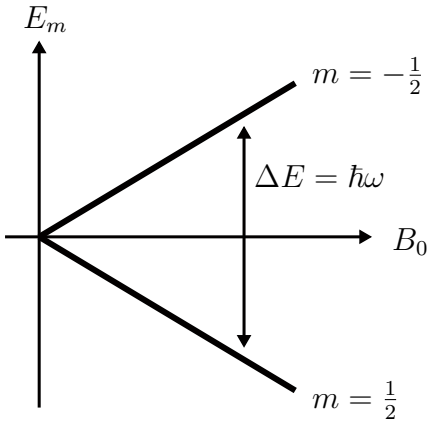

Figure 2.1: *Zeeman effect: Splitting of a spectral line in the presence of a static magnetic field into several components for a spin 1/2-nuclei.*

The occupation numbers, N_{m_I} ($m_I = +1/2$; $m_I = -1/2$), of the two (for $I = \frac{1}{2}$ nuclei) energy levels, $E_{m_I - 1}, E_{m_I}$, are Boltzmann distributed [37, p.145] with

$$\frac{N_{-1/2}}{N_{+1/2}} = e^{\frac{-\Delta E}{k_B T}} \tag{2.6}$$

with Boltzmann's constant, $k_B = 1,3806504 \cdot 10^{-23}$J/K^2, and temperature, T.

Applying the selection rule, $\Delta m_I = \pm 1$, one can use Planck's law, $\Delta E = \hbar\omega$, to derive [37, p.145]:

$$\hbar\omega = E_{m_{I-1}} - E_{m_I} = -\gamma\hbar B_0, \tag{2.7}$$

$$\omega = -\gamma B_0, \tag{2.8}$$

with the absorption frequency ω. As a consequence of Boltzmann's law more spins populate the lower energy level, where $\vec{\mu} \parallel \vec{B_0}$ is valid. At a field strength of 3 Tesla and at room temperature the ratio is 0.99998. This means, out of 10,000 protons 5001 can be found in the lower and 4999 can be found in the upper energy level.
How can these equations be used to get an insight into the human body? Considering that a drop of water contains about 10^{23} protons, this occupation difference constitutes a (macroscopic) magnetic moment. According to Hanson [38], classical treatment based on the macroscopic magnetisation, $\vec{M} = \sum \vec{\mu}/V$, is sufficient to understand the principles of MRI. Consequently, the following chapters are based on the classical theory of electrodynamics and dynamics of large nuclear spin ensembles.

2.1.2. Bloch Equations Part I: Equation of Motion

Magnetic resonance imaging employs the principle of nuclear induction, also called nuclear magnetic resonance. It was discovered and analysed first by Felix Bloch, who was awarded together with Edward Mills Purcell the Nobel Prize in Physics 1952 "*for their development of new methods for nuclear magnetic precision measurements and discoveries in connection therewith*". Following Bloch's approach [39] the Bloch equations are derived step by step:
According to the classical theory the magnetisation, $\vec{M}$, in a magnetic field, $\vec{B}$, experiences a torque, $(\vec{M} \times \vec{B})$, equal to the rate of change, $\gamma \cdot \frac{dI}{dt}$, of its angular momentum. Employing Equation (2.4), which is valid in the classical regime, the equation of motion can be derived [40]:

$$\frac{d\vec{M}}{dt} = \gamma \cdot \vec{M} \times \vec{B}. \tag{2.9}$$

For a constant magnetic field, $\vec{B} = (0, 0, B_0)^\top$, Equation (2.9) simplifies to

$$\begin{aligned} \frac{d\vec{M}_x}{dt} &= \gamma M_y B_0, \\ \frac{d\vec{M}_y}{dt} &= -\gamma M_x B_0, \\ \frac{d\vec{M}_z}{dt} &= -0, \end{aligned} \tag{2.10}$$

which can easily be decoupled and solved:

$$\begin{aligned} M_x(t) &= M_x(0)\cos(\gamma B_0 t) - M_y(0)\sin(\gamma B_0 t), \\ M_y(t) &= M_y(0)\sin(\gamma B_0 t) + M_y(0)\cos(\gamma B_0 t), \\ M_z(t) &= M_z(0). \end{aligned} \tag{2.11}$$

The magnetisation in the presence of a constant magnetic field is rotating with frequency

$$\boxed{\omega_L = \gamma B_0} \tag{2.12}$$

about the direction of B_0. $f_{\text{Larmor}} = \frac{\omega_L}{2\pi}$ is called Larmor frequency. The Larmor frequency for protons at $B_0 = 1$ T is $f_{\text{Larmor}} = \frac{\omega_L}{2\pi} = 42,58$ MHz [37, p.148].

2.1.3. Excitation

So far only constant magnetic fields (B_0) were discussed. To observe the resonance phenomenon, excitation has to be performed. This means to tip the longitudinal magnetisation (M_z) (partially). For excitation a second, rotating magnetic field, B_1, also called RF field, is necessary and is introduced with the following assumptions:

- The rotating field is weak compared to the constant field: $B_1 \ll B_0$
- Its angular frequency, ω, is in the same range as the Larmor frequency: $\omega \approx \omega_L$ (this explains the name magnetic resonance, see the subsequent sections 2.1.5)

Further assumptions are that all spins are exposed to only the external magnetic field: interactions between neighbouring spins, electric fields of the surrounding electrons and thermal motion is neglected. Then the Bloch equations (2.9) have to be solved for
$\vec{B} = (B_1(t)\cos\omega t\cos\phi(t), B_1(t)\sin\omega t\sin\phi(t), B_0)^\top$, where ϕ denotes the varying angle between $\vec{B}_1$ and the x-axis.

2.1.3.1. Non-selective Excitation

The simplest way of excitation is non-selective excitation where the whole sample volume is excited. Using the equation of motion (2.9), one obtains with

$\vec{B} = (B_1(t)\cos\omega t\cos\phi(t), B_1(t)\sin\omega t\sin\phi(t), B_0)^\top$:

$$\frac{d}{dt}\begin{pmatrix} M_x \\ M_y \\ M_x \end{pmatrix} = \begin{pmatrix} 0 & -\omega_L & \gamma B_1(t)\sin\omega t \sin\phi(t) \\ \omega_L & 0 & \gamma B_1(t)\cos\omega t \cos\phi(t) \\ -\gamma B_1(t)\sin\omega t \sin\phi(t) & -\gamma B_1(t)\cos\omega t \cos\phi(t) & 0 \end{pmatrix} \cdot \begin{pmatrix} M_x \\ M_y \\ M_z \end{pmatrix}, \quad (2.13)$$

where $\phi(t)$ labels the phase of the RF pulse, $B_1(t)$ the amplitude modulation function and ω is the angular frequency of the excitation field.

2.1.3.2. Rotating Frame Transformation

For convenience, Equation (2.13) is transformed into a frame of reference[1], which rotates about the z axis at the frequency, ω, of the excitation field. The connection between laboratory frame and the rotating frame is [41]:

$$\vec{M} = \mathbf{R}_z(\omega t)\vec{M}_{rot} = \begin{pmatrix} \cos\omega t & \sin\omega t & 0 \\ -\sin\omega t & \cos\omega t & 0 \\ 0 & 0 & 1 \end{pmatrix} \cdot \begin{pmatrix} M_{x'} \\ M_{y'} \\ M_{z'} \end{pmatrix}, \quad (2.14)$$

and

$$\vec{B} = \mathbf{R}_z(\omega t)\vec{B}_{rot}. \quad (2.15)$$

Then the equation of motion (2.9) in the rotating frame is [41]

$$\frac{d}{dt}\vec{M}_{rot} = \gamma\vec{M}_{rot} \times \vec{B}_{eff} \quad (2.16)$$

with the effective field, $\vec{B}_{eff} = \vec{B}_{rot} + \frac{\vec{\Delta\omega}_{rot}}{\gamma}, \vec{\Delta\omega}_{rot} = (0, 0, -\omega)^\top$, where $\vec{\Delta\omega}_{rot}$ denotes the off-resonance contribution of term rotating with a different frequency as the rotating frame. Introducing the complex magnetisation $M_\perp(t) = M_x(t) + iM_y(t)$, the two frames of reference are connected by $M_\perp(t) = M'_\perp(t)e^{-i\omega t}$ and $M_z(t) = M'_z(t)$.

Considering excitation on-resonance (i.e. transmitting the RF pulse at $\omega = \omega_{\text{Larmor}}$) and zero phase angle, $\phi(t) = 0$, in the rotating frame and using $\omega_1 = \gamma B_1$, Equation (2.13) becomes

$$\frac{d}{dt}\mathbf{M}_{rot} = \begin{pmatrix} 0 & 0 & 0 \\ 0 & 0 & \omega_1(t) \\ 0 & -\omega_1(t) & 0 \end{pmatrix} \mathbf{M}_{rot}. \quad (2.17)$$

This excitation will rotate the magnetisation by an angle, α, along the $x-$ axis, expressed by

[1] called rotating frame of reference, denoted by primed axes or subscript rot.

the rotation matrix, $\mathbf{R}_x(\alpha)$[2], yielding a magnetisation

$$\vec{M}(t) = \mathbf{R}_x \left(\int_0^t \gamma B_1(\tau) d\tau \right) \vec{M}(0) \ . \tag{2.18}$$

The argument of the rotation matrix is called the **flip angle**,

$$\alpha = \gamma B_1 \int_0^t f(\tau) d\tau \ . \tag{2.19}$$

It specifies the amount of magnetisation flipped onto the transverse plane. If a **rectangular pulse** is considered,

$$f(\tau) = \begin{cases} 1 & 0 < \tau < T \\ 0 & \text{otherwise} \end{cases} \tag{2.20}$$

the integral simply becomes

$$\alpha = \gamma B_1 t \ . \tag{2.21}$$

So far only on-resonance behaviour was considered; i.e. the excitation of all spins rotating at Larmor frequency. A rectangular excitation pulse allows one to treat the excitation of off-resonant spins by looking at the frequency spectrum of the excitation pulse. In case of a rectangular pulse, the Fourier transform yields a widespread, sinc-shaped frequency spectrum, which gets wider as the pulse gets shorter. Thus all spins with off-resonances within this bandwidth are excited. Usually, rectangular, short (= non-selective or hard) RF pulses are employed for MR in order to excite all spins.

2.1.3.3. Selective Excitation

Excitation of the whole volume enforces the usage of time consuming 3D readouts as the whole volume contributes to the received signal. This limitation can be overcome by the reduction of the imaging problem for example to a two dimensional problem (slice-selective excitation) or by reducing the size of the excited volume (slab-selective excitation). Selective excitation is generally achieved by the simultaneous emission of radio frequency fields and gradient pulses. One common example is the **slice-selective excitation** where a slice with limited thickness

[2] $\mathbf{R}_x(\alpha)$ is defined as $\begin{pmatrix} 1 & 0 & 0 \\ 0 & \cos\alpha & \sin\alpha \\ 0 & -\sin\alpha & \cos\alpha \end{pmatrix}$

is excited. This can be done by the emission of sinc ($=^{\sin(x)}/_{x}$) shaped RF pulses under the presence of a constant slice selection gradient. The frequency spectrum of such a pulse can be obtained by Fourier transforming the excitation pulse. A desired rectangular slice profile will then require an ideal sinc pulse of infinite duration. Usually, the slice thickness in MRI is defined as the portion of spins at the resonance frequency plus / minus the off-resonant area between the two half bandwidth limits of the pulse. Accompanied by the induced gradients the resonance frequency varies locally and slice selection is achieved (cf. Figure 2.2).

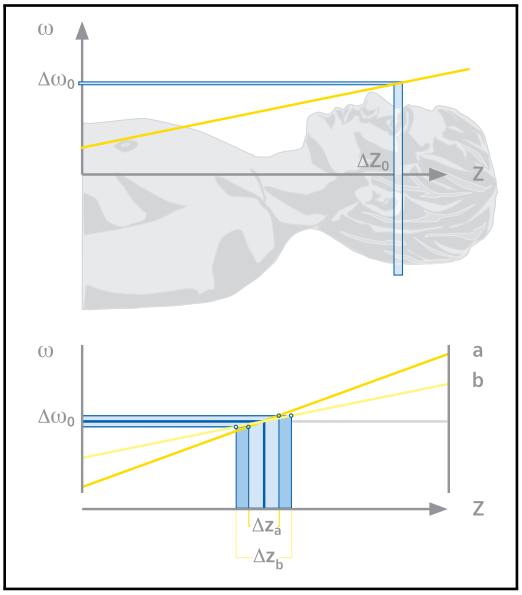

Figure 2.2: *Slice selection: A gradient (a,b) changes the resonance frequency (ω_0) locally, the RF pulse selects the spins which fit the resonance condition (blue slice) [42].*

The equation of motion (2.9) in the rotating frame for slice-selective excitation reads:

$$\dot{\vec{M}}_{rot}(z,t) = \begin{pmatrix} 0 & \gamma g_z z & 0 \\ -\gamma g_z z & 0 & \omega_1(t) \\ 0 & -\omega_1(t) & 0 \end{pmatrix} \vec{M}_{rot}(z,t) \ . \tag{2.22}$$

Unfortunately, there is no analytical solution of Equation (2.22) in the general case. The equations can be decoupled by application of the **small tip angle approximation** [41], which is valid for:

- initially pure longitudinal magnetisation $M_z(0) = M_0$
- **weak** RF pulses resulting in flip angles of $\alpha < 30°$
- and as a consequence $M_z(t) \approx M_z(0)$

The small tip angle approximation results in the simplified and decoupled equation

$$\dot{\vec{M}}_{rot} = \begin{pmatrix} 0 & \gamma g_z z & 0 \\ -\gamma g_z z & 0 & \omega_1(t) \\ 0 & 0 & 0 \end{pmatrix} \vec{M}_{rot} \ . \tag{2.23}$$

Though originally designed for low flip angle excitations, the small tip angle approximation can be used with high precision, also for excitations with flip angles well above 30° [43]. Solving Equation (2.23) for a pulse of duration τ starting at time t gives:

$$M_{\perp}(\tau, z) = iM_0 e^{-i\gamma g_z z \frac{\tau}{2}} \mathcal{F}\left\{\gamma B_1\left(t + \frac{\tau}{2}\right)\right\} \ . \tag{2.24}$$

The excited magnetisation is determined by the gradient amplitude and the Fourier transform of the RF pulse. The additional phase factor ($e^{-i\gamma g_z z \frac{\tau}{2}}$) in Equation (2.24) describes the dephasing of the spins during the excitation due to the slice selection gradient. Rephasing can be achieved by the application of a gradient with opposite polarity and halved moment (as only the half pulse duration does appear in the phase factor). This so-called refocussing gradient will become important in the following sections, e.g. 2.3.1.
A rotation of the slice is achieved by a rotation of the gradient system, i.e. by appropriately chosen currents driving the gradient coils. An off-centre shift is achieved by intentionally shifting the centre frequency of the transmitter.

2.1.4. Bloch Equations Part II: Relaxation

Until now, the equations of motion for magnetisation in a magnetic field were introduced neglecting all kinds of interactions between neighbouring spins. These simplifications have to be reassessed in practise, as the spin environment affects their dynamics. In particular, the presumption of no internuclear interactions and no thermal agitation has to be reconsidered. Internuclear interaction generates internal fields which are considerably weaker than the external fields applied, but nevertheless of importance due to their cumulative effects over longer periods of time [39]. Felix Bloch added phenomenological terms to the equation of motion (the Bloch equations, (2.25)), which describe the behaviour of spins in interaction with external ($\vec{B}$) **and** internal fields.

$$\begin{aligned} \frac{d\vec{M}_{x,y}}{dt} &= \gamma(\vec{M} \times \vec{B})_{x,y} - \frac{M_{x,y}}{T_2} \\ \frac{d\vec{M}_z}{dt} &= \gamma(\vec{M} \times \vec{B})_z + \frac{M_0 - M_z}{T_1}. \end{aligned} \tag{2.25}$$

These internal fields are considered by introducing two relaxation times, the longitudinal relaxation time, T_1, and the transverse relaxation time, T_2, as well as an equilibrium value, M_0.

2.1.4.1. Longitudinal Relaxation (T_1)

The energy, $E = -\vec{m} \cdot \vec{B} = -B_0 M_z$, (see also Eq. (2.5)) of the total spin system is connected with the z-magnetisation; major changes (due to thermal perturbations) of the total energy are therefore necessarily due to changes in the z-component of the magnetisation. At equilibrium, the longitudinal component of the magnetisation, M_z, is maximal, $M_z = M_0 \propto B_0$. Applying an arbitrary RF pulse decreases M_z but if the external field, B_1, is switched off, M_z regrows back to M_0 during the relaxation process. Bloch assumed an exponential behaviour of the magnetisation, described by $M_z(t) = M_0 + (M_z(0) - M_0)\, e^{-\frac{t}{T_1}}$, where the characteristic time constant, T_1, was named thermal or longitudinal relaxation time [39], sometimes it is called spin-lattice relaxation time. T_1 was defined as the time which is required by M_z to regrow to $\left(1 - \frac{1}{e}\right)$ after a RF pulse with 90° flip angle.
Longitudinal relaxation is caused by thermal motion, interactions (vibrations, rotations, field fluctuations) of the spins with their surroundings, the system tends to its energy minimum and the absorbed energy is dissipated to the surroundings. This energy conformation happens essentially by stimulated transmissions - and is therefore most effective if the field fluctuations are in the range of the Larmor frequency [41]. Examples are dipole-dipole interactions with other protons or electrons. Focussing on free water (small molecules), the T_1 values are quite long as the molecules move quickly. Bound water, e.g. bound on proteins, moves much slower and its relaxation times are shorter (cf. Chapter 3). Of practical interest is the fact that different tissues of the human body have different relaxation times due to their diverse water content and surroundings (Table 2.1).

Tissue	$\mathbf{T_1}$**/ s**	$\mathbf{T_2}$**/ ms**
Free water	≈ 4	≈ 1000
Muscle	$0,73 \pm 0,13$	47 ± 13
Heart	$0,75 \pm 0,12$	57 ± 16
Liver	$0,42 \pm 0,09$	43 ± 14
Kidney	$0,59 \pm 0,16$	58 ± 24
Spleen	$0,68 \pm 0,19$	62 ± 27
Fat	$0,24 \pm 0,07$	84 ± 36

Table 2.1: *Examples of relaxation times at $B_0 = 1$ T ([37, p.150]).*

2.1.4.2. Transverse Relaxation ($\mathbf{T_2}$)

Internuclear actions with neighbouring nuclei as well as magnetic moments generated by paramagnetic ions do not change the total energy of the spin system. However, these local fields influence the transverse components of the magnetisation. The resonance frequency is shifted

slightly by these fields, different spins have different resonance frequencies. As a consequence, the spins start to loose their phase coherence leading to a decay of the total transverse magnetisation[3]. Again, exponential decay is assumed and described by $M_{x,y}(t) = -e^{\frac{-t}{T_2}} \cdot M(t=0)$; the time constant T_2 is called transverse relaxation or spin-spin relaxation time. Transverse relaxation is an entropy effect - contrary to the energy effect of longitudinal relaxation [37].

2.1.5. Signals

2.1.5.1. Signal Detection

Excitation of a spin system by an α-pulse around the x'-axis will change the magnetisation vector according to:

$$\begin{aligned} M_x(0) &= -M_0 \sin\phi, \\ M_y(0) &= \ M_0 \sin\alpha \cos\phi, \\ M_z(0) &= \ M_0 \cos\alpha. \end{aligned} \tag{2.26}$$

The angle between B_1 and the x'-axis is given by the dephasing angle, ϕ, which is zero directly after excitation as the spins are in phase. According to the Bloch equations (2.25), the magnetisation is time dependent:

$$\begin{aligned} M_\perp(t) &= M_\perp(0) e^{-i(\phi+\omega_L t)-\frac{t}{T_2}}, \\ M_z(t) &= M_0 + (M_z(0) - M_0)\, e^{-\frac{t}{T_1}}. \end{aligned} \tag{2.27}$$

In pursuance of Faraday's law, the electromotive force, EMF, induced in a nearby placed receiver coil is equal to the time rate of change of the magnetic flux, Φ, through the coil:

$$EMF(t) = -\frac{\partial \Phi(t)}{\partial t}, \tag{2.28}$$

The magnetic flux, Φ, through an object, A, within a magnetic field, $\vec{B}$, is defined by

$$\Phi(t) = \int\limits_{\text{Volume}} \vec{B} \cdot \vec{M} d\vec{r}. \tag{2.29}$$

Note that due to the surface integral in (2.29) only the transverse components of $\vec{M}$, i.e. $\vec{M}_\perp$ contribute to the magnetic flux. Rewriting Equation (2.29) and neglecting the longitudinal

[3]This effect is similar to the slice-selective excitation where the applied slice selection gradient causes the dephasing.

components leads to

$$EMF(t) = -\int\limits_{\text{Volume}} \left(B_x(\vec{r}) \frac{\partial M_x(\vec{r},t)}{\partial t} + B_y(\vec{r}) \frac{\partial M_y(\vec{r},t)}{\partial t} \right) d\vec{r}. \tag{2.30}$$

For technical reasons (see e.g. [41]), the x- and y- components are shifted by a 90° phase - one can obtain phase and amplitude information of the signal which is proportional to the transverse magnetisation $M_\perp = M_x + iM_y$ (quadrature detection).
Using the quadrature detection, Equation (2.30) can be rewritten (cf. [44]) to derive the equation describing the received signal, S, the signal equation:

$$S(t) = \int\limits_{\text{Volume}} M_{xy}(\vec{r},0) e^{-i\gamma\Delta B(r)t} e^{-t/T_2^*} d\vec{r}. \tag{2.31}$$

2.1.5.2. FID and Signal Equation

The Free Induction Decay (FID) is an essential module of MR sequences. It is the reception of the induced signal following excitation, the received signal is described by the signal equation (2.31). Other basic modules are spin echo (cf. Section 2.1.6) and gradient echo.

The magnetisation within an isochromatic bulk[4], dM_{xy}, within the object of interest can be characterized by its spin spectral density, $\rho(\omega)d\omega$. Rewriting the signal equation leads to

$$S(t) = \sin\alpha \int\limits_{-\infty}^{\infty} \rho(\omega) e^{-i\omega t} e^{-t/T_{2(\omega)}} d\omega. \tag{2.32}$$

Considering a spin system composed of a single spectral component resonating at frequency, ω_0, the received signal (the FID) is (according to Eq. (2.32))

$$S(t) = M_0 \sin\alpha \, e^{-i\omega_0 t} e^{-t/T_2}. \tag{2.33}$$

Figure 2.3 displays the signal evolution and visualises the term free induction decay.

2.1.5.3. Effective Transverse Relaxation T_2^*

Static inhomogeneities (= small variations in B_0, e.g. caused by local susceptibility gradients or due to hardware imperfections) cause spin dephasing as well (cf. Figure 2.4).
Assuming a Lorentzian distribution of the field inhomogeneities, the spectral density has to be

[4] Isochromats are spins, which experience the same magnetic field and have therefore the same resonance frequency.

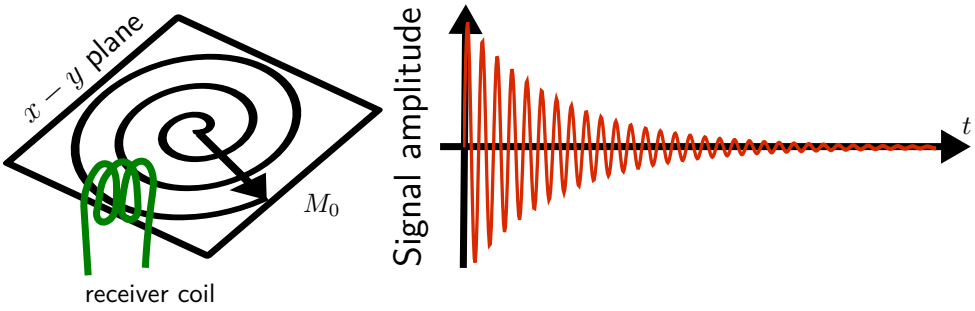

Figure 2.3: *FID signal. The receiver coil detects the decaying transverse magnetisation.*

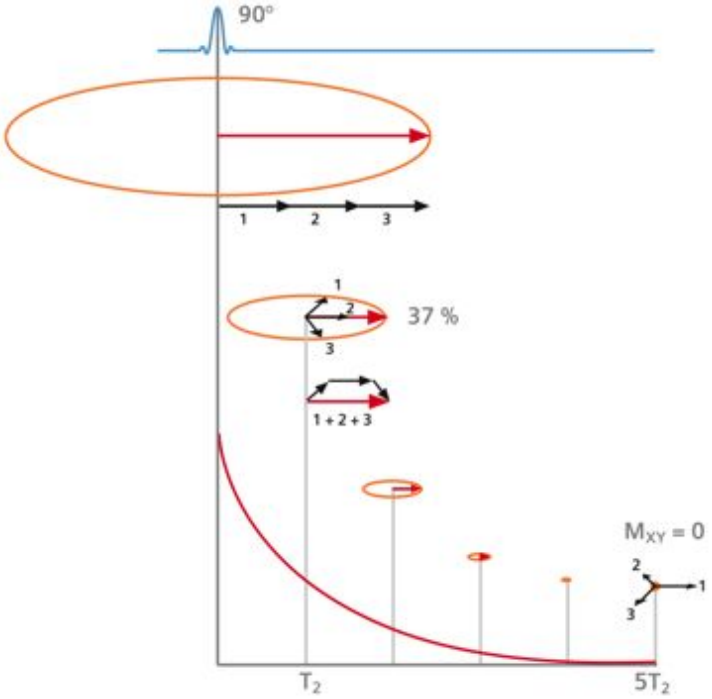

Figure 2.4: *Dephasing spins [42].*

modified as

$$\rho(\omega) = M_0 \frac{(\gamma \Delta B_0)^2}{(\gamma \Delta B_0)^2 + (\omega + \omega_0)^2}. \tag{2.34}$$

Including these inhomogeneities into Equation (2.32) its solution becomes

$$S(t) = \pi \, \gamma \, \Delta B_0 \, M_0 \sin \alpha \, e^{-i\omega_0 t} e^{-t/T_2^*}, \tag{2.35}$$

where

$$\frac{1}{T_2^*} = \frac{1}{T_2} + \gamma \Delta B_0. \tag{2.36}$$

In the presence of such inhomogeneities the transverse relaxation time is shorter and is termed T_2^*. In Figure 2.3 T_2^* is visible as the envelope of the decaying (FID) signal.

Equations (2.35) and (2.36) are commonly used in MRI, however, they are only valid if the local field fluctuations origin from a Lorentzian distribution. Then the envelope function of an FID is an exponential with the effective relaxation time, T_2^*. The Bloch equations assume exponential relaxation but this is not necessarily the case [44, p.111]. For example in the presence of nonlinear field gradients [45] or linear field gradients within one voxel the signal decay is not pure exponential but e.g. sinc modulated.

2.1.6. Spin Echo, T_2 and T_2^*

Disturbing the magnetisation by two successive RF pulses produces a so-called spin echo (cf. [46]), a second, weaker signal which follows an FID. Applying a 90° pulse followed by a 180° pulse after a time, τ, is the most used pulse series of a spin-echo sequence. Combinations of other flip angles are possible as well (but produce smaller signal intensities). Figure 2.5 displays a spin echo sequence.

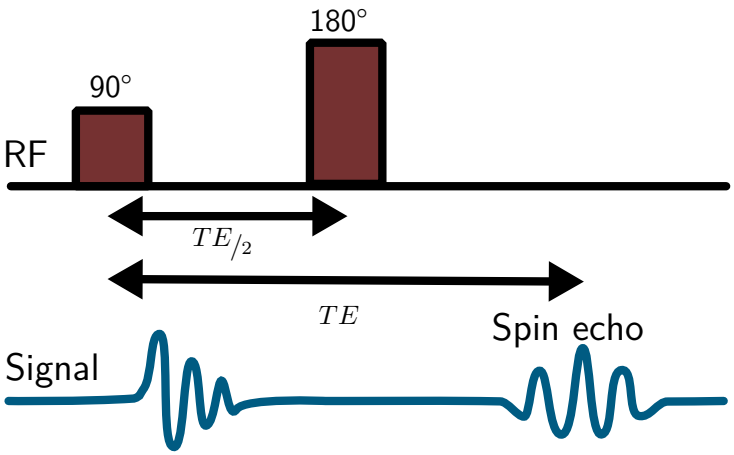

Figure 2.5: *Spin echo.*

The first pulse flips the magnetisation completely into the transverse plane (x-y plane), a FID can be observed - the transverse magnetisation decays due to the loss of phase coherence of the spins. After a time, $\tau = {}^{T_E}/_2$, the second pulse (180°) inverts the diverging spins and causes again their convergence. At time TE the spins are in phase again and the signal increases - the spin echo can be observed.

In terms of equations, the dephasing angle (cf. Equation (2.26)), ϕ, is described by

$$\phi(t) = \int_{t_0}^{t} \omega(\tau) d\tau, \tag{2.37}$$

where ω denotes off-resonance contribution due to B_0 inhomogeneities. The first pulse acts at time t_0. The 180° pulse inverts its sign ($\phi = \phi + \pi = -\phi$) and at time TE the integral equals zero, if $\omega = \gamma B_0$ is time independent. This is sketched in Figure 2.6. It has to be noted that a

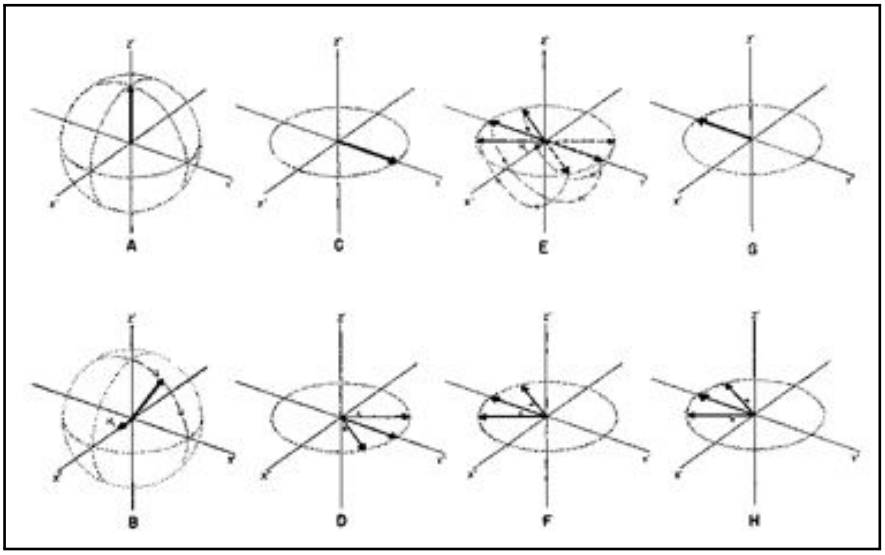

Figure 2.6: *Creation of a spin echo [47]: A) All spins are aligned parallel to B_0. B,C) M_z is flipped into the x-y-plane by the 90° pulse. D) Spins dephase due to B_0 inhomogeneities. E) The spins are inverted by the 180° pulse. F) The spins converge, they rephase again. G) All spins are in phase ⇒ the echo can be detected. H) The spins dephase again.*

spin echo can only revert static field inhomogeneities ($\Delta\omega = \gamma \Delta B_0$ time independent). Dynamic field inhomogeneities differ between the two times and are therefore not rephased - the integral is not zero. This difference is reflected in the **two** transverse relaxation times: The FID is enveloped by T_2^* (static inhomogeneities) while the amplitude of the spin echo is modulated by T_2. Repeated pulsing with 180° pulses demonstrates the T_2 decay, illustrated in Figure 2.7.

2.2. Spatial Encoding

Bridging the gap from Nuclear Magnetic Resonance to Magnetic Resonance Imaging requires a technique to spatially resolve the received signals. Therefore the basic idea of magnetic resonance imaging can be employed: “make the precessional frequency a function of position!”

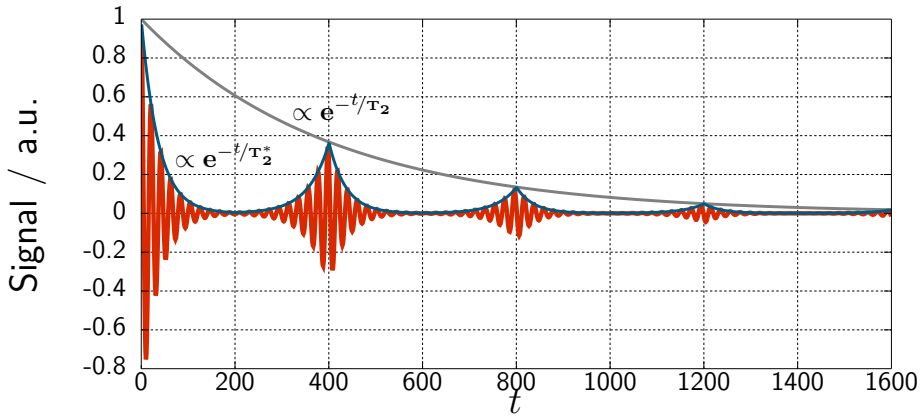

Figure 2.7: *Signal decay in a multiple-echo spin echo sequence. Successive echoes are enveloped by T_2 while the FIDs are shaped with T_2^* due to field inhomogeneities.*

2.2.1. Phase and Frequency Encoding

Section 2.1.3.3 already introduced slice-selective excitation. For imaging, spatial encoding of the remaining xy-plane is required; therefore two more gradients, the frequency encoding gradient, G_x, and the phase encoding gradient, G_y, have to be applied orthogonal to each other.
The phase encoding gradient acts first as it has to be completed before the resonance signal is detected. This gradient triggers different resonance frequencies along the gradient direction (cf. Figure 2.8) and creates a spatially dependent phase shift

$$\Phi_{G_y}(y,t) = \int_0^t \omega_G(y,\tau)d\tau = \gamma\, y \int_0^t G_y(\tau)d\tau. \tag{2.38}$$

The longer the phase encoding gradient is on duty or the stronger it is, the larger are the phase differences of the correlated single spins (Figure 2.9). The phase shift is maintained after switching off the gradient while the precession frequency, ω_0, remains the same for all spins within the slice.

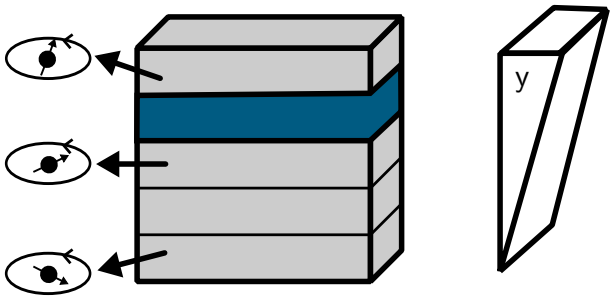

Figure 2.8: *Phase encoding: each horizontal line can be identified by their unique phase.*

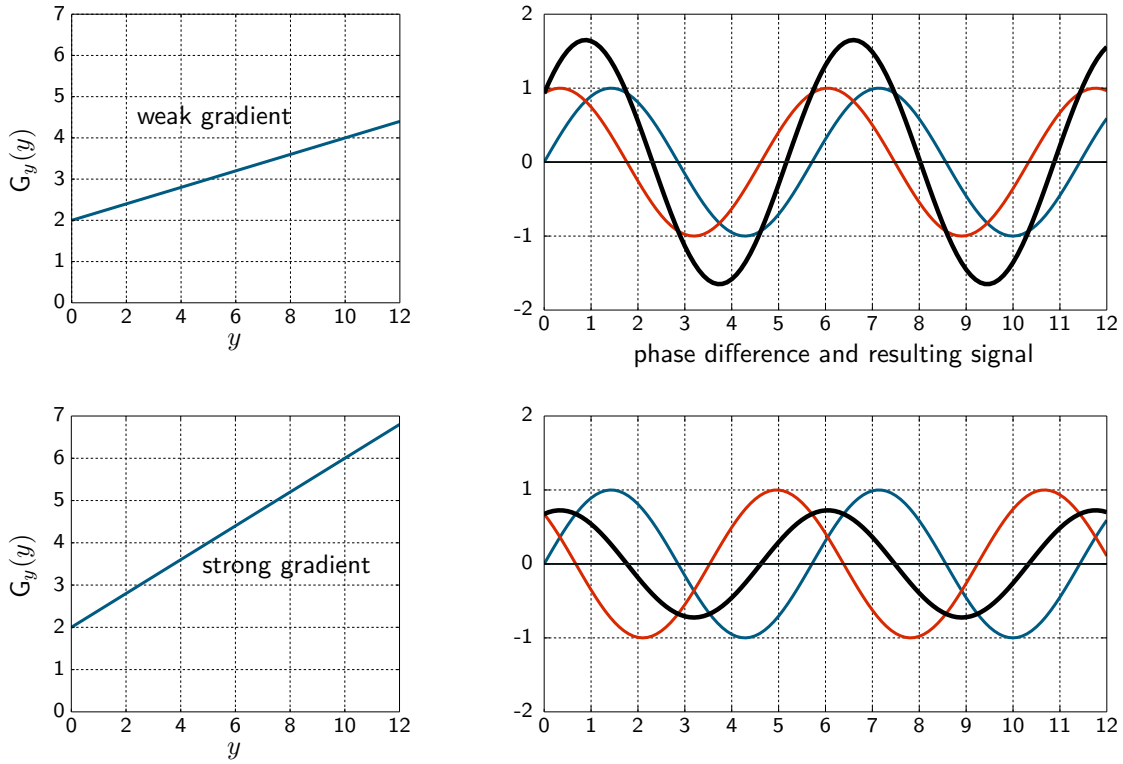

Figure 2.9: *The signal amplitude (black) depends on the phase difference of the single oscillations (red and blue) and therefore on the phase encoding gradient.*

Upon phase encoding, the MR signal is measured. During reception, the frequency encoding takes place. Again a linear gradient, G_x, is applied and enforces different resonance frequencies - resulting in different phase shifts

$$\Phi_{G_x}(x,t) = -\gamma\ x \int_{t_0}^{t_x} G_x(\tau)d\tau \tag{2.39}$$

along the x-axis (Figure 2.10). Phase and frequency encoding change the phase of the magnetisation. In other words, the magnetisation vector is turned (with respect to the location) in the complex x-y plane. Focussing on a single voxel (voxel = *vo*lume *el*ement, pixel in 3D), the magnetisation after spatial encoding reads

$$M_{xy}(x,y,\Phi_{G_x},\Phi_{G_y},t) = M^0_{xy} e^{i(\Phi_{G_x}(x,t)+\Phi_{G_y}(y,t))} \tag{2.40}$$

with M^0_{xy}, the magnetisation prior encoding. Therefore, each voxel emits a unique signal. During

reception all unique signals are received at the same time and add up to the measured signal

$$S(\Phi_{G_x}, \Phi_{G_y}) \propto \sum_{\text{Volume}} M_{xy}(x, y, t_0) e^{i\left(\Phi_{G_x}(x)+\Phi_{G_y}(y)\right)}. \tag{2.41}$$

As the spin distribution is continuous, the sum has to be replaced by the integral

$$S(\Phi_{G_x}, \Phi_{G_y}) \propto \int_{\text{Volume}} M_{xy}(x, y, t_0) e^{i\left(\Phi_{G_x}(x)+\Phi_{G_y}(y)\right)} dxdy. \tag{2.42}$$

Defining the wave number, k_j, $j = \{x, y\}$ as

$$k_j = \frac{\Phi}{j} = \gamma \int G_j(\tau) d\tau \tag{2.43}$$

leads to:

$$\begin{aligned} S(k_x, k_y) &\propto \int_{\text{Volume}} M_{xy}(x, y, t_0) e^{-i(k_x x + k_y y)} dxdy, \\ S(\vec{k}) &\propto \int_{\text{Volume}} M_{xy}(\vec{x}, t_0) e^{-i\vec{k}\cdot\vec{x}} d\vec{x}. \end{aligned} \tag{2.44}$$

A closer look on Equation (2.44) discloses that the magnetisation and the measured MR signal are linked by the Fourier transform. As this transformation can be inverted, the spatial information (e.g. anatomical structures) can be gained by the inverse Fourier transform of the received signal:

$$M_{xy}(\vec{x}) \propto \int_{\text{Volume}} S(\vec{k}) e^{i\vec{k}\cdot\vec{x}} d\vec{x}. \qquad \text{"Signal equation"} \tag{2.45}$$

2.2.1.1. The k-Space Formalism

The MR imaging process can be described using the k-space formalism. Equation (2.44) introduced the wave number, k. Moreover, the phase terms in this equation can be interpreted as a trajectory through the reciprocal space, the k-space. Image and k-space are connected by the Fourier transform. The centre of the k-space represents the observed signal without any gradients switched on. Applying G_x is equivalent to travelling along the k_x axis in k-space (cf. Figure 2.11, 2.12 and Figure 2.13).

Discretisation Until now, the formalism was continuous. In reality, the MR signal is acquired digitally and therefore discrete. As a consequence, the k-space is not a continuous construct but is build up of discrete points. The spacing between these points, Δk, determines the field of

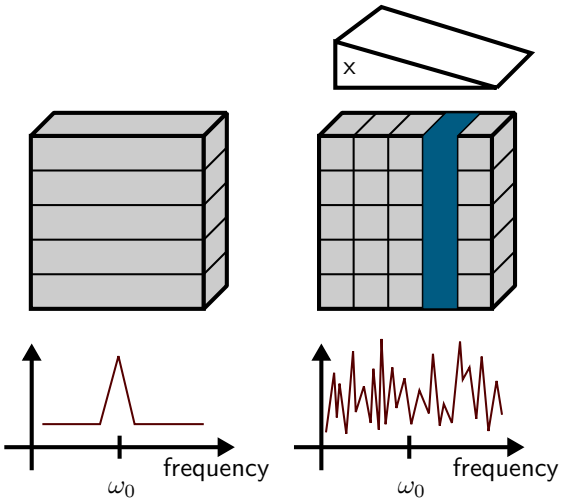

Figure 2.10: *Frequency encoding: on the left is a phase encoded slice, all spins within one line precess with the same Larmor frequency while the phase differs. On the right the read out gradient (frequency encoding gradient) is on duty and each row possesses its own resonance frequency. All signals add up to the received signal which can be decomposed by the inverse Fourier transform.*

view (FOV) which is given by[5]

$$\mathrm{FOV}_{x,y,z} = \frac{1}{\Delta k_{x,y,z}} \ . \tag{2.46}$$

In contrast, the extent of the sampled k-space will determine the spatial resolution, which corresponds to the highest sampled spatial frequency (usually referred to as $\vec{k}_{max}$), and therefore,

$$\delta_{x,y,z} = \frac{\mathrm{FOV}_{x,y,z}}{N_{x,y,z}} = \frac{1}{k_{\mathrm{max},x,y,z}} \ . \tag{2.47}$$

The k-space representation is equivalent to a representation of the object in the real space and thus, if all necessary spatial frequencies are acquired it is possible to reconstruct an image of the object from the k-space data.
Image acquisition happens typically by subsequently filling the k-space, primarily line by line[6]: The phase encoding gradients, k_y, are held constant for one line while frequency encoding, $k_x \in [-k_{max}, k_{max}]$, is varied to walk along the whole line in k-space (Figure 2.11 and 2.12).
Image contrast is stored in the area around the k-space centre ($\widehat{=} k_x = k_y = k_z = 0$) while details and edges are located at the border. The whole imaging process is displayed in Figures 2.13 and 2.14.

3D Imaging Until now, slice-selective imaging was explained. "Real" 3D imaging can be performed, if the slice selection gradient, G_z, is replaced by another phase encoding gradient

[5] this is a property of the discrete Fourier transformation
[6] Other trajectories are possible as well, referred to as non-cartesian imaging.

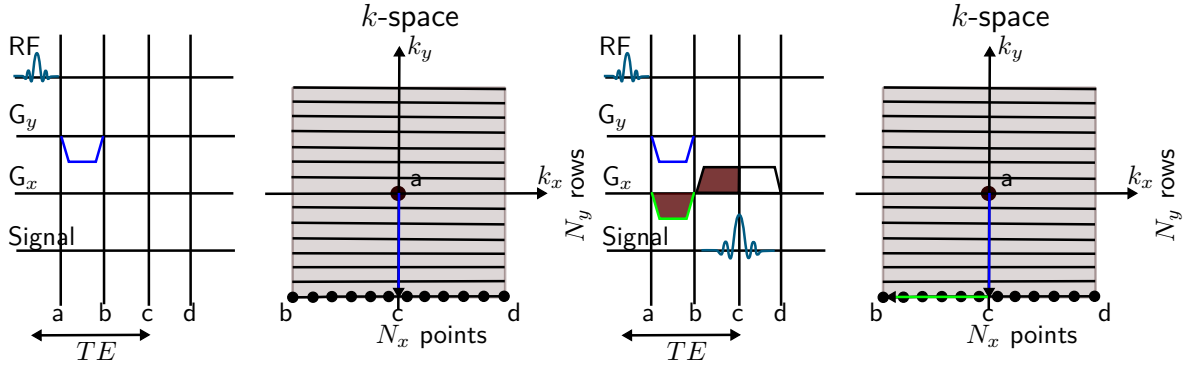

Figure 2.11: *Filling the k-space: the line which will be acquired is addressed by the phase encoding gradient, G_y, (blue arrow). Image information (black dots) is obtained while the echo occurs with the frequency-encoding gradient on.*

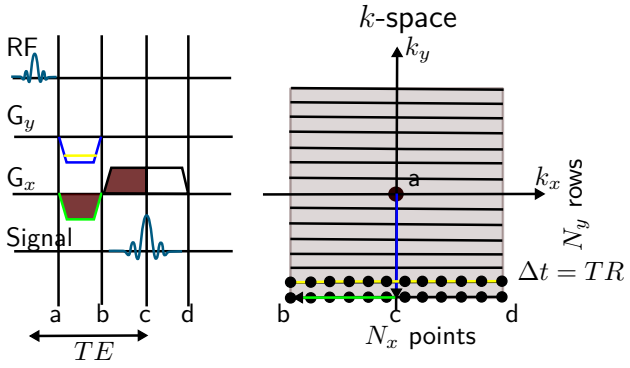

Figure 2.12: *Adjusting the phase encoding gradient, G_y (yellow), gives the next line in k-space.*

in slice direction (z direction) before readout. As a consequence, for n slices n repetitions in z direction are needed and the image can be reconstructed by a 3D Fourier transform.

2.3. Pulse Sequence Diagrams

Merging the fundamentals of MRI explained in the previous sections leads to pulse sequence diagrams. These are schemes, which describe the subsequent steps needed to acquire a MR image. The basic run of a sequence includes excitation of the spins with a slice-selective pulse, phase encoding, frequency encoding and finally readout. Each pulse sequence is repeated with repetition time, TR, as often as phase encoding steps are required to fill the k-space. Basically one distinguishes between Spin Echo (SE) and Gradient Echo (GRE) sequences.

2.3.1. Spin Echo Sequence

Figure 2.13 displays the timing diagram of a Spin Echo sequence. The three gradients required for spatial encoding are the slice selection gradient, G_S, the frequency encoding gradient, G_F, and the phase encoding gradient, G_P.

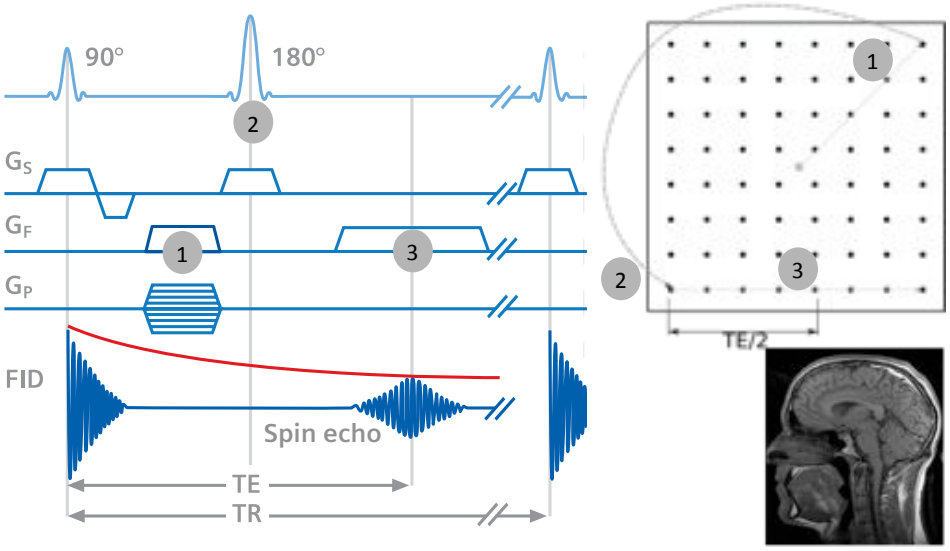

Figure 2.13: *Timing diagram of a spin echo sequence [42] and the corresponding k-space trajectory (courtesy Daniel Brenner): During an appropriate slice selection gradient, G_S, the magnetisation is flipped by a 90° pulse. Phase encoding by G_P occurs and at the echo time, TE, the echo is recorded with the frequency encoding gradient, G_F, activated. The whole procedure is repeated with a different phase encoding gradient after time TR.*

- Slice selection:
  - Each time an excitation pulse is applied to the system, a slice selection gradient assures that this pulse acts only within the slice or area of interest.
  - The slice selection gradient is followed by a rephaser gradient to maintain the spins' phase coherence.
- Phase encoding:
  - A phase shift is generated by the G_P gradients and assigns a phase to the spins. In the k-space formalism, this is equivalent to going along the k_y axis. The area of this gradient changes in each TR cycle to cover the whole k-space. 1
- Frequency encoding:
  - The G_F gradient ensures that the k-space is filled symmetrically, the spins start to dephase. 1

- Inversion pulse (Spin Echo):
  - The dephasing magnetisation is inverted by an 180° pulse at $TE/2$ (cf. Section 2.1.6 likewise), the slice selection gradient ensures, that this happens only within the slice of interest. In k-space, this is represented by taking the complex conjugate. 2
- Echo and readout:
  - The echo occurs $TE/2$ after the inversion pulse. 3
  - Frequency encoding by G_F gives the spatial encoding for the third dimension. G_F is also called readout gradient.

Spin Echo sequences provide usually high quality images as static inhomogeneities are zeroed out.

2.3.2. Gradient Echo Sequence

Gradient Echoes (cf. Figure 2.14) are characterised by a rephasing gradient instead of an 180° pulse. The 90° excitation pulse flips the magnetisation to:

$$M_z = M_0 \tag{2.48}$$

$$M_\perp = 0. \tag{2.49}$$

Then relaxation takes place. M_z recovers back to M_0 and the spins dephase resulting in a decay of the transverse magnetisation $M_\perp$. The "natural" dephasing due to different resonance frequencies, ω, is accelerated in a Gradient Echo sequence by a gradient, $\vec{G}(\tau)$, resulting in a faster dephasing process 1. The phase, ϕ, changes in the presence of the gradient to [48, p.472]

$$\phi(\vec{r}, t) = \gamma \, \vec{r} \int_0^t \vec{G}(\tau) d\tau. \tag{2.50}$$

If the gradient is switched on and off in a way that the integral vanishes at a time TE, a Gradient Echo or Gradient Recalled Echo occurs as the spins are rephased in that moment 2. Equation (2.50) neglects dephasing due to field inhomogeneities, which cannot be restored by a Gradient Echo - in opposite to a Spin Echo. As a consequence, the signal intensity in a Gradient Echo is modulated with T_2^* instead of T_2 in a Spin Echo - Gradient Echoes are much more sensitive to susceptibility changes. One advantage of a Gradient Echo is that shorter measurement times are possible due to the missing refocusing pulse and the accelerated Echo generation.

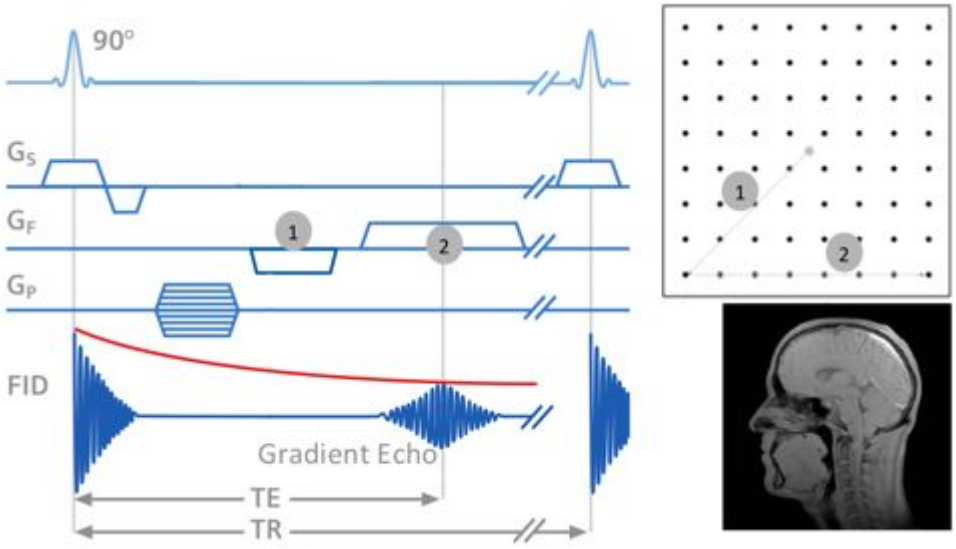

Figure 2.14: *Gradient Echo [42] and the corresponding k-space trajectory (courtesy Daniel Brenner), cf. Section 2.3.2 for details.*

The main differences between Gradient and Spin Echo are the (missing) 180° pulse and the frequency-encoding gradient. A Spin Echo employs two gradients with the same sign while in a Gradient Echo two gradient lobes with different sign are applied. The different sign is attributed to the inversion pulse.

2.4. Steady-State and Saturation

2.4.1. Steady-State

Considering a simple gradient echo pulse sequence, the Bloch equations (2.25) can be solved to predict the MR signal obtained by this sequence. If the repetition time, TR, is in the order of T_1 of the sample or shorter, the spins are not fully relaxed when the next pulse disturbs the magnetisation. Disturbing the magnetisation repeatedly (equally spaced in time) by RF pulses will lead to the development of a steady-state magnetisation, M_{SS}, which is smaller than the thermal equilibrium value, M_0. The quantity of M_{SS} is determined by the T_1 value of the tissue as well as by the TR and the flip angle of the RF pulses.
The value of M_{SS} can be determined using the Bloch equations by looking at the longitudinal magnetisation after a series of n pulses with a flip angle, α, applied after a time, TR (cf. Figure 2.15).

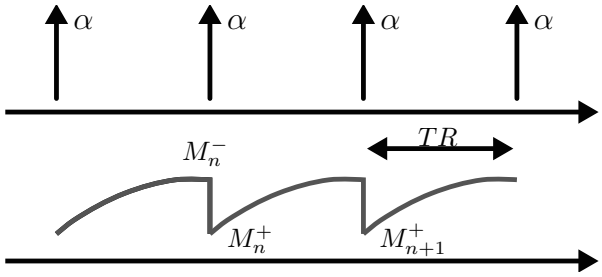

Figure 2.15: *Repeated gradient echo sequence: A string of readout pulses separated by TR, resulting in a steady-state magnetisation.*

The longitudinal components before (M_n^-) and after (M_n^+) the n-th pulse are related by

$$M_n^+ = M_n^- \cos\alpha. \tag{2.51}$$

Subsequently to the first pulse, the magnetisation is

$$M_1^+ = M_1^- \cos\alpha. \tag{2.52}$$

After a time, $t = T_R \gg T_2$, relaxation took place (with the abbreviation $E_1 = e^{-\frac{T_R}{T_1}}$):

$$\begin{aligned} M_1^+(T_R) = M_2^- &= M_0 + [M_z(t=0) - M_0]\, E_1 \\ &= M_0 + \left[M_1^- \cos\alpha - M_0\right] E_1 \\ &= M_0 + \left[M_1^+ - M_0\right] E_1 \end{aligned} \tag{2.53}$$

or, in general:

$$\begin{aligned} M_n^+(T_{R,n}) = M_{(n+1)}^- &= M_0 + [M_z(t = T_{R,n}-) - M_0]\, E_1 \\ &= M_0 + \left[M_n^- \cos\alpha - M_0\right] E_1 \\ &= M_0\,[1 - E_1] + M_n^- \cos\alpha E_1 \\ &= M_0\,[1 - E_1] + M_n^+ E_1. \end{aligned} \tag{2.54}$$

During the subsequent interpulse interval (of duration TR), the longitudinal component will relax to

$$M_{n+1}^- = M_n^+ E_1 + M_0(1 - E_1). \tag{2.55}$$

The steady-state condition is given by

$$M_{n+1}^{-} = M_n^{-} = M^{-}. \tag{2.56}$$

Mixing all together, the so-called Ernst equation is derived:

$$\begin{aligned} M_{n+1}^{-} = M_n^{-} = M^{-} & \qquad (2.57) \\ \Leftrightarrow \quad M_{n+1} = M_n^{-} \cos\alpha E_1 + M_0(1 - E_1) = M_n^{-} & \\ \Leftrightarrow \quad M_n^{-}(1 - \cos\alpha E_1) = M_0(1 - E_1) & \\ \Leftrightarrow \quad M_n^{-} = \frac{M_0(1 - E_1)}{(1 - \cos\alpha E_1)}. & \qquad (2.58) \end{aligned}$$

The steady-state transverse magnetisation is then given by

$$M_{\perp}^{SS} = M_n^{-} \sin\alpha \propto \text{Signal}. \tag{2.59}$$

2.4.2. Saturation

Applying several pulses or very large flip angles to a spin system will **saturate** the spins. Solving the Bloch equations in the rotating frame for a continuous wave[7] irradiation ($B_1^{rot} = \gamma\omega_1$) with relaxation for large values of ω_1,

$$\frac{d}{dt}\mathbf{M} = \begin{pmatrix} -\frac{1}{T_2} & 0 & 0 \\ 0 & -\frac{1}{T_2} & \omega_1(t) \\ 0 & -\omega_1(t) & -\frac{1}{T_1} \end{pmatrix} \mathbf{M} - \begin{pmatrix} 0 \\ 0 \\ \frac{1}{T_1} \end{pmatrix} \mathbf{M}_0, \tag{2.60}$$

shows that the magnetisation vector approaches zero for all components (cf. Figure 2.16). This state is called saturation.

2.5. Contrasts

MR as an intrinsic multimodal imaging method offers different contrasts, which enables a wide range of applications. First, varying the different parameters, TR and TE, emphasises the different relaxation times depending on the choice of parameters. The basic contrasts are summarised in Table 2.2 and image examples are shown in Figures 2.17 to 2.19. Comparing these images shows the large potential of MRI- but this is only the tip of the iceberg. Other contrast mechanisms are, for example, diffusion, phase contrast, perfusion or magnetisation transfer. Even

[7] Continuous wave (CW) irradiation was of importance in particular in the early times on NMR. It is by definition an electromagnetic wave of constant amplitude and frequency. For NMR excitation, the frequency is chosen to be the Larmor frequency, as a consequence, it provides constant irradiation in the rotating frame.

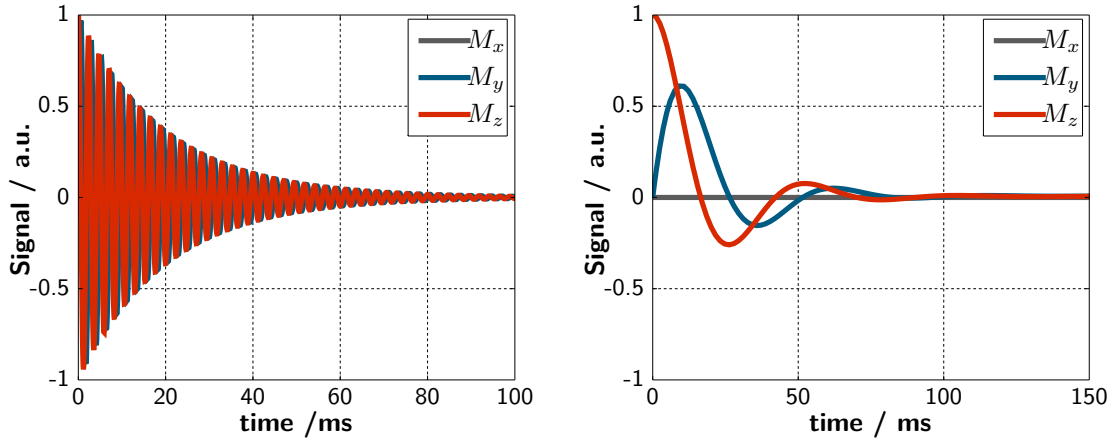

Figure 2.16: *Saturation following continuous wave irradiation ($T_1 = 100ms$, $T_2 = 10ms$, $B_1 = 10\mu T$ in the left image, $B_1 = 0.5\mu T$ in the right image). For details, please see text.*

more possibilities arise, if contrast agents are used. But this is off the topic and can be read for example in [37]. This work focuses on magnetisation transfer (MT). Details on this kind of contrast will be covered in Chapter 3.

	T_1- weighted image	T_2- weighted image	proton density weighted image
TR	$TR \approx T_1$	$TR \gg T_1$	$TR \gg T_1$
TE	$TE \ll T_2$	$T_E \approx T_2$	$TE \ll T_2$

Table 2.2: *Summary: imaging parameters and their effect on the image contrast.*

2.6. Hardware for Magnetic Resonance Imaging

Magnet The principle item of any MR system is its magnet which generates the static field B_0. Nowadays supra-conductive magnets with coils made of Nb-Ti are used primarily. To maintain the supra-conductivity, the magnets are cooled by liquid helium and liquid nitrogen. Sometimes the magnets are actively shielded to confine the magnetic field within a smaller area.

Gradient system Three gradient coils provide the linear changing magnetic fields required for encoding. The isocenter, which is located in the middle of the magnet, is the location where all three gradient fields (G_x, G_y, G_z) equal zero. Compared to the main magnetic field, B_0, the gradient fields are weak (about 40 $^{\mathrm{mT}}/_{\mathrm{m}}$).

RF System The RF system is build up by a transmit coil with amplifier and a receive coil with amplifier. Depending on the application, different kinds of coils are employed.

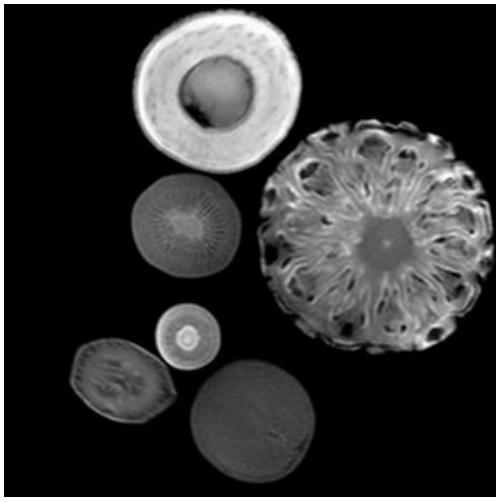

Figure 2.17: *T_1 weighted image.*

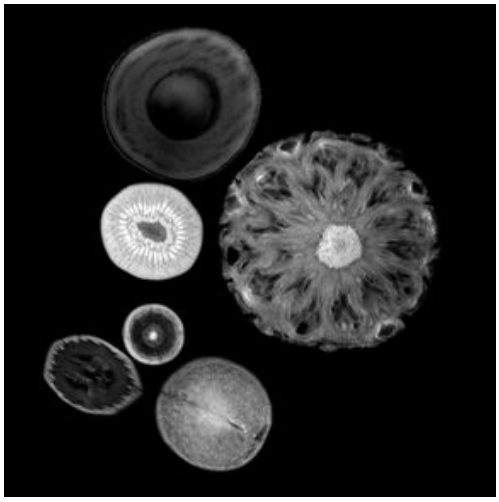

Figure 2.18: *T_2 weighted image.*

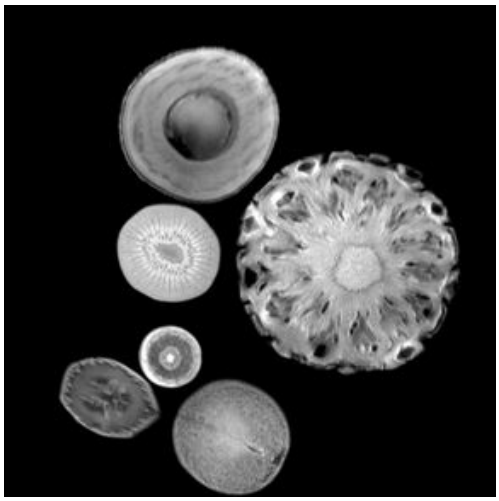

Figure 2.19: *Proton density weighted image.*

Shim coils To readjust the homogeneity of the magnetic field (which is important for image quality) when a patient or object is placed within the magnet shimming is performed. Therefore, additional shim currents are produced in the gradient system (linear) and by the higher order shim coils. The magnetic field produced by these coils add up to the main magnetic field and can be adjusted in order to improve the local homogeneity.

Image Reconstruction and Host Several computers are used to control the gradients and the RF system as well as to calculate and reconstruct the MR images based on the raw data obtained by the MR hardware.

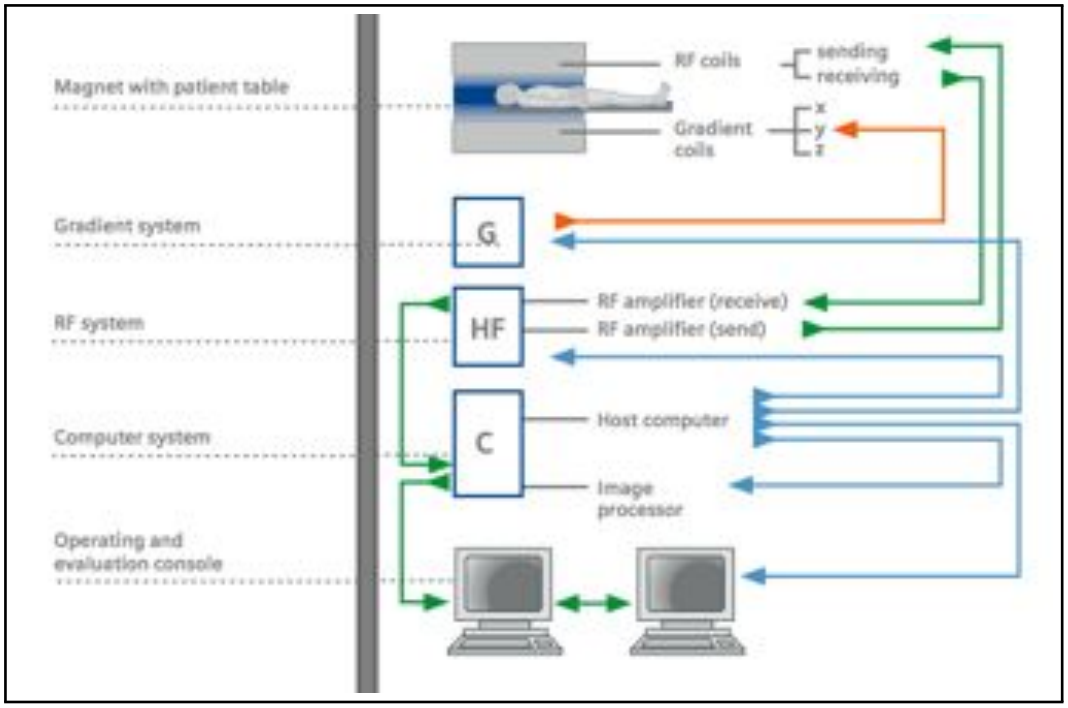

Figure 2.20: *Hardware of a MR-system [42].*

3. Magnetisation Transfer and Chemical Exchange Saturation Transfer

Image contrast in Magnetic Resonance Imaging is determined by properties of the hydrogen nuclei, embedded in water or fat ("free protons"). T_1, T_2 and proton density, ρ, weighting are the common image contrasts, see Section 2.5. Hydrogen nuclei in molecules other than water and fat ("macromolecules", "bound protons", "solid pool protons") also participate in the MR imaging process but, due to their low concentration, short T_2, or both, they cannot be easily observed directly in MR images. In conventional MR sequences, the imaging gradients cannot be switched instantaneously and the signal of the short T_2 protons has vanished before the imaging gradients can encode an image. Nevertheless, through **m**agnetisation **t**ransfer (MT), also called saturation transfer, such macromolecules can be measured indirectly with MR. By means of exchange, these components with short T_2 become visible in some cases.

Chemical **e**xchange **s**aturation **t**ransfer (CEST) is another MRI contrast mechanism, which is usually associated with **c**ontrast **a**gents (CAs). CEST contrast agents hold protons, which are characterised by a slightly different resonance frequency, ω_{CEST}, than the resonance frequency of mobile water protons, ω_0. Furthermore, these protons undergo chemical exchange with their environment. Again, this exchange mechanism facilitates an indirect measurement of the CEST agent.

This Chapter highlights the differences and similarities between MT and CEST (cf. Section 3.1) and introduces the theoretical framework for MT and CEST effects (the Bloch-McConnell equations, 3.2) in NMR and MRI. An overview over commonly used methods to employ MT (Section 3.3) and CEST effects (Section 3.4) for imaging is provided. Finally, the process of saturation is described in Section 3.5.

Both, CEST and MT influence the MR imaging process and thus modify the existing contrast.

This might be the desired effect in many cases, but there are some cases where the influence of MT (and CEST) is not desired (cf. Chapter 7 and 8.2).

3.1. MT and CEST: Similarities and Differences

CEST and MT contrasts are dominated by the exchange of magnetisation. Therefore, they are, in many way, similar in their physical mechanisms and the same mathematical framework, the two-pool model (see Section 3.2.1), can be applied to describe both. Both effects become visible after some presaturation of the non-water-pool and the visible effect is some signal reduction of the water signal due to exchange processes. Before the mathematical model is presented, the similarities and differences between CEST and MT are summarised - some details will be presented in the subsequent sections.
Both contrast mechanisms are measured similarly. The imaging procedure for MT and CEST imaging is divided into two parts:

Presaturation Pulse: Initially, the protons associated with the "invisible" pool are saturated (see Section 2.4.2) by several presaturation pulses. The effects (signal loss, saturation, change in contrast) occurring as a consequence of to the presaturation module are then recorded by an imaging sequence.

Imaging Sequence: After presaturation any imaging sequence can be used to monitor the saturation effects. Common sequences are Spin Echo, Gradient Echo or EPI sequences. Contingent on the choice of the sequence used, some more saturation effects arising from the imaging part can spoil the results by adding additional saturation to the invisible pool, e.g. by the slice selection process.

Depending on the imaging sequence, it might be necessary to repeat the saturation pulses in order to maintain the spin saturation during the experiment. The MT / CEST imaging process is described in depth in the following sections.

Although CEST and MT contrast can be generated in a similar way, some features differ.
Magnetisation Transfer is characterized by:

- Two spin pools which are treated as having *identical chemical shifts* (or identical resonance frequencies) and can be distinguished only by their relaxation parameters.
- A *spectral width* as large as *10* kHz of the semi-solid or macromolecular phase which is approximately field strength independent.

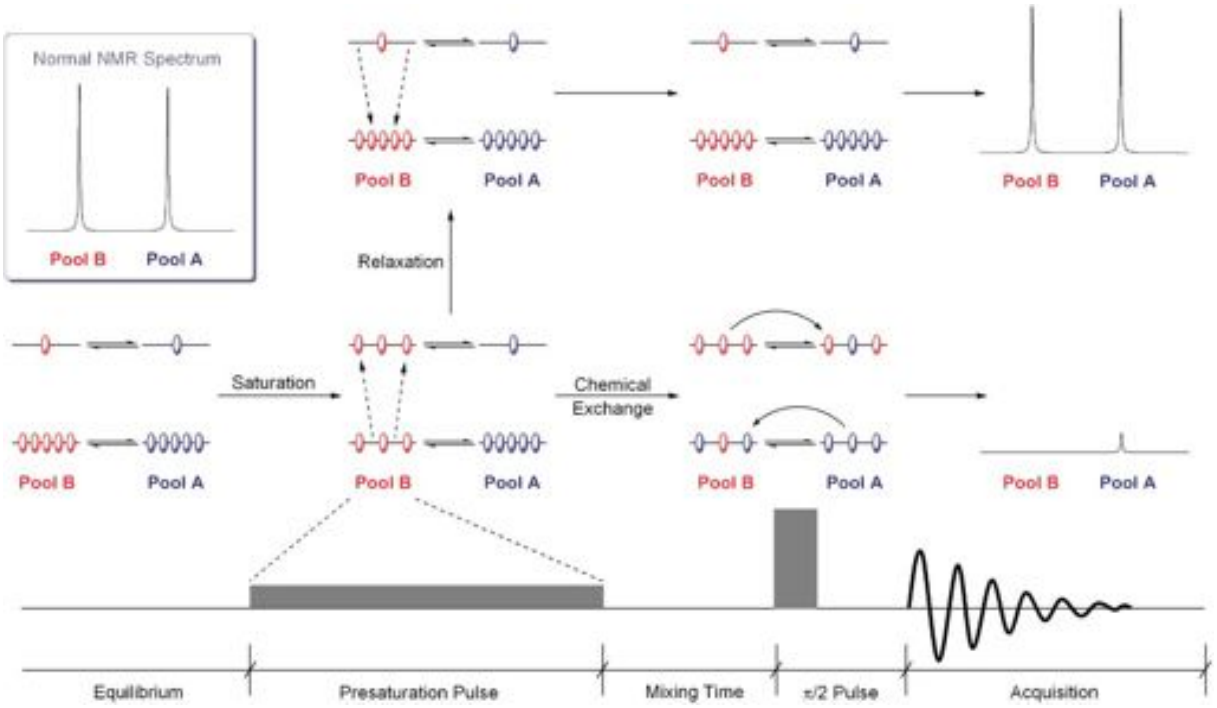

Figure 3.1: *The exemplified imaging process for CEST: A presaturation pulse applied to pool B alters the distribution of spins in this pool. If the relaxivity, $R_1^B = \frac{1}{T_1^B}$, of pool B is fast relative to the rate of chemical exchange with pool A, the spins promoted to the high energy state will relax back to the equilibrium Boltzmann distribution and a normal NMR spectrum or MR image is obtained. However, if chemical exchange is the faster process, the population densities of the high energy level will equilibrate altering the distribution of spins in pool A, reducing the bulk magnetisation of this pool. This results in a reduced signal intensity of pool B is reduced, but that of pool A is reduced as well[49].*

- Two possible molecular mechanisms are responsible for MT: *dipolar coupling* (protons from macromolecular phase → protons of hydration water on macromolecular surface → protons of unbound bulk water) and *chemical exchange* (exchangeable protons of some nearby site).

- MT can be detected over a *large frequency range* (up to 100 kHz). This is due to dipolar-dipolar interaction and chemical shift anisotropy for semi solid macromolecules in tissue groups (e.g. -OH, -SH, -NH), which mix with the ”pure“ water protons.

- Approximately *symmetric* appearance of *z-spectra* (see 3.4) with respect to water resonance with one very large peak.

- The frequency of the presaturation pulse can vary.

In contrast, **Chemical Exchange Saturation Transfer** is characterised by (cf. Figure 3.1):

- The spin system is thought to consist of two (or more) proton pools with *different chemical shifts / different resonance frequencies* and different relaxation parameters. As a consequence, the CEST saturation effect is *frequency specific*.
- It originates from mobile molecules and depends only on *chemical exchange*.
- It is usually detected in a *small chemical shift range* (less than 5 ppm); using the more advanced PARACEST agents, the range can be larger (up to several 100 ppm).
- *z-spectra* are asymmetric usually with *two well separated peaks*, a water and a CEST peak.
- Transverse magnetisation related exchange terms have to be included in the modified Bloch equations, as the transverse relaxation times are not necessarily short.
- The frequency of the presaturation pulse has to be matched to the CEST agent.

NMR spectra of MT and CEST are displayed in Figure 3.2, their z-spectra and the main different features are summarised in Figure 3.3.

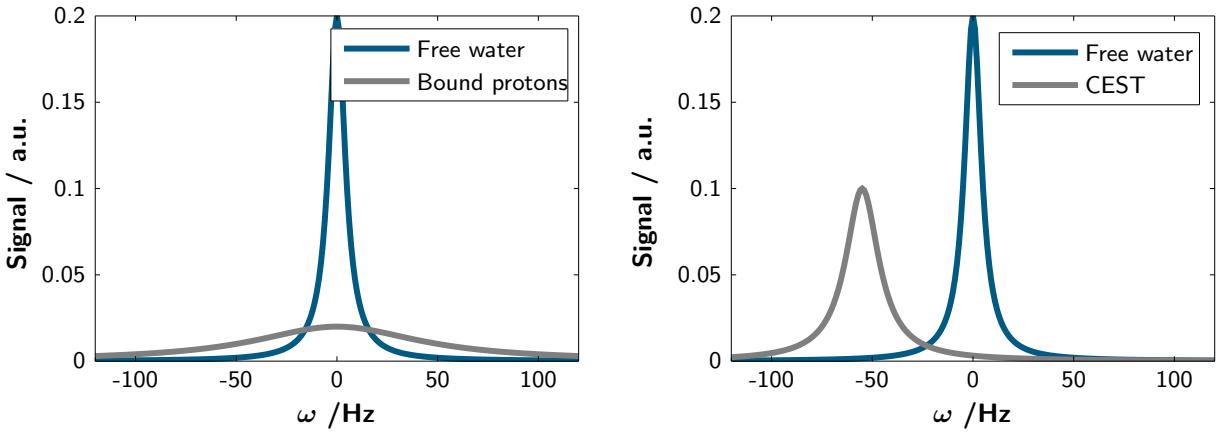

Figure 3.2: *Sketch of NMR spectra of an MT species (left) and a CEST system (right).*

3.2. Mathematical Framework

3.2.1. The Two Pool Model

In order to understand MT and CEST, usually a model of two (or more) pools is applied. Thus, all protons contributing to the imaging process are sorted into one of the two (or more) "pools":

Pool A is usually the "free water pool", which is associated with the liquid water protons one observes in "conventional" MRI. In the case of MT, this pool is characterised by long

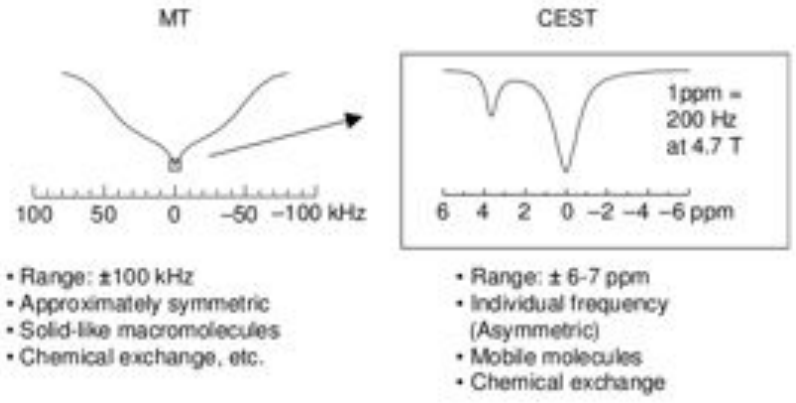

Figure 3.3: *Simulations of typical z-spectra for conventional MT and CEST. The CEST effect usually appears at a very narrow frequency range around the water resonance and is not taken into account in the common MT experiments [50].*

T_2 values (in the range of ms). For convenience, the equilibrium magnetisation in this compartment is often normalised to unity ($M_0^A = 1$). In contrast,

Pool B contains the bound protons with very short T_2 values (MT, μs range) or shifted resonance frequency (CEST, T_2 in the range of ms), respectively. Usually the equilibrium magnetisation, M_0^B, of this compartment is much less than that of pool A.

The two-pool model is the preferred model for a quantitative interpretation of MT [51] and CEST [52, 53]. It employs a set of modified Bloch equations, also called Bloch-McConnell equations [29]. For some applications even more exchanging pools might be desired. Depending on the tissue or contrast agent, a three- or four-pool model can be applied. In each case, the individual pools are characterised by their parameters T_1, T_2, M_0, ω_0 and optionally by their exchange rate(s). The extension of the Bloch-McConnell equations to n pools will be covered in Section 6.1.1. More information on the application of the three-pool model was given for example by McGowan [54] and Forsen et al. [55], the four-pool model was described by Li et al. [56].

The characteristics of the protons associated with pool B differ for MT and CEST:

Bound Protons, MT: The protons associated with pool B cannot (for different reasons) be considered as belonging to viscous fluid. Tissue, for example, contains a large amount of mobile protons and a smaller amount of bound water molecules, which form a hydration layer around the macromolecules and proteins [37]. The hydrogen protons in such macromolecules are strongly bound and have therefore very short T_2 relaxation times. As the line width (spectral response) in MR spectra is inversely related to T_2 [57, p.40], these

macromolecules have broad absorption lines compared to the free water protons (see Figure 3.2).

Bound and free protons obey permanently mutual collisions - the two systems are coupled via intermolecular, dipole-dipole interaction and chemical exchange. Thus, in addition to direct spin-lattice relaxation (T_1) an additional relaxation path between the bound and free protons exists and allows a transfer of saturated protons. This influences the observed T_1 value

$$\frac{1}{T_1^{observed}} \approx \frac{1}{T_1^{free}} + \frac{f}{T_1^{bound} + \frac{1}{k_{BA}}}, \tag{3.1}$$

where f denotes the ratio of immobile water molecules to free water molecules, ($f \ll 1$), k_{BA} the exchange rate from the immobile to the free protons and T_1^i the longitudinal relaxation times of the two pools [58].

CEST: Pool B is the presaturated pool, containing the CEST CAs or proteins (Amide Proton Transfer).

Exchange between the two pools is usually described by two exchange rates, k_{AB} (pool A to pool B) and k_{BA} (pool B to pool A).

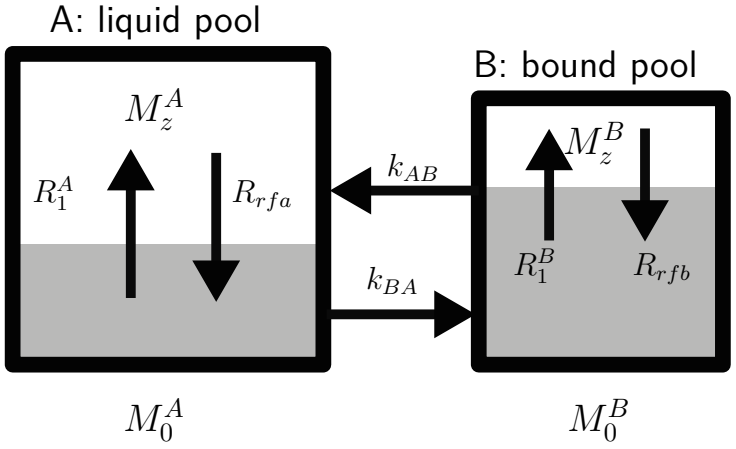

Figure 3.4: *Sketch of the two-pool model.*

In each pool (represented as a box in Figure 3.4), at any instant in time, some of the spins are in the longitudinal orientation, represented by the upper, unshaded portion of the compartment and some spins are saturated, represented by the lower shaded portion in Figure 3.4. The fraction of longitudinal spins and saturated spins depends on the prior irradiation (R_{rfa}, R_{rfb}) history (see Section 2.4.2). When the irradiation is turned off, time-dependent changes in the model are represented by the rate constants: R_1^A, R_1^B and the exchange rates, k_{AB} and k_{BA}.

$R_1^A = \frac{1}{T_1^A}$ and $R_1^B = \frac{1}{T_1^B}$ are the longitudinal relaxation rates of pool A and B, R is the exchange rate between pools A and B (see Figure 3.4). The exchange rates are related with the residence lifetimes of the spins in the corresponding pools, e.g. $RM_{0B} = k_{AB} = \frac{1}{\tau_A}$. For the whole process, mass balance is assumed, which means

$$M_0^A k_{AB} \approx M_0^B k_{BA}. \tag{3.2}$$

3.2.2. The Bloch-McConnell Equations

The dynamics of this coupled system can be described using a set of modified Bloch equations, commonly known as the Bloch-McConnell equations. In the following equations, $\vec{B_1}$, is the applied RF field strength and the parameters $\vec{\omega}_1(t) = \gamma \vec{B}_1(t)$, $\omega_A = \omega_0 = \gamma B_0$, $\omega_B = \omega_{CEST}$, $\Delta\omega_i = \omega - \omega_i$, $R_1^i = {}^1/_{T_1^i}$ and $R_2^i = {}^1/_{T_2^i}$ are introduced; $i \in \{A, B\}$. M_0 is the equilibrium magnetisation. $\vec{\omega}_1(t)$ is decomposed into its amplitude $\omega_1(t)$ and phase $\phi(t)$. The Bloch-McConnell equations are [51, 52, 53]:

$$\frac{d}{dt}M_z^A(t) = R_1^A(M_0^A - M_z^A(t)) + k_{BA}M_z^B(t) - k_{AB}M_z^A(t) + \omega_1(t)\left(\cos\phi(t)M_y^A(t) - \sin\phi(t)M_x^A(t)\right) \tag{3.3}$$

$$\frac{d}{dt}M_z^B(t) = R_1^B(M_0^B - M_z^B(t)) - k_{BA}M_z^B(t) + k_{AB}M_z^A(t) + \omega_1(t)\left(\cos\phi(t)M_y^B(t) - \sin\phi(t)M_x^B(t)\right) \tag{3.4}$$

$$\frac{d}{dt}M_x^A(t) = -R_2^A M_x^A(t) + k_{BA}M_x^B(t) - k_{AB}M_x^A(t) - \Delta\omega_A M_y^A(t) + \omega_1(t)\sin\phi(t)M_z^A(t) \tag{3.5}$$

$$\frac{d}{dt}M_x^B(t) = -R_2^B M_x^B(t) - k_{BA}M_x^B(t) + k_{AB}M_x^A(t) - \Delta\omega_B M_y^B(t) + \omega_1(t)\sin\phi(t)M_z^B(t) \tag{3.6}$$

$$\frac{d}{dt}M_y^A(t) = -R_2^A M_y^A(t) + k_{BA}M_y^B(t) - k_{AB}M_y^A(t) + \Delta\omega_A M_x^A(t) - \omega_1(t)\cos\phi(t)M_z^A(t) \tag{3.7}$$

$$\frac{d}{dt}M_y^B(t) = -R_2^B M_y^B(t) - k_{BA}M_y^B(t) + k_{AB}M_y^A(t) + \Delta\omega_B M_x^B(t) - \omega_1(t)\cos\phi(t)M_z^B(t). \tag{3.8}$$

They can be alternatively expressed as

$$\frac{d}{dt}\begin{pmatrix} M_X^A(t) \\ M_Y^A(t) \\ M_Z^A(t) \\ M_X^B(t) \\ M_Y^B(t) \\ M_Z^B(t) \end{pmatrix} = \begin{pmatrix} 0 \\ 0 \\ R_1^A M_0^A \\ 0 \\ 0 \\ R_1^B M_0^B \end{pmatrix} + \begin{pmatrix} -r_2^A & -\Delta\omega_A & \omega_1(t)\sin\phi(t) & k_{BA} & 0 & 0 \\ \Delta\omega_A & -r_2^A & -\omega_1(t)\cos\phi(t) & 0 & k_{BA} & 0 \\ -\omega_1(t)\sin\phi(t) & \omega_1(t)\cos\phi(t) & -r_1^A & 0 & 0 & k_{BA} \\ k_{AB} & 0 & 0 & -r_2^B & -\Delta\omega_B & \omega_1(t)\sin\phi(t) \\ 0 & k_{AB} & 0 & \Delta\omega_A & -r_2^B & -\omega_1(t)\cos\phi(t) \\ 0 & 0 & k_{AB} & -\omega_1(t)\sin\phi(t) & \omega_1(t)\cos\phi(t) & -r_1^B \end{pmatrix} \begin{pmatrix} M_X^A(t) \\ M_Y^A(t) \\ M_Z^A(t) \\ M_X^B(t) \\ M_Y^B(t) \\ M_Z^B(t) \end{pmatrix}, \tag{3.9}$$

where

$$\begin{aligned} r_1^A &= R_1^A + k_{AB}, & r_2^A &= R_2^A + k_{AB}, \\ r_1^B &= R_1^B + k_{BA}, & r_2^B &= R_2^B + k_{BA}. \end{aligned} \tag{3.10}$$

3.3. MT Image Contrast

If the bound proton pool is saturated selectively, its saturation can be transferred to the water spins due to collisions with the mobile water protons - a substantial effect on MR image contrast can be measured. The saturation transfer reduces the longitudinal magnetisation [37]

$$M_z^{sat} = \frac{M_z^{free}}{1 + rT_1^{free}}, \tag{3.11}$$

where r denotes the magnetisation transfer rate and M_z^{free} the longitudinal magnetisation of the free water protons excluding coupling. In MT MRI it is customary to calculate the Magnetisation Transfer Ratio, MTR,

$$\mathrm{MTR} = \frac{M_0 - M_{\mathrm{SAT}}}{M_0} = 1 - \frac{M_{\mathrm{SAT}}}{M_0}, \tag{3.12}$$

where M_0 denotes the longitudinal magnetisation without any presaturation pulse and M_{SAT} is the longitudinal magnetisation obtained with a presaturation pulse. It is an ongoing discussion if the MTR defines a quantitative parameter. Indeed, the **MTR is not a quantitative parameter**, as M_{SAT} is highly sequence dependent and is also influenced e.g. by the acquisition scheme (how the k-space is filled) and the hardware limitations.

By selective saturation it is possible to monitor the bound protons indirectly, this special kind of image contrast is called magnetisation transfer contrast [59].
The challenge is to selectively saturate the bound protons. There are different approaches which will be described in Section 3.5.

3.4. z-Spectrum

To evaluate CEST properties, the so-called CEST or z-spectrum is very useful and prevalent. In such a spectrum, RF saturation effects on water are displayed as a function of saturation frequency offset relative to water, which is assigned to 0 ppm. To obtain a z-spectrum, a preparation pulse is applied to the bound spin system at a frequency offset, $\Delta\omega$, from the water resonance. The preparation pulse partially saturates the bound proton spins and the cross relation between the two pools also causes the water proton magnetisation to decrease. A second

pulse on-resonance with the water signal at the conclusion of the preparation pulse reads the effect on the water resonance. A plot of the water signal intensity as a function of the preparation pulse offset yields a representation of the CEST spectrum (see Figure 3.5).

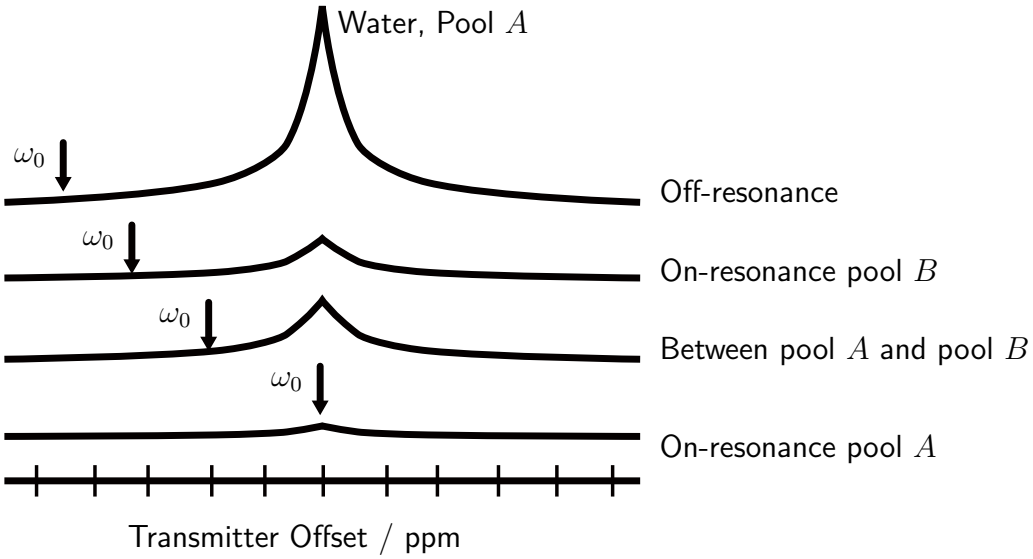

Figure 3.5: *Principle of z-spectroscopy in which water saturation is measured as a function of irradiation frequency. When saturation RF pulses are applied at protons in magnetic contact with water, e.g through chemical or dipolar exchange, the water signal has extra reduction. When irradiation is close to the water resonance, direct saturation or "spillover" occurs.*

This spectrum is called z-spectrum because of its origins in z-magnetisation transfer [60] or MT spectrum or CEST spectrum. An example for a z-spectrum of CEST effects is shown in Figure 3.6.

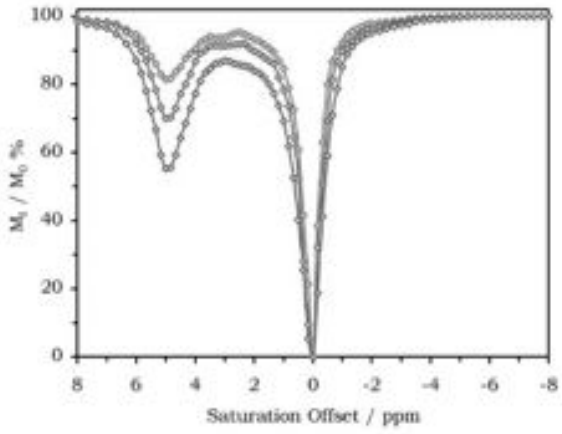

Figure 3.6: *z-spectra of different solutions of barbituric acid recorded at 300 MHz [49].*

3.5. Saturation Methods for MT

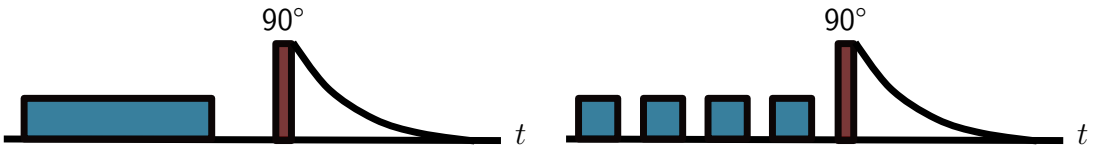

Figure 3.7: *Two pre-pulse designs for MT preparation. Left: continuous wave, right: pulsed RF.*

Imaging strategies for MT contrast utilise saturation prepulses which are designed to selectively saturate the bound proton pool. Currently there are two main approaches to achieve saturation. One is the continuous wave (CW) technique, which was already noted in 2.4.2, the other is pulsed MT (see Figure 3.7).

3.5.1. The CW Approach

In CW MR imaging, off-resonance RF pulses of several seconds in duration (with a given amplitude and frequency) are used to saturate the semi-solid pool preferentially with respect to the liquid pool. CW pulses allow one to apply an almost perfect frequency selective pulse. Saturation and MT exchange between the two pools are observed in the liquid pool when a steady state has been achieved [61].

3.5.1.1. Advantages and Disadvantages

- CW experiments are best for characterizing mechanisms of the MT process, one obtains a good and clean separation between the amount of saturation of the two pulses [51].
- Since off-resonance pulses are applied, water and fat are not excited [62].
- Insensitive to B_0 inhomogeneities [62].
- Likely to run into SAR limits as off-resonance excitation needs more energy to saturate [51].
- Clinical RF transmitters are likely to run into problems, as they are commonly designed for pulsed RF excitation[51].
- CW saturation does not excite **all** short T_2 species [62].

Most clinical MR systems (including those used for this work) cannot apply CW pulses - their RF amplifier is not designed for the long duty cycles which are required for CW presaturation. Therefore, this approach will not be discussed further.

3.5.2. The Pulsed MT Approach

CW irradiation with continuous off-resonance pulses differs from the pulsed approach, where a pulse series is employed to saturate the bound pool. Pulsed saturation can be achieved by on-resonant transparent pulses (see Appendix A or [61]) or by the application of several pulses off-resonance. The latter is easy to implement and requires no additional hardware or pulse designs over and above those required for conventional MR imaging [54]. Therefore, the approach has some advantages compared to CW MT. Mc Gowan et al. used a pulse sequence [63] based on a gradient echo sequence. They placed 19 ms shaped pulses at intervals within each TR period. These pulses replaced pulses used for fat saturation pulses and consisted of the central lobe of a sinc function. Contrast from T_1 and T_2 weighting in the MT images was reduced by using short echo times (5 ms) and low flip angles of 5-7°. A TR of 140 ms was used and four signals were averaged. The effective saturation power varied according to γB_1 values of 65.5, 113.5, 154.1 and 160.0 Hz for one, two, three, five, and six saturation pulses, respectively. The feasibility of monitoring MT with pulsed off-resonance presaturation pulses was checked in the piglet brain. The resulting z-spectrum is displayed in Figure 3.8.

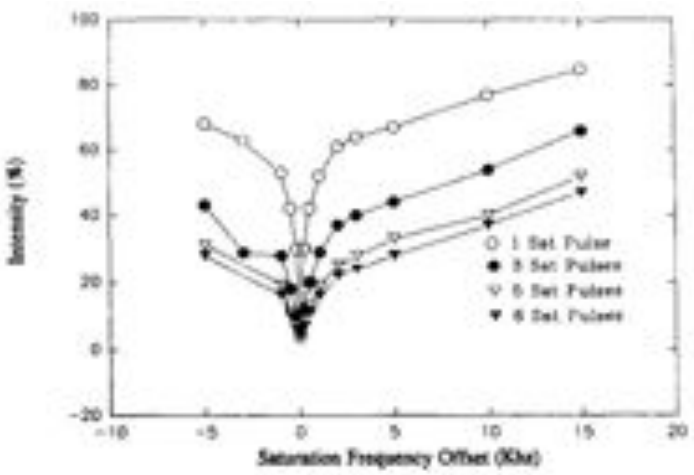

Figure 3.8: *z-spectrum in the piglet brain using off-resonance pulsed presaturation [63].*

Side effects Off resonance presaturation can be a side effect in slice-selective imaging. As slice selection is obtained by RF pulses of limited bandwidth, the regions aside the selected slice experience an off-resonance pulse. This leads to MT and saturation effects in any MRI sequence, a fact that has to be considered e.g. for quantitative imaging (see Chapter 7 and Chapter 8).

3.5.2.1. Summary, Pros and Cons of Pulsed MT

Pulsed MT can be performed using on or off-resonance pulses. The latter requires higher RF field strengths, as the signal amplitude decreases with off-resonance frequency. This is because the effective magnetic field in the rotating frame of reference tilts due to off-resonance irradiation. On the other hand, the nutation angle transversed by the magnetisation increases as the transmission frequency moves off-resonance. These two effects partially cancel, resulting in a slowly decreasing signal amplitude with increasing off-resonance frequency. To maintain a constant flip angle, the RF power must therefore increase [41, p. 111].
This disadvantage disappears, if the RF pulse is on-resonance. The most RF efficient magnetisation transfer preparation should occur with binomial saturation pulses applied on-resonance [62]. Saturation by on-resonance pulses benefits from:

- Transmission on-resonance requires less energy transfer - SAR limits are reached [62].
- Conventional RF transmitters can be used.
- Excitation of all short T_2 species [62].
- Sensitive to B_0 inhomogeneities, therefore it is possible that water and fat signals are suppressed unintentionally [62].

3.6. Other Approaches

Generally, any off-resonance RF pulse in an MR imaging sequence saturates the macromolecular pool to some degree. This can cause some unintended MT effects in other imaging sequences, but vice versa, every imaging sequence, applying off-resonance RF pulses can be used to monitor MT. Examples are given in the literature, e.g. Bieri and Scheffler in 2007 [64].

4. Quantification of the Longitudinal Relaxation Time

Most clinical applications of MRI focus on qualitative imaging, where image contrast is not only influenced by the tissue parameters (T_1, T_2, M_0) but is also strongly dependent on sequence parameters such as TR, TE or the flip angle, α, and the sequence with its characteristic pulse and gradient waveforms. Furthermore, the hardware itself (scanner, coils, subject) has an influence on the final MR image. As a consequence, measurements obtained at various dates or of different volunteers or at distinct MR sites are not quantitatively comparable to each other (i.e. in absolute numbers).

In contrast, quantitative imaging (qMRI) allows one to compare studies obtained on different volunteers or at diverse timepoints or even for different scanners by means of numbers rather than local contrast differences[1].

Quantitative imaging, or parameter mapping, requires dedicated sequences as well as additional postprocessing, but this disadvantage is outweighted by comparative results. Common quantitative methods are T_1 mapping, T_2 mapping, T_2^* mapping and water mapping [1].

Mapping the longitudinal relaxation time, T_1, is one major interest in qMRI. In particular for brain imaging, T_1 mapping is an important concern. For example, white and grey matter tissue can be accurately segmented based on T_1 values. Most importantly, changes in T_1 values can be a sensitive indicator of pathological changes, such as tumours [17] or hepatic encephalopathy [5]. T_1 maps provide a prerequisite for measurements of the permeability of the blood-brain barrier [15], the local water content [7, 6] or *quantitative* tracer kinetics [65, 66]. By means of T_1 mapping, one can monitor the effects of radiation therapy [67] and the response of tumour therapy [68]. Some of these applications can also be addressed by PET measurements but these suffer from the drawbacks of low resolution, exposure to ionizing radiation as well as the low availability.

Depending on the desired application and the conditions, several different T_1 mapping methods have been developed. The most common ones are introduced in this Chapter.

[1] If relaxation times are to be quantified, the field strength has to be the same.

4.1. Inversion Recovery Sequences

The simplest method to obtain T_1 is the inversion recovery (IR) sequence. It comprises a 180° pulse and a readout module, e.g. a Spin Echo or a FID readout, which is delayed by a time, TI, called inversion time. By means of the IR preparation the M_z magnetisation is inverted and therefore evolves during TI with

$$M_z(t) = M_0 \left(1 - 2e^{-\frac{t}{T_1}}\right). \tag{4.1}$$

The readout is then performed, e.g. by a 90° pulse which flips the M_z magnetisation into the signal reception plane enabling the M_z magnetisation to be measured. After waiting for full relaxation, the pulse sequence is repeated with different values for TI. The T_1 relaxation time can be fitted from the data acquired. The process is sketched on the left in Figure 4.1, while the graph in Figure 4.1 shows a typical T_1 relaxation curve.

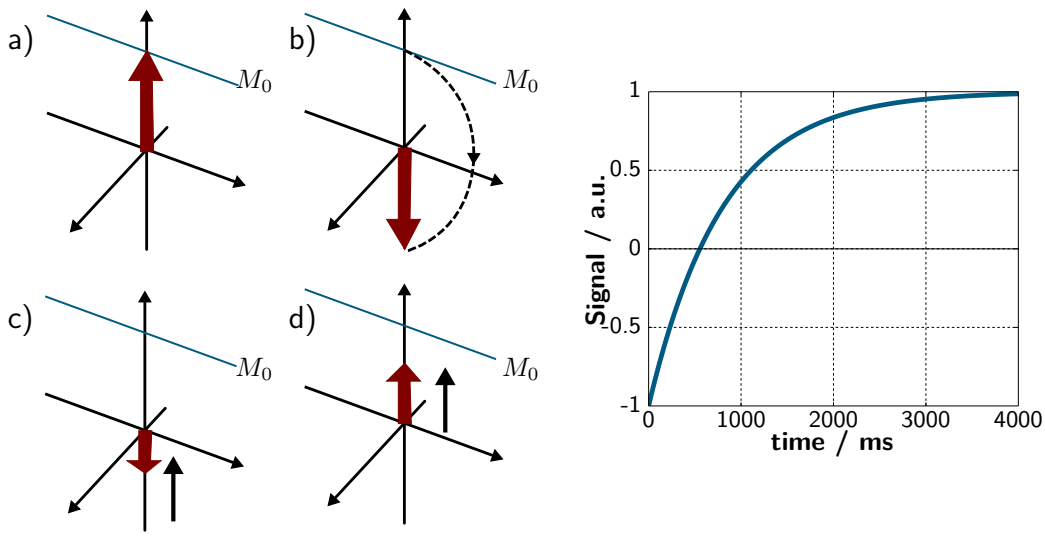

Figure 4.1: ***Left:*** *Scheme of the IR sequence: (a) Equilibrium magnetisation before the inversion. (b) Inverting the magnetisation. (c) and (d): Regrowing longitudinal magnetisation.* ***Right:*** *The amplitude of the measured signal, plotted for $T_1 = 800\,ms$, at different TI gives the T_1 relaxation curve displayed on the right.*

4.2. Gradient Echo with Multiple Flip Angles

Another commonly used method for T_1 estimation is based on the acquisition of several (at least two) spoiled gradient echoes with short TR and different flip angles [69], α.

The Ernst equation which applies in that case (derived in 2.4.1) is given by:

$$M_z^{SS} = M_0 \frac{(1 - E_1)}{(1 - \cos \alpha E_1)}, \tag{4.2}$$

$$E_1 = e^{-\frac{TR}{T_1}}, \tag{4.3}$$

with the steady-state transverse magnetisation,

$$M_\perp^{SS} = M_z^{SS} \sin \alpha \propto \text{Signal}. \tag{4.4}$$

The Ernst equation gives the signal intensity obtained by a gradient echo sequence with perfect spoiling. The flip angle dependence can be employed to obtain T_1 by measuring the signal intensity with several flip angles and fitting the measured signal to Equation (4.4). Figure 4.2 shows the signal behaviour for a T_1 of 1400 ms as a function of the flip angle, α, at a TR of 500 ms. In theory, two measured flip angles are sufficient to obtain T_1. This method will be

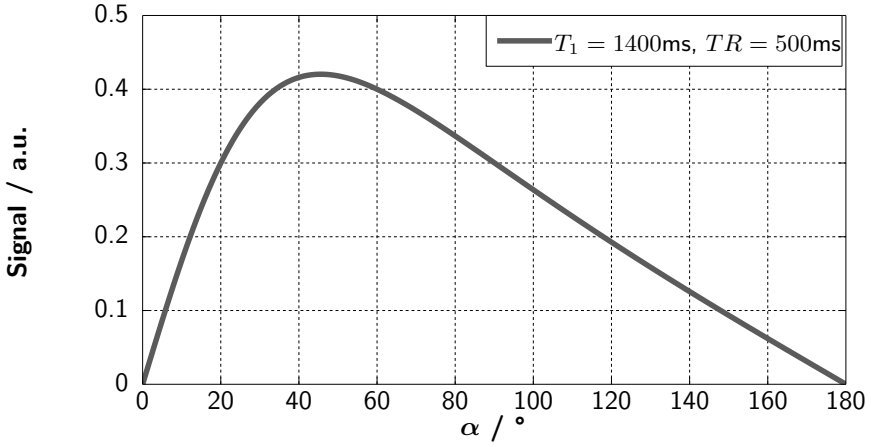

Figure 4.2: *Signal intensity calculated based on the Ernst equation* (4.4) *for* $T_1 = 1400ms$, $TR = 500ms$.

referred to as the "variable flip angle" or "Ernst method".

4.3. The Look-Locker Method

IR methods suffer from long acquisition times as full relaxation is a prerequisite for each TI measurement. The approach presented by Look and Locker [70] overcomes the problem of long acquisition times and inefficient sampling by applying a set of small flip angle pulses (α) during each repetition period (see Figure 4.3). The application of several α pulses leads to the evolution of a steady state magnetisation, M_∞, (for a derivation see 2.4.1). Moreover, the relaxation curve is modified, as the relaxation approaches the steady state magnetisation instead

of the equilibrium magnetisation, M_0:

$$\begin{aligned} M(t) &= M_{SS} - (1 + M_{SS})e^{-t/T_1^*}, \\ \frac{1}{T_1^*} &= \frac{1}{T_1} - \frac{\ln(\cos\alpha)}{TR} \\ M_{SS} &= M_0 \frac{1 - e^{-TR/T_1}}{1 - \cos\alpha e^{-TR/T_1}} = M_0 \frac{1 - e^{-TR/T_1}}{1 - e^{-TR/T_1^*}}, \end{aligned} \tag{4.5}$$

where TR denotes the time between the subsequent α pulses.

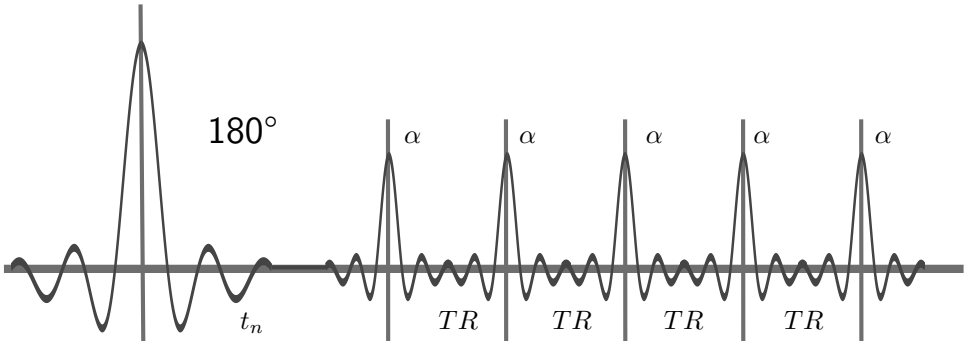

Figure 4.3: *Look-Locker pulse train*

The Look-Locker method for T_1 quantification has been modified, improved and adopted commonly (e.g. [71, 65, 72]). One Look-Locker based method is called TAPIR.

4.3.1. TAPIR

The Look-Locker approach allows one to quantify T_1 with high precision and accuracy. The utilisation of steady-state imaging allows faster imaging of a large number of sampling points. However, there is room for improvement, in particular if one aims to quantify more than one slice. Shah et al. presented in 2001 a Look-Locker based method named TAPIR (T_1 mapping with partial inversion recovery) which uses a clever sampling strategy to obtain data from several slices and timepoints along the recovery curve in a shorter time period [73, 74, 75]. Figure 4.4 shows the sequence diagram.

The signal intensity, S, measured by the TAPIR sequence is given by:

$$S = M_0 \; m \sin(\alpha) \tag{4.6}$$

with

$$m = \frac{M}{M_0} = m_{SS} + (m_1 - m_{SS})\, e^{-(t - t_n)/T_1^*}. \tag{4.7}$$

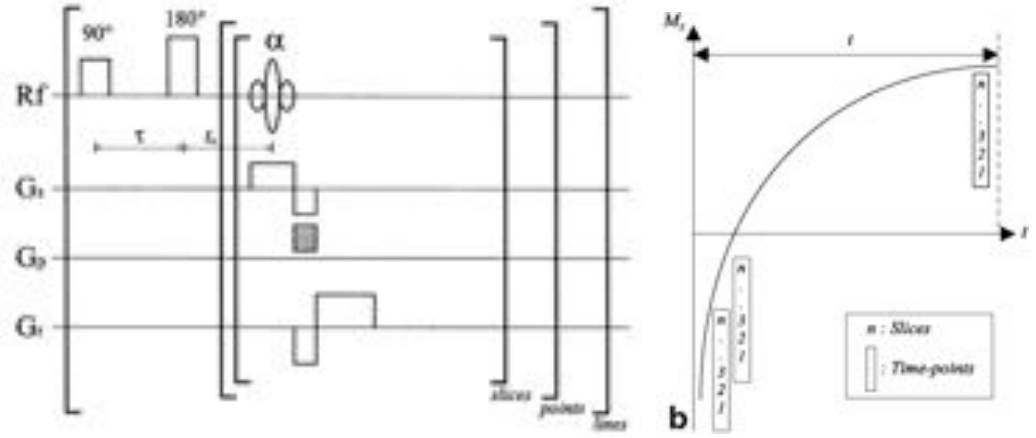

Figure 4.4: *Sequence diagram of the TAPIR sequence: The time separation between 90° and 180° is not shown to scale. Following application of a non-selective 90° pulse, the transverse magnetisation thus created dephases during the delay period, τ. Thereafter, a non-selective 180° pulse inverts recovered longitudinal magnetisation and any residual transverse magnetisation is spoiled by large crusher gradients (not shown). The magnetisation is then repeatedly sampled by means of multiple slice selective α pulses. Note that while repeating the "slices" and "points" loops the same set of k-space lines is acquired while different slices and timepoints are acquired. The whole pulse sequence is then repeated for the next set of lines. [74]*

m_1 denotes the magnetisation[2] after the 90° $-\tau-$ 180° $-t_n$ preparation, with the inversion efficiency, IE,

$$m_1 = 1 - e^{-t_n/T_1}\left(1 + IE\left(1 - e^{-\tau/T_1}\right)\right), \tag{4.8}$$

and T_1^* is the "Look-Locker" relaxation time,

$$\frac{1}{T_1^*} = \frac{1}{T_1} - \frac{\ln(\cos\alpha)}{TR}. \tag{4.9}$$

m_{SS} denotes the magnetisation in the steady state,

$$m_{SS} = \frac{1 - e^{-TR/T_1}}{1 - \cos\alpha \cdot e^{-TR/T_1}}, \tag{4.10}$$

t_n denotes the time between the inversion and the first acquisition of slice n. T_1 is then estimated by fitting the data points sampled with TAPIR to Equation (4.6). Equation (4.6) neglects T_2^* decay, as it will only reduce the apparent value of M_0 and thus only compromise the quantitative nature of M_0 [74]. This has to be considered, if M_0 quantification is of interest.

[2] Lower case magnetisations, $m_i, i \in \{SS, 1, ...\}$, are normalised magnetisations: $m_i = {}^{M_i}/_{M_0}$.

5. The Longitudinal Relaxation Time in the Presence of Chemical Exchange or Magnetisation Transfer

An integral part of accurate mapping of the longitudinal relaxation time is a detailed knowledge of factors affecting the observed T_1 values [76, 7]. An important factor that might spoil the precision of measured T_1 values is the presence of bound protons in different environments and the effect thereof on the free water pool via magnetisation transfer (MT) [77, 78, 25, 29]. It is well known that MT offers an additional contrast mechanism (see Chapter 3), [79, 51, 80, 81, 82, 83, 84], as the transverse magnetisation is decreased if the magnetisation in the bound proton pool is saturated, e.g. by the application of presaturation pulses.

Incidental MT effects are present in basically all MR sequences, in particular in sequences which use a large number of high flip-angle pulses (RARE [85], TSE [86, 87]) and there has been renewed interest in studying the MT effect of on-resonance pulses, for example in 3D imaging [25, 88].

Proper T_1 quantification therefore requires consideration of MT as suggested for example by Meara et al. [89] and Ou et al. [25]. This implies the assumption of a biexponential recovery instead of a monoexponential one as well as the consideration of signal attenuation caused by off-resonance saturation. Many more -usually unknown- sample parameters as well as the imaging sequence itself have a considerable impact on the final T_1 map. Therefore, it is difficult to quantify the effect of MT on T_1. This chapter aims to describe influences of MT on T_1, based on the Bloch-McConnell equations and the two-pool model. In addition, the necessary steps for correct T_1 quantification in the presence of MT are derived. The existing theory was extended to several pools with the known side effects[1] of even more parameters modelling the system.

[1] smaller residuals but decreasing robustness, increasing variance of the model predictions, less precise estimations of single parameters

5.1. Problem Description and Motivation

First, the scope of T_1 mapping in the presence of magnetisation transfer has to be defined. There are two effects which have to be considered for T_1 mapping of substances undergoing MT:

- Biexponential recovery, see Section 5.1.2.
- Incidental saturation effects and signal attenuation due to slice selection or other off-resonance RF pulses.

For the estimation of T_1, two cases have to be distinguished:

- Standard T_1 mapping, neglecting the influences of MT.
- Mapping the MT relaxation times with modified signal equations.

Which of the two models should be applied has to be decided depending on the application.

5.1.1. Standard T_1 Mapping

Usually, "standard T_1 mapping" (by any one of the sequences described in Chapter 4) is performed, regardless of whether any MT effects are present or not. In particular for clinical applications, the MT effect is often neglected though it is known to be influential. Using the classical Bloch equations to derive a signal equation which is used for the T_1 fit leads to erroneous estimations of T_1. This error can be attributed to MT, but it originates by the application of an inappropriate model. Part of this work (see Section 8) was to investigate how strongly the effect of MT spoils the results of established T_1 mapping methods.

5.1.2. Mapping the Longitudinal Relaxation in the Presence of MT

The approach presented in this section considers MT influences in particular for T_1 estimation by the application of the two-pool model. Solving the Bloch-McConnell equations for two exchanging systems reveals the biexponentiality of the M_z recovery:
The Bloch-McConnell equations (3.8) for the evolution of M_z following an RF pulse assuming zero transverse magnetisation are:

$$\begin{aligned} \frac{dM_z^A}{dt} &= R_1^A(M_0^A - M_z^A) + k_{BA}M_z^B - k_{AB}M_z^A \\ \frac{dM_z^B}{dt} &= R_1^B(M_0^B - M_z^B) - k_{BA}M_z^B + k_{AB}M_z^A. \end{aligned} \tag{5.1}$$

The solution is:

$$\begin{aligned} M_z^A(t) &= M_0^A + C_1 e^{-\lambda_1 t} + C_2 e^{-\lambda_2 t} \\ M_z^B(t) &= M_0^B + \tilde{C}_1 e^{-\lambda_1 t} + \tilde{C}_2 e^{-\lambda_2 t}. \end{aligned} \tag{5.2}$$

The correct eigenvalues, λ_1 and λ_2, are given e.g. by Forsen [90] or Pike [81]:

$$\begin{aligned}\lambda_{1,2} = &\frac{1}{2}\left(R_1^A + k_{AB} + R_1^B + k_{BA}\right) \\ &\mp \frac{1}{2}\sqrt{\left(R_1^A + k_{AB} + R_1^B + k_{BA}\right)^2 - 4\left(R_1^A R_1^B + k_{AB} R_1^B + k_{BA} R_1^A\right)}.\end{aligned} \tag{5.3}$$

C_1, C_2, $\tilde{C}_1$ and $\tilde{C}_2$ are functions of the sample parameters ($R_1^A = 1/T_1^A$, $R_1^B = 1/T_1^B$, k_{AB}, k_{BA}, M_0^A, M_0^B) and the initial conditions. According to Equation (5.2), the complete solution can be written in matrix formulation with $\vec{M}_z = \left(M_z^A, M_z^B\right)^\top$ and $\vec{M}_0 = \left(M_0^A, M_0^B\right)^\top$

$$\vec{M}_z(t) = \mathbf{K}\vec{M}_z(0) + \mathbf{L}\vec{M}_0, \tag{5.4}$$

with:

$$\begin{aligned}\mathbf{K} &= \begin{pmatrix} \frac{e^{-\lambda_1 t}\left(\lambda_2 - R_1^A - k_{AB}\right) - e^{-\lambda_2 t}\left(\lambda_1 - R_1^A - k_{AB}\right)}{\lambda_2 - \lambda_1} & \frac{k_{BA}\left(e^{-\lambda_1 t} - e^{-\lambda_2 t}\right)}{\lambda_2 - \lambda_1} \\ -\frac{\left(e^{-\lambda_1 t} - e^{-\lambda_2 t}\right)\left(\lambda_2 - R_1^A - k_{AB}\right)\left(\lambda_1 - R_1^A - k_{AB}\right)}{k_{BA}\left(\lambda_2 - \lambda_1\right)} & \frac{e^{-\lambda_1 t}\left(-\lambda_1 + R_1^A + k_{AB}\right) - e^{-\lambda_2 t}\left(-\lambda_2 + R_1^A + k_{AB}\right)}{\lambda_2 - \lambda_1} \end{pmatrix} \\ \mathbf{L} &= \begin{pmatrix} \frac{e^{-\lambda_1 t}\left(-\lambda_2 + R_1^A\right) - e^{-\lambda_2 t}\left(-\lambda_1 + R_1^A\right)}{\lambda_2 - \lambda_1} + 1 & 0 \\ \frac{e^{-\lambda_1 t}\left(\lambda_2 - R_1^A\right)\left(\lambda_1 - R_1^A - k_{AB}\right) - e^{-\lambda_2 t}\left(\lambda_1 - R_1^A\right)\left(\lambda_2 - R_1^A - k_{AB}\right)}{k_{BA}\left(\lambda_2 - \lambda_1\right)} & 1 \end{pmatrix}\end{aligned} \tag{5.5}$$

or, using mass balance ($k_{AB} M_0^A = k_{BA} M_0^B$), the matrix elements in $\mathbf{L}$ can be shifted to

$$\mathbf{L} = \begin{pmatrix} \frac{e^{-\lambda_1 t}\left(-\lambda_2 + R_1^A - k_{AB}\right) - e^{-\lambda_2 t}\left(-\lambda_1 + R_1^A - k_{AB}\right)}{\lambda_2 - \lambda_1} + 1 & \frac{k_{BA}\left(e^{-\lambda_1 t} - e^{-\lambda_2 t}\right)}{\lambda_2 - \lambda_1} \\ \frac{\left(e^{-\lambda_1 t} - e^{-\lambda_2 t}\right)\left(\lambda_2 - R_1^A - k_{AB}\right)\left(\lambda_1 - R_1^A - k_{AB}\right)}{k_{BA}\left(\lambda_2 - \lambda_1\right)} & \frac{\left(e^{-\lambda_1 t} - e^{-\lambda_2 t}\right)}{\left(\lambda_2 - \lambda_1\right)} \end{pmatrix}. \tag{5.6}$$

Relaxation is then determined (see Equation (5.2)) by a biexponential function with the slow recovery rate, λ_1, and the fast recovery rate, λ_2. It should be noted that the biexponential recovery is not only the sum of the two exponential recovery curves of the single pools but there are also contributions of the exchange, as one can see in Equation 5.3 and in Section 7.1. Using n pools ($n > 2$) introduces not biexponential but n-exponential recovery.

5.1.2.1. Practical Considerations

In MRI experiments, due to the short T_2 relaxation times of the bound proton pool, only the free pool is observed. The difference between monoxeponential and biexponential recovery in an inversion recovery experiment for pool A is displayed in Figure 5.1. The parameters used are given in the figure caption, full inversion of pool A and full saturation of pool B was assumed for this solution of the Bloch-McConnell equations. The difference is only visible for very short inversion times, as the influence of the fast recovery rate is much smaller than the slow recovery

rate. In many cases, a separation of the biexponential nature of the recovery curve is not possible, e.g. due to few acquisition points or low SNR. Neglecting the fast recovery rate, λ_2, and fitting the data to a single exponential leads then to a different estimated relaxation rate, called $T_1^{putative/observed} \neq T_1^A$.

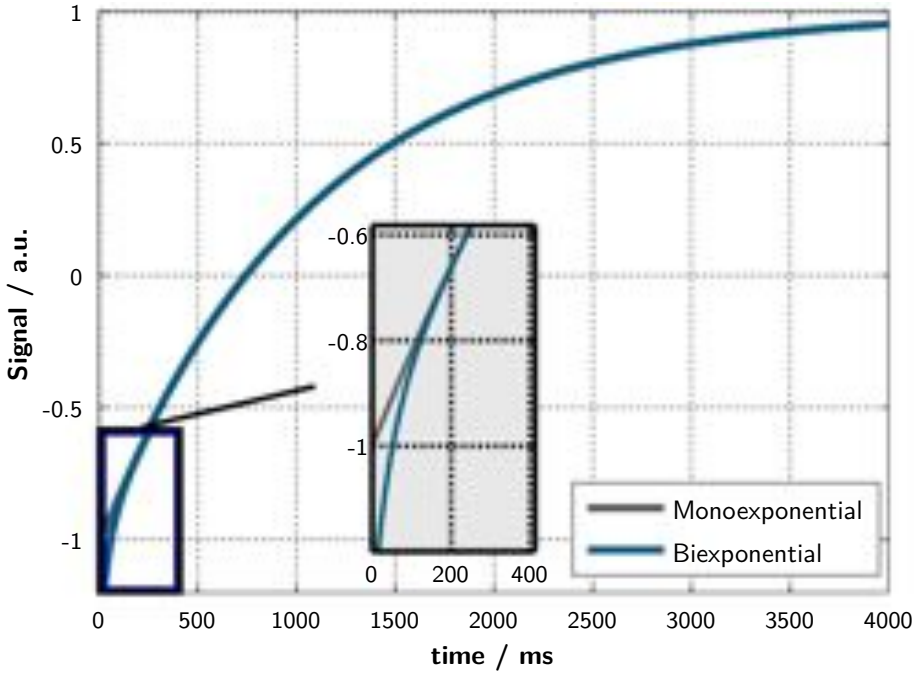

Figure 5.1: *Monoexponential and biexponential recovery of the M_z magnetisation. Parameters were based on the white matter data provided by Stanisz [82], $T_1^A = 1084\,ms$, $T_1^B = 1000\,ms$, $M_0^B = 0.161 M_0^A$, $k_{AB} = 3.197\,Hz$.*

In this work, any given T_1 value which is influenced by MT is called $T_1^{putative}$, if it results from a simulation, and it is called $T_1^{observed}$ if it was measured.

5.2. Adapted Signal Equations for Estimation of the Longitudinal Relaxation Time in the Presence of MT

The established T_1 mapping methods are based on the "classical" Bloch equations. In the presence of MT, the Bloch-McConnell equations have to be used and, therefore, the signal equations have to be adapted.

5.2.1. Inversion Recovery Sequences

The modified signal equation for inversion recovery sequences was already derived in Section 5.1.2, Equation (5.4).

5.2.2. GRE with Multiple Flip Angles

To map T_1 using several gradient echoes with different flip angles in the presence of MT requires some more calculations to obtain the modified signal equations are required. First of all, the steady state magnetisation in the presence of MT is derived. The solution for M_z of the Bloch-McConnell equations (no pulse) in matrix form (cf. Equation (5.4)) is given as

$$\vec{M}_z(t) = \mathbf{K}\vec{M}_z(0) + \mathbf{L}\vec{M}_0 \tag{5.7}$$

with

$$\mathbf{K} = \begin{pmatrix} \frac{e^{-\lambda_1 t}\left(\lambda_2 - R_1^A - k_{AB}\right) - e^{-\lambda_2 t}\left(\lambda_1 - R_1^A - k_{AB}\right)}{\lambda_2 - \lambda_1} & \frac{k_{BA}\left(e^{-\lambda_1 t} - e^{-\lambda_2 t}\right)}{\lambda_2 - \lambda_1} \\ -\frac{\left(e^{-\lambda_1 t} - e^{-\lambda_2 t}\right)\left(\lambda_2 - R_1^A - k_{AB}\right)\left(\lambda_1 - R_1^A - k_{AB}\right)}{k_{BA}\left(\lambda_2 - \lambda_1\right)} & \frac{e^{-\lambda_1 t}\left(-\lambda_1 + R_1^A + k_{AB}\right) - e^{-\lambda_2 t}\left(-\lambda_2 + R_1^A + k_{AB}\right)}{\lambda_2 - \lambda_1} \end{pmatrix} \tag{5.8}$$

$$\mathbf{L} = \begin{pmatrix} \frac{e^{-\lambda_1 t}\left(-\lambda_2 + R_1^A\right) - e^{-\lambda_2 t}\left(-\lambda_1 + R_1^A\right)}{\lambda_2 - \lambda_1} + 1 & 0 \\ \frac{e^{-\lambda_1 t}\left(\lambda_2 - R_1^A\right)\left(\lambda_1 - R_1^A - k_{AB}\right) - e^{-\lambda_2 t}\left(\lambda_1 - R_1^A\right)\left(\lambda_2 - R_1^A - k_{AB}\right)}{k_{BA}\left(\lambda_2 - \lambda_1\right)} & 1 \end{pmatrix} \tag{5.9}$$

with

$$\begin{aligned} \lambda_{1,2} = &\frac{1}{2}\left(R_1^A + k_{AB} + R_1^B + k_{BA}\right) \\ &\mp \frac{1}{2}\sqrt{\left(R_1^A + k_{AB} + R_1^B + k_{BA}\right)^2 - 4\left(R_1^A R_1^B + k_{AB} R_1^B + k_{BA} R_1^A\right)}. \end{aligned} \tag{5.10}$$

Assuming that each pulse applied to the system acts as

$$\vec{M}_z{}^+ = \mathbf{S}\vec{M}_z{}^-, \tag{5.11}$$

with $\vec{M}_z{}^-$ denoting the longitudinal magnetisation prior to the pulse and $\vec{M}_z{}^+$ the longitudinal magnetisation after the pulse. The matrix $\mathbf{S}$ is a diagonal matrix with diagonal elements S_A and S_B. S_A and S_B represent the fractal saturation (i.e. $S_i \in [-1, 1]$) of the pools following saturation and excitation pulses. For an idealised pulsed MT sequence in which the semi-solid component is completely saturated by each pulse without any direct saturation of the liquid component, $S_B = 0$ and $S_A = \cos\alpha$ [81]. For example, $S_A = \hat{S}_A \cos\alpha$, where $\hat{S}_A$ represents the direct saturation of pool A by any MT saturation pulse and $\cos\alpha$ the saturation produced by the excitation pulse.

The steady-state magnetisation can be derived using the geometric series (see e.g. [81]) as

$$\vec{M}_z^{SS} = \left[\mathbb{1} - \mathbf{KS}\right]^{-1}\mathbf{L}\vec{M}_0 \tag{5.12}$$

with $\mathbb{1}$ denoting the identity matrix.
The solution is

$$M_z^{SS,MT,PoolA} = M_0^A \cdot \frac{\lambda_1\left(1 - S_B E_1^{MT}\right)\left(1 - E_2^{MT}\right) - \lambda_2\left(1 - E_1^{MT}\right)\left(1 - S_B E_2^{MT}\right) + R_1^A\left(E_1^{MT} - E_2^{MT}\right)(S_B - 1)}{\lambda_1\left(1 - S_B E_1^{MT}\right)\left(1 - \cos\alpha E_2^{MT}\right) - \lambda_2\left(1 - \cos\alpha E_1^{MT}\right)\left(1 - S_B E_2^{MT}\right) - \left(R_1^A + k_{AB}\right)\left(E_1^{MT} - E_2^{MT}\right)(\cos\alpha - S_B)}, \tag{5.13}$$

where $E_1^{MT} = e^{-\lambda_1 T_R} = e^{-\frac{T_R}{T_1^{observed}}}$, $E_2^{MT} = e^{-\lambda_2 T_R}$ and $S_B \in [-1, 1]$ denotes the factor accounting for the direct saturation of the bound proton pool B. Rearrangement of Equation (5.13) gives

$$M_z^{SS,MT,PoolA} = M_0^A \cdot \frac{\left(1 - E_1^{MT}\right)\left(1 - S_B E_2^{MT}\right) + \frac{\left(R_1^A - \lambda_1\right)}{\left(\lambda_1 - \lambda_2\right)}\left(E_1^{MT} - E_2^{MT}\right)(S_B - 1)}{\left(1 - \cos\alpha E_1^{MT}\right)\left(1 - S_B E_2^{MT}\right) + \frac{\left(R_1^A + k_{AB} - \lambda_1\right)}{\left(\lambda_1 - \lambda_2\right)}\left(E_1^{MT} - E_2^{MT}\right)(S_B - \cos\alpha)}. \tag{5.14}$$

For biological tissues and gel samples ($k_{AB}, R_1^A, R_1^B \ll k_{BA}$), according to Ou and Gochberg [25], the following approximations to the first order in $1/k_{BA}$ are valid

$$\lambda_2 \approx k_{BA} \tag{5.15}$$

$$\frac{R_1^A + k_{AB} - \lambda_1}{\lambda_2 - \lambda_1} \approx \frac{\frac{M_0^B}{M_0^A}}{1 + \frac{M_0^B}{M_0^A}} \tag{5.16}$$

$$\frac{R_1^A - \lambda_1}{\lambda_2 - \lambda_1} \approx 0 \tag{5.17}$$

$$E_2^{MT} \approx 0. \tag{5.18}$$

This leads to a simpler form of Equation (5.14):

$$M_\perp^{SS,MT,PoolA} = M_0^A \sin\alpha \cdot \frac{\left(1 - E_1^{MT}\right)}{\left(1 - E_1^{MT}\cos\alpha\right) + A\left(\cos\alpha - S_B\right)E_1^{MT}}. \tag{5.19}$$

5.2.3. TAPIR

Similar modifications are necessary if the TAPIR signal equation for the two-pool model is derived. The steady state magnetisation was already derived (Eq. (5.12)) as

$$\vec{M}_{SS} = \left[\mathbb{1} - \mathbf{KS}\right]^{-1}\mathbf{L}\vec{M}_0. \tag{5.20}$$

In the presence of MT, the magnetisation $\vec{M}_1$, i.e. the magnetisation after the $90° - \tau - 180° - t_n$ preparation, has to be derived based on the two-pool model. The matrix representation (5.7) allows one to do this easily:

$$\vec{M}_1(t_n) = \mathbf{K}(t_n)\left\{\mathbf{S}(180°)\left[\mathbf{K}(\tau)\mathbf{S}(90°) + \mathbf{L}(\tau)\right] + \mathbf{L}(t_n)\right\}\vec{M}_0 \tag{5.21}$$

after some cumbersome calculations and approximations ($e^{-\lambda_2 \tau} = 0, e^{-\lambda_2 t_n} = 0$) Equation (5.21) changes to

$$\begin{aligned} M_1^A(t) \approx \; M_0^A \frac{e^{-\lambda_1 t_n}}{(\lambda_2 - \lambda_1)^2} \Bigg[& \left(1 - e^{-\lambda_1 t_n}\right)(\lambda_1 - \lambda_2)\left(R_1^A - \lambda_2\right) + \\ & S_B^{180^\circ}\left[k_{AB}(\lambda_2 - \lambda_1) + e^{-\lambda_1 \tau}\left(R_1^A - \lambda_2\right)\left(R_1^A + k_{AB} - \lambda_1\right)\right] + \\ & \left(R_1^A + k_{AB} - \lambda_1\right)\left(\lambda_1 - \lambda_2 - S_A^{180^\circ} e^{-\lambda_1 t_n}\left(\lambda_2 - R_1^A\right)\right) + \\ & S_B^{90^\circ} k_{AB} e^{-\lambda_1 \tau}\left[S_B^{180^\circ}\left(R_1^A + k_{AB} - \lambda_1\right) - S_A^{180^\circ}\left(R_1^A + k_{AB} - \lambda_2\right)\right] \Bigg]. \end{aligned} \tag{5.22}$$

The final signal equation for the two-pool model for TAPIR is given as

$$M_z(t) = \mathbf{K}(t)\mathbf{S}(\alpha)\mathbf{M}_1(t) + (\mathbb{1} - \mathbf{K}(t)\mathbf{S}(\alpha))\,\vec{M}_{SS}. \tag{5.23}$$

5.2.4. Note

The equations derived above give the solutions of the two-pool Bloch equations for the M_z component. Effects of excitation pulses as well as saturation effects and exchange to and from the transverse magnetisation components are neglected. The equations describe the behaviour of the longitudinal magnetisation and its evolution between excitation pulses. Excitation is usually effectively modelled as instantaneous rotation and contraction of the net magnetisation vector [81], here denoted as $\mathbf{S}$.

In particular in case of the TAPIR sequence, the effects of exchange and relaxation of the transverse magnetisation might give a significant contribution to the signal observed, which results in a different (more complex) signal equation, which cannot be solved analytically. Numerical simulations of these using the Bloch-McConnell equations are performed in Chapter 8 and 8.2.

6. Development of a Simulation Framework for MT and CEST: JEMRIS MT

MRI simulations are desired in many cases and can provide additional insight. For example, safety considerations for living tissue as well as for the MRI hardware suggest the use of simulations prior to the implementation of new processes on real MRI hardware. Likewise, the work involved in implementing new ideas on MRI scanners often requires thorough evaluation through simulations. In addition, simulators can serve as a basis for comparison in quality assurance for data acquisition as well as data processing. Another advantage of simulations is the possibility to modify the parameters of the *virtual* sample in order to check their influence on the results obtained with real **measurements** [91].

In particular for quantitative imaging, simulations are an excellent way to check the performance and accuracy of different quantitative MR sequences. As the input parameters (such as T_1 and T_2) are well known, one can check, if the parameters obtained by the evaluation of a dedicated sequence give accurate results. In particular, quantitative CEST and MT imaging is quite a challenge, as there are many degrees of freedom and usually many parameters need to be determined simultaneously. Using simulations, one can investigate known and new methods and check whether they provide an accurate and precise reproduction of the quantitative parameters (see Chapter 4).

The Juelich MR Group designed a tool for MRI simulations called JEMRIS, the Juelich Extensible MRI Simulator (http://www.jemris.org, [30]). This simulation package is able to simulate arbitrary MR sequences on specified *virtual* samples. It employs a variable time-stepping differential equations solver[1] to compute the Bloch equations numerically.
The existing framework of JEMRIS was modified (see Section 6.1.2) in order to simulate magnetisation transfer and CEST effects based on the well-known two-pool model, which was extended

[1] CVODE, https://computation.llnl.gov/casc/sundials/main.html

to n exchanging pools. This Chapter describes the necessary steps which were performed to include the Bloch-McConnell equation into the existing simulation framework.

6.1. Implementation and Theory

6.1.1. The n-Pool Model for Magnetisation Transfer

The Bloch-McConnell equations which describe systems obeying magnetisation transfer and/or CEST (Section 3.2.1) were extended to an n-pool model. Each pool is characterised by its properties, M_0, T_1, T_2 and $\Delta\omega$. The exchange properties between the different pools are given in the exchange matrix, k_{ex},

$$k_{ex} = \begin{pmatrix} 0 & k_{1,2} & \cdots & k_{1,N} \\ k_{2,1} & 0 & \cdots & k_{2,N} \\ \vdots & \vdots & \ddots & \vdots \\ k_{N,1} & k_{N,2} & \cdots & 0 \end{pmatrix}. \tag{6.1}$$

Then the n-pool Bloch equations for pool i are given as:

$$\dot{M}_x^i = -\left(\frac{1}{T_2^i} + \sum_{\substack{l=1 \\ i\neq l}}^{n} k_{i,l}\right) M_x^i - (\omega_i - \omega_{RF}) \cdot M_y^i - \omega_y \cdot M_z^i + \sum_{\substack{l=1 \\ i\neq l}}^{n} k_{l,i} \cdot M_x^l \tag{6.2}$$

$$\dot{M}_y^i = -\left(\frac{1}{T_2^i} + \sum_{\substack{l=1 \\ i\neq l}}^{n} k_{i,l}\right) M_y^i + (\omega_i - \omega_{RF}) \cdot M_x^i + \omega_x \cdot M_z^i + \sum_{\substack{l=1 \\ i\neq l}}^{n} k_{l,i} \cdot M_y^l \tag{6.3}$$

$$\dot{M}_z^i = -\left(\frac{1}{T_1^i} + \sum_{\substack{l=1 \\ i\neq l}}^{n} k_{i,l}\right) M_z^i + \left(\frac{1}{T_1^i}\right) \cdot M_0^i - \omega_x \cdot M_x^i + \omega_y \cdot M_y^i + \sum_{\substack{l=1 \\ i\neq l}}^{n} k_{l,i} \cdot M_z^l \tag{6.4}$$

As the original version of JEMRIS covers only a single spin ensemble without any possible exchange, some major changes had to be programmed:

6.1.1.1. Modified Bloch Equations

The modified Bloch equations (Eq. (6.2) and (6.4)) were implemented into the existing framework of JEMRIS. This extends the complexity of the calculations, as the number of coupled differential equations increases by a factor of $3n$.

6.1.1.2. *Virtual* Sample of Exchanging Spins

One major modification of JEMRIS included a change of the sample field structure. In order to consider different pools, the structure of the existing sample had to be changed significantly. The standard sample (one-pool, no exchange) consists of several isochromat ensembles, each characterised by its relaxation properties ($R_1 = 1/T_1$, $R_2 = 1/T_2$), its M_0, the spin location and optionally varying ω_0 values to account for T_2^* or chemical shift effects. This established system had to be extended for n pools. Each isochromat ensemble (at one location) has now n different M_0 values, relaxation times and ω_0 values. Different frequencies represent different resonance frequencies of the distinct pools, a feature needed in particular for CEST simulations. As a consequence, the sample size increases by a factor of n. Additionally, the exchange matrix which describes the exchange properties of the n pools has to be passed to JEMRIS. The exchange rates are stored in a square matrix as shown in Equation (6.1). It is sufficient to fill the upper triangle of the exchange matrix, as the lower triangle is filled using mass balance, see Section 6.1.1.3. Specifying the number of exchanging pools determines the matrix size expected by JEMRIS.

6.1.1.3. Mass Balance

In general, mass balance is assumed for the exchanging spins when applying the two-pool model [92]. Mass balance means

$$M_0^i k_{ij} = M_0^j k_{ji}. \tag{6.5}$$

To ensure that mass balance is covered for isochromats with different M_0 values as well, the implementation of JEMRIS MT uses a global exchange matrix k_{ex} where only the upper triangle of the exchange matrix (6.1) has to be specified by the user. For each isochromat, the lower triangle is filled automatically by the simulation software based on Equation (6.5), maintaining mass balance.

6.1.2. Software Design

The Bloch-McConnell equations were included into the JEMRIS framework. A class diagram of the modified JEMRIS MT version is shown in Figure 6.1. The model was extended with the Bloch-McConnell solver (red framed). To maintain the functionality, the blue classes had to be modified.

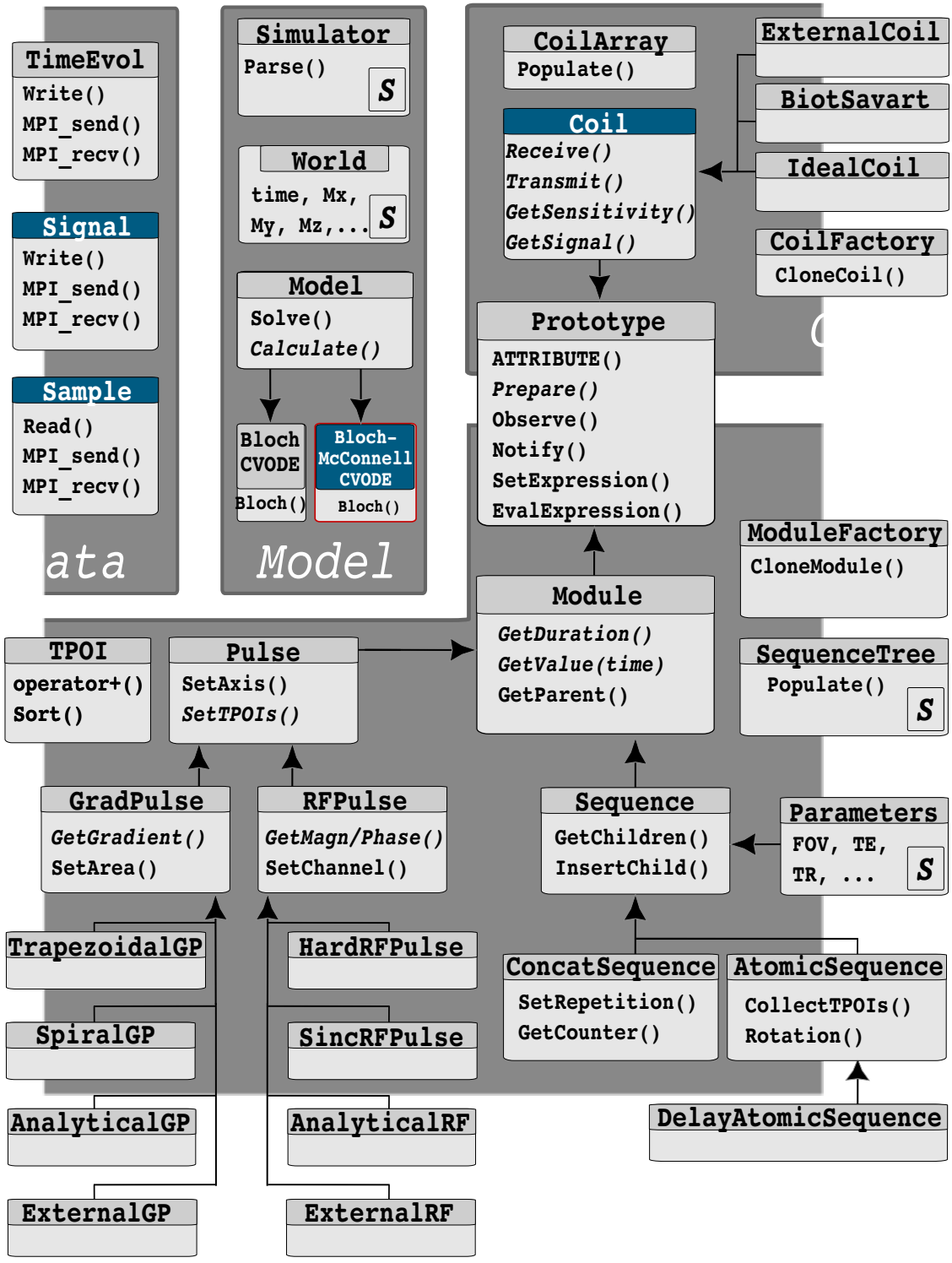

Figure 6.1: *Schematic class diagram of JEMRIS MT, please see text for further information.*

6.2. z-Spectra as an Example for CEST and MT Simulations

This section presents some z-spectra (cf. Section 3.4) as an example for the large variety of possible applications of JEMRIS MT. More simulation results are presented in the subsequent sections, in the special context of quantitative imaging. Spectroscopic simulations for MT and CEST effects have already been performed e.g. [51] and [92]. Therefore, it is possible to compare these simulations with the ones performed with the JEMRIS MT package. Furthermore, JEMRIS MT allows one to simulate the imaging process, which hugely extends the number of possible applications.

6.2.1. Samples and Sequence

z-spectra were simulated for different *virtual* samples as well as for different sequence parameters to show potential applications. MT parameters for the simulations are listed in Table 6.1. The values mimic a 4% agarose phantom, as determined by Henkelman et al. [51]. Sample parameters for the *virtual* sample used for the CEST simulations were taken from Woessner et al, [92], and are summarised in Table 6.2. A z-spectrum is usually composed of:

- A reference measurement, usually a 90°or α excitation followed by a readout.
- A presaturation period, (CW or) pulsed excitation with varying off-resonance, a spoiler gradient and a 90°or α excitation followed by a readout period.

Simulations of MT z-spectra were obtained using 90°excitation, a readout of 10000 points within a TR of 100 s to allow for full relaxation. Four hundred off resonance excitations were spaced equally from -40 KHz to 40 KHz.

Parameter	Pool A	Pool B
$\mathbf{M_0}$	1	0.011
$\mathbf{T_1}$/ms	2456	1000
$\mathbf{T_2}$/ms	32	0.0129
$\mathbf{\Delta\omega}$/ Hz	0	0
$\mathbf{k_{AB}}$/Hz	2.1	

Table 6.1: *Simulation parameters for a* virtual *4% agarose sample, used for z-spectra simulations.*

6.2.2. Results

6.2.2.1. MT

Henkelman et al. [51] **measured** z-spectra for **physical** agarose samples of different concentrations following saturation by continuous wave irradiation (Figure 6.2). To emphasise the

Parameter	*Virtual* sample 1		*Virtual* sample 2		*Virtual* sample 3	
	Pool A	Pool B	Pool A	Pool B	Pool A	Pool B
M_0	1	$7.272 \cdot 10^{-4}$	1	$3.636 \cdot 10^{-4}$	1	$3.636 \cdot 10^{-4}$
T_1/ms	2000/indicated	100	1000	100	1000	100
T_2/ms	100/indicated	80	200	100	200	100
$\Delta\omega/kHz$	0	20	0	20	0	20
k_{AB}/Hz	2.1816		1.818		0.1818	

Table 6.2: *Simulation parameters for the* virtual *CEST sample, used for z-spectra simulations.*

influence of exchange on the z-spectra, they *simulated* a *virtual* 2% agarose sample with and without exchange (Figure 6.3, right).

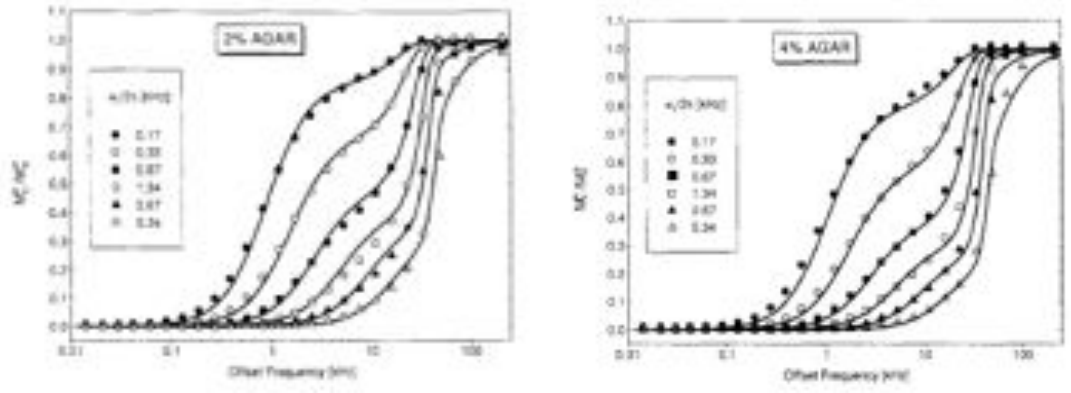

Figure 6.2: *z-spectra* ***measured*** *by Henkelman et al. [51] following CW irradiation.*

Clinical scanners are usually not able to perform CW saturation as their amplifiers are not designed for long duty cycles. Therefore, JEMRIS MT was employed to *simulate* z-spectra of a *virtual* 4% agarose sample saturated with pulsed irradiation. The results are displayed in Figure 6.3. The upper lines show the *simulated* z-spectra without exchanging spins, the lower ones with exchanging spins. Comparing the JEMRIS MT results for pulsed saturation (Figure 6.3, left) with Henkelman's results, one can resume that the effects are similar, but CW irradiation produces a "hump" which is not visible in the pulsed results.

6.2.2.2. CEST

Woessner et al. [92] performed *simulations* on CEST z-Spectra. Selected *simulations* were repeated in pulsed mode, using 300 off-resonance excitations spaced equally from -30 kHz to 30 kHz. The results are displayed in Figure 6.4 and Figure 6.5.

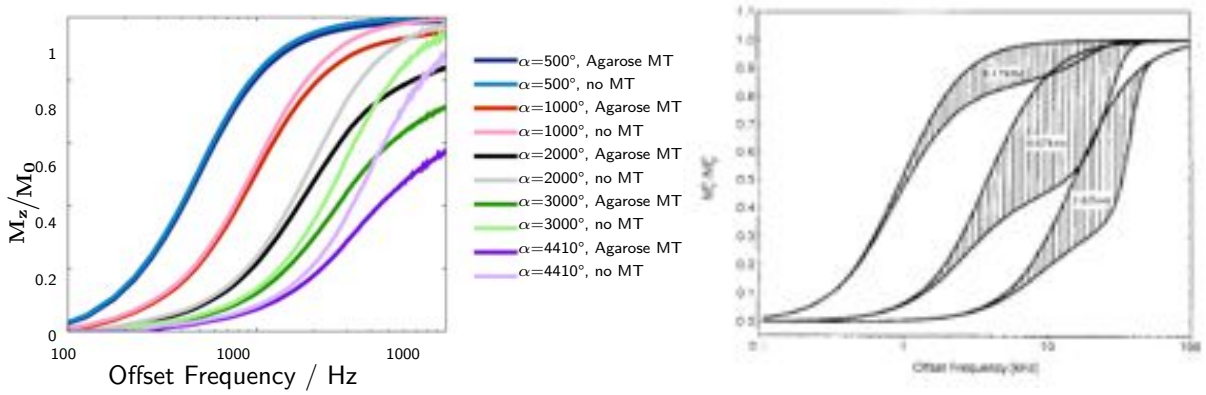

Figure 6.3: *JEMRIS MT results for pulsed presaturation (50 sinc-shaped presaturation pulses of different saturation flip angles, $BW = 50\,Hz$) of a* virtual *agarose sample (left) compared to Henkelmans simulations for CW irradiation (right), [51].The upper curves show the z-spectrum without exchange, the lower with exchange.*

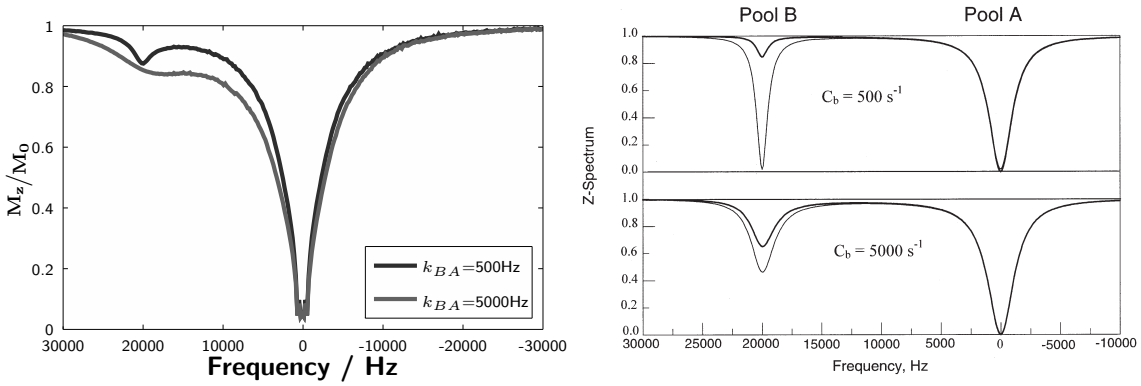

Figure 6.4: *Simulations of CEST z-spectra. Left: JEMRIS CEST results (*virtual *samples 2 and 3) for pulsed MT (70 sinc-shaped presaturation pulses of 4000° saturation pulses, $BW = 50\,Hz$) and different k_{BA} values.*
Right: Simulation results obtained by Woessner et al. [92], the parameters used are these of the virtual *samples 2 and 3 given in Table:6.2: "Simulated z-spectra for a two-pool exchange system with bulk water (pool A) at zero and bound water (pool B) at 20000 Hz, illustrating the differences between slow ($k_{BA} = 500\,Hz \hat{=} k_{AB} = 0.1818\,Hz$) and fast $k_{BA} = 5000\,Hz \hat{=} k_{AB} = 1.818\,Hz$) exchanging systems. The thin line peak centred at 20000 Hz in each panel shows the amount of pool B spins saturated by a 512 Hz B_1 pulse of long duration. The thick line peak centred at 20000 Hz shows the net decrease in bulk water intensity (M_z^A/M_0^A) following a steady-state exchange between the irradiated B spins and the A spins."*

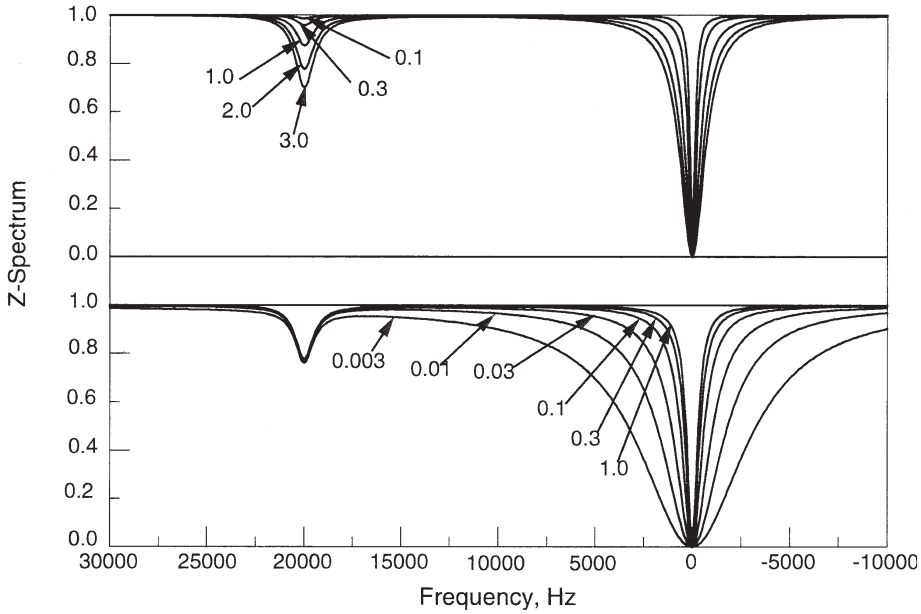

Figure 6.5: *Woessners' simulation of CEST z-spectra [92]: "Simulated two-pool z-spectra showing the dependencies of M_z on the T_1^A and T_2^A values. The upper graph is for $T_2^A = 0.1\,s$ and various T_1^A values in units of s, as indicated in the graph. The lower graph is for $T_1^A = 2\,s$ and various T_2^A values in units of s, as indicated in the graph.*

6.2.3. Discussion

This evaluation aims to check the performance of JEMRIS MT by comparing JEMRIS MT results with existing simulations. As clinical scanner are usually not able to perform CW irradiation, the pulsed approach was preferred for these simulations. As not every detail has been published by Henkelman and Woessner, an exact reproduction of their results was not possible. However, the results are qualitatively comparable and thus validate the *simulation* approach.

6.2.3.1. MT

The *virtual* as well as the **physical** agarose sample, undergoing MT shows similar z-spectra, there is more saturation of the free pool with exchange than without. The effect increases, if more saturation pulses are applied, as one would expect and as it was shown by Henkelman et al. [51].

6.2.3.2. CEST

The *simulation* results of the *virtual* CEST sample are in good agreement with Woessner's *simulations*. The *simulations* obtained by Woessner et al. were based on CW irradiation, compared to the pulsed approach simulated with JEMRIS MT. Two main differences can be noticed. First,

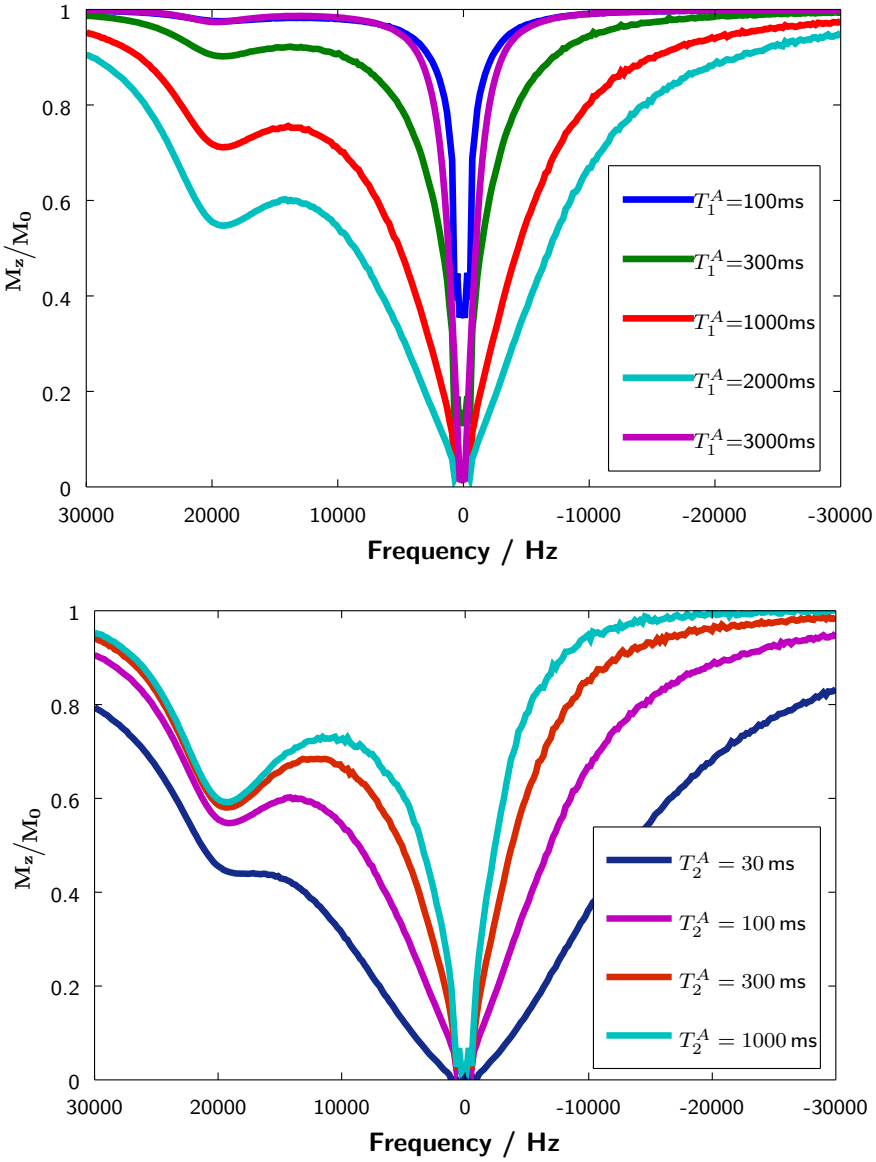

Figure 6.6: *Pulsed saturation CEST simulations performed with JEMRIS MT. Top: JEMRIS CEST results (*virtual *sample 1) for pulsed saturation (70 sinc-shaped presaturation pulses of 4000° saturation pulses, BW = 50 Hz) and different T_1^A values. Bottom: JEMRIS CEST results (*virtual *sample 1) for pulsed MT (70 sinc-shaped presaturation pulses of 4000° saturation pulses, BW = 50 Hz) and different T_2^A values.*

the JEMRIS MT results show some kind of secondary peaks around the centre frequency. This effect arises from the usa of sinc-shaped saturation pulses. Despite that, the z-peaks of the JEMRIS *simulation* are not as well separated as the ones simulated by Woessner. Again, this originates in the different *simulation* parameters. As Figure 6.7 shows, the peaks are less separated, if more saturation is achieved. Therefore, one can conclude that the effective saturation in the JEMRIS MT simulations is larger than the saturation achieved by the CW irradiation.
In summary, *simulations* of z-spectra obtained with pulsed saturation give results which are qualitatively comparable with the CW approach. This means that parameter changes, e.g. for varying exchange rates or different relaxation times manifest in similar changes. However, as the saturation effect of pulsed and CW irradiation differs, the results are not exactly the same and differ in their quantitative behaviour.

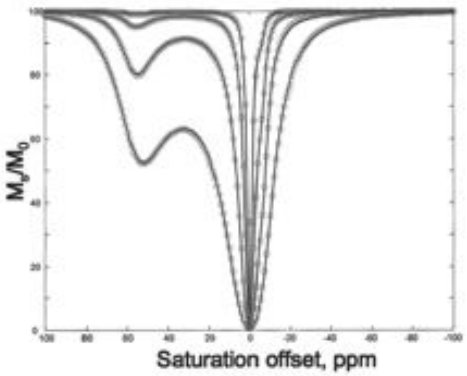

Figure 6.7: *The circles show an experimental z-spectrum of a 10mM aqueous solution of EuDOTAM* ***measured*** *by Woessner. The* ***measurements*** *were performed at 4.7T with different B_1 values of 109, 229, 505 and 1020 Hz, in descending order from the graph [92].*

7. Effects of Magnetisation Transfer and Saturation on Longitudinal Relaxation

T_1 quantification in the presence of MT is a rather difficult task, as was already noted in Chapter 5. The simulation framework presented in Chapter 6 was employed to investigate the effects of MT on T_1. First, the putative or observed relaxation rate was introduced (Section 7.1). Influences of sample variations on the putative / observed T_1 values were analysed by means of a *virtual* agarose sample (Section 7.1.1). It transpired that the putative / observed T_1 values are always shorter than the largest single-pool T_1 value. As a next step, effects of saturation on the estimated T_1 values were investigated (Section 7.2). Whether $T_1^{putative/observed}$ changes if the sample underwent some form of saturation, e.g. by slice selection or presaturation pulses, was evaluated. Our results showed, that $T_1^{putative/observed}$ can be used as a quantitative parameter, if the saturation process is considered in the signal equation. In case of the simulated IR sequence, this can be performed in a simple way by fitting an additional saturation parameter and therefore a three-parameter rather than a two-parameter fit.

7.1. Intrinsic Shortening of T_1 in the Presence of MT

The equations describing the evolution of the longitudinal magnetisation in the presence of MT were already introduced in Chapter 5. The relaxation process is modelled by a biexponential function:

$$M_z^A(t) = M_0^A + C_1 e^{-\lambda_1 t} + C_2 e^{-\lambda_2 t} \tag{7.1}$$

$$M_z^B(t) = M_0^B + \tilde{C}_1 e^{-\lambda_1 t} + \tilde{C}_2 e^{-\lambda_2 t} \tag{7.2}$$

with

$$\begin{aligned} \lambda_{1,2} = &\frac{1}{2}\left(R_1^A + k_{AB} + R_1^B + k_{BA}\right) \\ &\mp \frac{1}{2}\sqrt{\left(R_1^A + k_{AB} + R_1^B + k_{BA}\right)^2 - 4\left(R_1^A R_1^B + k_{AB} R_1^B + k_{BA} R_1^A\right)}. \end{aligned} \tag{7.3}$$

C_1, C_2, $\tilde{C}_1$ and $\tilde{C}_2$ are functions of the sample parameters, $R_1^A = 1/T_1^A$, $R_1^B = 1/T_1^B$, k_{AB}, k_{BA}, M_0^A, M_0^B, and the initial conditions.
As the fast recovery rate, λ_2, is difficult to observe with state-of-the-art MRI equipment, it is usually neglected. Instead, fitting to a monoexponential recovery curve is usually performed and gives a relaxation time, called $T_1^{putative} = 1/\lambda_1 \neq T_1^A$, in simulations and $T_1^{observed} = 1/\lambda_1$ in measurements, respectively.
This relaxation rate differs from the single relaxation rates, T_1^A and T_1^B, of the system. Assuming that the free water pool (pool A) is much larger than the bound water pool (pool B), one would expect that the system is dominated by the T_1^A relaxation time. However, the relaxation rates, $T_1^{putative}$ or $T_1^{observed}$, are influenced by all sample parameters (the exchange rate, the single relaxation times and the ratio of the pool sizes). These cross relations complicate the quantification of the recovery rates.
Figure 7.1 visualises the influence of different parameter combinations in simulation on the value for $T_1^{putative} = 1/\lambda_1$ based on Equation (7.3).

An approximation for $T_1^{putative}$ in the presence of proton exchange (two pools) for small M_0^B was reported by Bloembergen et al. [93] and derived by Luz et al. [58]:

$$\frac{1}{T_1^{putative}} \approx \frac{1}{T_1^A} + \frac{M_0^B}{T_1^B + \frac{1}{k_{BA}}}. \tag{7.4}$$

As a first evaluation of its ability, the simulation framework JEMRIS MT was employed to assess the validity of those approximation by examining the influence on $T_1^{putative}$. It should be noted that the JEMRIS simulation approach is closer to reality as the approach leading to the approximation (7.4), as JEMRIS also includes relaxation during excitation as well as the M_x and M_y evolution which considers the cross terms to the Bloch McConnell Equations (3.8). The transverse terms were neglected (cf. Equation (5.1)) in the derivation of Equation (7.2).

7.1.1. Sample and Sequence

Sample

Simulations were performed on a *virtual* 4% agarose sample. In order to use sample parameters which mimic reality as good as possible, the quantitative parameters suggested by Henkelman et al. [51] were used as a basis. Pool A denotes the free water pool, while Pool B denotes the restricted or bound pool. Henkelman's measurement were performed at 1.5 T. All measurements obtained in this thesis were performed at a 3 T scanner, the dominating T_1^A as well as T_2^A of pool A were modified as described below, to reflect the field strength dependence of the relaxation

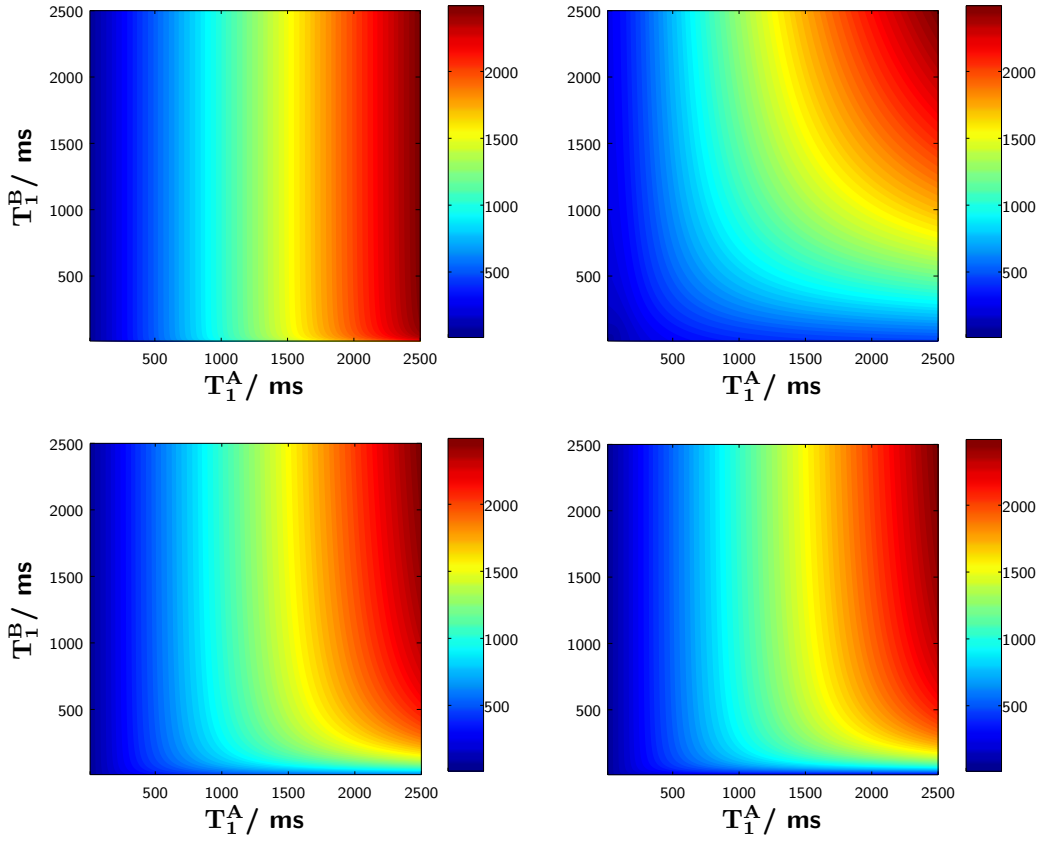

Figure 7.1: *$T_1^{putative}$ / ms (colourbar) for different parameter combinations. From top left to bottom right: $M_0^B = 0.001 M_0^A$ and $k_{AB} = 300\,Hz$, $M_0^B = 0.5 M_0^A$ and $k_{AB} = 2\,Hz$, $M_0^B = 0.05 M_0^A$ and $k_{AB} = 2\,Hz$ and $M_0^B = 0.051 M_0^A$ and $k_{AB} = 100\,Hz$. The plots were created using Equation (7.3) and $T_1^{putative} = \frac{1}{\lambda_1}$.*

rates. T_1 was assessed experimentally (for details see Section 7.2) using a spectroscopic IR sequence and the T_1^A value was calculated using Equation (7.4). T_2^A was assumed to be the same as the total T_2 measured with a spectroscopic sequence; a reasonable assumption as T_2^B is very short and M_0^B is small, therefore $M_\perp^B$ is small and does not give a large contribution to the signal. Those measured values were then used to adopt the *virtual* sample, its values are summarised in Table 7.1. To study the sensitivity of $T_1^{putative}$ on variations of the input

Parameter	Pool A	Pool B
$\mathbf{M_0}$	1	0.011
$\mathbf{T_1/ms}$	2456	1000
$\mathbf{T_2/ms}$	54	0.0129
$\mathbf{\Delta\omega/Hz}$	0	0
$\mathbf{k_{AB}/Hz}$	163.63	

Table 7.1: *Simulation Parameters for the* virtual *MT sample based on [51], modified for 3 Tesla.*

parameters, the basic set of *virtual* sample parameters presented in Table 7.1 was modified. In each *simulation*, one parameter, either T_1^B or M_0^B/M_0^A or k_{AB}, was varied over a specific range.

Sequence

Figure 7.2 shows an inversion recovery free induction decay sequence (IR-FID). This sequence (without the presaturation module, see later) was employed to study the effect of MT on the putative T_1 values through simulations. Simulations allow one to change the sample parameters at will, e.g. the exchange (rates) can be altered arbitrarily. Those *simulations* were used to study the influence of MT on the putative T_1 value obtained. The sequence started with an inversion of the magnetisation with a 5-lobe sinc pulse of bandwidth = 1 KHz, flip angle=180°. After an inversion time, TI, of duration $TI = m \cdot 65\,\text{ms}$, $m = 1...M$, M denoting the number of repetitions, a second 5-lobe sinc pulse with a flip angle of 90° was applied. Thereafter, a read-out of 2000 points within 2000 ms was performed. The *simulations* were performed as 2D simulations, thus effects such as imperfect slice selection or crosstalk between slices are avoided. The recovery of M_z (assuming monoexponential recovery) is determined by Equation (4.1). Considering imperfect inversion by introducing a correction factor, μ, the equation reads

$$|M_z(T_I)| = \left| M_0 \left(1 - 2\mu e^{-\frac{T_I}{T_1^{putative}}} \right) \right|. \tag{7.5}$$

$T_1^{putative}$ values were obtained by fitting the *simulated* signal intensities to Equation (7.5) using the nonlinear least squares fitting algorithm (part of the `fit` function) provided by MATLAB for the 50 different TI. The *simulation* results were compared with the approximation in Equation (7.4).

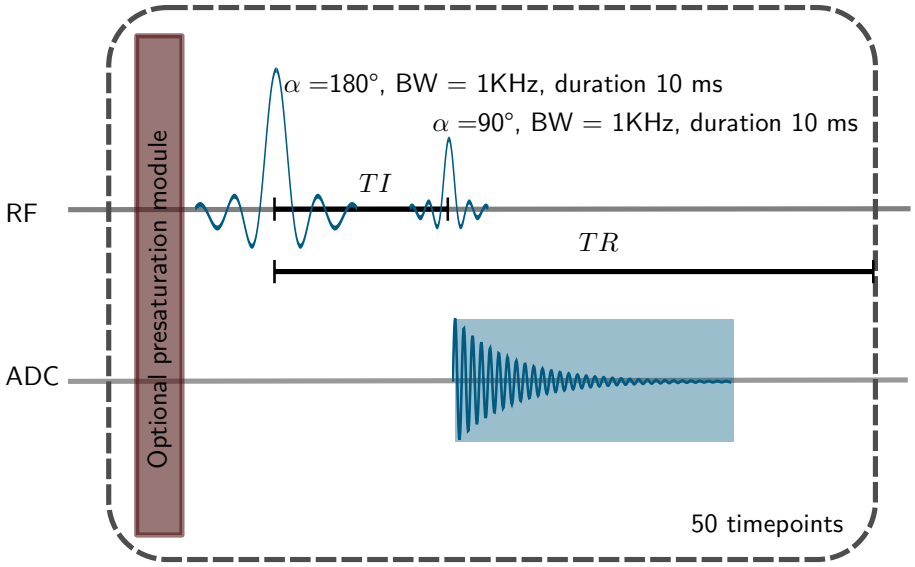

Figure 7.2: *IR-FID sequence used for the* simulations *displayed in Figure 7.4. TI was 65ms, all other parameters are given in the sequence diagram.*

7.1.2. Results

JEMRIS MT provides the summed signal of both pools, as one would measure, but it also outputs the signals of each pool separately. This allows one to distinguish the effects of each single pool, if necessary. In case of MT *simulations*, M_0^B is usually rather small while T_2^B is very short, leading to a very fast T_2 decay of the small pool. Therefore, the direct contribution of pool B to the *observed* signal is rather low - the pool B curves are almost invisible compared to those of pool A. Importantly, however, due to the exchange, the magnetisation of pool A is influenced by pool B.

To obtain the $T_1^{putative}$ values, the FID generated by the IR-FID sequence was monitored and M_z was calculated as the integrated spectrum for each TI. The resulting relaxation curve of M_z as well as the result of the fitting procedure are displayed in Figure 7.3. T_1^A, T_1^B, k_{AB} and M_0^B were varied in order to check the validity of Equation (7.4). The results are displayed in Figure 7.4. The dashed line displays $T_1^{putative}$ calculated with Equation (7.4) using the *simulation* parameters while the stars give the values for $T_1^{putative}$ fitted using the *simulation* result. The results demonstrated in Figure 7.4 show that the approximation (7.4) is valid for a broad range of T_1^A and T_1^B values, as well as for $M_0^B \ll M_0^A$. The curves diverge for larger M_0^B values.

7.1.3. Discussion

This section investigated the potential benefits arising from the usage of MT simulations for T_1 estimations. The *simulations* presented here provide clear support for the fact that the *putative*

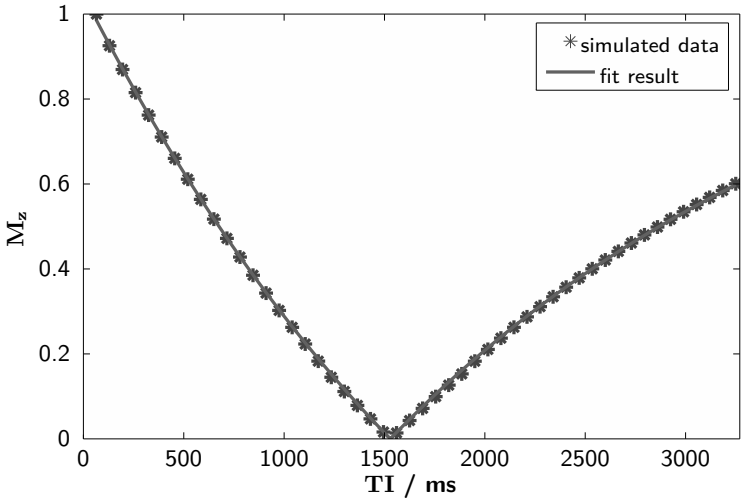

Figure 7.3: *M_z recovery curve* simulated *with JEMRIS MT and the fitting result.*

T_1 values are shorter in the presence of exchange. Magnetisation transfer opens another relaxation path, accelerating longitudinal relaxation. Furthermore, the simulations confirmed the validity of the approximation given in Equation (7.4) as a good estimate of $T_1^{putative}$. Although this approximation is based on the z-component of the Bloch McConnell Equations, Equation (7.4) was verified by means of the IR-FID *simulations*, if M_0^B is small enough ($M_0^B < 0.1\ M_0^A$). It fails for larger M_0^B values ($M_0^B > 0.1 M_0^A$). The *simulations* obtained here employ no imaging gradients. Potential effects arising from the imaging process will be discussed in subsequent chapters.

The shortening of $T_1^{putative}$ in the presence of MT is depicted in Figure 7.4. For example both a larger pool B (the restricted protons) as well as larger differences in $T_1^{A,B}$ of the single pools, increase the MT effect and lead to a shorter total relaxation time $T_1^{putative}$. In contrast, without any exchange ($k_{AB} = 0$), $T_1^{putative}$ is given by the mean T_1 relaxation time of both pools weighted by each respective pool size. Magnetisation transfer changes the putative T_1 values if the relaxation curve is fitted to a monoexponential decay. Biexponential fitting is usually redundant, as the effect of the fast recovery rate is rather small. Including biexponential M_z recovery increases the number of fitting parameters and biexponential fitting is an extremely ill-posed problem (cf. Chapter 8). Although the goodness of the fit increases with the number of free parameters, the values for the single parameters are less reliable, especially if noisy data are fitted.
In summary, MT shortens $T_1^{putative}$ intrinsically and this shortening should be independent of the spectroscopic or imaging sequence - see Section 7.2.

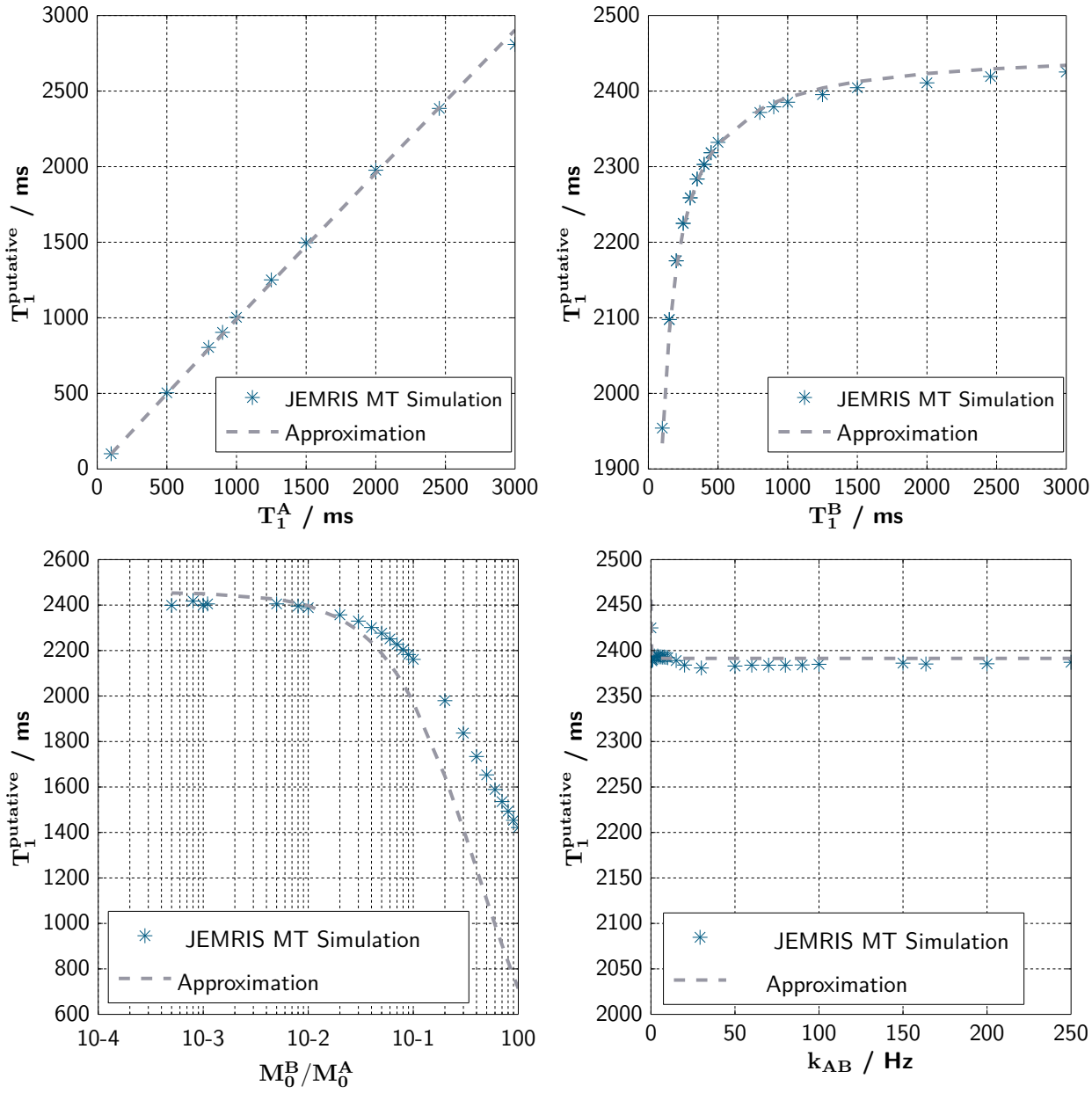

Figure 7.4: *Parameter dependence of $T_1^{putative}$.* ***Top row:*** *$T_1^{putative}$ for T_1^A and T_1^B variations, the approximation* (7.4) *is very good for all* simulated *values.*
Bottom left: *Parameter dependence of $T_1^{putative}$ on M_0^B variations, the approximation* (7.4) *is valid for smaller M_0^B values.*
Bottom right: *$T_1^{putative}$ is not as stable for different k_{AB} values, but the approximation gives a good estimate on the T_1 values one can observe.*

7.2. Longitudinal Relaxation after Saturation of the Bound Proton Pool

As described above, the longitudinal relaxation constant arising from monoexponential fitting in the presence of MT, $T_1^{putative}(simulations)$ or $T_1^{observed}$ (**measurements**), is always shorter than the largest "intrinsic relaxation times, $\max(T_1^A, T_1^B)$. Furthermore, the MT effect manifests itself generally in partial saturation of magnetisation.
This section will answer the question if and how the **measured** T_1 relaxation time obtained by inversion recovery experiments is influenced by MT effects after partial saturation of the bound proton pool. Moreover, possible modifications of the signal equations are discussed to incorporate MT effects and enhance the precision of $T_1^{putative}$ for inversion recovery sequences.
To eliminate possible influences of the imaging gradients, a spectroscopic inversion recovery sequence (IR-FID, see 7.2.1.2) was *simulated* to obtain $T_1^{putative}$. *Simulations* were then confirmed by corresponding **measurements**. Then, as a comparison, an inversion recovery spin echo sequence (described in 7.2.1.2, Figure 7.5) employing imaging gradients was *simulated* and **measured**. The aim was to examine the imaging process itself and any influences thereof on the final result for $T_1^{putative}$.

The IR-FID and the IR-SE sequences were *simulated* and **measured** with and without saturation of the bound proton pool. Long TR allows for full relaxation and this has the advantage that no effects such as stimulated echoes or imperfect spoiling influence the outcome. 2D simulations not only avoid crosstalk between slices but also effects arising from imperfect slice profiles. Therefore *simulation* results can be compared with **measurements** obtained without excessive consideration of possible artefacts.

7.2.1. Simulations

7.2.1.1. Sample

The same *virtual* agarose sample as described in Section 7.1.1 was used for the *simulations*. Its parameters are summarised in Table 7.1.

7.2.1.2. Sequence

Presaturation Module: *Simulations* were obtained using the IR-FID method described in Section 7.1.1 and using an IR-SE sequence, described below. Both sequences were equipped with a flexible module[1] dealing with Gaussian presaturation pulses. This adaptable module allows one

[1]The "default" presaturation module (used unless otherwise stated) applied 45 Gaussian saturation pulses with a nominal flip angle of 180°, a bandwidth of 600 Hz and 1.5 kHz off-resonant. A 4 ms spoiler with an amplitude

to choose different pulses and parameters for presaturation. Thus, effects of different presaturation modules on the signal as well as on the T_1 values can be studied. Pulsed presaturation was chosen, as the scanner hardware does not allow operating in continuous wave mode.

IR-FID: The sequence displayed in Figure 7.2 was *simulated* with and without the presaturation module (described above) prior to the 180° inversion pulse. A *simulation* cycle contains 51 *simulations*, each with a different TI ranging from 10 ms up to 51 · 80 ms.
The $T_1^{putative}$ values were fitted based on the recovery curve of the signal, S, obtained for different TI (Equation (7.5)). Two approaches were tested in the following. First, full inversion and no saturation effect ($\mu = 1$) was assumed, which was represented by a two parameter fit of Equation (7.5), where μ was set to 1. Then a three-parameter fit was obtained, incorporating imperfect inversion with μ as a third fitting parameter. Each *simulation* cycle was repeated 80 times. SNR of 100 (last simulated inversion time) with added Gaussian noise was assumed before fitting. Consequently, the estimated T_1 values were Gaussian distributed with mean and standard deviation.

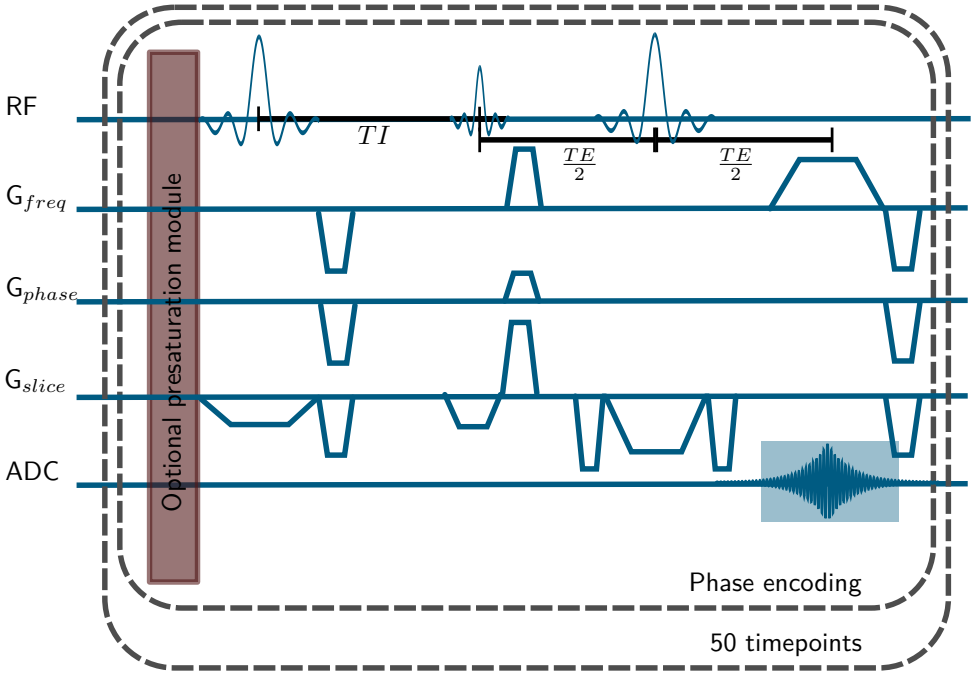

Figure 7.5: *IR-SE sequence diagram displaying the sequence used for simulations.*

IR-SE: An IR-SE imaging sequence (see Figure 7.5) was extended with the "default" presaturation module described in 7.2.1.2. The *simulation* parameters include: FOV=100×100 mm^2,

of 2 $^{mT}/_{m}$ succeeds each pulse.

image matrix=32 × 32 voxel, TR =15,000 ms, TE = 10 ms, with the first TI at 10 ms, once more expanded by up to 50 increments of 80 ms. The simulations were performed with and without the presaturation module. SNR of 100 with added Gaussian noise was assumed, thus noise was added accordingly to both (with and without presaturation) *simulation* results. Then the $T_1^{putative}$ fitting procedure was repeated 5 times, resulting in 980 voxel (5 · 32 · 32 voxel - background voxel) within the phantom and their corresponding $T_1^{putative}$ values.

7.2.1.3. Results

Spectroscopic *simulation* results are displayed as blue circles with error bars in Figure 7.6. All values are summarised in Table 7.2. Comparing the part with and without the presaturation module reveals how crucial it is to fit the saturation parameter, μ, in order so account for saturation effects. This is visualised in the upper row in Figure 7.7, which shows the *simulated* signal for different TI *simulated* with the MT presaturation module and both fitting methods. Given appropriate fitting of μ, MT presaturation pulses hardly affect $T_1^{putative}$ and yield it a reliable quantity in IR *simulations*. A Students' t-test was performed to check for significant differences between the $T_1^{putative}$ values with and without presaturation. Neglecting μ gives significantly different results with and without presaturation pulses ($p < 0.0001$) while the *simulation* results considering μ show no relevant differences in $T_1^{putative}$ between the two approaches (p=0.44 for *simulations*).

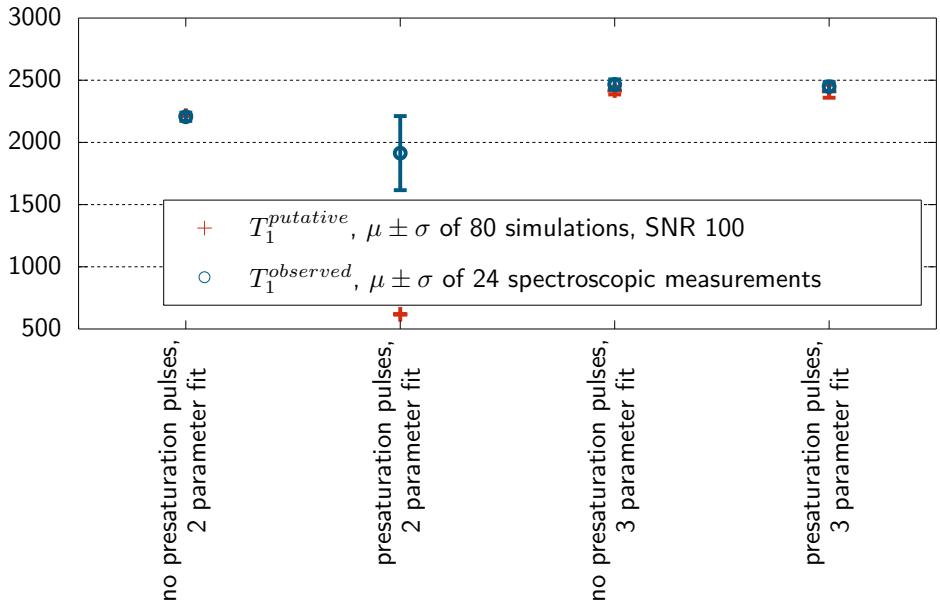

Figure 7.6: *Summary of all* simulation *and* ***measurement*** *results with a two and three parameter fit and with and without the presaturation pulses.*

It comes at no surprise that imaging sequences are affected likewise as the IR-FID. This can be appreciated in the IR-SE simulations. Subsequently, $T_1^{putative}$ was fitted with and without μ for

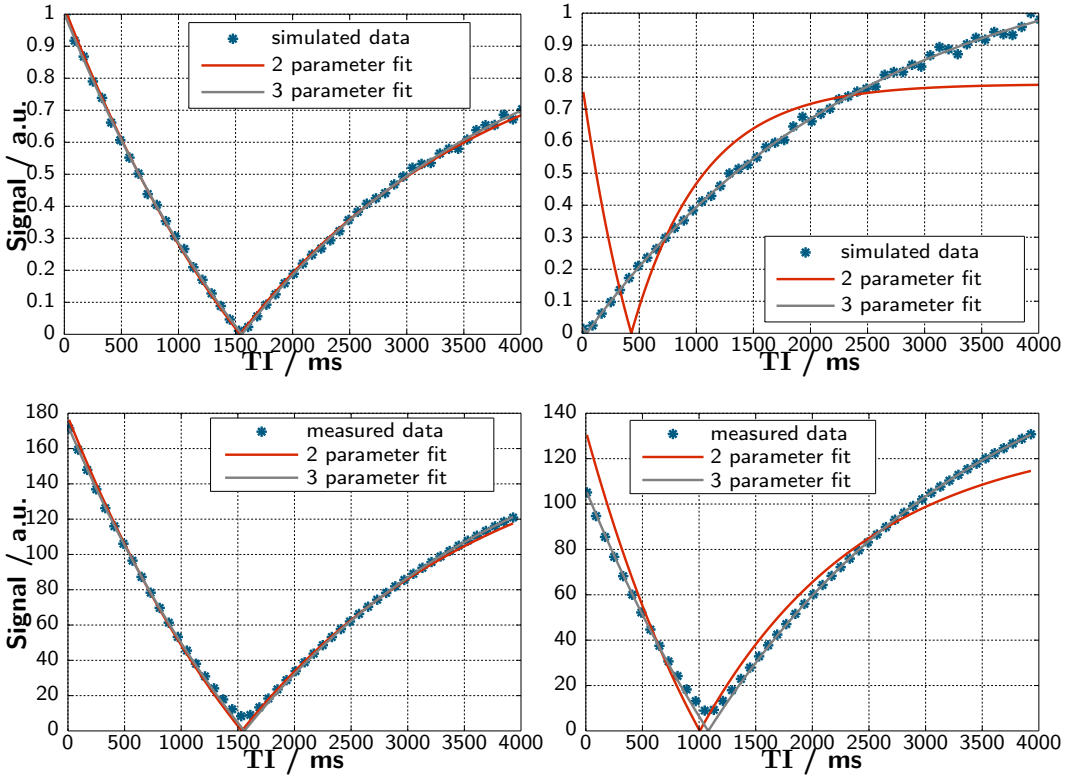

Figure 7.7: *A comparison of* simulation *results with* ***measured*** *results and 2- and 3-parameter fits thereof.* ***Top row:*** Simulation *results without (left) and with (right) the presaturation module. Results are shown for the two and the three parameter fit.* ***Bottom row: Measurement*** *results without (left) and with (right) the presaturation module. The fits were obtained considering two or three parameters respectively. The left figure, without the presaturation module, already shows a difference between the two and the three parameter fit, which is not visible in the simulations. This difference can be attributed to the imperfect inversion which is present in measurements.*

each voxel, giving rise to the results for $T_1^{putative}$ as well as the results of the t-test ($p < 0.001$ for a two-parameter fit, $p = 0.21$ for the three-parameter fit), which are merged in Table 7.2.

7.2.2. Measurements

The results obtained by *simulations* were then confirmed by **measurements**. All **measurements** were performed on a SIEMENS Tim Trio, 3 Tesla, MRI scanner (Siemens AG, Erlangen, Germany), which was equipped with a 35 kW MKS RF power amplifier and a gradient system capable of an amplitude of 40 mT/m at a slew rate of 200 mT/(m ms). All sequences were developed in-house. To highlight the difference between *simulations* and **measurements**, the "T_1" value arising from monoexponential fitting is named $T_1^{observed}$ if obtained by **measurements**.

7.2.2.1. Sample

Phantom experiments were performed on a **physical** sample with 4% agarose dissolved in distilled water. Its parameters obtained spectroscopically were: $T_1^{observed} = 2456$ ms, $T_2 = 54$ ms.

7.2.2.2. Sequence

IR-FID: The IR-FID sequence consists of an SLR inversion pulse (Shinnar-Le Roux, [94][2]) followed by a 90° excitation pulse after TI. The SLR inversion pulse was chosen to achieve a better inversion pulse profile, a possible source of artefacts not present in the 2D only simulations. All other sequence parameters are the same as in the *simulations*, 2 averages and 2048 data points were obtained.
Prior to the spectroscopic IR sequence, the presaturation module (above) was inserted with varying numbers of Gaussian presaturation pulses, ranging from no pulse, as a reference, to 50 pulses, with the RF amplifier enforcing the upper limit. The same $T_1^{observed}$ fitting procedure as for the *simulation* results was used. **Measurements** were performed with and without the presaturation module and, for better statistics, i.e. to allow for the application of a Students' t-test, each **measurement** was repeated 24 times. The **measurements** were repeated with different parameters of the presaturation module (e.g. different bandwidth, different offset frequency).

IR-SE: Lastly, an SLR inversion pulse was included prior to a Spin Echo Sequence. The flexible MT preparation module (7.2.1.2, default parameters) was inserted at the very beginning of each TR cycle. **Measurements** were obtained both with and without the presaturation

[2]SLR pulses usually provide better slice profiles than "normal" sinc pulses and therefore provide a better spatial selection of the desired slice.

module for different TI values. Data were acquired with TR = 15000 ms, TE = 5.78 ms, FOV=148×74 × 30 mm^3, flip angle=90°, image matrix=64×64×1, TI =110, 160, 260, 560, 910, 1210,1560, 1860, 2160, 2510, 2810, 3160, 3460, 3760, 4110, 4410 ms. **Measurements** were performed on a fewer number of TI points compared to the *simulations* while covering the identical time frame. $T_1^{observed}$ was fitted as a 2 parameter fit (μ=1) and as a 3 parameter fit (with μ). The **measurements** were repeated 19 times in order to improve statistics and to permit a t-test.

7.2.2.3. Results

Figure 7.8 shows some images of the agarose tube from the the IR-SE **measurements** with different TI values. A typical T_1 map estimated from the IR-SE is shown in Figure 7.9.

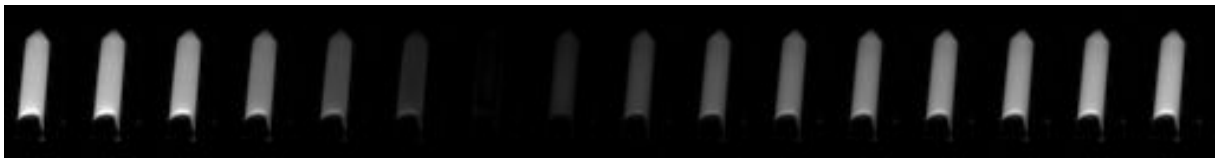

Figure 7.8: *Results of the IR-SE **measurements** with 16 different TIs, increasing from left to right (see text) and without any presaturation.*

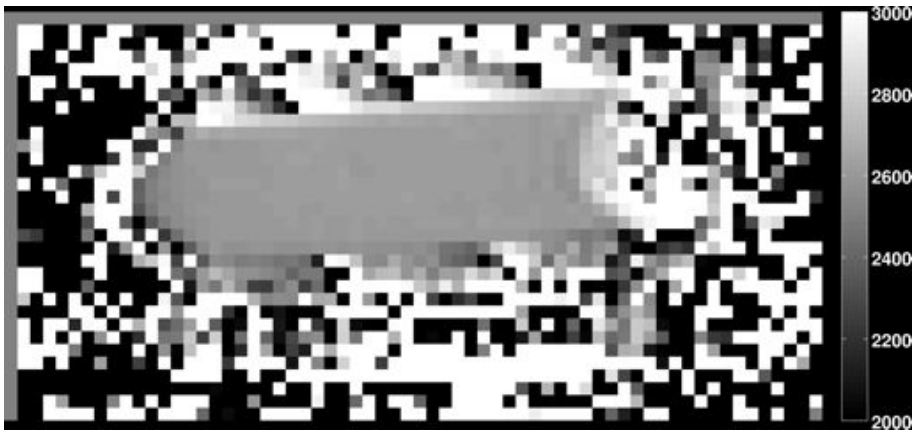

Figure 7.9: *T_1 map calculated by means of the 16 different TIs (see text) without any presaturation.*

Simulation results were further confirmed by spectroscopic **measurements**, the results are summarised in Table 7.2 and in Figure 7.6 (red stars). In **measurements** the necessity of fitting three parameters is even more obvious. The lower part of Figure 7.7 shows values **measured** with the MT presaturation module and both fitting methods. The results with and without presaturation pulses for the two-parameter fit differ significantly as confirmed by a Students' t-test ($p < 0.0001$). The results considering μ show no relevant differences in $T_1^{observed}$ between the two approaches ($p = 0.08$). The saturation effect originating from MT is mirrored in the

	2 Parameter Fit		t-test with and without pre-saturation	3 Parameter Fit		t-test with and without pre-saturation
	No Pre-saturation Module	Pre-saturation Module		No Presaturation Module	Pre-saturation Module	
Simulation IR-FID, $T_1^{putative}$/ms	2215 ± 3	618 ± 2	$p < 0.001$	2417 ± 30	2411 ± 51	$p = 0.44$
Measurement IR-FID, $T_1^{observed}$/ms	2206 ± 33	1914±298	$p < 0.001$	2466 ± 40	2447 ± 37	$p = 0.08$
Simulation IR-SE, $T_1^{putative}$/ms	2387 ± 30	634 ± 42	$p < 0.001$	2455 ± 187	2506±593	$p = 0.09$
Measurement IR-SE, $T_1^{observed}$/ms	2032±210	1622±396	$p < 0.001$	2467 ± 38	2459 ± 51	$p = 0.61$

Table 7.2: *Results of the IR-SE* simulations *and* ***measurements****.*

correction factor μ. The mean μ obtained from the bound proton pool with the 3 parameter fit suggests 0.89 ± 0.026 without presaturation and 0.75 ± 0.13 with presaturation pulses. The difference is significant ($p < 0.0001$) for the **measurements**. Changing the MT preparation module (e.g. less pulses or presaturation pulses with higher flip angles, different bandwidth or off-resonance) lead a different value for the inversion efficiency while the estimated T_1 values did not change (data not shown). This once more supports the thesis that MT modulates the μ while $T_1^{observed}$ based on spectroscopic **measurements** is the same with and without presaturation pulses. Again, the results are given in Table 7.2.

The $T_1^{observed}$ values in the IR-SE **measurements** are very close to the values measured spectroscopically. No significant changes ($p = 0.61$) in the $T_1^{observed}$ value for the IR-SE **measurements** with and without presaturation pulses were identified by the Students' t-test (Figure 7.10). The standard deviation of $T_1^{observed}$ values within the **physical** sample tube of all IR-SE **measurements** does not exceed 37 ms, thus is less than 2%. The small deviations of the $T_1^{observed}$ values between measurement and simulation can be attributed to differences in the parameters of the real, **physical** sample and the *virtual* sample used for simulations as well as the contribution of noise and power limitations of the RF amplifier in the **measurements**. The difference between the two and the three parameter fit in the **measurements** (c.f Figure 7.7) without presaturation can be attributed to imperfect inversion.

7.2.3. Discussion

While Section 7.1 showed that $T_1^{putative/observed}$ changes in the presence of MT, 7.2 shows that this does *not affect the quantitative nature of the longitudinal relaxation time* - if the MT effect

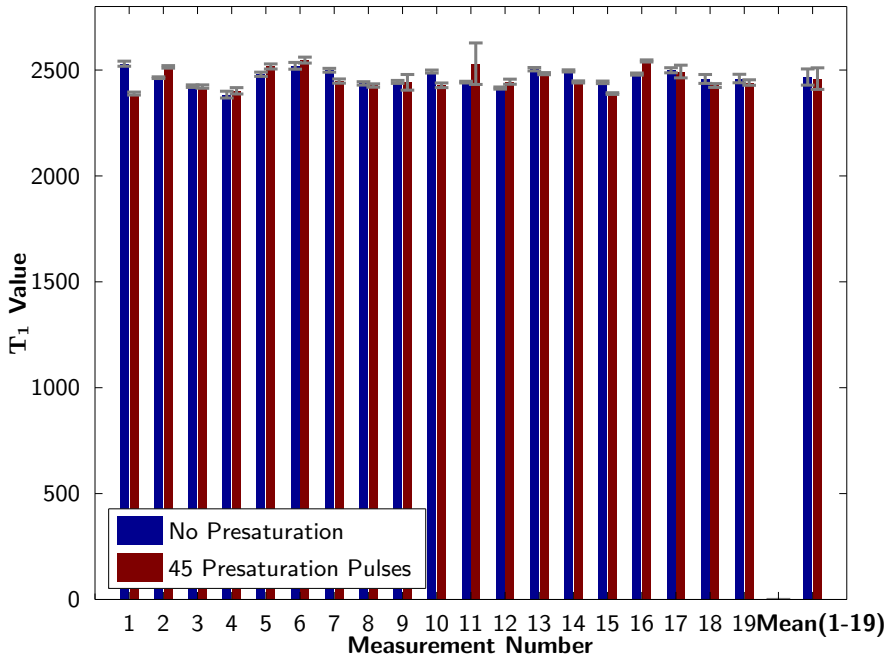

Figure 7.10: *Results of the 19 IR-SE* ***measurements****. The T_1 values displayed here were calculated with a three parameter fit. Although the results vary about 6% between the* ***measurements*** *and with and without the presaturation module, there is no significant difference as confirmed by a t-test.*

is taken into account. The longitudinal relaxation time, obtained by any sequence in the presence of MT, is not T_1^A but $T_1^{putative/observed}$. As the sample parameters (T_1^A, T_1^B, k_{AB}, ...) of a given sample or tissue are constant and cannot be switched on or off, the resulting $T_1^{observed}$ value of the given sample is always the same and therefore quantitative. This was verified in this work and the results presented show, that $T_1^{putative/observed}$ is - even in the presence of MT - a quantitative parameter. However, this holds true only, if the MT influence on the signal equation used for the fitting procedure was considered correctly. In case of an IR-SE experiment, this is rather simple and can be done by introducing an additional parameter, μ, which describes the effect of saturation as well as imperfect inversion. The MT effect decreases the magnetisation after the 180° pulse - less magnetisation is observed. This modifies the initial conditions of the solution of Equation (7.5) and can be summarised in the correction factor μ. Using a three parameter fit, variations between prepulsed experiments and those without the presaturation module are below the noise level, a fact underlined by the results of the t-test. For simple inversion recovery experiments this approach can be easily motivated, as the observed magnetisation is decreased due to the MT exchange. This results in lower signals, which is the same situation as if the inversion pulse was not played out correctly. Therefore, the problem can be solved by means of a three parameter fit (M_0, T_1, μ) given that a sufficient amount of data

points are acquired. Concluding the results presented here, it is important to consider MT for quantitative imaging, if saturation pulses are applied on purpose or accidentally. Depending on the sequence, the pulses applied might generate MT saturation. In turn, this changes the fitting equation and the model has to be adapted. In case of an IR-SE sequence, this can be done by the introduction of one additional fit parameter. The situation becomes more complex for fast T_1 mapping methods such as TAPIR [73, 75] or DESPOT1 [95, 11], where a steady state of the magnetisation is employed to accelerate the imaging process. Here, the transition to steady state and the steady state itself will depend on the MT sample as well as on the imaging parameters. To correctly account for MT effects, more than four parameters ($T_1^A, T_1^B, M_0^A, M_0^B$, different saturation effects of both pools, ...) need to be fitted, which complicates the procedure and leads to less reliable results. In that case, the fitting result will strongly depend on the initial guess of the fitting parameters as well as the fitting model employed, as will be shown in the next section.

The results presented here justify the simulation approach. As the *simulations* are in accordance with the **measurements**, it is possible to employ the simulation framework for further investigations. As the framework is rather flexible this opens the door for more studies. In particular it will be very useful to thoroughly investigate MT effects on quantitative parameters as well as to validate existing and new methods for quantitative MT studies.

8. Measuring the Longitudinal Relaxation Time in the Presence of Magnetisation Transfer

In this Chapter, the performance of some commonly used T_1 mapping methods was analysed in the presence of MT. The first Section employs simulations of different samples and a quartet of T_1 mapping methods. The *virtual* samples aimed to mimic brain tissues as well as a 4% agarose sample. The quantification methods under investigation were a spectroscopic inversion recovery, a spin-echo inversion recovery, the Ernst method based on the acquisition of several gradient echoes with different flip angles and a Look-Locker type sequence, named TAPIR.

The precision and accuracy of the selected T_1 mapping methods was investigated for similar *virtual* samples in the presence and absence of MT and the differences arising therein were analysed. MT was considered by performing biexponential fitting or by neglecting the early timepoints, where the fast recovery of the bound pool dominates. Furthermore, the effect on $T_1^{putative}$ when neglecting MT was thoroughly investigated. It was shown that biexponential fitting performed well for high SNR and inversion recovery methods. However, similar accuracy and precision of the IR methods could be achieved by measuring only larger TI times and therefore neglecting the fast recovering component - without requiring high SNR values. T_1 quantification based on the Ernst equation transpired to be less accurate, especially, as one would expect, for few sample points. These methods suffer from lower precision but it could be shown that the additional T_1 error arising from the neglect of MT is within the error of the method itself, at least for the samples simulated.

8.1. Precision and Accuracy of T_1 Mapping Methods in the Presence of MT

Chapter 5 described different sequences to map T_1 relaxation times under consideration of MT. As shown, it mandates the incorporation of many additional parameters. Assuming the simplest

two-pool model describing MT, the system is not only defined by M_0, T_1 and T_2 but also by M_0^B, T_1^B and T_2^B. Furthermore, each pulse applied might act differently on the two pools - recall the **S** matrix in Chapter 5. This introduces even more degrees of freedom to the system - the more pulses applied, the more new parameters have to be considered.
All these effects have to be included into the fitting routine to estimate T_1. The drawbacks are obvious:

- Fitting more parameters requires more measured points and, as a consequence, longer measurement times.
- Nonlinear fitting routines, which have to be dealt with, have no unique solution. If the initial values are not well chosen, the optimisation routine is likely to run into local minima, resulting in erroneous parameter estimates.
- A high SNR is required to keep the errors small - again this prolongs the measurement time.
- The higher the number of fitting parameters, the less stable the fit [96]. On the other hand, even very noisy data can be fitted with a very small residual, if many free parameters are allowed. But then the precision of the estimators is rather poor.
- In particular, fitting of a biexponential function is extremely ill-conditioned and in the presence of noise the results do not inspire much confidence[1].

Reviewing those aspects, one might ask if it makes sense to quantitatively consider the effect of MT. The simplest approach (IR measurement), which includes MT, is based on biexponential recovery - all other methods are even more complicated. Bearing in mind that *in vivo* measurements need to be performed fast and usually suffer from low SNR and/or few measurement timepoints, the hopeless operation is even more desperate. Thus, one has to decide which of several options to use:

- Using a monoexponential model, which might not be best to describe the system will result in much more stable fit results, especially in the presence of noise.
- Using the more appropriate two-pool model but paying the price of many unknown parameters which have to be fitted leading to a higher variance in the determined parameters.

[1] This problem was well described by Forman S. Acton, who described the scenario of fitting an equation of the type $Ae^{at} + Be^{bt}$ in his book "Numerical Methods that Work" [96, p.253] as follows: "... it is well known that an exponential equation of this type is *extremely* ill conditioned. That is, there are many combinations of (a, b, A, B) that will fit most exact data quite well indeed (will you believe four significant figures?) and when experimental noise is thrown into the pot, the entire operation becomes hopeless. But those with faith in science do not always read the book - and must be spanked or counselled. At the very last, keep them from obstructing progress and the computer! "

No matter which approach is chosen, for *in vivo* measurements the accuracy and precision of the estimated T_1 values are not as high as for spectroscopic, phantom or post mortem measurements.

Finally, one question remains: What are we interested in?
This is indeed the most important question, the answer will strongly depend on the application and purpose of the study. First, parameter mapping, and as such T_1 mapping, has a large range of applications, as already mentioned (Chapter 4). The most important point, however, is the reliability of the measured parameter. This means, no matter when, how or with which system one measures, the obtained T_1 should be the same for identical samples.
This study aims to explore the accuracy and precision of several T_1 mapping methods neglecting and considering MT. This includes the application of the "conventional" approach using the Bloch equations (Chapter 4) and, in contrast, the approach based on the Bloch-McConnell equations described in Chapter 5.
As no well characterised **physical** MT sample exists[2], answering this question is a perfectly adapted application for a simulation study performed with JEMRIS MT. The simulations will allow one to check the influences of different sequences and fitting methods on a sample with known parameters.
Simulations of similar *virtual* samples including and neglecting MT were performed and the accuracy and precision of different methods for T_1 mapping were compared.

8.1.1. Methods

8.1.1.1. Samples

As already mentioned, it is hard to find a suitable **physical** MT sample with well defined parameters. In contrast, *simulations* allow one to compare mapping results to the *virtual* sample input values. Consequently, the choice of the parameters used for the *virtual* sample is crucial. The *virtual* sample parameters should approximate the "real life" as well as possible. Taking everything (see Chapter 5) into account, the six *virtual* samples described in Table 8.1 were selected. The choice can be justified: first, the *virtual* samples should mimic *in vivo* human brain tissue. Unfortunately, there is little literature reporting on the two-pool parameters *in vivo*. The values given by Stanisz et al. [82] were therefore taken to be the reference. The *virtual* two-pool white matter sample is more strongly influenced by MT compared to the *virtual* grey matter sample. Additionally, a *virtual* agarose sample was simulated, as this is one of the MT phantom samples which can be prepared very easily. **Physical** agarose samples were characterised by Henkelman et al. [51], these values were used for the *virtual* agarose sample. As Henkelman's

[2] this means there is no phantom or substance, where all **physical** sample parameters as the exchange rate, the pool sizes and the different relaxation times describing MT are reliably known (cf. [97])

values were measured at 1.5 T and not at 3 Tesla, as the field strength available, the relaxation times for the *virtual* agarose sample were slightly modified to account for the different field strengths [98]. Another crucial point is influence of the biexponential recovery. To check this, a "similar"*virtual* one-pool sample was created. The T_1 value of the *virtual* one-pool sample was chosen to be the putative T_1 value, $T_1^{putative}$, defined as $\frac{1}{\lambda_1}$ in Equation (7.3). This allows for a direct comparison to the estimated T_1 value. Of course, the T_1 values of the single pool will differ from the obtained or putative $T_1^{putative/observed}$ value of a two-pool sample. But as long as the $T_1^{putative/observed}$ can be mapped in a quantitative manner, this will be sufficient for most applications[3].

Sample	Agarose 1 Pool	Agarose 2 Pool		WM 1 Pool	WM 2 Pool		GM 1 Pool	GM 2 Pool	
Parameter	Pool A	Pool A	Pool B	Pool A	Pool A	Pool B	Pool A	Pool A	Pool B
$\mathbf{M_0}$	1	1	0.011	1	0.861	0.139	1	0.95	0.05
$\mathbf{T_1}$/ ms	2417	2456	1000	1071	1084	1000	1748	1820	1000
$\mathbf{T_2}$/ ms	54	54	0.0129	69	69	0.01	99	99	0.0091
$\mathbf{\Delta\omega}$/ Hz	0	0	0	0	0	0	0	0	0
$\mathbf{k_{AB}}$/ Hz	-	163.63		-	3.197		-	2	
$\mathbf{T_1^{putative}}$/ ms	2417	2417		1071	1071		1748	1748	

Table 8.1: *Simulation parameters for the different MT samples based on [51] (modified for 3 Tesla) and [82].*

8.1.1.2. Sequences

Different established sequences for T_1 mapping were simulated using various parameter combinations in order to investigate the influence of MT on the estimated T_1 values. The sequence parameters used were optimised as described in Appendix B.

IR-FID The spectroscopic inversion recovery FID sequence consists of a 180° inversion pulse[4], followed by a 90° pulse[4] delayed by the inversion time, TI, and a readout[5]. 42 different inversion times were simulated, starting from 5 ms up to 4010 ms. Figure 8.1 shows the components of the magnetisation simulated with JEMRIS MT as well as the cumulated signal for different TIs (right).

IR-SE: The inversion-recovery, spin-echo sequence[6] was simulated for 20 different TIs. Inversion and refocussing were realised by hard pulses[7].

[3] Specific studies on the exchange behaviour or the two pools itself will be naturally impossible with that approach - but this is a different task and question to answer.
[4] sinc shaped, bandwidth = 1 KHz, bandwidth time product = 5
[5] 2000 ms duration, acquiring 2000 points
[6] The sequence parameters were: TR = 15 s, TE =10 ms, FOV = 100 × 100 mm^2, resolution of 32×32 voxel, a Hann filter was applied to smooth the ringing artefacts.
[7] both hard pulses had a duration of 0.1 ms, the flip angle was 180° for inversion and 90° for refocussing.

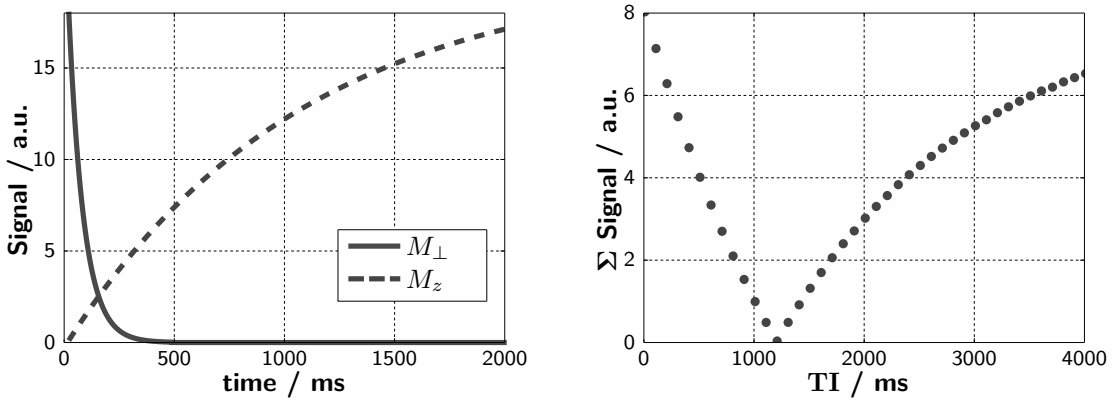

Figure 8.1: *The signal decay simulated with JEMRIS MT (left) and the summed signals for different TI values (right).*

Multiple Flip Angle Approach: A spoiled gradient echo[8] was *simulated*. The TR was chosen under consideration of MT as described in Section B.2. The flip angle of the 0.1 ms hard pulse was varied in order to fit T_1 based on the Ernst equation. 21 flip angles between 5° and 105°, spaced by 5° were simulated (cf. Figure 8.2).

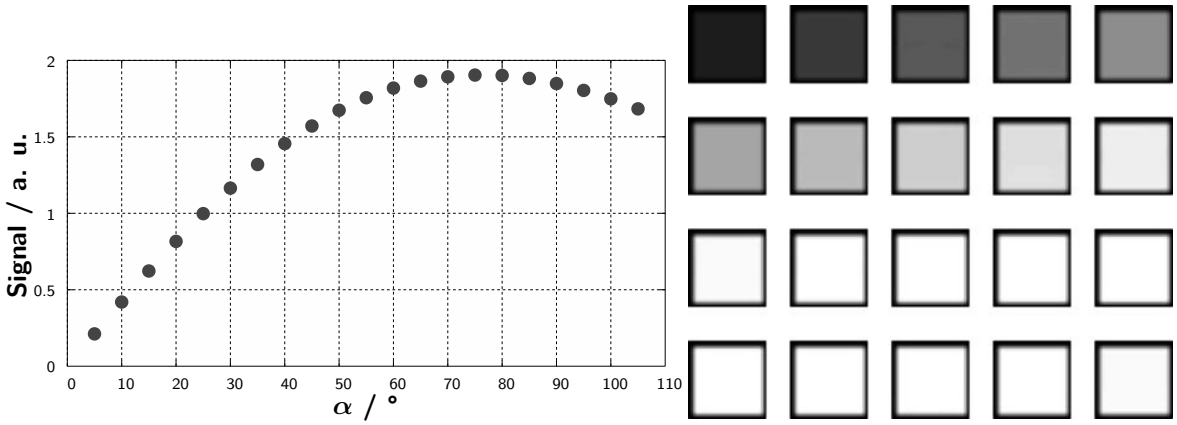

Figure 8.2: *Signal evolution in one voxel, simulated with JEMRIS MT (left) and the images obtained by the simulation, scaled to the same intensity (right). The flip angle increases from 5° (top left) to 100°(bottom right).*

Look-Locker based Method TAPIR: The TAPIR sequence, described in 4.3.1 was implemented and simulated only for a single slice in order to save calculation time. Therefore, the TAPIR sequence is rather a Look-Locker sequence with a magnetisation preparation module.

[8]Sequence parameters: $TR = 2500$ ms, TE =10 ms, FOV = 100×100 mm, matrix size of 32×32 voxel. A Hann filter was applied to smooth ringing artefacts and 5 dummy prescans were applied to approach the steady-state.

8.1.1.3. Fitting and Evaluation

T_1 maps were obtained based on the signal equations presented in Chapter 4 and 5. All simulated sequences were fitted using the nonlinear least squares routine FIT, provided by MATLAB. Depending on the sequence, different approaches were chosen to obtain T_1:

IR-FID: All of the 42 simulated signals were used to fit T_1. This was repeated 576 times in order to achieve the same statistics as for the imaging sequences.

IR-FID MT: All 42 timepoints were fitted to a biexponential function and the inverse slow recovery rate was used as T_1.

IR-FID late timepoints: 39 timepoints, starting with a TI of 210 ms were used for fitting. As shown in 5.1, the relaxation curves differ for short TI values. If one wants to selectively obey the slow component from the biexponential recovery curve, fitting only the late timepoints should increase the accuracy, as the fast recovering component has already recovered. MR imaging is usually dominated by the slow component, as the imaging process takes time. During imaging most of the fast fraction has already recovered.

IR-SE: All 21 timepoints were used for T_1 fitting.

IR-SE MT: All 21 timepoints were used to obtain T_1 as the inverse slow recovery rate based on biexponential fitting.

IR-SE late timepoints: Again, only the simulated signals for $TI \geq 210$ ms were used in order to obtain the slow recovery rate.

Ernst 2 FAs: The Ernst equation (2.59) was used to calculate T_1 based on the signals (S_1, S_2) acquired with two different flip angles, $(\alpha_1 = 40°, \alpha_2 = 100°)$:

$$T_1 = -\frac{T_R}{\ln\left(\frac{\frac{S_1}{S_2}\sin\alpha_2 - \sin\alpha_1}{\frac{S_1}{S_2}\sin\alpha_2\cos\alpha_1 - \sin\alpha_1\cos\alpha_2}\right)} \tag{8.1}$$

Ernst 5 FAs: Simulated signals of GRE with flip angles $\alpha = 10, 30, 50, 70, 90°$ were used to fit the Ernst equation (2.59).

Ernst 10 FAs: GRE with flip angles of $\alpha = 10, 20, 30, 40, 50, 60, 70, 80, 90, 100°$ were simulated and the signal was fitted to the Ernst equation (2.59).

Ernst 21 FAs: All signals of the simulated GRE were used to obtain T_1 based on the Ernst equation (2.59).

Look-Locker FA40: The TAPIR sequence described above, simulated with a flip angle of 40°.

Look-Locker FA25: The TAPIR sequence described above, simulated with a flip angle of 25°.

Look-Locker FA20: The TAPIR sequence described above, simulated with a flip angle of 20°.

Look-Locker FA20 late timepoints: The TAPIR sequence described above simulated with a flip angle of 20°, only the late 42 timepoints were used for the fitting procedure.

Look-Locker FA20 early timepoints: The TAPIR sequence described above, simulated with a flip angle of 20°, fitting was obtained using the first 20 timepoints.

Look-Locker FA15: The TAPIR sequence described above, simulated with a flip angle of 15°.

The bold printed names will be used again in Section 8.1.2.1.

Ernst 21 FAs, Ou Approximation for MT: T_1 was estimated under consideration of MT employing Ou's approximation [25] of the extended Ernst equation considering MT. The simulated data were fitted to

$$M_{\perp}^{SS,MT,PoolA} = M_0^A \cdot \sin\alpha \frac{\lambda_1\left(1-S_B E_1^{MT}\right)\left(1-E_2^{MT}\right)-\lambda_2\left(1-E_1^{MT}\right)\left(1-S_B E_2^{MT}\right)+R_1^A\left(E_1^{MT}-E_2^{MT}\right)(S_B-1)}{\lambda_1\left(1-S_B E_1^{MT}\right)\left(1-\cos\alpha E_2^{MT}\right)-\lambda_2\left(1-\cos\alpha E_1^{MT}\right)\left(1-S_B E_2^{MT}\right)-\left(R_1^A+k_{AB}\right)\left(E_1^{MT}-E_2^{MT}\right)(\cos\alpha-S_B)}. \tag{8.2}$$

Prior to the fitting, Gaussian noise was added assuming an SNR of 500 to 20. All sequences (except of the spectroscopic FID) were *simulated* on a 32×32 matrix size. The object appeared within a smaller range, so the images were masked to a 24×24 matrix to exclude noise contributions from outside the *virtual* sample in the final evaluation. Subsequently, the mean T_1 value as well as the standard deviation of the *simulated virtual* sample were calculated.

The accuracy,

$$\Delta(T_1) = 100 - \frac{\text{mean}(T_1^{calculated}) - T_1}{T_1} \cdot 100, \tag{8.3}$$

and precision,

$$\sigma(T_1) = 100 - \frac{\text{std}(T_1^{calculated})}{T_1} \cdot 100, \tag{8.4}$$

of the different methods were obtained based on the T_1 values which were used as input value for the *simulations*. For the case of one pool, this was just the T_1 value, for two pools the expected "spectroscopic" value was calculated as the putative $T_1^{putative} \approx \frac{1}{\lambda_1}$ value as given in (7.3).

8.1.2. Results

8.1.2.1. Comparison of the Different Methods

Accuracy and precision of T_1 were calculated for all methods and all *virtual* samples

- without added noise,
- for a SNR of 100 (thick error bars) and
- for a SNR of 30 (thin error bars).

The Ideal Case: T_1 Mapping Methods without added Noise: The academic case of MRI images without any noise present was evaluated in the beginning. The corresponding *simulation* results are presented in Figure 8.3, 8.4 and 8.5.

One-Pool Samples:
Focussing on the *virtual* one-pool sample, displayed in light blue for a variety of phantoms, one can show that all methods give a very good estimate of T_1, independent of the sample used. The deviation from the input value is less than 2% with one exception.

The ***virtual* one-pool agarose sample** (Figure 8.3) shows the largest deviations (about 2%) for the IR-FID sequence considering MT by biexponential fitting and the Look-Locker sequences. T_1 estimation by means of the Look-Locker sequence gives more accurate results for smaller flip angles in case of the *virtual* agarose sample. All other methods give an accuracy better than 1% for the *virtual* agarose sample.

The ***virtual* one-pool sample mimicking white matter** gives accurate results (deviation less than 1%) for all simulated methods.

The ***virtual* grey matter sample simulated without MT** shows a good accuracy with a maximum deviation of 4%. Look-Locker based methods employing a large flip angle of 40° are the one most likely to fail. The other methods provide a high accuracy with deviations less than 1%.

The methods which consider the MT effect in some way (e.g. by biexponential fitting or neglecting the early timepoints, Figure 8.3) are more likely to fail in case of the *virtual* one-pool sample due to the fitting problems discussed in the introductory part of this Section (8). The largest deviations in the estimated T_1 value for the *virtual* one-pool sample can be found for the Look-Locker sequences - obviously a careful choice of sequence parameters is necessary if T_1 is estimated based on Look-Locker sequences. Parameter optimisation for Look-Locker type

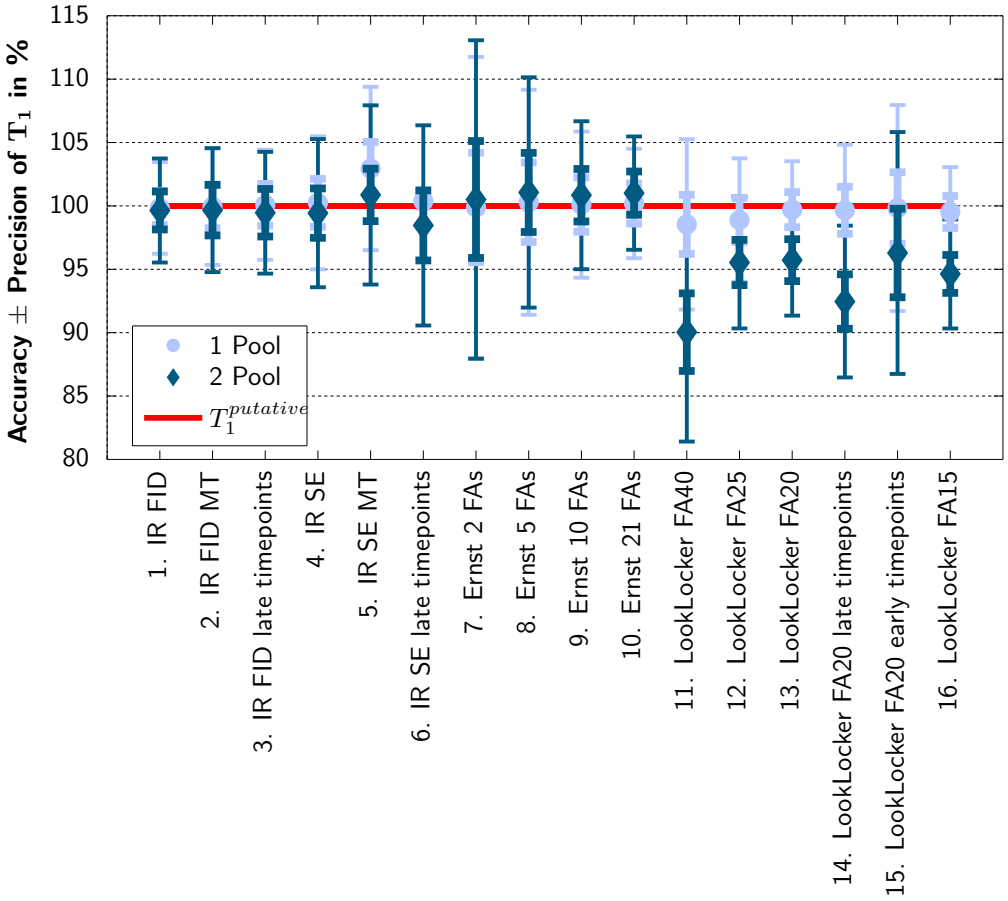

Figure 8.3: *Comparison of the different methods for T_1 mapping reveals an accuracy of the calculated T_1 values better than 10% for the* **virtual *agarose sample*** *even in the presence of MT. The thick errorbars show the precision for an estimated input SNR of 100, the thin error bars the precision for an SNR of 30.*

sequences is important but challenging, as there are a lot of sequence parameters influencing the final result. However, even if the parameters are not well chosen, the accuracy of the Look-Locker methods remain within the 4% limit.

Two-Pool Samples:

At first glance, two-pool *simulations* do not look very convincing, especially if one considers, that no noise is present, which might spoil the results. All methods show an accuracy of better than 20% for the *simulated* samples but a closer look at the details is worthwhile. The methods employing inversion pulses are reliable, if either the MT equation is used for fitting or if the first timepoints (recorded very soon after the inversion pulses) are neglected for fitting. The methods based on the Ernst equation show an accuracy better than 5 % even for the two-pool sample.

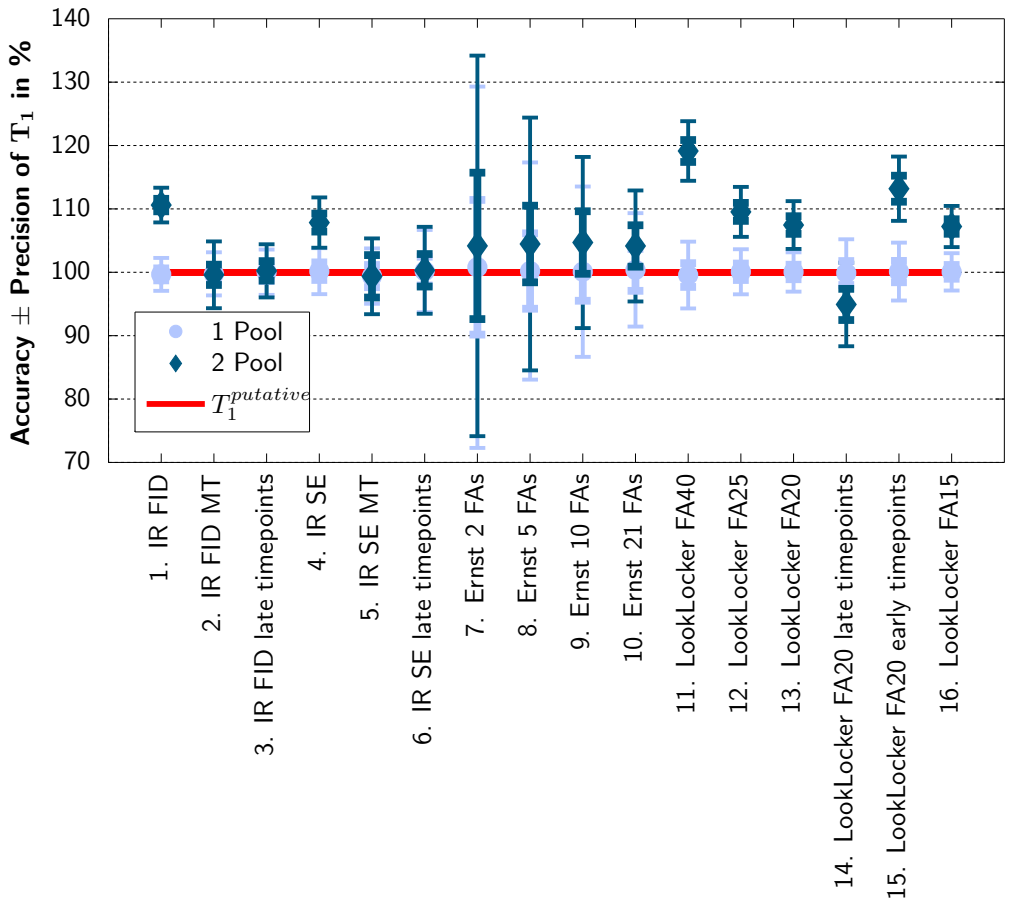

Figure 8.4: *Comparing the* simulated T_1 *mapping methods for the* **virtual *white matter*** *sample shows, that all methods provide an accuracy better than 20%. Moreover, all methods except the Look-Locker based methods show an accuracy better than 10%. The precision is given by the error bars, the thick ones for SNR 100, the thin ones for SNR 30.*

The ***virtual* two-pool agarose sample** shows the largest deviations from the nominal $T_1^{putative}$ for the Look-Locker based methods. The IR and Ernst equation based methods give reliable results with a deviation less than 2% even for the two-pool sample .

The ***virtual* two-pool white matter sample** is the one with the largest variations in $T_1^{putative}$ within the different T_1 mapping sequences and evaluations. The IR methods give reliable $T_1^{putative}$ estimates, if MT was considered by biexponential fitting or by neglecting the early timepoints shortly after inversion. The $T_1^{putative}$ value estimated by means of the Ernst equation is slightly overestimated compared to the expected $T_1^{putative}$, independent of the number of angles simulated. In contrast, $T_1^{putative}$ calculated on the basis of the Look-Locker type sequence

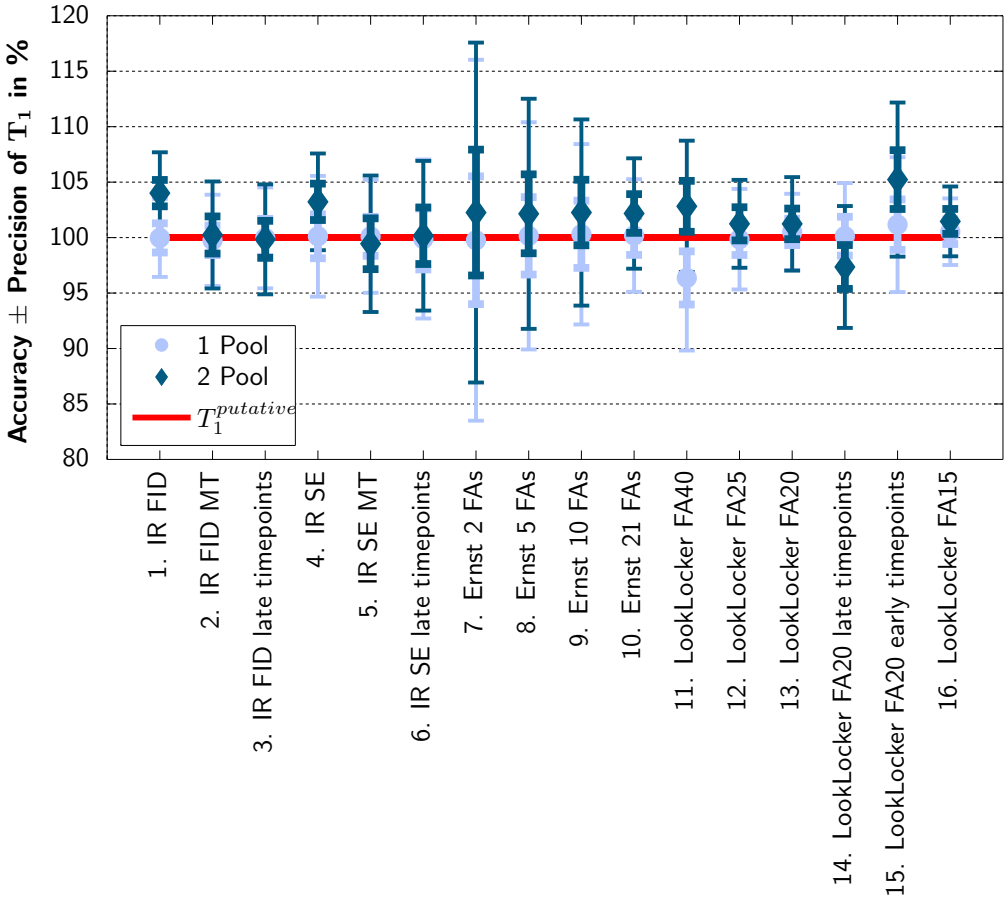

Figure 8.5: *The* **virtual *grey matter*** simulations *give a precision better than 5% for all methods. The Look-Locker type sequences reveal a larger variation in the precision even for the* virtual *one-pool sample. Again the thick error bars represent the precision for SNR 100 and the thin ones for SNR 30.*

seems to deviate from the nominal value in a rather arbitrary fashion.

The ***virtual* grey matter sample with the two exchanging pools** shows a behaviour similar to that of the *virtual* white matter sample. IR methods which consider MT give accurate results ($\leq 1\%$). The Ernst equation methods overestimate $T_1^{putative}$ by about 2% and the Look-Locker results vary non-systematically. In all cases, the Look-Locker based methods show a much higher variation in the estimated $T_1^{putative}$ values depending on the sequence parameters as well as a lower precision. The sensitivity of the estimated $T_1^{putative}$ values on the sequence parameters for Look-Locker based methods will be discussed in Section 8.1.3 and a detailed evaluation is presented in Section 8.2.

The Realistic Case: T_1 Mapping Methods in the Presence of Noise: The different methods to estimate T_1 show a different precision and accuracy. In the absence of noise, the accuracy can be determined with one *simulation* only, the determination of the precision of a method requires the *simulation* of the same *virtual* sample with different noise levels. Adding noise to the input data gives a distribution of T_1 values, where the width of the distribution is related to the SNR. This was carried out in the context of this work.
The different methods show dissimilar sensitivity to noise, which results in different standard deviations of the T_1 distribution, mirrored in the precision of the sample (according to Equation (8.4)).

One-Pool Samples:

The ***virtual* one-pool agarose sample** at an SNR of 100 (Figure 8.3, thick error bars) provides reliable T_1 estimates with a precision of about 3 to 5 %. The inversion recovery sequence has the highest precision (about 1%), the Ernst approach using two flip angles has the lowest precision with an error of about 5%. Again, the Look-Locker methods show the largest variations - the precision can be 2 or 5 %, depending on the flip angle. Less SNR of the input values (SNR 30, Figure 8.3, thin error bars) gives less precision for all methods. The characteristic changes are the same as for an SNR of 100, e.g. the two point method gives the lowest precision.

The ***virtual* white matter sample** simulations (Figure 8.4) show larger deviations from the nominal value and its precisions is worse than the *virtual* agarose sample. In particular, the two point method fails even for the *virtual* one-pool sample at the high SNR of 100 (thick error bars), where the precision is worse than 10%. For lower SNR of 30 (thin error bars), the precision is worse than 30%. The Look-Locker methods as the IR sequences have a precision (in the one-pool case) of about 5%.

Simulation of the ***virtual* grey matter sample** (Figure 8.5) show precise T_1 estimates with an error below 10% for SNR 100 (thick error bars) and an error below 15% for SNR 30 (thin error bars) in all cases. The most precise method is based on the IR, the worst is the two point Ernst method with an error of 9% for SNR 100 and 15% for SNR 30.

Two-Pool Samples:

All *virtual* two-pool samples have comparable or slightly worse precisions compared to the *virtual* one-pool samples. This is independent of the sequence and the sample. In addition, for the two-pool samples the two point method gives the largest error and the IR methods have the advantage of highest precision. The accuracy is strongly influenced by the type of the sample, i.e. if a one or two-pool sample was used. The precision is independent of the sample type but

depends mainly on the number of sample points.

8.1.2.2. SNR Dependence

Section 8.1.2.1 showed that the precision and accuracy of a given T_1 mapping method depend on the sample as well as on the method. Furthermore, the SNR of the input values affects the resulting precision. Consequently, the SNR dependence was evaluated for each sample and method. The following figure (Figure 8.6) exemplifies the SNR dependence of the different methods on the T_1 precision for the WM sample. The precision of the T_1 estimation increases for all *virtual* samples and methods with increasing SNR. The SNR dependence of the precision depends strongly on the T_1 mapping sequence. The sample kind and type has only a minor effect on the resulting precision.

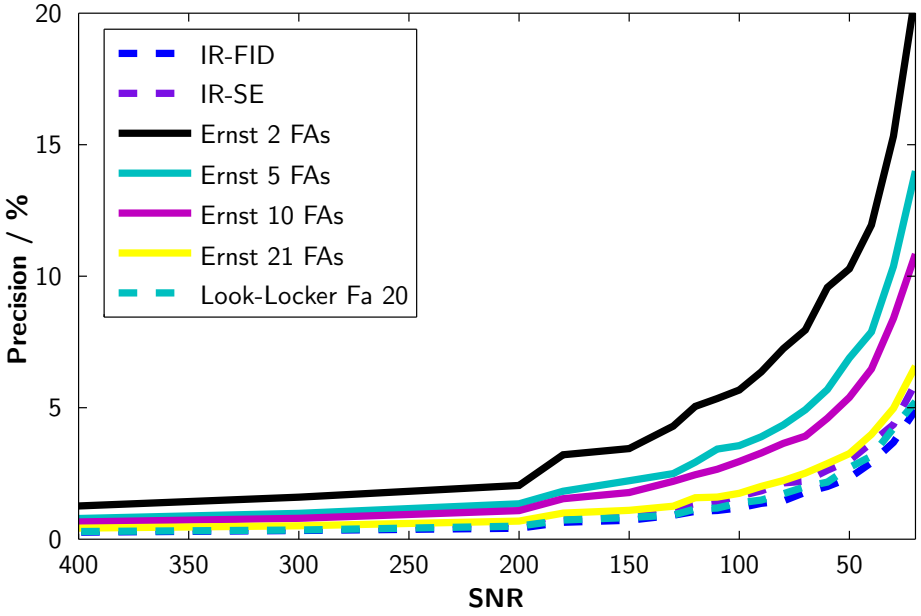

Figure 8.6: *SNR dependence for the precision of the different T_1 mapping methods,* virtual *WM sample. There is no qualitative difference between the precision of the* virtual *one and the two-pool sample.*

8.1.2.3. Ou's Approach for Consideration of MT

In 2008, Ou et al. [25] presented a method to obtain quantitative T_1 maps based on single-slice spoiled gradient echo data under consideration of MT effects. The corresponding theory was already covered in Section 5.2.2. The obtained signals can be fitted to

$$M_{\perp}^{SS,MT,PoolA} = M_0^A \cdot \sin\alpha \frac{\lambda_1\left(1-S_B E_1^{MT}\right)\left(1-E_2^{MT}\right)-\lambda_2\left(1-E_1^{MT}\right)\left(1-S_B E_2^{MT}\right)+R_1^A\left(E_1^{MT}-E_2^{MT}\right)(S_B-1)}{\lambda_1\left(1-S_B E_1^{MT}\right)\left(1-\cos\alpha E_2^{MT}\right)-\lambda_2\left(1-\cos\alpha E_1^{MT}\right)\left(1-S_B E_2^{MT}\right)-\left(R_1^A+k_{AB}\right)\left(E_1^{MT}-E_2^{MT}\right)(\cos\alpha-S_B)}. \tag{8.5}$$

Thus, MT is considered by the introduction of additional fitting parameters, S_B, R_1^A, k_{AB}, λ_1 and λ_2. In total, 6 parameters have to be fitted. Ou et al. [25] already noted that the "robustness of the fitting routine varies for each parameter". Ou's Monte Carlo *simulations* on the robustness show that "an SNR larger than 50 is sufficient to determine T_1^{MT} reasonably".

Sample	$\mathbf{T_1^{putative}}$	$\mu_{\mathbf{MC}}(\mathbf{T_1^{Ou}}) \pm \sigma_{\mathbf{MC}}(\mathbf{T_1^{Ou}})$	$\mu_{\mathbf{MC}}(\mathbf{T_1^{Ernst}}) \pm \sigma_{\mathbf{MC}}(\mathbf{T_1^{Ernst}})$
Agarose, 1 Pool	2417 ms	2239 ± 4588 ms	2414 ± 43 ms
Agarose, 2 Pool	2417 ms	2300 ± 2776 ms	2394 ± 42 ms
White matter, 1 Pool	1071 ms	1122 ± 861 ms	1068 ± 38 ms
White matter, 2 Pool	1071 ms	1097 ± 403 ms	1025 ± 39 ms
Grey matter, 1 Pool	1748 ms	1685 ± 743 ms	1745 ± 35 ms
Grey matter, 2 Pool	1748 ms	1659 ± 942 ms	1711 ± 34 ms

Table 8.2: *Mean (μ_{MC}) and standard deviation (σ_{MC}) of the T_1 value estimated using Equation* (8.5) *(T_1^{Ou}) and Equation* (4.4) *(T_1^{Ernst}) based on 50,000 Monte Carlo simulations.*

Figure 8.7 shows the histograms of the estimated T_1 values with the Ou method and the Ernst approach in 50.000 simulations with an SNR of 100. Large outliers with T_1 values larger than twice the expected $T_1^{putative}$ were set to zero for the histogram visualisation (but not for the calculations). The mean T_1 values (cf. Table 8.2), estimated by Equation (8.5) are accurate (cf. Table 8.3), but the standard deviations are large - the precision is about 40% in the best case of white matter but exceeds 100% for the agarose sample. The low precision can be attributed to the simultaneous fitting of 6 parameters. The start values were chosen as: $M_0^A = \max(Signal), \lambda_1 = 1/1200$ Hz, $\lambda_2 = 4\,\text{Hz}$, $k_{AB} = 0.003\,\text{Hz}$ and $S_B = 0.5$. The start values used for the fit are closest to the WM sample parameters. This might explain why the WM results are more precise than the others. In practise, the sample parameters are unknown, therefore a routine which provides reliable results independent of the start values is desired.

A direct comparison of the SNR dependence between Ou's approach and T_1 estimation of the WM sample based on the Ernst equation, neglecting MT, can be found in Figure 8.8. Please note, that the precision of Ou's method is - in contrast to the Ernst approach - independent of the SNR and the variations depend on the sample. This substantiates the suspicion that the cost function of the problem is adverse.
Summarising the simulation results of the Ou approach shows that the six parameter fit works best for white matter but its robustness is weak. If the approach presented by Ou is used to obtain T_1 in the presence of MT, the results should be judged with caution, especially if the sample and thereby the start values are unknown and the data are noisy. The resulting T_1 values

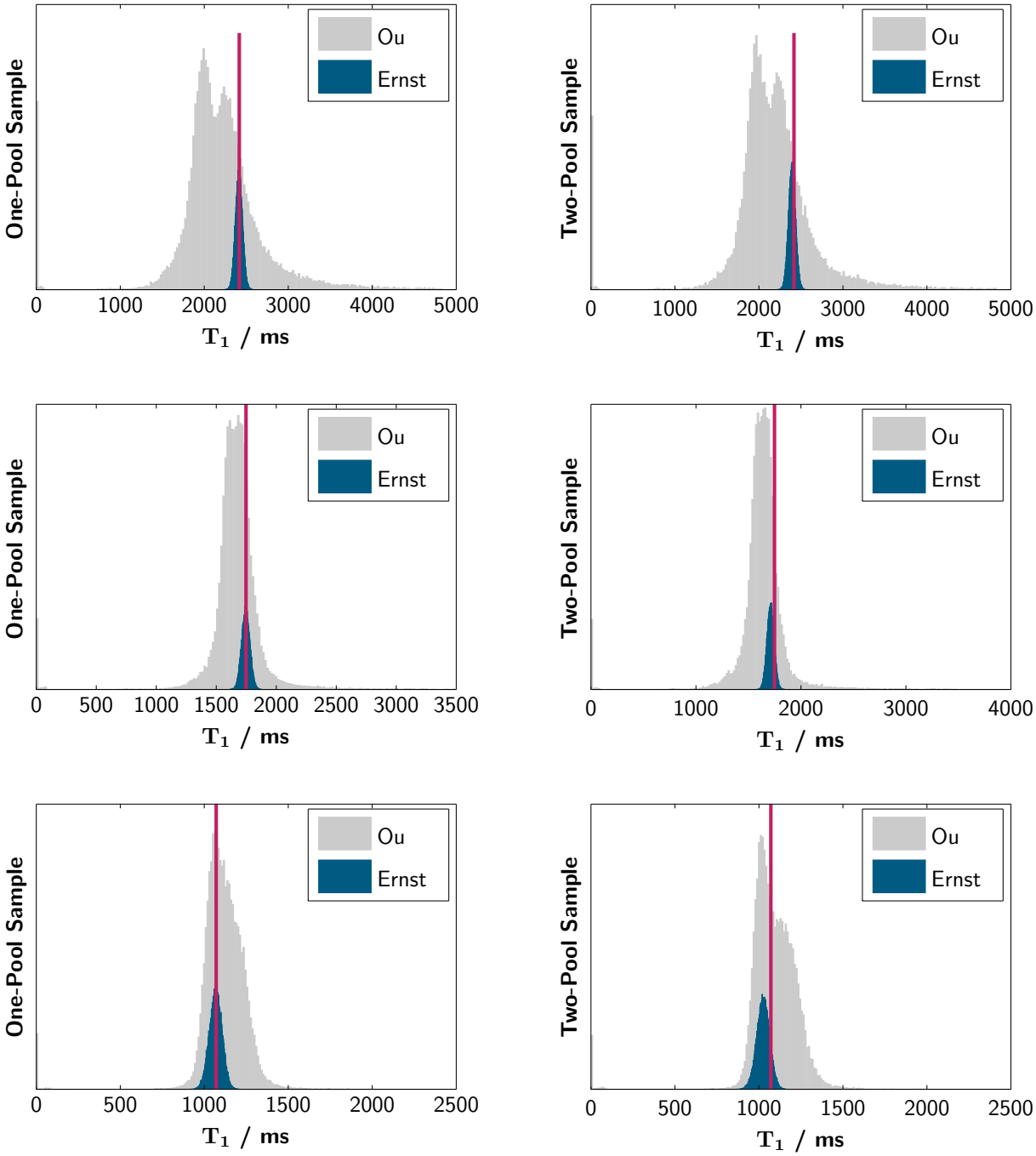

Figure 8.7: *Results of the Monte Carlo* simulation *based on 50,000 repetitions and an SNR of 100. The histograms show the distribution of the T_1 values calculated with Ou's approach (grey) compared to the standard Ernst approach (blue). From top to bottom:* virtual *Agarose sample,* virtual *WM and GM sample. T_1 values larger than twice the $T_1^{putative}$ were set to zero for a better visualisation. The red lines show the nominal $T_1^{putative}$ value.*

Sample	Accuracy (Δ) / %	Precision (σ) / %
Agarose, 1 Pool	-7.4	190
Agarose, 2 Pool	-4.8	114
White matter, 1 Pool	4.8	80
White matter, 2 Pool	2.4	37
Grey matter, 1 Pool	-3.6	42
Grey matter, 2 Pool	-5.1	53

Table 8.3: *Precision and accuracy in percent of the nominal T_1 value of the $T_1^{putative}$ estimated with the Ou approach by means of 50,000 Monte Carlo simulations. Applying Ou's approach to the one-pool sample is shown in grey as the results are obtained by the usage of a wrong model.*

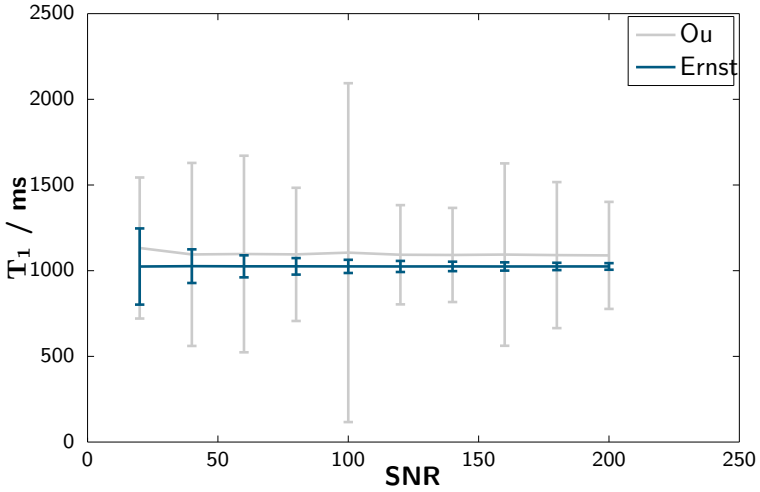

Figure 8.8: *SNR dependence of the Ou and the Ernst approach.*

are likely to lack precision and accuracy.

8.1.3. Discussion

8.1.3.1. Comparison of the Different Methods

The One-Pool Samples: Generally, a comparison of the different T_1 mapping methods and their application to different (*virtual*) one-pool samples reveals that the T_1 estimates for any one-pool sample (light blue line, Figures 8.3, 8.4 and 8.5) give a good estimate of the T_1 values of all *simulated* samples. The established methods *simulated* in this study provide a high degree of accuracy almost independent of the sample parameters. The precision varies with the number of sampled or simulated timepoints as well as with the SNR of the input data. The SNR influence is nonlinear but independent of the sample. Consequently, it follows, that MT does not alter the precision.

A closer look at some details is worthwhile and will give additional insight into the problems

which might arise in case of MT:

Biexponential Fitting: the results presented here show one outlier (method 5, Figure 8.3) with a high deviation from the nominal values even for the *virtual* one-pool sample. This result can be explained as follows: the IR SE MT method uses the biexponential model to fit the expected MT induced biexponential recovery curve. In case of the one-pool sample, the recovery curve is in fact monoexponential. A stable fit routine should reveal the monoexponential curve even if a biexponential function is the model function. However, as mentioned above, biexponential fitting is an extremely ill-conditioned problem and the results of such a fit are - especially in the presence of noise - not reliable.

Choice of Sequence Parameters: while the Look-Locker simulations for the white matter sample are very accurate and show no parameter dependence, the T_1 values of the grey matter and agarose samples, estimated with the Look-Locker based methods are sensitive to the sequence parameters chosen, even in case of the one-pool sample. This can be attributed to the fact that the T_1 value of the white matter sample is the lowest T_1 value within the *simulated* ones. Zaitsev et al. [74] already noted that the precision of T_1 estimated with TAPIR, which was used for the simulations, is worse for larger T_1 values. Additionally, the sequence parameters used in the simulations were optimised for a mean T_1 value of 1744 ms and not for each expected T_1 individually. The price one pays for the shorter acquisition times, which can be realised by means of the Look-Locker approach, is either a lower accuracy or the necessity of a very careful optimisation of the sequence parameters with regard to the expected sample parameters. Consequently, the sequence parameters of Look-Locker type sequences should be well chosen in order to obtain highly accurate results.

Number of Sampled Points and SNR: under the assumption of equal SNR of the input data, the different methods show a different precision. As given by the theory, more sample points give larger precision, if the SNR is the same. On the other hand, according to the theory of the Cramer-Rao lower bounds [99, 100, 101] the results of any parameter estimation of a sample containing only one T_1 value are more precise, if less sampling points at higher SNR are used. Then the sampling pattern can be optimised for the T_1 value one expects. However, this approach is not optimal for *in vivo* measurements. First, one expects a T_1 distribution rather than only one value and therefore a broad coverage of the Ernst curve is to be preferred in most cases. In any case, a specific optimisation of the sampling pattern under consideration of the expected SNR as well as the possible T_1 distribution by means of the Cramer-Rao theory is recommended.

The Ernst method employing two flip angles gives the T_1 estimate with the lowest precision while the IR as well as the Look-Locker based methods (which employ a large number of points for data fitting) show a small standard deviation of the estimated T_1 values and accordingly a high precision.

The Two-Pool Samples: the *simulation* results presented in 8.1.2.1 show that all methods can provide reliable $T_1^{putative}$ values within an accuracy of 5% even in the presence of MT, if the parameters (TI, flip angle, number of timepoints) are well chosen. The different methods to obtain T_1 are more or less prone to errors, if MT is present. A detailed analysis of the methods investigated here is therefore mandatory.

Inversion Recovery FID and SE: focussing on the inversion recovery based methods (method 1 to 6) reveals that it is better (in case of MT) not to use values of TI that are too short. This can be understood as the biexponential behaviour of the recovery curve is only dominant at the early timepoints, cf. Figure 5.1. This vindicates the approach of neglecting the early timepoints, and as a consequence, the final T_1 estimation is much more stable and less influenced by the MT effect as the fast recovering component is neglected. The alternative - fitting the recovery curve to a biexponential model - might improve the result (cf. WM, Figure 8.4) but as biexponential fitting is an ill-posed problem it requires a large number of sampling points to provide reliable data. This approach is not as trustworthy and requires longer measurement times than the "late timepoints" approach. Utilising the later timepoints leads to an accuracy of better than 2% for all IR methods and samples.

The Ernst Approach: T_1 estimations of MT samples based on the application of the Ernst equation tend to overestimate T_1. For the *virtual* samples simulated, this overestimation is within 5% of the nominal value. As the standard deviation of the estimated T_1 distribution is large, especially if only a few datasets are acquired, the error caused by MT is much smaller than the error of the method itself. As a consequence, focussing on one voxel within the sample, it is not possible to determine if it is a one- or two-pool sample voxel. To resolve the difference between the T_1 distribution of the one- and the two-pool sample, a high SNR and the acquisition of at least 10 different flip angles is mandatory. Furthermore, a successful discrimination between the two *virtual* samples requires a large sample consisting of several voxels to maintain the statistics. Those prerequisites are hard to fulfil, as relaxation values of tissue are usually distributed over a wide range. Additionally, the prerequisite of obtaining a high SNR or many datasets within the standard timeframe of about an hour measurement time for volunteers and half an hour for patient measurements is demanding. Another crucial prerequisite for correct estimation of T_1 by means of the Ernst equation is a precise knowledge of the actual flip angle in each voxel. Depending on

the field strength and the coil used for transmission, the actual flip angle deviates from the nominal angle - higher field strengths incorporate larger flip angle imperfections. For example, at 3 Tesla the real flip angle might differ from the theoretical angle by up to 30% [102]. As a consequence, the actual flip angle has to be measured and all successive T_1 estimations are biased by the accuracy and precision of the flip angle measurement - the flip angle error propagates to the final T_1 value; possible flip angle bias was not included in the *simulations*. Real **measurements** employing the Ernst method are therefore rather sensitive to errors arising not only from MT and low SNR but also from imperfect flip angle estimates.

In summary, the Ernst approach which is based on only a few acquisition points, e.g. the two point method, is prone to noise influences and shows a large width of the distribution of the estimated T_1 values. Uncertainties in the flip angle applied will introduce additional uncertainty to the T_1 values. However, the precision and accuracy of the Ernst based T_1 estimation is almost independent of the usage of the one or the two-pool model. The curves cannot be separated by visual inspection. Using more points, e.g. 10, or even better 21, increases the precision. Especially for *in vivo* measurements, an optimised balance between acquisition time and precision has to be obtained in order to obtain a reliable T_1 quantity. The inversion recovery sequence provides the most accurate results with the smallest error, but one has to pay the price of longer acquisition times.

Look-Locker based Methods: the accuracy and precision of the T_1 results obtained with the Look-Locker type sequence depend on the sample as well as on the sequence parameters. The investigations carried out so far do not reveal any correlations e.g. between accuracy and sequence parameters. A more detailed investigation of the parameter dependence of the Look-Locker based method can be found in Section 8.2.

8.1.4. Conclusions

All T_1 mapping methods simulated in this work show an accuracy better than 2% for the *virtual* one-pool samples, given that the sequence parameters are carefully chosen and the input SNR is larger than 50. This is highly acceptable, as "real" measurements are noisy and the noise induced error (precision) is usually at least in the 5% range (see Section 8.1.2.2). Therefore, one can conclude that the methods simulated and applied here can be employed to estimate T_1 of samples which do not show magnetisation transfer effects with high precision. Otherwise, the simulations presented in this chapter clearly support the notion that the observed T_1 values are influenced by MT. The one- and the two-pool samples show a different precision and accuracy

for the different samples.

The different methods show a different sensitivity to the effects of MT. While inversion recovery measurements provide a stable and reliable estimate of the T_1 values, especially if the inversion times are not too short, the methods employing a steady-state are prone to influences arising from MT. For the case of a single-slice; spoiled gradient echo, these effects were investigated by Ou et al. [25]. Their suggestion of using a modified steady-state equation to account for MT by the introduction of additional fitting parameters gave rise to large errors for the *virtual* samples used here. Although the large number of fitting parameters (6 or 7) increases the goodness of the fitting result, the values for the single parameters are less reliable and prone to fit errors e.g. due to local minima. Our simulations revealed that results obtained with Ou's approach have to be treated with care; the estimated parameters vary strongly for different input sample parameters (mimicking WM, GM or agarose) as well as for different SNRs. To overcome the high systematic uncertainty of the method, many different flip angles and a high SNR are required. The total measurement time required to obtain appropriate data is probably too high for *in vivo* measurements, especially if patients are the subject of the study.

The Look-Locker based methods use a combination of steady-state imaging and inversion recovery. Thus, the steady-state problems known from the Ernst approach propagate to the signal equation and the effects of MT on the final T_1 estimation can no longer be fitted with admissible results. The signal equation for Look-Locker based methods can be derived (see Section 5.2.3) but as each pulse acts differently on the two pools, each pulse introduces another fit parameter - fitting all free parameters cannot be performed within a scientific framework.

The precision and accuracy of the estimated T_1 values, shown here by means of simulations, depend on the sample type (one- or two-pool), on the sequence type (IR-SE, spoiled GRE / Ernst approach, Look-Locker) and also on the input SNR. However, the effect of the sequence and the SNR seem to be larger than the effect of MT. Especially in the presence of noise, the differences between the one- and two-pool sample are usually hidden within the measurement errors and therefore cannot be separated reliably.

The study lacks comparison to experimental MRI measurement data. Several reasons can be listed as to why no direct comparison with *in vivo* studies was part of this study. First, there is no MT sample with well defined MT and relaxation parameters [97]. The commonly used agarose or Bovine Serum Albumin (BSA) samples are not sufficiently stable and their MT and relaxation properties are not in the range of *in vivo* white and grey matter. Especially the

exchange rates have a large impact on the estimated T_1 and those values differ strongly for WM, GM, agarose and BSA. Moreover, the quantitative parameters of these samples differ not only from the values expected for *in vivo* grey and white matter but also from sample to sample. Additionally, these samples suffer from poor long term stability and are difficult to reproduce. Another aspect is that they are sensitive to changes e.g. in temperature and the pH which makes any comparison even more difficult. Post mortem tissue has different relaxation properties and it is not clear if the effect of magnetisation transfer is similar to *in vivo* tissue, however, most certainly it is not. For these reasons, phantom and / or post mortem measurements do not allow for a direct comparison of *simulation* and **measurement**.

Direct *in vivo* measurements of all methods were not performed due to the long measurement times. Methods of acceleration, e.g. EPI readout, partial fourier or parallel imaging were excluded as their influence on T_1 estimation in combination with MT have not been studied yet.

In addition, simulations can take advantage of the possibility of switching the MT effect on and off at discretion. Especially for quantification, realistic simulations are superior as the sample parameters are known and stable. As a consequence, one can be sure that no denaturation or temperature changes or any other influence from the environment degrade the results.

Care has been taken to evaluate the simulation programme JEMRIS MT:

- The performance of the software was tested before and compared to **physical** agarose samples - the results of *simulation* and **measurement** showed good agreement (Chapter 6 and 7.2).
- The special issue of Look-Locker type sequences was *simulated* and tested *in vivo* (Chapter 8.2) and the *simulation* results were consistent to the measured results.

Thus, the results presented here can be taken as reliable and a transfer from *simulation* to **measurement** is admissible.

In summary, the *simulations* performed show, that the effect of MT on T_1 quantification is expected to be within the errors of the *simulated* T_1 mapping sequences and can therefore be neglected in many cases, especially *in vivo*.

8.2. Inversion Time Dependence of the Longitudinal Relaxation Time using Look-Locker Type Sequences

The importance and practical significance of T_1 mapping is one of the highest among the established qMRI applications. The broad range of applications was triggered especially by the development of Look and Locker [70], who presented a fast method to obtain T_1 by means of inversion recovery measurements (IR) in 1970. After inverting the magnetisation, the method employs multiple radiofrequency pulses during T_1 relaxation to sample several timepoints and thereby track the recovery of the magnetisation (see Chapter 4.3). The Look-Locker approach allows one to estimate T_1 much faster than by means of simple IR experiments, as it is not necessary to wait for full relaxation. Furthermore, several timepoints can be sampled within the same measurement, allowing for a more precise relaxation time mapping, especially in the presence of noise.

In 1986, Graumann et al. adapted the Look-Locker sequence for T_1 estimation to imaging purposes [103, 10]. The so-called TOMROP sequence acquires single-slice images after an inversion at multiple timepoints. Based on those fundamentals, many adoptions of the Look-Locker sequence have been presented to fit specific purposes. Some prevalent sequences are the snapshot FLASH based modification presented by Deichmann and Haase [104] and the EPI-based readout introduced by Gowland and Mansfield [65]. Other modifications have been presented e.g. by Brix [10], Kingsley [105, 106] and Messroghli [107]. Shah et al. [73] presented a method named TAPIR, which allows multi-slice, multi-time-point data acquisition through the reordering of acquired k-space data prior to reconstruction. The principle of interleaving slices and timepoints allows for extremely efficient data acquisition and enables the recovery curve to be sampled with a high temporal resolution.

All these Look-Locker type methods have in common that they allow for fast and precise mapping of the longitudinal relaxation time by sampling several timepoints along the recovery curve. As these methods are much more time-efficient than others, they are less prone to motion artefacts. Beyond that, the acquisition of several timepoints gives highly reliable results even in the presence of noise. Those benefits lead to a broad acceptance of the Look-Locker based methods even for clinical applications [108]. The broad range of possible applications of T_1 mapping (based on Look-Locker sequences) requires a thorough evaluation of the potential factors influencing the final parameter map. Issues related to imperfect inversion have been investigated by Kingsley [106], Deichmann [104] and Zaitsev [74]. General optimisations of several sequences have been reported e.g. by Freeman [71], Gowland [109] and Zaitsev [74]. One issue, which, to our knowledge, has not yet been exploited thoroughly, is the effect of magnetisation transfer, arising from dipolar cross-relaxation or chemical exchange on quantitative T_1 maps estimated

by Look-Locker type sequences.

Simulations of Look-Locker based methods to estimate T_1 in the presence of MT (see Chapter 8.1) revealed a dependence of the sequence parameters chosen on the estimated T_1 value. Drawing a parallel between the inversion recovery methods and the Look-Locker methods, which both apply inversion pulses, the effect of the inversion time, TI, was inspected. Chapter 8.1 showed that the influence of MT is stronger for shorter TI values. For that reason, TAPIR with different TI values was subject to a simulation and *in vivo* study.

8.2.1. Methods

The study was performed as a simulation study first, the simulation results were then verified by *in vivo* measurements on 10 healthy volunteers.

8.2.1.1. Simulations

Samples: the samples used for these simulations have already been described in Section 8.1.1.1. The agarose sample as well as additional MT samples, covering a larger parameter space (exchange rate k_{AB}, T_1^B, M_0^B/M_0^A), were also simulated in order to investigate the effects of the MT parameters on the final T_1 map. All sample parameters are summarised in Table 8.4, f denotes the M_0-ratio, $f = \frac{M_0^B}{M_0^A}$.

Sequence: the Look-Locker type sequence TAPIR, presented before (see section 8.1.1.2, Figure 8.9) was simulated with different TI values. The sequence parameters are listed in Table 8.5. TI values of 10, 20, 30, 40, 50, 60, 70, 80, 90, 100, 150 and 200 ms were simulated with JEMRIS MT. Each TI simulation was performed separately and for each sample type (WM, GM, Agarose). T_1^{fit} was obtained for each sample and TI, the results were analysed for accuracy and precision as well as by a comparison of the mean $T_1^{putative}$ values calculated based on the given sample parameters.

Evaluation: each TI simulation and sample provided a specific signal, S(timepoint), for each of the 45 timepoints. T_1^{fit} was obtained by fitting the simulated signal, S, to Equation (4.6) using an in-house MATLAB routine, neglecting potential MT effects. Simulation of the inversion efficiency was not necessary as no hardware imperfections hamper the inversion. At the end, for each TI a specific T_1^{fit} value was obtained and $T_1^{fit}(TI)$ could be evaluated. The curve can be described by means of the empirical function

$$T_1^{fit}(TI) = \eta - \beta e^{-\frac{TI}{\kappa}}, \tag{8.6}$$

Sample	M_0 Pool A	M_0 Pool B	T_1/ ms Pool A	T_1/ ms Pool B	T_2/ ms Pool A	T_2/ ms Pool B	k_{AB}	$T_1^{putative}$/ ms
Agarose 1 Pool	1		2417		54		-	2417
Agarose 2 Pool	1	0.011	2456	1000	54	0.0129	163.63	2417
Grey Matter 1 Pool	1		1748		99		-	1748
Grey Matter 2 Pool	0.95	0.05	1820	1000	99	0.0091	2	1748
GM 1 Pool	1		1748		99		-	1748
GM 2 Pool, $k_{AB} = 5$ Hz	0.95	0.05	1820	1000	99	0.0091	5	1748
GM 1 Pool	1		1748		99		-	1748
GM 2 Pool, $k_{AB} = 10$ Hz	0.95	0.05	1820	1000	99	0.0091	10	1748
White Matter 1 Pool	1		1071		69		-	1071
White Matter 2 Pool	0.861	0.139	1084	1000	69	0.01	3.197	1071
White Matter 2 Pool: $k_{AB} = 0.5$ Hz	0.861	0.139	1084	1000	69	0.01	0.5	1071
White Matter 2 Pool: $k_{AB} = 1$ Hz	0.861	0.139	1084	1000	69	0.01	1	1071
White Matter 2 Pool: $k_{AB} = 2$ Hz	0.861	0.139	1084	1000	69	0.01	2	1071
White Matter 2 Pool: $k_{AB} = 3$ Hz	0.861	0.139	1084	1000	69	0.01	3	1071
White Matter 2 Pool: $k_{AB} = 4$ Hz	0.861	0.139	1084	1000	69	0.01	4	1071
White Matter 2 Pool: $k_{AB} = 5$ Hz	0.861	0.139	1084	1000	69	0.01	5	1071
White Matter 2 Pool: $k_{AB} = 7$ Hz	0.861	0.139	1084	1000	69	0.01	7	1071
White Matter 2 Pool: $k_{AB} = 10$ Hz	0.861	0.139	1084	1000	69	0.01	10	1071
White Matter 2 Pool: $k_{AB} = 15$ Hz	0.861	0.139	1084	1000	69	0.01	15	1071
White Matter 2 Pool: $T_1^B = 200$ ms	0.861	0.139	1084	200	69	0.01	3.197	708
White Matter 2 Pool: $T_1^B = 500$ ms	0.861	0.139	1084	500	69	0.01	3.197	937
White Matter 2 Pool: $T_1^B = 1500$ ms	0.861	0.139	1084	1500	69	0.01	3.197	1128
White Matter 2 Pool: $T_1^B = 2000$ ms	0.861	0.139	1084	2000	69	0.01	3.197	1159
White Matter 2 Pool: f =0.05	0.9524	0.0476	1084	1000	69	0.01	3.197	1080
White Matter 2 Pool: f =0.161	0.861	0.139	1084	1000	69	0.01	3.197	1071
White Matter 2 Pool: f =0.2	0.8333	0.1667	1084	1000	69	0.01	3.197	1069
White Matter 2 Pool: f =0.25	0.8	0.2	1084	1000	69	0.01	3.197	1066
White Matter 2 Pool: f =0.3	0.7692	0.2308	1084	1000	69	0.01	3.197	1063
White Matter 2 Pool: f =0.4	0.7143	0.2857	1084	1000	69	0.01	3.197	1059
White Matter 2 Pool: f =0.5	0.6667	0.3333	1084	1000	69	0.01	3.197	1055
White Matter 2 Pool: f =1	0.5	0.5	1084	1000	69	0.01	3.197	1041
White Matter 2 Pool: f =0.161, T_1^B =200 ms	0.861	0.139	1084	200	69	0.01	3.197	708
White Matter 2 Pool: f =0.2, T_1^B =200 ms	0.8333	0.1667	1084	200	69	0.01	3.197	668
White Matter 2 Pool: f =0.25, T_1^B =200 ms	0.8	0.2	1084	200	69	0.01	3.197	627
White Matter 2 Pool: f =0.3, T_1^B =200 ms	0.7692	0.2308	1084	200	69	0.01	3.197	595
White Matter 2 Pool: f =0.4, T_1^B =200 ms	0.7143	0.2857	1084	200	69	0.01	3.197	546
White Matter 2 Pool: f =0.5, T_1^B =200 ms	0.6667	0.3333	1084	200	69	0.01	3.197	512

Table 8.4: *Samples used in the Look-Locker simulations with different TIs. All WM 2 pool samples were also simulated as one pool samples with the same $T_1^{putative}$ as the two pool sample.*

where η, β and κ are empirical factors. The meaning of these factors was also analysed within this study.

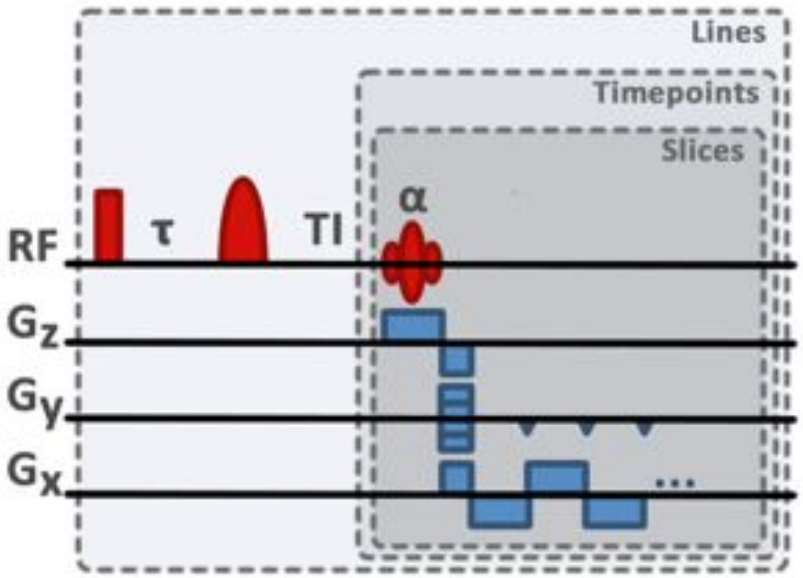

Figure 8.9: *Schematic representation of the TAPIR sequence diagram.*

TAPIR Sequence Parameters	
TR	175 ms
TE	5 ms
flip angle	20°
τ	4 s
timepoints	45
slices	1

Table 8.5: *TAPIR sequence parameters used in the simulations. Details of the TAPIR specific parameters can be found in Chapter 4.3.*

8.2.1.2. *In vivo* Measurements

Measurements: for the assessment of the TAPIR TI-dependence, TAPIR T_1 maps with different TI values were acquired in 10 male healthy volunteers (age = 32 ± 6 years). Written informed consent was obtained from all subjects prior to the scan. All acquisitions were performed on a 3 T whole-body system (Tim Trio System, Siemens Medical, Erlangen, Germany), employing a 32-channel receive head coil. The measurement protocol included a scout image, a whole brain MP-RAGE with an isotropic resolution of 1 mm for anatomy and reference as well as 10 TAPIR acquisitions. The TAPIR parameters used are listed in Table 8.6 and TI values of 11, 20, 30, 40, 50, 60, 80, 100, 120 and 140 ms were obtained. As described by Deichmann [110], a gain in the T_1 accuracy can be achieved by employing a hyperbolic secant inversion pulse instead of a rectangular inversion pulse, which was part of the original TAPIR sequence [73]. The duration of the hyperbolic secant adiabatic pulse employed here was 8.192 ms, its amplitude,

Amp, and phase, ϕ, are modulated with $Amp(t) = \mathrm{sech}(b * t)$ and $\phi(t) = \mu \log(Amp(t))$ with $b = 4.5\,{}^{1}/_{\mathrm{s}}$ and $\mu = 5$. The inversion efficiency was obtained according to [74] with the same TI and lower resolution. The sequence parameters used for the *in vivo* measurement differ from the simulated sequence in some points for various reasons. The TR of the simulation is much longer, as only one slice was simulated; the effective TR is then comparable to the measurements. To avoid cross-talk effects, the slice gap was set to 100%. The *in vivo* delay time, τ, was much shorter than the simulated one. The simulations used a τ of 4 seconds, as suggested by Zaitsev [74]. However, *in vivo* optimisation revealed that a τ of 2.4 s is the better choice [111]. Further changes between simulation and *in vivo* protocol arise from hardware limitations as well as time constraints. The acquisition time for the total protocol was about 48 minutes.

TAPIR Sequence Parameters	
TR	10 ms
TE	3.09 ms
flip angle	23°
τ	2.4 s
bandwidth	300 Hz / Pixel
in plane resolution	1.5 mm · 1.5 mm
timepoints	25
iPAT (Grappa)	3
averages	1
slices	8
slice thickness	2 mm
slice gap	100%

Table 8.6: *TAPIR sequence parameters used in the* in vivo *experiments. Details of the TAPIR specific parameters can be found in Chapter 4.3.*

Evaluation: T_1^{fit} maps were obtained using the same in-house tool based on a MATLAB routine as for the simulations. Any MT effects were neglected for fitting, resulting in T_1^{fit}. The data processing chain started with a smoothing of the IE measurements. A 3-parameter fit of T_1^{fit}, M_0 and the actual flip angle, α_{actual}, was obtained on the TAPIR data taking into account the additional IE measurements. The flip angle maps were then smoothed, a reasonable approach, as B1 inhomogeneities are slowly varying. The smoothed flip maps were then included in a second, two parameter fit to estimate T_1^{fit} and M_0. This two-fold approach gives rise to much more stable results, especially for the M_0 maps but also for the T_1 maps.

WM was segmented using a custom-built region growing algorithm using 4 seedpoints per slice and TI and a segmentation threshold of 40 ms. This approach neglects voxel with large partial volume effects arising from the rather large slice thickness of 2 mm. The mean and standard deviation of the T_1^{fit} distribution within the segmented WM were derived for each T_I measure-

ment.
The TI dependence of T_1^{fit} was plotted and Equation (8.6) was fitted using a robust non-linear fitting algorithm provided by MATLAB.

8.2.2. Results

8.2.2.1. Simulations

All simulations were evaluated without and with added noise equivalent to an SNR of 50 of the input data, which is close to *in vivo* conditions. For each TI the T_1^{fit} value was calculated based on the TAPIR signal equation (4.6) and mean T_1^{fit}, the accuracy, Δ, and precision, σ, with respect the the putative $T_1^{putative}$ were calculated according to Equations (8.3) and (8.4). The results are shown in Figure 8.10 for the agarose sample and in Figure 8.11 for GM and WM. They reveal a dependence of the T_1^{fit} on the TI used in the sequence, if the two pool sample was used. The error bars in the plots represent the standard deviation across the voxels of the simulated sample (SNR 50).

Agarose Sample: The T_1^{fit} values of the agarose sample, shown in Figure 8.10, are not significantly influenced by the different TI values. The difference between the one pool and the two pool sample is less than 5%. However, the difference is not within the precision expected for an SNR of 50. The MT effect results in an overestimation of the fitted T_1^{fit} value, compared to the putative values, $T_1^{putative}$, one would obtain without MT. The agarose sample has a putative $T_1^{putative}$ of 2417 ms. The longitudinal relaxation time of the larger pool (A), T_1^A, was set to 2456 ms. The estimated T_1^{fit} of the simulated sample is much closer to its T_1^A than to its putative $T_1^{putative}$. Any assumed influence of different TI values is only visible without any noise, under SNR conditions similar to *in vivo* measurements, the slight rise in the fitted T_1^{fit} value is hidden within the standard deviation.

Grey Matter Sample: While the one pool sample remains unaffected by different TI values, the two pool grey matter sample shows a clear dependence of the estimated T_1^{fit} value on the TI value (Figure 8.11). The two curves can be separated for an SNR of 50. T_1^{fit} exponentially increases for increasing TI values.

White Matter Sample: The two pool white matter sample is expected to be influenced more strongly by MT compared to the grey matter sample. The reasons for the stronger MT effect

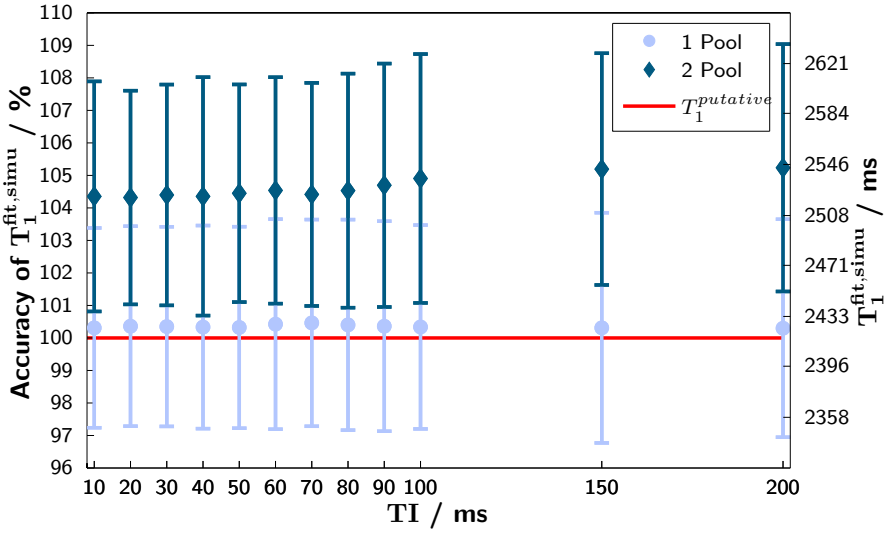

Figure 8.10: ***Agarose sample****, estimated T_1^{fit} of the one pool and two pool sample in absolute values and scaled to the expected $T_1^{putative}$. The error bars indicate the precision for an SNR of 100. The left upright axis shows the corresponding accuracy and precision calculated by means of the expected $T_1^{putative}$, the right vertical axis shows the absolute mean T_1^{fit} value with the standard deviation.*

are the larger bound pool fraction of WM as well as the different exchange rates. The larger MT influence manifests itself through a stronger TI dependence of the $T_1^{fit}(TI)$ plot, as visible in the lower plot of Figure 8.11. The difference in T_1^{fit} for the simulated TI range is about 15%, compared to about 4% for the grey matter sample (Figure 8.11, top).

Influence of the Sample Parameters: All samples show that the T_1^{fit} of the one pool sample obtained with the Look-Locker sequence has high accuracy and precision, while the two pool samples undergoing MT reveal different T_1^{fit} estimates for different TI values. According to theory (cf. Section 5.2.3), the putative $T_1^{putative}$ is a function of $T_1^A, T_1^B, k_{AB}, M_0^A, M_0^B$ as well as the sequence parameters, e.g. flip angle and TR. To check the influence of the different MT parameters on the $T_1^{fit}(TI)$ plot, the exchange rate, k_{AB}, the T_1 of the bound pool, T_1^B, and the M_0 ratio, f, were varied and several samples with different parameters were simulated. The results are displayed for several exchange rates in grey (Figure 8.12) and white matter (Figure 8.13), in Figure 8.14 for various T_1^B values in WM and in Figure 8.15 and 8.16 for different fractions, $f = {}^{M_0^B}/_{M_0^A}$ as well as T_1^B values.

As the $T_1^{fit}(TI)$ curve shows an exponential behaviour (cf. Figure 8.11), the empirical equation

$$T_1^{fit}(TI) = \eta - \beta e^{-\frac{TI}{\kappa}} \tag{8.7}$$

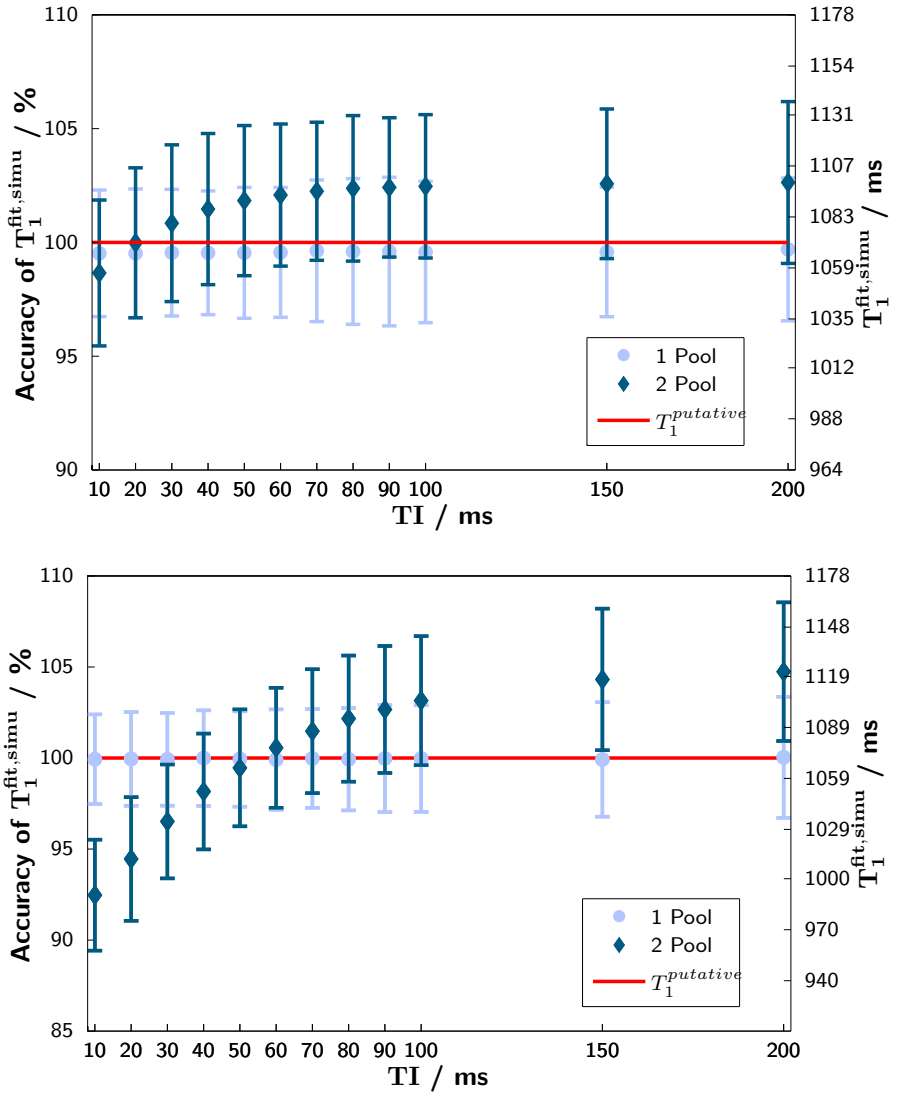

Figure 8.11: ***GM*** *(top) and* ***WM*** *(bottom) sample, estimated T_1^{fit} of the one pool and two pool sample in absolute values and scaled to the expected $T_1^{putative}$. The error bars indicate the precision for an SNR of 100. The left upright axis shows the corresponding accuracy and precision calculated by means of the expected $T_1^{putative}$, the right vertical axis shows the absolute mean T_1^{fit} value with the standard deviation.*

was fitted to the data, the fit results are displayed as lines in Figure 8.12 to 8.16. The root mean squared error, $RMSE$ was utilized as a filter: $RMSE$ values larger than 2 were not considered for further analysis. The largest $RMSE$ values were found for those cases, where the TI range was too small and no plateau could be found in the $T_1^{fit}(TI)$ dependence.

For very short exchange rates, as shown in Figure 8.12, the fitted T_1^{fit} values are underestimated compared to the putative $T_1^{putative}$ value, in the presence of MT. This changes with increasing

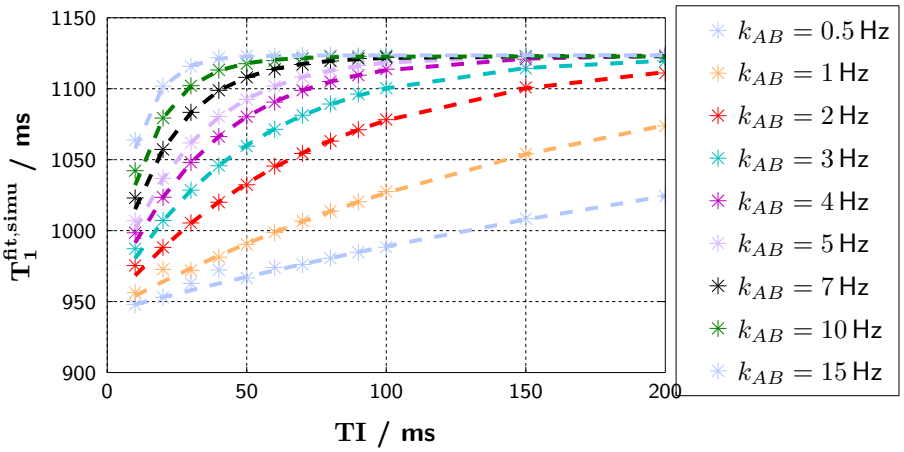

Figure 8.12: *The TAPIR TI dependence (∗) plotted for the two pool **white matter** sample with different values for the exchange rates. The dashed lines (−−) show the fitting result of the data to Equation* (8.6)*, the corresponding parameters are listed in Table 8.7.*

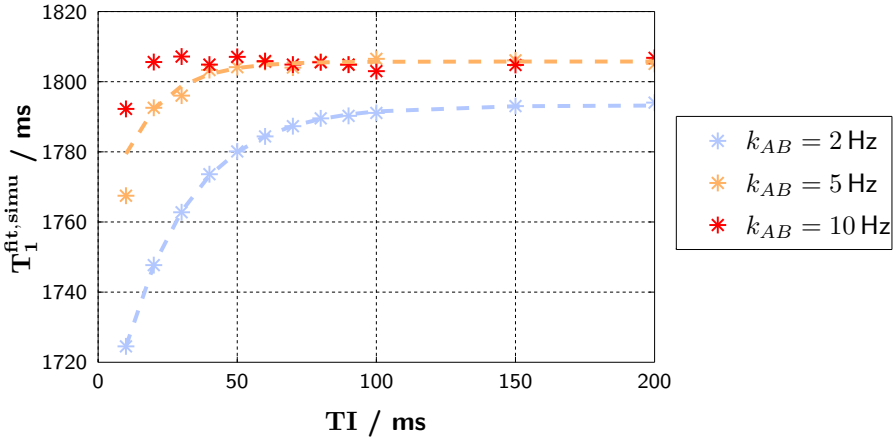

Figure 8.13: *The TAPIR TI dependence (∗) plotted for the two pool **grey matter** sample with different values for the exchange rates. The dashed lines (−−) show the fitting result of the data to Equation* (8.6)*, the corresponding parameters are listed in Table 8.7. Since the fit for $k_{AB} = 10$ Hz did not converge, not fit results is shown.*

exchange rates. The exponential behaviour of the $T_1^{fit}(TI)$ curve, which was revealed for the grey matter MT sample is also visible for white matter. As the dynamic range decreases with increasing TI values, some influence on the precision is expected. However, the precision decreases only about 0.5% between the shortest simulated TI and the longest TI.

The behaviour of the $T_1^{fit}(TI)$ curve is strongly dependent on the exchange rate, k_{AB}. The plateau T_1^{fit} value approaches T_1^A rather than the $T_1^{putative}$ and is about the same for all exchange rates. The transition to the plateau depends on the exchange rate. Samples with faster exchange rates (larger k_{AB} values) arrive the plateau earlier than slower exchange rates. For

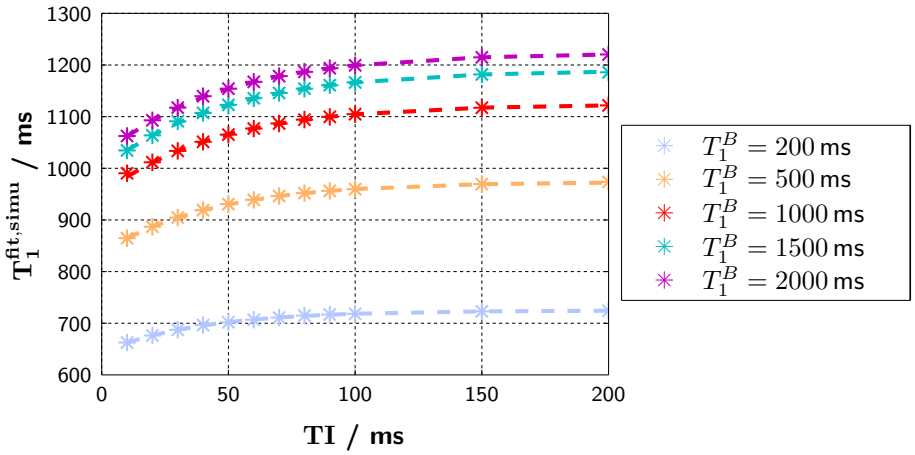

Figure 8.14: *Varying the longitudinal relaxation time of the bound pool (**WM** sample), T_1^B, changes the fit parameters, η and β, defining the range of $T_1^{putative}$ values for the simulated TI values.*

higher exchange rates, the MT effect manifests itself only in an overestimation of the T_1^{fit} values compared to the one pool sample neglecting MT. As observed for the agarose sample, the T_1^{fit} for larger TI values converges to the T_1^A (here 1820 ms) rather than to the $T_1^{putative}$ (here 1748 ms).

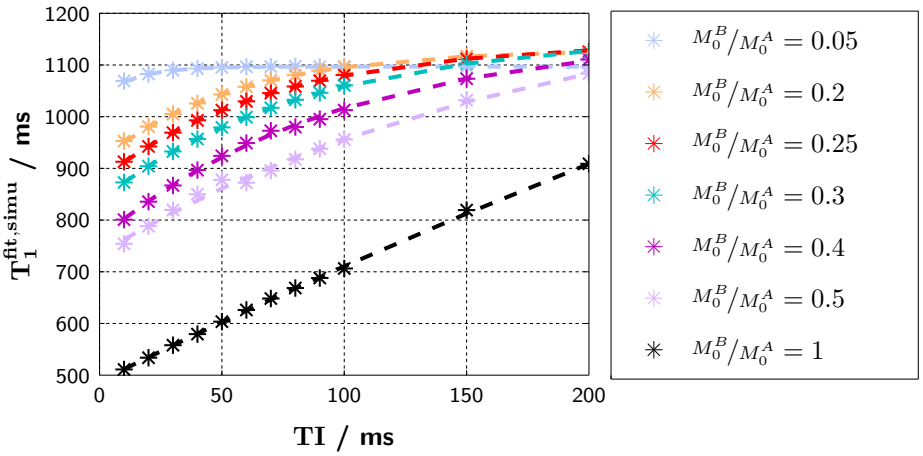

Figure 8.15: *The TAPIR TI dependence ($*$) plotted for the two pool **white matter** sample with different values for M_0^B/M_0^A and a T_1^B of 1000 ms. The dashed lines ($--$) show the fitting result of the data to Equation* (8.6)*, the corresponding parameters are listed in Table 8.7.*

The key question arising in conjunction with the $T_1^{fit}(TI)$ dependence of Look-Locker type sequences is the meaning of the fit parameters in Equation (8.7). To explore any potential connection between the MT sample parameters $(f, T_1^A, T_1^B, k_{AB})$ and the fit parameters $(\eta, \beta$

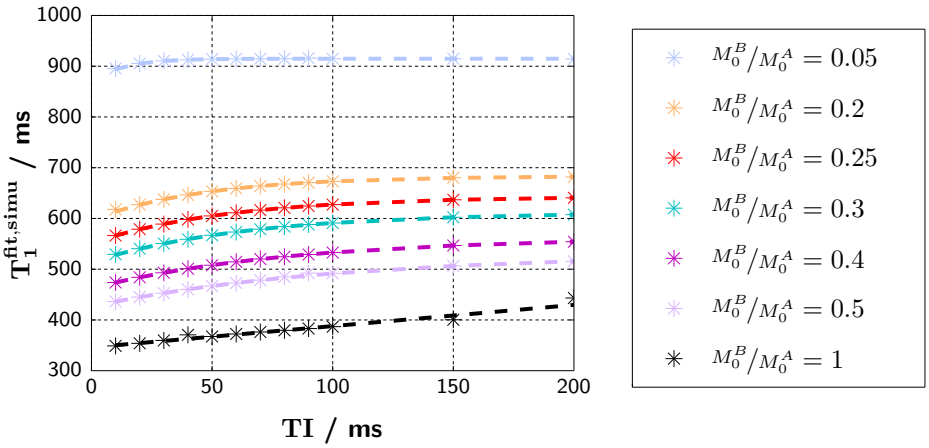

Figure 8.16: *The TAPIR TI dependence ($*$) plotted for the two pool **white matter** sample with different values for M_0^B/M_0^A and a T_1^B of 200 ms. The lines ($--$) show the fitting result of the data to Equation* (8.6)*, the corresponding parameters are listed in Table 8.7.*

and κ) some reasonable connections between the fit parameter and the sample values were analysed in the following. Table 8.7 summarises all fit results for the samples simulated.
The exchange rate has a major influence on the $T_1^{fit}(TI)$ behaviour. As seen in Figure 8.12, the plateau value is reached for shorter TI values if the exchange rate, k_{AB}, is larger. Fitting the interrelation of the estimated T_1^{fit} and the TI for the different exchange rates shows a linear dependence on the empirical parameter $1/\kappa$, while η and β remain at a constant level (cf. Figure 8.17 and 8.20).

The results for varying T_1^B are shown in Figure 8.19 and in Figure 8.20. Considering the different $T_1^{putative}$ values connected with the dissimilar T_1^B values of the simulated samples shows that the fit parameters η and β are proportional to the changes in the estimated $T_1^{putative}$ (Figure 8.19), while κ is almost unaffected (Figure 8.20), mean(κ) $= 45 \pm 3$ ms compared to mean(κ) $= 36 \pm 22$ ms for the k_{AB} span).

8.2.2.2. *In vivo* Measurements

The results obtained by the simulations were verified *in vivo*. WM segmentation based on the region-growing algorithm worked well. An example of the WM segmentation in one volunteer

f	$\mathbf{k_{AB}}$ / Hz	$\mathbf{T_1^A}$ / ms	$\mathbf{T_1^B}$ / ms	$T_1^{putative}$	η	β	κ / ms	RMSE
0.16	0.5	1084	1000	1071	1149	203	412.1	3.20
0.16	1	1084	1000	1071	1153	205	207.0	2.61
0.16	2	1084	1000	1071	1127	175	79.2	1.66
0.16	3	1084	1000	1071	1124	169	51.5	1.44
0.16	3.197	1084	1000	1071	1125	169	48.1	1.28
0.16	4	1084	1000	1071	1125	167	38.2	1.28
0.16	5	1084	1000	1071	1125	165	30.7	1.00
0.16	7	1084	1000	1071	1123	161	21.7	0.97
0.16	10	1084	1000	1071	1123	158	15.1	0.85
0.16	15	1084	1000	1071	1124	167	9.8	0.51
0.16	3.197	1084	200	708	725	80	39.4	0.41
0.16	3.197	1084	500	937	974	137	44.3	0.42
0.16	3.197	1084	1000	1071	1125	169	48.1	1.28
0.16	3.197	1084	1500	1128	1189	191	46.7	0.99
0.16	3.197	1084	2000	1159	1223	199	46.9	0.54
0.05	3.197	1084	1000	1080	1097	55	14.6	0.47
0.16	3.197	1084	1000	1071	1125	169	48.1	1.28
0.2	3.197	1084	1000	1069	1132	215	56.2	0.66
0.25	3.197	1084	1000	1066	1141	265	68.6	0.80
0.3	3.197	1084	1000	1063	1152	317	82.2	1.08
0.4	3.197	1084	1000	1059	1161	397	98.8	4.19
0.5	3.197	1084	1000	1055	1245	511	174.6	8.75
1	3.197	1084	1000	1041	2545	2057	868.3	2.74
0.2	3.197	1084	200	668	684	83	50.6	0.85
0.25	3.197	1084	200	627	643	92	57.2	0.15
0.3	3.197	1084	200	595	612	97	65.8	0.33
0.4	3.197	1084	200	546	563	101	82.9	0.18
0.5	3.197	1084	200	512	528	103	93.5	1.46

Table 8.7: *Summary of all simulated samples and their fitted $T_1^{fit}(TI)$ dependence along with the root means squared error (RMSE) of the fit. Some parameter dependencies are visualized in Figures 8.17 to 8.20. Samples with a RMSE larger than 2 (grey shaded) were excluded from further analysis and visualisation.*

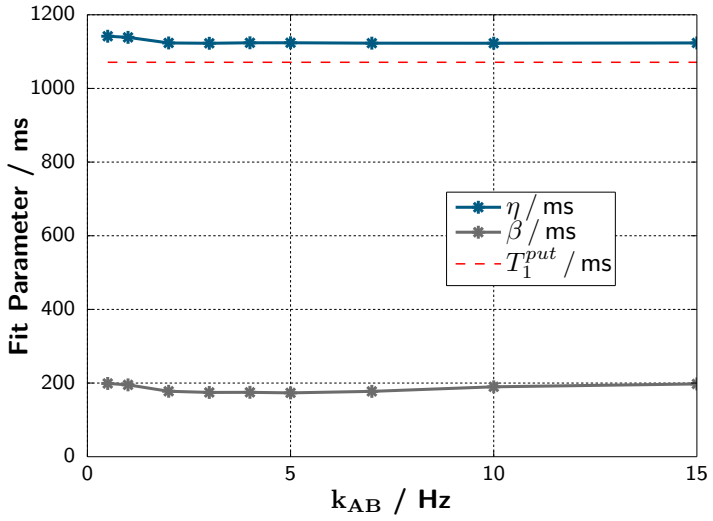

Figure 8.17: *The fit parameters η and β, which define the start and plateau $T_1^{putative}$ are very stable for different exchange rates.*

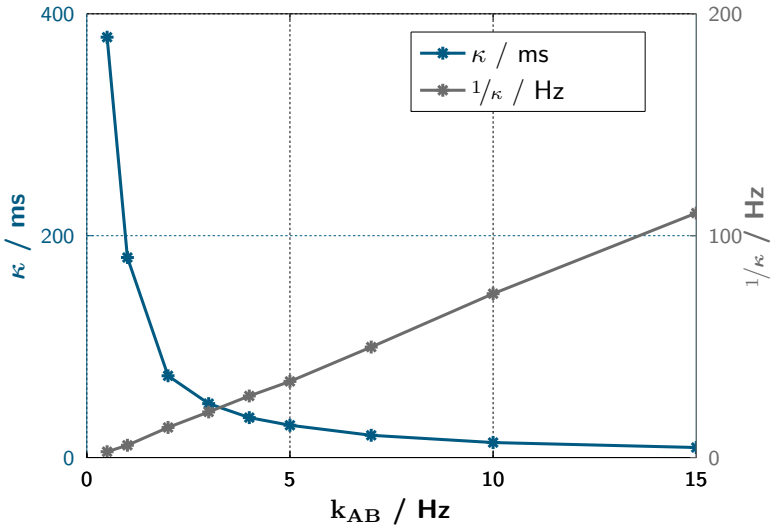

Figure 8.18: *The inverse of the exponential fit parameter, κ, shows a linear relationship with the exchange rate, k_{AB}.*

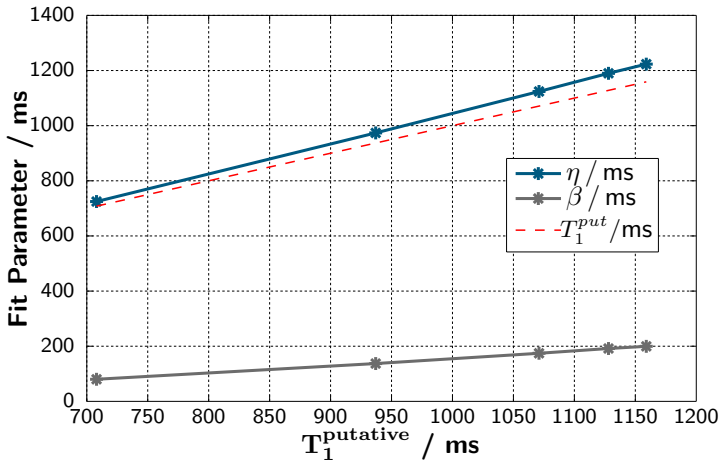

Figure 8.19: *Comparing the fit parameters, η and β with the $T_1^{putative}$ reveals a linear relationship.*

for a given slice and different TI is depicted in Figure 8.21. Figure 8.22 shows the segmentation in the same volunteer for all slices at fixed TI.

Even from this single T_1 map, a variation of the T_1 values in the different slices is visible (Figure 8.23). Plotting the mean T_1^{fit} for the different slices obtained from one measurement at a fixed TI, as shown in Figure 8.23, highlights the slice dependent changes in T_1^{fit} due to the different effective TIs. The slices were acquired from inferior to superior, which means that the first slice (top left) has a shorter effective TI than the last slice (bottom right in Figure 8.22).

Including all measured TI values, the T_1^{fit} values obtained with TAPIR showed a similar TI dependency for all volunteers as it was found in the simulations. Figure 8.24 shows a typical

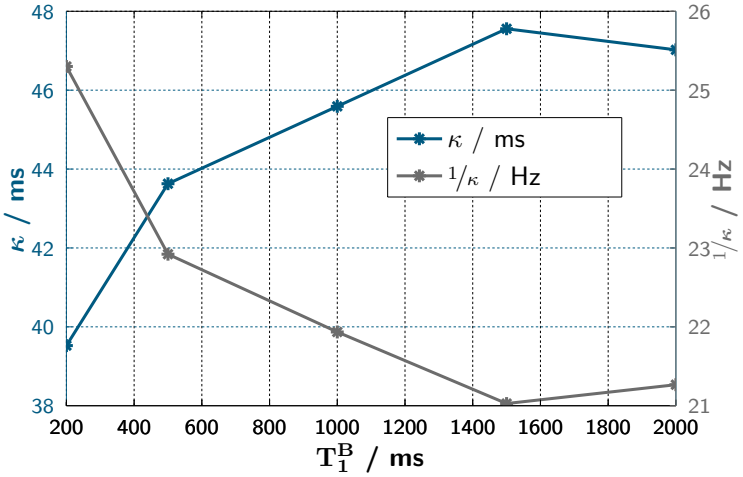

Figure 8.20: *The exponential fit parameter, κ, is more or less unaffected by changes in T_1^B. The variations are in a range of 10 ms, compared to the variation over 400 ms for different exchange rates.*

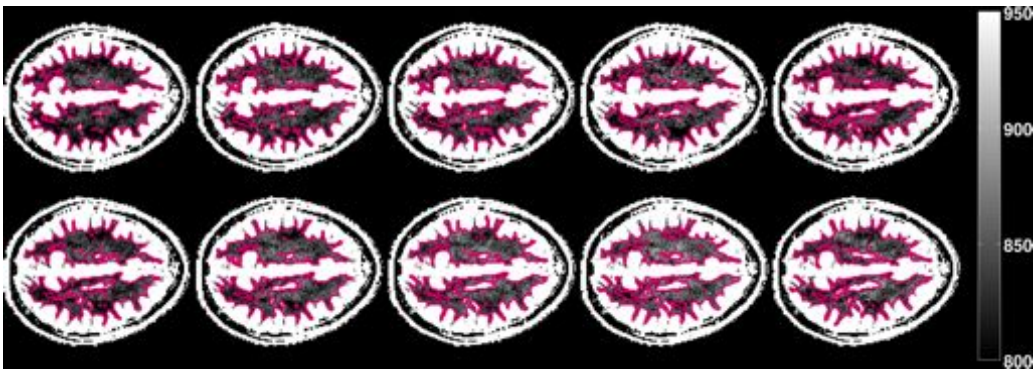

Figure 8.21: *Typical WM ROI (outlined in red) for one slice and several TI values. T_1^{fit} increases for increasing TI values (top left to bottom right). The colourbar displays the T_1 values in ms.*

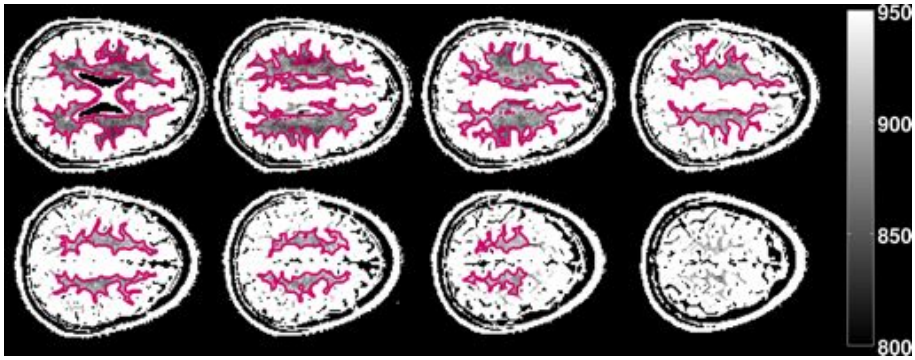

Figure 8.22: *Typical WM ROI for the brain volume obtained. The colourbar displays the T_1 values in ms.*

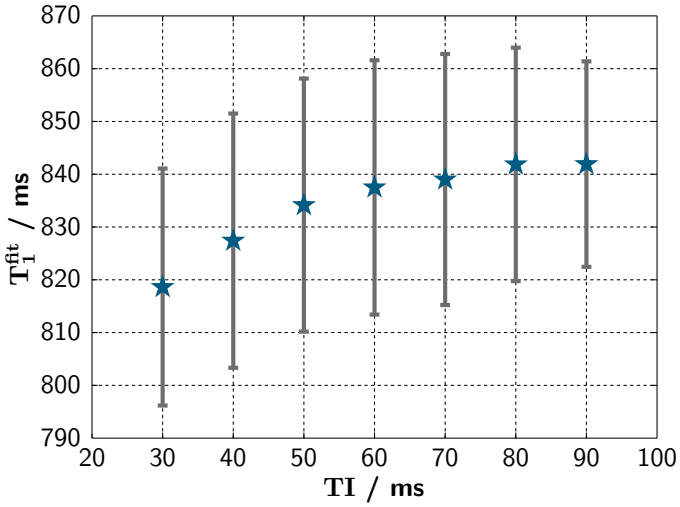

Figure 8.23: *$T_1^{fit}(TI)$ dependence obtained from one measurement and different slices. The diagram shows mean ± standard deviation calculated within the WM ROI obtained by the region growing algorithm (Figure 8.22).*

plot of the $T_1^{fit}(TI)$ obtained *in vivo*. The plot shows the mean T_1^{fit} value per TI (stars) along with the standard deviation (error bars) within the WM region of interest (ROI). The curve resulting from the fitting procedure is shown in grey.

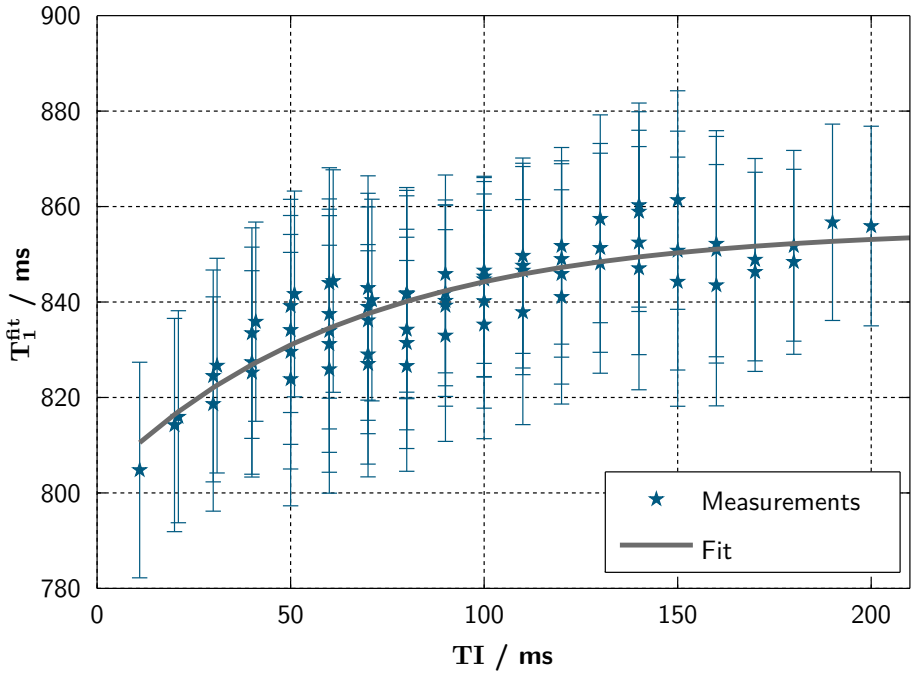

Figure 8.24: *Typical results of the* in vivo *measurements of TAPIR with different TI values. The stars mark the mean T_1^{fit} from the selected WM ROI, the error bars show the standard deviation. Fitting the measured values on the function* (8.6) *gives the curve shown in grey.*

WM ROI selection and fitting were performed for all volunteers. The fit parameters η, β and κ are displayed in Table 8.8. While the empirical parameters η and β are quite stable, the κ parameter, which is - according to the simulations - connected with the exchange rate, shows a larger inter-subject variation. The results confirm that the estimated T_1^{fit} value is increases with increasing TI. While the changes in T_1^{fit} are stronger for short effective TIs in the range of 10 to 80 ms, the T_1^{fit} values are quite stable for the effective TI values from 100 to 200 ms.

Fit Parameter:		η	β	κ
Subject	1	902	37	68
	2	932	69	41
	3	855	53	64
	4	910	63	116
	5	917	58	40
	6	889	54	81
	7	899	62	50
	8	880	55	61
	9	881	55	70
	10	937	70	44
$\mu \pm \sigma$		900 ± 25	58 ± 9	64± 23

Table 8.8: *Resulting parameters obtained by estimating $T_1^{fit}(TI)$ for the 10 volunteers.*

8.2.3. Discussion

Although the findings shown in this work were obtained specifically with the T_1 mapping sequence, TAPIR, the results can, in principle, be translated to any other Look-Locker like sequence. The investigations performed here allow two major conclusions to be drawn. First, in order to decrease any influences on T_1 parameter estimation, it is recommended to use the Look-Locker sequence with longer TI. Although that decreases the dynamic range, the bound pool affects the results less. Focussing on the simulation results, the standard deviation is not significantly larger than for the larger dynamic range. However, the estimated T_1 value varies for the shorter TI values. Time efficient sequences, such as TAPIR, where each slice haas a different TI are especially affected by this effect. As each slice has a different effective TI ($TI_{effective}$ = TI + slicenumber*TR), the choice of short TI values gives rise to different T_1^{fit} values, increasing with the acquired slice. However, every Look-Locker like sequence will show the TI dependence. In general, the strength of the influence on the final T_1 maps is a function of the sampling pattern and the individual TI in each voxel or slice. Our work showed that the effect is in the range of about 5% *in vivo*, but especially if the generated T_1 maps are used for continuative postprocessing, as e.g. for DCE, the expected MT effects should be minimised. Therefore, the same TI should be used for all measurements. If there exist different effective TI values, as in the TAPIR sequence, a rather long TI (>80 ms) is advised. If one compares several

T_1 maps, obtained with Look-Locker like sequences on different scanners, different subjects or at several timepoints, one should be aware of an additional error of up to 5% if various sequences and different TI values were used.

On the other hand, the findings could be used as a novel method to generate quantitative MT maps. It is known from the literature that quantification of MT is a rather difficult task, limited usually by long acquisition times and the limited brain coverage as well as the requirement of fitting many free parameters. In turn, this requires a very high SNR as well as a lot of sampled points which prolongs the measurements [112]. Many models employ physically meaningful constraints on the fitting parameters in order to reduce the number of free parameters [113, 114]. These approaches have been successfully tested in healthy subjects but it remains unclear if pathologies exist, where the constraints falsify the results. To our knowledge, all quantitative MT models are either semi-quantitative, meaning that the results are highly dependent on the acquisition parameters, or they are based on fitting of many free parameters (> 5), probably eased by some constraints. At worst, the signal equation to be fitted exhibits biexponential behaviour, thus rendering the fitting process strongly ill-posed [96].

The approach presented here is advantageous in some regards. Fitting the empirical function (cf. Equation (8.6)) gives rise to only three parameters, η, β and κ, characterising the 2 pools. This could allow for faster measurements with larger brain coverage. Less data points are necessary for reliable fitting and the results are more likely to be stable while no constraints on the fitting parameters are necessary. However, further investigation of the empirical fit parameters and their relation to MT is necessary. The simulations suggest that the fit parameters, η and β, give some information about the T_1 values of the single pools, scaled by an unknown proportionality constant. Parameter κ is inversely proportional to the exchange rate k_{AB}. Further research is required to uncover either the functional relation including the constant of proportionality or a direct connection between the empirical parameters and a disease of interest.

8.2.4. Conclusions

In conclusion, a new approach was developed to characterise MT parameters by means of Look-Locker type sequences with varying TI values. Simulations as well as *in vivo* measurements suggest that variations in TI of Look-Locker type sequences might constitute a potential method to estimate changes in the exchange rate as well as the T_1 values of the bound and free water pool in tissue undergoing MT. On the other hand, we advise the use of TI values larger than 80 ms, to avoid interferences of MT on the estimated T_1 values, if MT is present.

9. An Application of T_1 Mapping: Calculating Blood-to-Brain Transfer Constants

Quantifying the longitudinal relaxation time, T_1, has been considered throughout this work. This final chapter aims to present an application of T_1 mapping; quantification of T_1 can provide a basis for measurements of the blood-brain barrier. The underlying model, the Patlak model, is derived in Section 9.2. Initially, the Patlak model was developed to evaluate data originating from nuclear medicine imaging following the injection of a radioactive tracer. The model was adapted to work on MRI data (cf. Section 9.3) and further optimisations have been developed in order to gain a higher fidelity of the results (cf. Section 9.4). Finally, a comparison of Patlak MRI data to FET-PET data was obtained (Section 9.5) and both methods were performed on patients suffering from different brain tumours (Section 9.6). The analysis was motivated by the desire to compare the conflicting information of the two different imaging modalities and to determine whether the results are consistent or divergent.

9.1. The Blood-Brain Barrier

The blood-brain barrier (BBB) separates the circulating blood from the extracellular brain fluid in the central nervous system. Its main function is, to protect the neuronal micro-environment from harmful substances within the circulating blood. Breakdown of the BBB is a known and important indicator of inflammations in neurological diseases. Diseases which are known to be associated with BBB dysfunctions are stroke, brain tumours, multiple sclerosis (MS), degenerative diseases and infections [115, 116, 117, 118]. Measurements of the BBB permeability provide information about the progress of a disease or its response to therapy. In order to characterise the BBB permeability, several models have been developed [31, 32, 2, 3]. One of them, the Patlak model is introduced and derived here.

9.2. The Patlak Model

The model presented by Patlak, Blasberg and Fenstermacher in 1981 [31, 32] aims to use multiple-time tissue uptake data to determine the blood-brain exchange of a given solute. The following section will follow Patlak's approach with some extensions for a better understanding.

9.2.1. Derivation of the Model

9.2.1.1. Simple two Compartment Model

To derive Patlak's equation, a simplified model is first assumed. It consists of two compartments (cf. Figure 9.1), marked i and l. The total number of particles within each compartment is denoted p_i and p_l, respectively. Some particles (representing e. g. some type of contrast agent) are marked (red ones, a_i, a_l) and all particles are allowed to exchange between the compartments as well as to leave or to enter the system from outside. The number of exchanging particles per unit time is given by the exchange numbers, $q_i, \kappa_{il}, \kappa_{li}$ and κ_i. The concentration of the marked particles outside is denoted with C_{outside}.

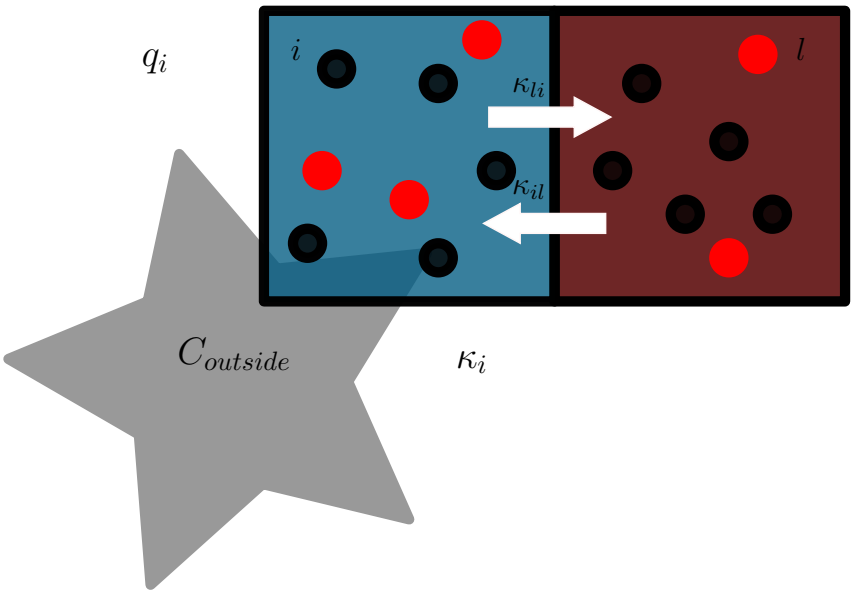

Figure 9.1: *Sketch of the simplest two compartment model.*

Focussing on compartment i, at time t_0 there are in total $p_i(t_0)$ particles and $a_i(t_0)$ marked

particles within the compartment. After a time, t_1, the number of particles is given by:

$$\begin{aligned} \Delta t &= t_1 - t_0 \\ p_i(t_1) &= p_i(t_0) + \sum_{l \neq i} \kappa_{il} \Delta t - \sum_{l \neq i} \kappa_{li} \Delta t - \kappa_i \Delta t + q_i \Delta t \\ a_i(t_1) &= a_i(t_0) + \sum_{l \neq i} \kappa_{il} \Delta t \frac{a_l}{p_l} - \sum_{l \neq i} \kappa_{li} \Delta t \frac{a_i}{p_i} - \kappa_i \Delta t \frac{a_i}{p_i} + q_i \Delta t C_{\text{outside}}. \end{aligned} \tag{9.1}$$

This leads to the differential equation:

$$\begin{aligned} \frac{dp_i}{dt} &= \sum_{l \neq i} \kappa_{il} - \sum_{l \neq i} \kappa_{li} - \kappa_i + q_i \\ \frac{da_i}{dt} &= \sum_{l \neq i} \kappa_{il} \frac{a_l}{p_l} - \sum_{l \neq i} \kappa_{li} \frac{a_i}{p_i} - \kappa_i \frac{a_i}{p_i} + q_i C_{\text{outside}}. \end{aligned} \tag{9.2}$$

From now on, only the marked particles are observed. Equation (9.2) can be rewritten by the introduction of an exchange matrix K with matrix elements

$$(k)_{il} = \begin{cases} \frac{\kappa_{il}}{p_l} & if \quad i \neq l \\ \frac{-(\sum_{l=1}^{n} \kappa_{li} + \kappa_i)}{p_i} & if \quad i = l \end{cases} \tag{9.3}$$

and $A = (a)_i$ as

$$\frac{da_i}{dt} = \sum_{i=1}^{n} k_{il} a_l + q_i C_{\text{outside}}. \tag{9.4}$$

Equation (9.3) then reads

$$\frac{dA}{dt} = KA + \vec{Q} C_{\text{outside}}. \tag{9.5}$$

9.2.1.2. Including the Plasma Compartment

The given model can be extended with a plasma compartment, as showed in Figure 9.2.

Then the equation for K (9.3) has to be modified to

$$(k)_{il} = \begin{cases} \frac{\kappa_{il}}{p_l} & if \quad i \neq l \\ \frac{-(\sum_{l=1}^{n} \kappa_{li} + \kappa_{bi} + \kappa_{pi})}{p_i} & if \quad i = l. \end{cases}$$

C_{outside} changes to C_p and Equation (9.5) reads then

$$\frac{dA}{dt} = KA + \vec{Q} C_p. \tag{9.6}$$

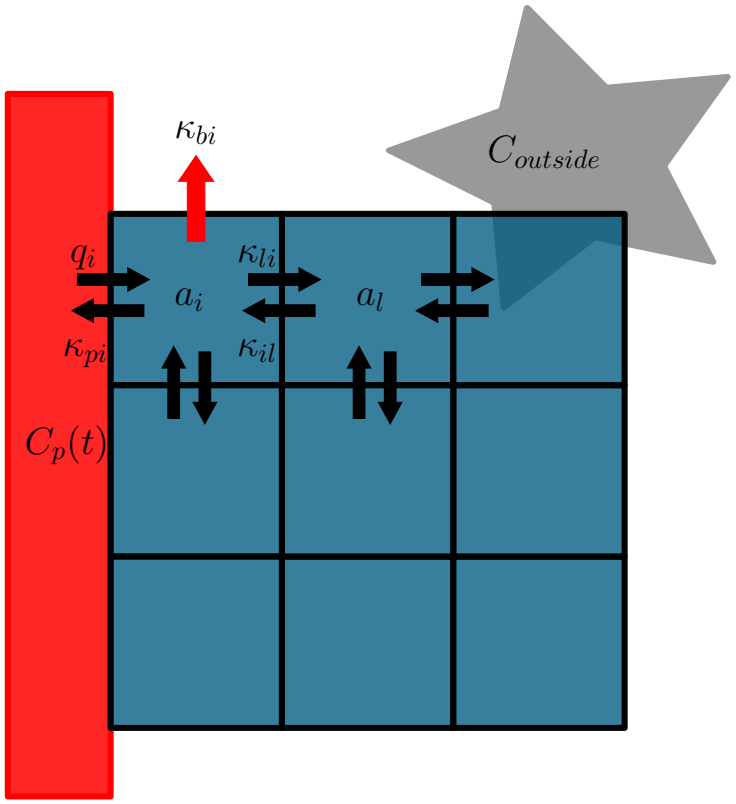

Figure 9.2: *Including the plasma compartment into the simple two compartment model.*

Solving Equation (9.6) gives

$$A(t) = e^{Kt} \int_0^t C_p(\tau) e^{-K\tau} d\tau \cdot \vec{Q}. \tag{9.7}$$

The plasma concentration, C_p, can be assumed to be decomposable [31] to $C_p = \sum_{i=1}^{m} b_i e^{-\beta_i t}$ where the β_i are real, non-negative and arranged in decreasing order (i.e. $\beta_1 > \beta_2 > ... > \beta_m \geq 0$). Rearrangement gives then

$$A(t) = e^{Kt} \sum_{i=1}^{m} b_i \int_0^t e^{-\beta_i \tau} e^{-K\tau} d\tau \cdot \vec{Q}. \tag{9.8}$$

Remembering the properties of K, namely the fact that the main diagonal elements are smaller than zero, while the off-diagonal elements are larger than zero shows that K is a matrix with a dominant main diagonal. According to [119], the matrix is non-singular and the eigenvalues of such a matrix have non-positive real parts. The diagonalisation of K gives $PKP^{-1} = D =$

$\mathrm{diag}(\lambda_1, ..., \lambda_n)$ with $\lambda_i = \alpha_i + i\gamma_i; \quad \alpha_i \leq 0 \ \ \forall i$. Then

$$\begin{aligned}
A(t) &= e^{Kt} \sum_{i=1}^{m} \int_0^t b_i e^{-\beta_i \mathbb{1} \tau} e^{-K\tau} d\tau \vec{Q} \\
A(t) &= P^{-1} e^{Dt} \sum_{i=1}^{m} b_i \int_0^t e^{-\beta_i \mathbb{1} \tau} e^{-D\tau} d\tau P \cdot \vec{Q} \\
A(t) &= P^{-1} e^{Dt} \sum_{i=1}^{m} b_i \int_0^t e^{-(\beta_i \mathbb{1} + D)\tau} d\tau P \cdot \vec{Q} \\
A(t) &= P^{-1} e^{Dt} \sum_{i=1}^{m} b_i \left(e^{Dt} - e^{\beta_i t \mathbb{1}} \right) (D + \beta_i \mathbb{1})^{-1} P \cdot \vec{Q} \\
A(t) &= P^{-1} e^{Dt} \sum_{i=1}^{m} b_i e^{Dt} (D + \beta_i \mathbb{1})^{-1} P \cdot \vec{Q} - P^{-1} e^{Dt} \sum_{i=1}^{m} b_i e^{\beta_i t \mathbb{1}} (D + \beta_i \mathbb{1})^{-1} P \cdot \vec{Q}
\end{aligned} \tag{9.9}$$

Assuming $\exists q$ with $\beta + q \ll \min_i |\alpha_i|$, which is valid e.g. in the case of a constant plasma level, then the following approximation is valid:
$\exists t > t^*$ with

$$\begin{aligned}
e^{-\beta_i t} &\gg \left| e^{Dt} \right|, \\
(D + \beta_i \mathbb{1}) &\approx D, \\
\sum_{i=1}^{q-1} b_i e^{-\beta_i t} &\ll \sum_{i=q}^{m} b_i e^{-\beta_i t}.
\end{aligned} \tag{9.10}$$

Using these approximations, it follows

$$\begin{aligned}
A(t > t^*) = P^{-1} e^{Dt} \sum_{i=1}^{m} b_i \underbrace{e^{Dt}}_{\approx 0} (D + \beta_i \mathbb{1})^{-1} P \cdot \vec{Q} \\
- P^{-1} e^{Dt} \underbrace{\sum_{i=1}^{q-1} b_i e^{\beta_i t \mathbb{1}}}_{\ll \sum_{i=q}^{m} b_i e^{-\beta_i t}} (D + \beta_i \mathbb{1})^{-1} P \cdot \vec{Q} \\
- P^{-1} e^{Dt} \underbrace{\sum_{i=q}^{m} b_i e^{\beta_i t \mathbb{1}}}_{\approx C_p(t)} \underbrace{(D + \beta_i \mathbb{1})^{-1}}_{D^{-1}} P \cdot \vec{Q}
\end{aligned} \tag{9.11}$$

and finally

$$\begin{aligned}
A(t > t^*) &\approx -C_p(t) P^{-1} e^{Dt} D^{-1} P \cdot \vec{Q} \\
&\approx -K^{-1} \vec{Q} C_p(t).
\end{aligned} \tag{9.12}$$

There exists a time $t > t^*$, where the system approaches a steady-state (e.g. if C_p is constant ($\beta_i = 0 \ \forall i$)). Then the amount of solute in each component of the exchangeable region (blue in

Figure 9.2) will "follow" the plasma concentration [32].

9.2.1.3. The Complete Patlak Model

Considering the complete Patlak model (Figure 9.3) now, the total amount of solute is denoted with A_m and it is given by:

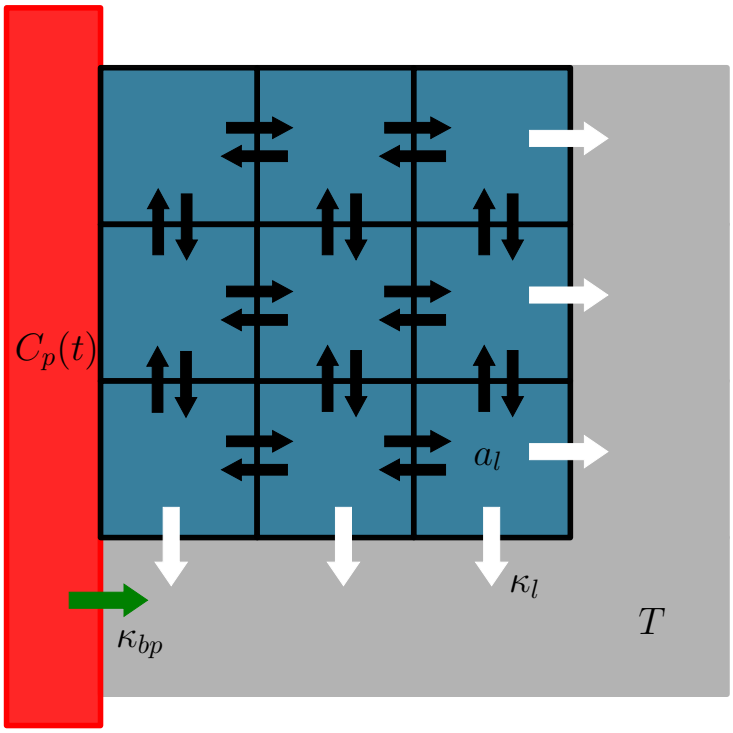

Figure 9.3: *Sketch of the complete Patlak model.*

$$\begin{aligned} \frac{dT(t)}{dt} &= G \cdot A(t) + k_{bp} \cdot C_p(t) \\ G &= \begin{pmatrix} k_1 & 0 & 0 \\ 0 & \ddots & 0 \\ 0 & 0 & k_n \end{pmatrix} \\ U_n &= \begin{pmatrix} 1 & \dots & 1 \end{pmatrix} \\ A_m &= U_n A(t) + T(t) + V_p C_p(t) \end{aligned} \tag{9.13}$$

This model is valid under the following assumptions [32]:

- single source (e.g. plasma) of the test solute (denoted with p)
- the solute concentration in the plasma, C_p, may vary with time

- rapid exchange of the solute between plasma and the reversible tissue region (denoted with r) with n compartments
- the solute can enter another tissue region, named the bound (b) or irreversible region, but it cannot leave this kind of tissue.
- there is no other "place to hide" for the solute than the three kinds of compartments
- first order kinetics are assumed, denoted with the exchange rates k_{il}
- the system is not altered by the solute
- metabolisation of the solute only occurs within the bound region
- in the beginning, the solute is only in the plasma.

Solving Equation (9.13) gives:

$$\begin{aligned} A(t) &= e^{Kt} \sum_{i=1}^{m} \int_0^t b_i e^{-\beta_i \mathbb{1} \tau} e^{-K\tau} d\tau \vec{Q} \approx -K^{-1} \vec{Q} C_p(t) \\ T(t) &= U_n G \int_0^t e^{Kt} \int_0^\tau C_p(\vartheta) e^{-K\vartheta} d\vartheta d\tau \vec{Q} + k_{bp} \int_0^t C_p(\tau) d\tau. \end{aligned} \tag{9.14}$$

Integrating by parts and rearrangement leads to:

$$A_m(t) = \left(-U_n G K^{-1} \vec{Q} + k_{bp}\right) \int_0^t C_p(\tau) d\tau + U_n \left(G K^{-1} + \mathbb{1}\right) A(t) + V_p C_p(t). \tag{9.15}$$

Defining the "rate of uptake for a constant plasma level", $K_i = U_n K^{-1} \vec{Q} + k_{bp}$, gives

$$A_m(t) = K_i \int_0^t C_p(\tau) d\tau + U_n \left(G + K\right) K^{-1} A(t) + V_p C_p(t). \tag{9.16}$$

Defining the "steady-state-space" of a region, $\mathbf{space}(A^{SS})$, as the ratio of the amount of solute in an exchangeable region relative to a constant plasma level as:

$$\mathbf{space}(A^{SS}) := \frac{\sum_{i=1}^{n} a_i}{C_p^{constant}} = U_n A \tag{9.17}$$

and the "space" of a region $\mathbf{space}(A)$ as the steady-state-space for that region, if all of the κ_{bi} values are zero (A_0).
Determining A_0:

$$\frac{dA_0}{dt} = K(\kappa_{bi} = 0) A_0 + \vec{Q} C_p \tag{9.18}$$

and remembering $\kappa_{ii} = \frac{-\left(\sum_{l=1}^{n} \kappa_{li}+\kappa_{bi}+\kappa_{pi}\right)}{p_i} \leq 0$ as well as $G = \begin{pmatrix} k_1 & 0 & 0 \\ 0 & \ddots & 0 \\ 0 & 0 & k_n \end{pmatrix}$ leads to

$$K(\kappa_{bi} = 0) = K + G \tag{9.19}$$

Thus, for the steady-state, where C_p is constant

$$\begin{aligned} A^{SS} &= -K^{-1}\vec{Q}C_p \\ A_0^{SS} &= -\left(K+G\right)^{-1}\vec{Q}C_p \\ &\Rightarrow -\vec{Q}C_p = KA^{SS} = -\left(K+G\right)^{-1}A_0^{SS} \\ &\Rightarrow (A - A_0) = \underbrace{\underbrace{K^{-1}}_{<0}\underbrace{GA_0}_{\geq 0}}_{\leq 0} \\ &\Rightarrow A \leq A_0 \end{aligned} \tag{9.20}$$

one can conclude

$$\begin{aligned} A_0 &\geq A \\ \Rightarrow \mathbf{space}(A) &\geq \mathbf{space}(A^{SS}) = \frac{U_n A^{SS}}{C_p}. \end{aligned} \tag{9.21}$$

This makes sense: if nothing can leak out into the bound region ($\kappa_{bi} = 0$) then the amount of solute in the exchangeable region is larger than if the solute can pass into the bound region. Applying some more algebra

$$\begin{aligned} \left(UK\right)_i &= -\left(\sum_{l=1}^{n} k_{li} + k_{bi} + k_{pi}\right) + \sum_{l=1}^{n} k_{il} = -(k_{bi} + k_{pi}) < 0 \\ \left(U(K+G)\right)_i &= -\left(\sum_{l=1}^{n} k_{li} + k_{bi} + k_{pi}\right) - k_{bi} + \sum_{l=1}^{n} k_{il} = -k_{pi} < 0 \\ \Rightarrow \left(UG\right)_i &= -k_{pi} - \left(UK\right)_i = k_i \end{aligned} \tag{9.22}$$

gives the following approximation for A_m:

$$A_m(t) = K_i \int_0^t C_p(\tau)d\tau + \underbrace{\underbrace{U_n\,(K+G)}_{<0}\underbrace{K^{-1}}_{\leq 0}\underbrace{A}_{\geq 0}}_{\geq 0} + V_p C_p(t).$$

$$A_m(t) = K_i \int_0^t C_p(\tau)d\tau + \underbrace{\underbrace{U_n A}_{\geq 0} + \underbrace{U_n G}_{\geq 0}\underbrace{K^{-1}}_{\leq 0}\underbrace{A}_{\geq 0}}_{\geq 0} + V_p C_p(t). \tag{9.23}$$

$$\Rightarrow U_n A \geq U_n\,(K+G)\,K^{-1}A \geq 0$$

$$\mathbf{space}(A) \geq \mathbf{space}(A^{SS}) = \frac{U_n A^{SS}}{C_P} \geq \frac{U_n\,(K+G)\,K^{-1}A^{SS}}{C_p(t)} := V_0 \geq 0$$

Finally, the working approximation for estimating the influx constant, K_i, can be derived as

$$\boxed{A_m(t > t^*) = K_i \int_0^t C_p(\tau)d\tau + (V_0 + V_p)\,C_p(t).} \tag{9.24}$$

Monitoring the amount of solute over time shows that a near steady-state distribution of the solute among the plasma and the compartment is usually rapidly achieved. If this is the case and the solute does not re-cross the barrier from the tissue back to the blood, then a straight line is visible if Equation (9.25) is plotted.

$$\frac{A_m(t > t^*)}{C_p(t)} = K_i \frac{\int_0^t C_p(\tau)d\tau}{C_p(t)} + (V_0 + V_p) \tag{9.25}$$

Fitting the linear potion of such a plot to the linear equation $y(t) = at + b$ gives the influx constant as well as a measure for the volume occupied by the contrast agent.

9.3. Applying the Patlak Model to Gd-DTPA MRI Data

MRI is the method of choice for non-invasive imaging at high resolution. Dynamic contrast-enhanced MRI (DCE) was developed in the 1990s and has been successfully employed for several applications, e.g. to measure tumour blood flow [13], brain perfusion, blood volume and the blood-brain barrier permeability [118, 14, 3, 2]. In that context, the Patlak approach can be, and has been, used for quantifying the unidirectional influx constant for low-permeating substances [32, 118]. In DCE-MRI the leakage of a contrast agent, usually Gd-DTPA, is measured quantitatively using dynamic MRI scanning, in which repeated scans are performed following a bolus injection [2].

9.3.1. The Patlak Model for DCE-MRI

Gd-DTPA is a commonly used contrast agent (CA) for MRI. It changes the relaxation rates, R_1, according to

$$R_1^{\text{with CA}} = \frac{1}{T_1^{\text{with CA}}} = \frac{1}{T_1^{\text{no CA}}} + RC(CA), \tag{9.26}$$

where R denotes the CA specific relaxivity and $C(CA)$ the concentration of the contrast agent. The relaxivity is temperature and field dependent and differs for various solutes (e.g. water, blood plasma, tissue, saline) [120, 121]. For the application of the Patlak model, it is important here, that the concentration of the agent is proportional to the change in the relaxation rates (cf. 9.3.1.2):

$$\begin{aligned} C_{tissue}(CA) &= R_{tissue}\left(\frac{1}{T_1^{\text{with CA}}} - \frac{1}{T_1^{\text{no CA}}}\right) = R_{tissue}\Delta R_1 \\ C_{plasma}(CA) &= R_{plasma}\frac{\Delta R_1}{1 - \text{Hematocrit}} \end{aligned} \tag{9.27}$$

The concentration of the contrast agent in blood plasma has to be corrected by the hematocrit[1] value, as the red blood cells do not incorporate the agent. Typical values for the specific relaxivity of plasma, R_{plasma}, at 3 Tesla are $\frac{1}{R_{Plasma}} = 3.3\frac{\text{l}}{\text{mmol s}}$ [120].
The relaxivity, $R = {}^{R_{tissue}}/_{R_{plasma}}$, as a proportionality constant can be neglected in the final Patlak equation (cf. Section 9.3.1.2). Then, the model equation reads:

$$\frac{C_{tissue}(t > t^*)}{C_{plasma}(t)} = K_i\frac{\int_0^t C_{plasma}(\tau)d\tau}{C_{plasma}(t)} + V, \tag{9.28}$$

with the following parameters:

- C_{tissue}: Tissue concentration (intra- and extra-vascular, $[C_{tissue}] = {}^{\text{mMol}}/_{\text{g}}$) of Gd-DTPA at time t.
- C_{plasma}: Arterial plasma concentration ($[C_{plasma}] = {}^{\text{mMol}}/_{\text{l}}$) at time t.
- K_i: Blood-to-brain transfer constant of the indicator (CA) ($[K_i] = {}^{\text{l}}/_{\text{s g}}$ or ${}^{1}/_{\text{s}}$, cf. 9.3.1.2).
- $V = V_0 + V_{plasma}$: Plasma volume per unit mass of tissue plus the volume of any space for which the exchange of Gd-DTPA with the plasma is rapid ($[V] = {}^{\text{l}}/_{\text{g}}$). V provides a measure for the cerebral blood volume (CBV) [118].

The transfer constant, K_i, can be obtained by two measurements: First, the acquisition of a T_1 map *prior* to the CA administration and then the acquisition of several T_1 maps at distinct

[1] The hematocrit (Ht or HCT) or packed cell volume (PCV) or erythrocyte volume fraction (EVF) is the proportion of blood volume that is occupied by red blood cells. It is normally about 48% for men and 38% for women [122].

timepoints *after* the administration of the contrast agent. To obtain the CA concentration in tissue, Equation (9.27) can be employed. For the concentration in plasma, alternatively called arterial input function (AIF), several possible approaches are utilised. They are presented in the next section.

9.3.1.1. Obtaining the Arterial Input Function

The literature describes three main approaches to obtain the AIF:

Blood sampling The AIF can be obtained by sampling arterial blood at several timepoints. Each sample can then be used to obtain T_1, e.g. by a spectroscopic measurement. This method provides a very accurate characterisation of C_{plasma}, but the drawbacks are a lower temporal resolution (in particular in animals, where the total blood volume limits the number of samples) and the fact that it is an invasive procedure.

Assume a similar AIF for all subjects This approach requires to take a blood sample from (at least) one person. The determined AIF is then used for all subjects. This method is quite simple but the drawbacks are obvious. Inter- and intra-subject variations are not considered. In particular in patients, where the vascular system might be disturbed, this method is likely to produce large errors.

Obtain AIF from the MRI data This approach gives the plasma concentration for each subject on a non-invasive basis. However, a large vessel within the FOV is required. The larger the ROI, the better the final precision. In particular in small vessels, the partial volume effect will influence the final result and the low SNR *in vivo* may give rise to a high systematic error. Furthermore, flow effects have to be considered.

9.3.1.2. A Note on the Units of a Patlak Plot

Comparing the units in Equation (9.26), one finds, that the units of C_{tissue} and C_{plasma} differ. While the plasma concentration is given in $^{\mathrm{mMol}}/_{\mathrm{l}}$, the typical tissue concentration is $^{\mathrm{mMol}}/_{\mathrm{g}}$. Although this makes sense, it might cause some confusion.
The application of Equation (9.26) on Gd-DTPA MRI data requires the knowledge of the (different) relaxivities, R_{plasma} and R_{tissue}. While the blood plasma relaxivity is well characterised, e.g. by Rohrer et al. or Pintaske et al. [120, 121], tissue relaxivity is not as well studied. However, tissue relaxivity is not mandatory for a Patlak plot. It is also valid, to use

$$\begin{aligned}\frac{C_{tissue}(t > t^*)}{C_{plasma}(t)} &= \frac{R_{tissue}}{R_{plasma}} K_i \frac{\int_0^t C_{plasma}(\tau)d\tau}{C_{plasma}(t)} + V\frac{R_{tissue}}{R_{plasma}} \\ &= \tilde{K}_i \frac{\int_0^t C_{plasma}(\tau)d\tau}{C_{plasma}(t)} + \tilde{V}.\end{aligned} \tag{9.29}$$

In that case, the units change to $[K_i]$ = a.u. $\frac{1}{\mathrm{s}}$ and $[V]$ = a.u. (e.g. [123]).
Another approach assumes the relaxivities of tissue and plasma to be equal [15, 124, 118], which implies that 1 g of tissue equals 1 ml of volume. According to Larsson and Tofts [3], this is approximately true. Under this assumption, the units are then $[K_i] = \frac{\mathrm{ml}}{\mathrm{g\,s}}$ and $[V] = \frac{\mathrm{ml}}{\mathrm{g}}$. The validity of the assumption of equal relaxivities of different tissue types is a matter of discussion since the early 1990s [3] and it is still unclear in 2011 [125]. One study, obtained by Donahue et al. [126] found no significant changes in the relaxivity in saline, plasma and cartilage. However, they reported all values as mmoles of Gd-DTPA per litre of tissue water and not per tissue volume. The water fraction of their samples was determined by comparing wet and dry weights; an approach which is highly invasive and therefore not applicable *in vivo*. As a consequence, the results cannot be transferred to *in vivo* conditions directly.
Furthermore, it is an open question, if e.g. tumour tissue obeys the same relaxivity as healthy tissue, white matter the same as grey matter etcetera. Consequently, the safe way to handle those uncertainties is to use arbitrary units for the volume, V and to scale the K_i values correspondingly to a.u. $\frac{1}{\mathrm{s}}$.

9.4. Optimisations for BBB Permeability Measurements based on the Patlak model

Application of the Patlak model on MRI data requires several steps to be performed. The post-processing chain is visualised in Figure 9.4. Compared to the first approaches, presented by Taheri et al. [15], several optimisations have been carried out in the framework of this thesis. First and most importantly, the linear part of the data have to be detected. The various approaches are summarised in Section 9.4.1. Another crucial part of the evaluation is to determine the AIF (Section 9.4.2). Further, motion correction has to be performed, as the measurements are performed over a time period of about 20 minutes (Section 9.4.3). Finally, one has to deal with noise-induced errors (cf. Section 9.4.4).

9.4.1. Finding the Linear Part of the Data

A Patlak plot shows a linear dependence if the amount of Gd-DTPA over time shows a near steady-state distribution of the CA among the plasma and the compartment and the solute does not re-cross the barrier from the tissue back to blood. Thus, the challenge is to find this linear part of the plot. The brute force method, used by Taheri et al. [15] is to fit all available data to a linear function. This might work, if the time period for data monitoring is well chosen. Furthermore, it requires that different tissue / brain regions / organs show a similar uptake behaviour of CA.

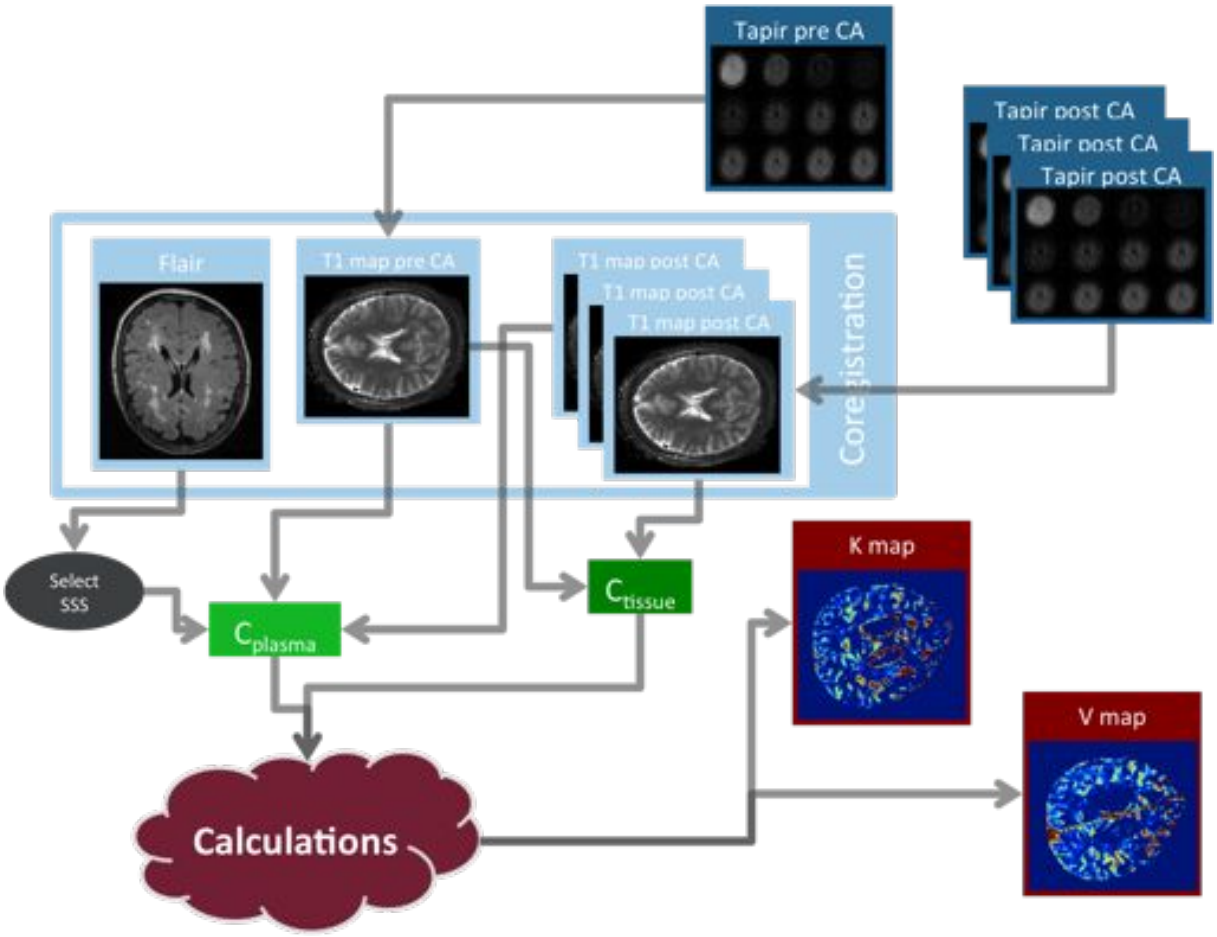

Figure 9.4: *The post-processing chain for the application of the Patlak model to TAPIR MRI data.*

However, typical Gd-DTPA MRI data are somewhat noisy, and the uptake behaviour differs in various regions (which is often the matter of interest and the reason for choosing the application of the Patlak approach) resulting in highly non-linear Patlak plots (cf. Figure 9.5). To find the linear section of this plot, three approaches were considered and compared:

9.4.1.1. Fitting all Data

In order to compare the impact of the more sophisticated methods presented subsequently, the Patlak plot was calculated using all measured timepoints without any preselection.

9.4.1.2. "Smidl Approach"

In 2008 Vaclav Smidl presented a method for a robust detection of the linear part of a Patlak plot [127]. It is based on probabilistic estimations using the Bayesian framework. Under the assumption of Gaussian noise and Bayes rule, the time bounds framing the linear part can be

estimated. An outlier reduction is also performed. The procedure is described in detail in [127].

9.4.1.3. Bravais-Pearson Correlation Coefficient

Considering two random variables X and Y with expected values μ_X and μ_Y and standard deviations σ_X and σ_Y, the empirical correlation coefficient (Bravais-Pearson correlation coefficient) is defined as:

$$\begin{aligned}\rho_{X,Y} &= \frac{\operatorname{cov}(X,Y)}{\sigma_X \sigma_Y} \\ &= \frac{E[(X-\mu_X)(Y-\mu_Y)]}{\sigma_X \sigma_Y} \\ &= \frac{\frac{1}{n}\sum_\nu (x_\nu - \bar{x})(y_\nu - \bar{y})}{\sqrt{\frac{1}{n}\sum_\nu (x_\nu - \bar{x})^2}\sqrt{\frac{1}{n}\sum_\nu (y_\nu - \bar{y})^2}}\end{aligned} \tag{9.30}$$

The correlation coefficient indicates the strength of a linear relationship between two variables. $\rho = 0$ means that there is no linear relationship between the two variables, while $\rho = 1$ can be interpreted as perfect correlation and a linear dependence between X and Y. Therefore, the Bravais-Pearson correlation coefficient can be employed as a measure for the linearity of data. One application is to find the linear part of Patlak data. The method used here is based on a sliding window technique. A window, defined by its width w_i and start position s_j, masks the Patlak data. The values for s and w are varied ($s_j, w_i; i \in \{0...(\max \text{patlak time - minwidth})\}; j \in \{\text{minwidth} \geq \cdot \text{ patlak timepoints}\}$ and the Bravais-Pearson correlation coefficient, $\rho(w_i, s_j)$, is then calculated for each dataset within the window defined by w_i and s_j. Finally, the maximum value of ρ defines the specific window used for the fitting of the Patlak data.

9.4.2. Obtaining the Arterial Input Function in Practise

In order to find the plasma concentration of the contrast agent administered, the method of using MRI was chosen. This allows one to obtain the AIF on an individual basis, a crucial point, which was highlighted by Rijpkema et al. [123]. A region of interest (ROI) containing the sinus sagittalis superior (SSS) was used to find the AIF. This approach was tested and evaluated by Ewing et al. [128], who noted that: "Approximation of the arterial input function by venous blood in the sagittal sinus is advantageous. Sagittal venous velocities are low, thus minimizing artefacts in the production of T_1 related images. The superior sagittal sinus is much larger than any cerebral artery and the blood in the central portion of the sinus can be imaged without partial volume effects. It was demonstrated that, on the time scale of our experiments, changes in R_1 are in good agreement with estimates of arterial concentration of Gd-DTPA."
The SSS can be easily detected (cf. Figure 9.8) using an MP-RAGE image post CA administration which is coregistered on the T_1 maps.
It is mandatory to choose the ROI within the SSS carefully. Usually the SSS encompasses a

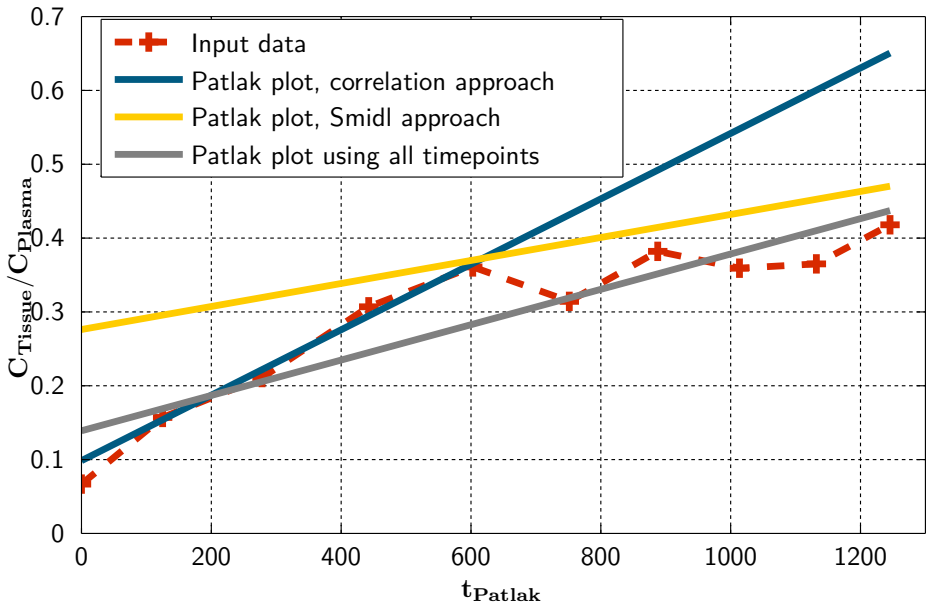

Figure 9.5: *Typical Patlak data (red) and the linear fit (blue, light blue and orange). The light blue line is the fitting result using all timepoints, the blue line used only the data within the linear window determined by the correlation coefficient. The orange line shows the result of the Smidl approach to find the linear part.*

few voxel in a calculated T_1 map with the imaging parameters chosen (cf. Section 9.6.1). As a consequence, a single voxel with a significant different signal intensity (e.g. due to partial volume effects) can spoil the shape of the AIF and noise in general might introduce wiggles in the AIF which propagate to the final permeability measurement. To keep the error attributed to this as small as possible, the mean values obtained from all voxel within the SSS was obtained. The AIF is assumed to be exponential, as it was suggested by [129][2]. Therefore, noise and partial volume effects can be reduced by fitting the AIF to

$$C_{Plasma}^{fitted} = ae^{-t/b} + c, \tag{9.31}$$

where t denotes the T_1 timepoints and the fit parameters a, b and c are obtained by a robust nonlinear fitting procedure (MATLAB (The MathWorks, Natick, USA)). c denotes the influence of noise on MRI data. The fitted AIF is then used for the final Patlak plot. Figure 9.9 shows the measured AIF and the fitted one, the influence on the final Patlak plot is displayed in Figure 9.10. The example shows, that the fitted AIF proves the smoother AIF and as a consequence, gives the better Patlak plot. Visual inspection of different points indicates that the results obtained by the fitted AIF show less outliers and therefore are more reliable than the measured

[2] Although McGrath used a biexponential model, for our purpose the monoexponential model is sufficient. The known problems of biexponential fitting (cf. 8) of noisy data are disregarded by that approach.

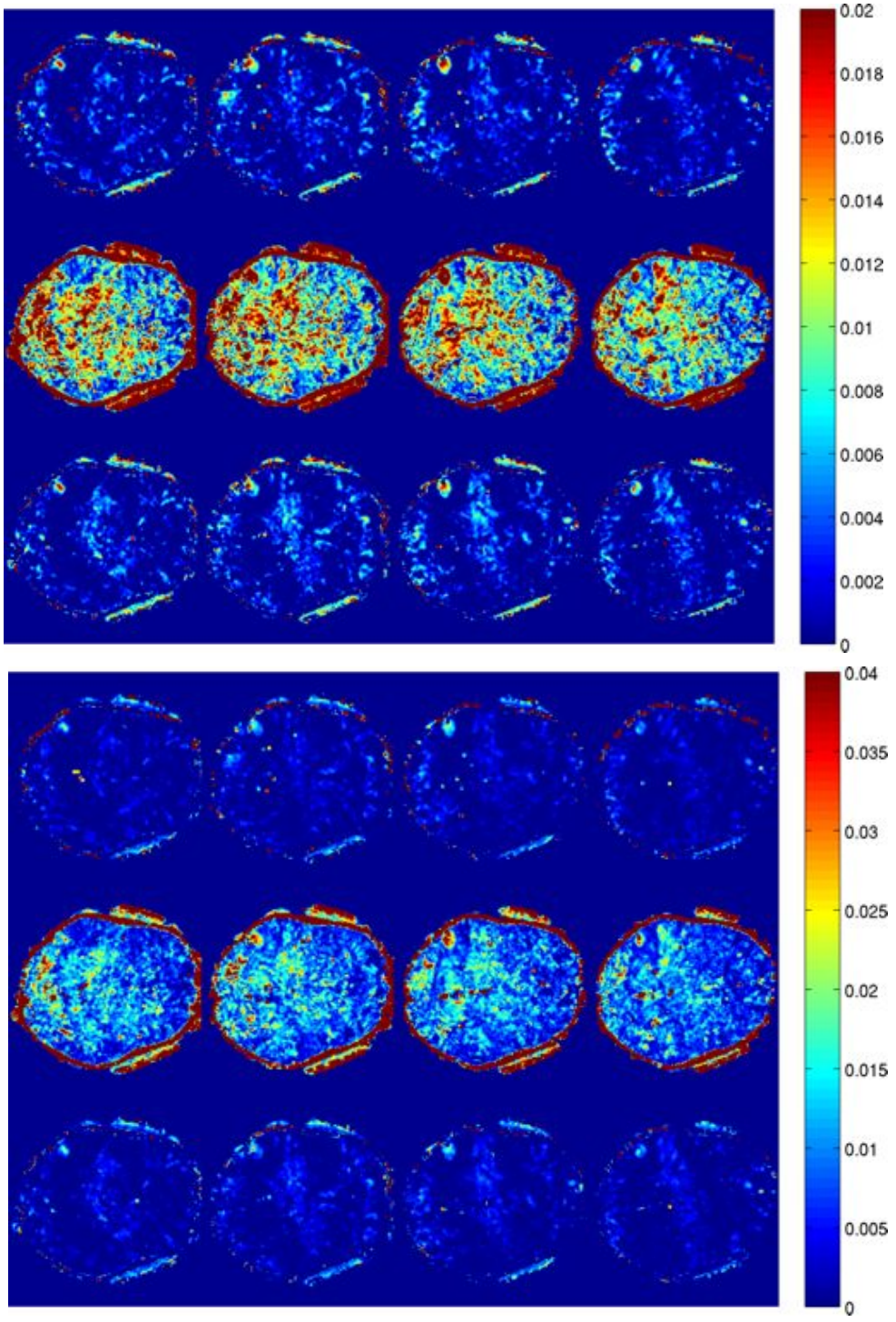

Figure 9.6: *K_i maps obtained with the three different approaches: top row using all timepoints, middle row using the correlation coefficient approach, bottom row using the Smidl approach. The two parts of the figure show the same map but they are scaled differently to visualise the differences in quantification and similarities in quality.*

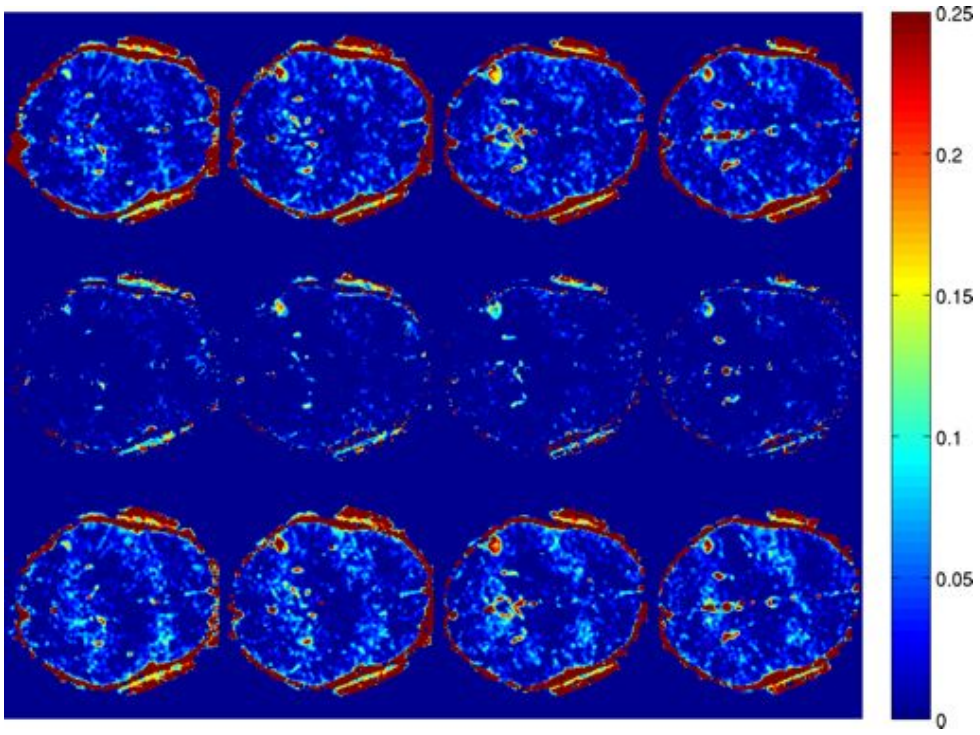

Figure 9.7: *V maps obtained with the three different approaches: top row using all time-points, middle row using the correlation coefficient approach, bottom row using the Smidl approach.*

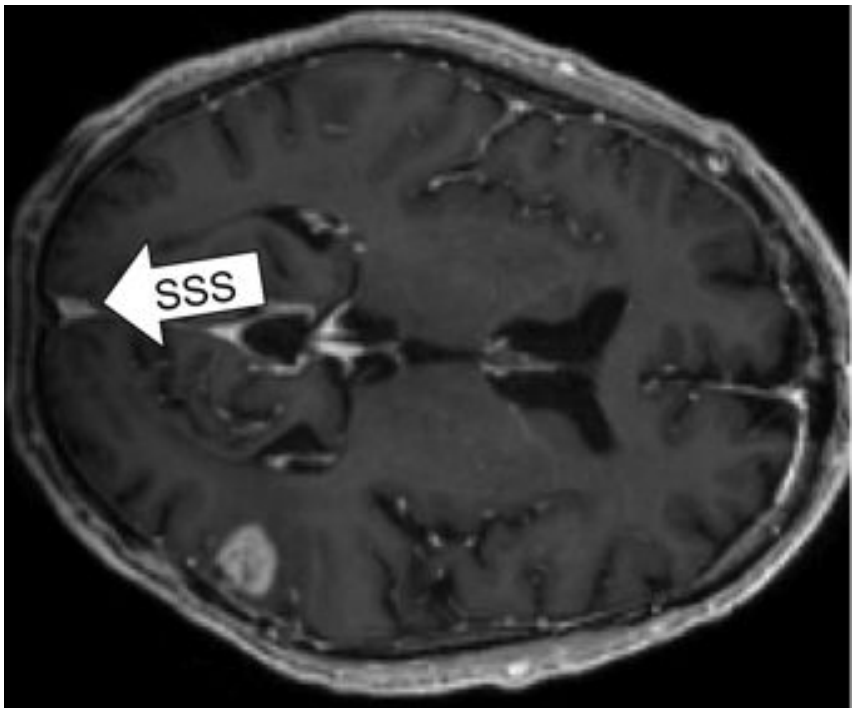

Figure 9.8: *Typical post CA MP-Rage image of a tumour patient with the SSS (arrow).*

ones, which are affected by noise.

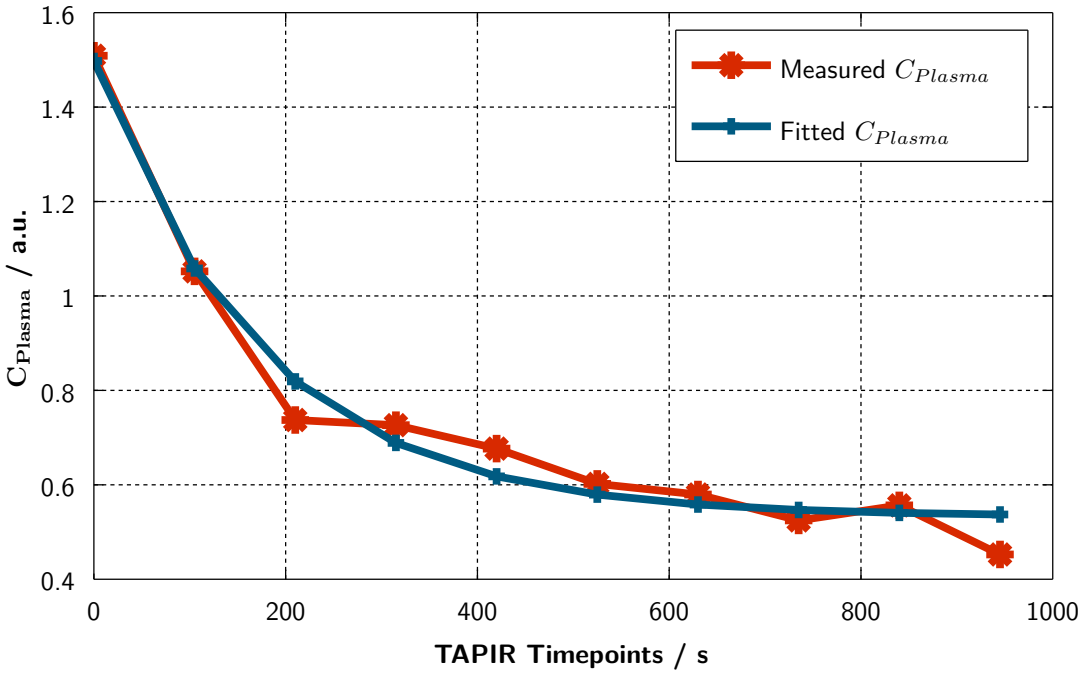

Figure 9.9: *The AIF (obtained from the SSS) is obtained by taking the average signal intensity in the SSS at all timepoints (red). The fitted AIF is shown in blue.*

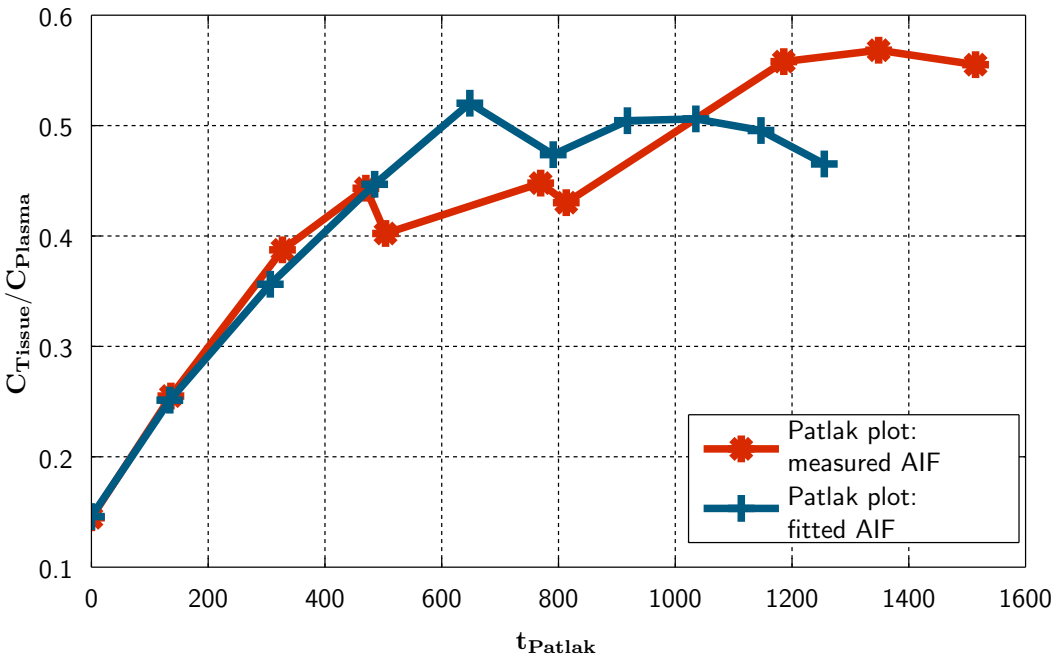

Figure 9.10: *Patlak plot obtained with the measured AIF and in comparison the Patlak plot obtained with the fitted AIF. Note that due to small variations in the plasma concentration the x and the y values change.*

9.4.3. Motion Correction and Coregistration

All obtained post CA images have to be spatially coregistered with the pre CA image. As all following calculations are obtained on a voxel-to-voxel basis, spatial alignment is mandatory. Coregistration was performed with the software package SPM8 provided by the Wellcome Trust Centre for Neuroimaging, London, UK.

9.4.4. Noise Handling and Smoothing

To reduce the influence of noise on the final permeability maps, several methods were compared. Two different types of smoothing; a Gaussian filter and a Wiener filter[3] were applied at on different stages of the evaluation. Considering the post-processing chain (Figure 9.4) shows that there are several possibilities to apply smoothing. Smoothing can be performed as follows:

- on the TAPIR data (this was excluded as smoothing prior to the fitting process distorts the T_1 estimation),
- on the T_1 maps,
- on the C_{tissue} maps,
- on the final K_i and V maps.

The different approaches were tested and compared. Figures 9.11 and 9.12 show the results. Based on comparison and visual inspection, the Wiener filter was selected to be applied on the C_{Plasma} and the final K and V maps.

9.5. Measuring the Blood-Brain Barrier Permeability: Evaluation and Comparison of MRI and PET

Measurements of the blood-brain barrier are useful for the characterisation and for the determination of disease progression (cf. Section 9.1). In 2011 Taheri et al. [15] presented a method to quantify the BBB permeability of humans *in vivo*. Their method is based on the sequential acquisition of several T_1 maps post administration of a low Gd-DTPA dose. This approach combines several benefits for the physician as well as the patient. Physicians profit from a method to obtain the BBB permeability which does not require positron emission tomography (PET) - the established method. The patients benefit from a non-invasive method without radiation

[3] A Wiener filter is a type of linear filter, which is applied to an image adaptively, tailoring itself to the local image variance. Where the variance is large, it performs little smoothing. Where the variance is small, a Wiener filter performs more smoothing. This approach often produces better results than linear filtering. The adaptive filter is more selective than a comparable linear filter, preserving edges and other high-frequency parts of an image [MATLAB]

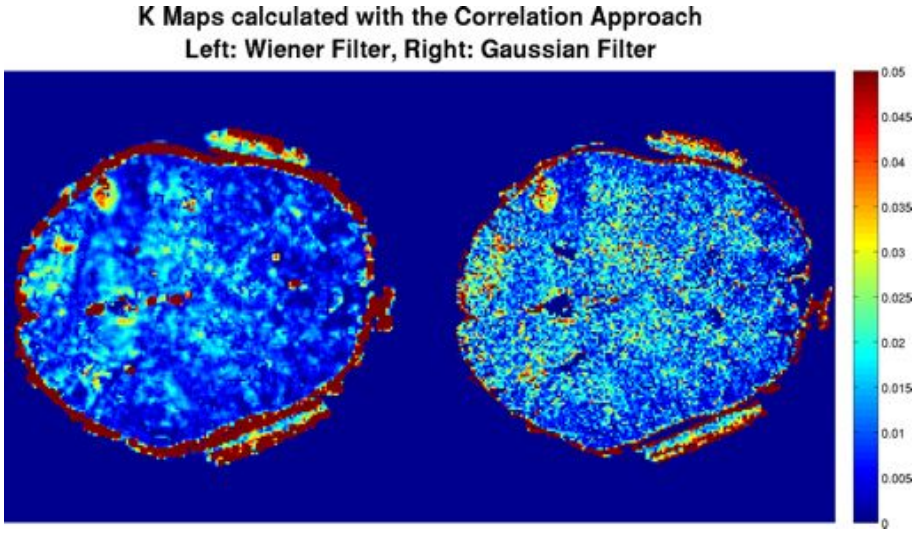

Figure 9.11: *K_i Maps of a Patlak fit, obtained with smoothing of C_{tissue} and the final K_i map.*

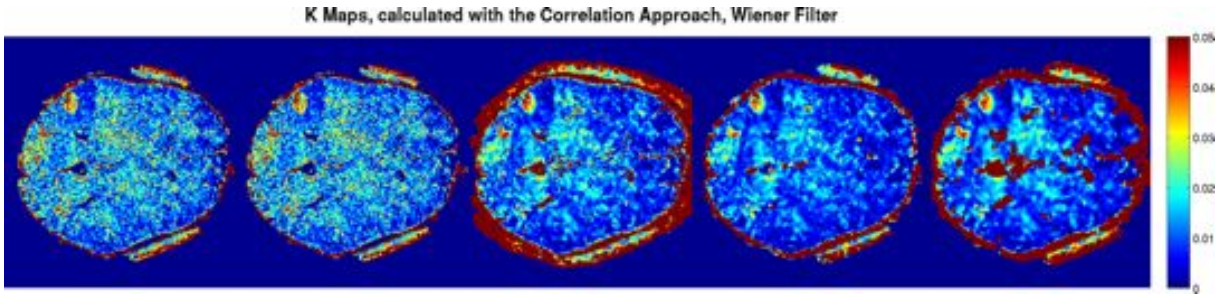

Figure 9.12: *from left to right: no filter, smoothed K_i map, smoothed T_1 and K_i map, smoothed C_{Plasma} and K_i map, smoothed T_1, C_{Plasma} and K_i and V map*

exposure as well as a lower dose (as used in normal clinical examinations) of a well tolerated contrast agent. In comparison to PET, MRI has a much higher availability as the infrastructural requirements are lower for MRI.

Permeability measurements with PET BBB permeability measurements with PET are usually obtained with Ga-68 EDTA or Rb-82. The choice of the tracer depends on the desired application, as they differ in their physical and chemical properties. However, one is not limited to the use of these two tracers. Any tracer whose uptake and delivery into brain tissue is not flow limited can act as a measure for the BBB permeability. However, a direct comparison of the permeability obtained with different methods is - due to various reasons - not possible. The BBB consists of a membrane which inhibits passage of larger particles. Besides that, the cells of the barrier actively transport metabolic products such as glucose across the barrier with specific proteins. From that it can be deduced that particles of different size or different biochemical

and physical properties are treated differently by the BBB. Whether a particle will pass the BBB depends not only on its size but also on its biochemical and physical characteristics. In addition, the results obtained from a PET scanner are influenced by the physical characteristics of the PET scanner as well as the way the study was performed and the performed steps for image processing [130]. Under some assumptions, MRI provides quantitative results in terms of e.g. mMol per gram and minute, cf. Section 9.3.1.2. However, it is an open point if these assumptions are valid. Consequently, a comparison of the BBB permeability on basis of different modalities and contrast agents is not possible in a quantitative manner. Despite these limitations, a comparison of MRI-based Patlak plot and PET images might provide valuable insight. The FET-PET measurements performed on the patients demonstrate the tumour extend but not necessarily the BBB function. So Taheri's method was adapted and improved (as described in Section 9.2) and the comparability of MRI and Patlak based estimations of the permeability, K_i, and the cerebral blood flow, V, were compared with FET-PET images. It was found that the permeability maps are in accordance with the FET-PET images for the glioblastoma while the patient with an astrocytoma shows no increased permeability within the tumour. Additional information can be gathered by looking at the blood volume maps.

9.6. Application: Measuring the Blood-Brain Barrier Permeability in Tumour Patients

For the assessment of the potential benefit of obtaining the blood-brain barrier permeability by means of a Patlak plot, 4 patients (male 3, female 1, age = 56 ± 16 years) suffering from different kinds of brain tumours were recruited. They underwent a FET-PET scan as well as a MRI acquisition with contrast agent administration.

9.6.1. Methods

The applicability of the Patlak method for measuring the blood-brain barrier was evaluated in tumour patients. MRI based Patlak plots were compared to a FET-PET scans .

9.6.1.1. Subjects

The different subjects were:

G1 Male, 74 years old, glioblastoma grade IV, imaged after tumour resection and chemotherapy.

G2 Male, 62 years old, oligodendroglioma grade II, images after tumour resection, radiotherapy and chemotherapy.

A1 Female, 54 years old, astrocytoma grade II, imaged after biopsy.

A2 Male, 34 years old, anaplastic astrocytoma grade II, imaged after surgery and chemotherapy, suspect of recurrence.

9.6.1.2. MRI Acquisition and Sequence Parameters

Written informed consent was obtained from all subjects prior to the scan. All MRI measurements were obtained on a 3T Tim Trio MR system, equipped with a BrainPET insert[4] as well as an eight channel receive and birdcage transmit coil (Siemens AG, Erlangen, Germany). Following conventional T_1- and T_2-weighted imaging, Gd-DTPA (Dotarem, Guerbet GmbH, Sulzbach/Taunus, Germany) was administered by a rapid intravenous bolus injection (15 ml, 0.5 M, 2.5 ml/s) using a Spectris MR injection system (Medrad, Inc.). The total acquisition time was about 45 minutes and consisted of a pre and two post contrast administration parts. The protocol pre CA included:

- Scout scan
- T_2 weighted images
- anatomical images (MP-RAGE) prior to CA
- T_1 map obtained with the TAPIR sequence
- Inversion efficiency mapping required for the T_1 fitting

Then 0.025 mmol / kg(Body weight) Gd-DTPA were injected by pump as a rapid intravenous bolus. This was followed by the acquisition of

- 10 TAPIR T_1 maps,

total duration of 15:30 min, the imaging parameters are listed in Table 9.1. These measurements provide the basis for the Patlak plots. Then a second dose of 0.075 mmol / Kg Gd-DTPA was injected and the third part consisting of

- anatomical images (MP-RAGE) post CA

was obtained.

[4]The BrainPET insert was within the scanner bore, but not used for the PET measurements.

TAPIR Sequence Parameters	
TR	23.1 ms
TE	11.7 ms
TI	20 ms
Flip Angle	30°
τ	2.4 ms
Bandwidth	495 Hz / Pixel
in plane resolution	1.14 mm × 1.14 mm
Timepoints	25
iPAT (Grappa)	2
EPI factor	5
Averages	1
Slices	6
Slice thickness	2 mm
Slice gap	100 %
Acquisition time per shot	1:33 min

Table 9.1: *TAPIR sequence parameters used for the permeability calculations. Details on the TAPIR specific parameters can be found in Section 4.3.*

9.6.1.3. PET Acquisition

The PET scans were obtained on an ECAT Exact HR+ (Siemens AG, Erlangen, Germany). Its detector is based on bismuthgermanate (BGO) scintillation crystals, the scanner has an axial FOV of 15.5 cm and a reconstructed image resolution of approximately 6 mm. Attenuation correction, based on a transmission scan which was recorded for 10 min previous to the actual PET measurement was performed. PET data were measured in 3D mode and were Fourier rebinned into 2D data. Head motion was recorded during the study in order to allow for appropriately motion correction of the reconstructed images. Corrections for attenuation, random and scattered coincidences and decay were performed in addition. Finally, 63 images of 128×128 voxel with a size of $2 \times 2 \times 2.45\,\mathrm{mm}^3$ were iteratively reconstructed using the ECAT 7.2 software.

The patients were injected with a dose of approximately 3 MBq / kg body weight ^{18}F-FET intravenously and subsequently a list mode acquisition with a duration of 50 min was started. The data were sorted into 16 time frames, each consisted of 5×1 min, 5×3 min and 6×5 min. The mean FET-PET data acquired in the time span of 20-40 min was used for analysis.

9.6.1.4. Permeability Calculations

The Patlak model presented in Section 9.2 with the optimisation shown in Section 9.4 was applied to the TAPIR MRI data obtained. The AIF was obtained be selecting a ROI within the SSS for each slice. The images were coregistered using SPM8 or the dedicated software

package VINCI (MPI Cologne) in order to visualise different orientations. Past coregistration, the same mask was copied to all measured timepoints and the resulting AIF timecurve was fitted as described in 9.4.2.

9.6.2. Results

Subject G1 Patient G1 suffers from a grade IV glioblastoma. Four slices within the tumour area were selected, the corresponding images are shown in Figure 9.13, 9.14, 9.15 and 9.16. The MP-RAGE images obtained post CA show good enhancement within the tumour region (Figure 9.13) while the tumour is almost not visible without contrast agent. The T_1 maps with and without CA (Figure 9.14) look different but the tumour area is not as striking as in the MP-RAGE images.

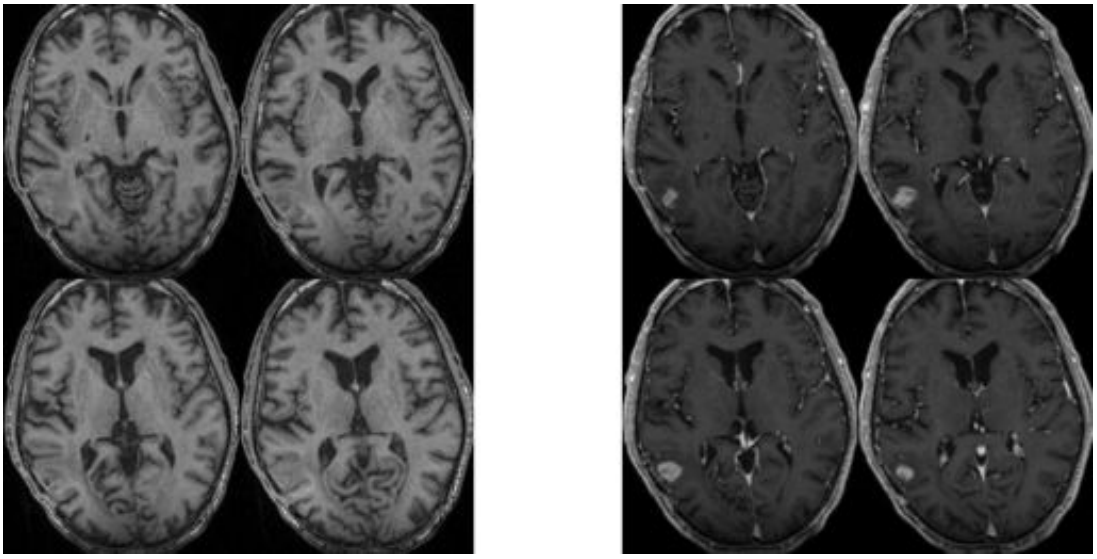

Figure 9.13: *MRI MP-RAGE images obtained from patient G1. The left image was obtained before CA administration, the right one afterwards.*

Good agreement between the permeability data and the FET-PET data was found (Figure 9.16 and 9.15). Increased permeability was detected within the tumour area. Correspondingly, the adjacent area appears less permeable since higher contrast agent accumulation within the tumour leads to less accumulation in the surrounding tissue. The maps visualising the cerebral blood flow, V, show that the tumour is better perfused than the surrounding tissue.

Subject G2 The second glioma patient, G2, shows FET uptake within a large region close to the SSS (Figure 9.17, top right). The corresponding hyperintense area in the post contrast MP-RAGE image (Figure 9.17, bottom right) appears much smaller compared to the PET result. The Patlak results suggest that the tumour area has an increased blood volume (Figure 9.17,

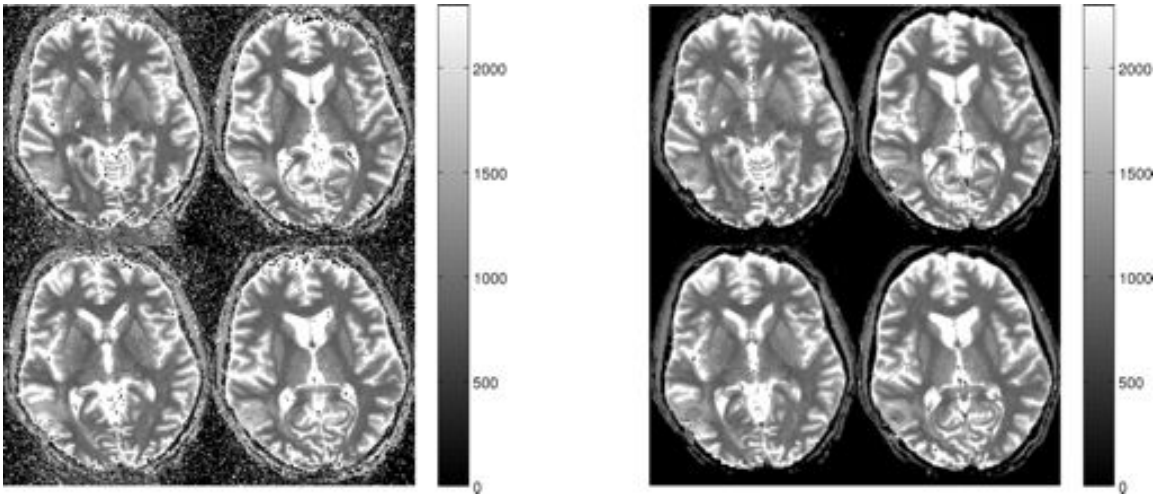

Figure 9.14: *T_1 maps (left pre CA, right post CA) obtained from patient G1.*

bottom left), the permeability is high within WM and even higher within the suspected tumour area (Figure 9.17, top left). The K-map results indicate that the patient's BBB is strongly disrupted.

Subject A1 Patient A1, who has an grade II astrocytoma, shows limited evidence of a BBB disruption (cf. Figure 9.18). Within the tumour, which is darker in the MP-RAGE images (bottom right, Figure 9.18) the permeability is reduced compared to the surrounding tissue. However, next to the tumour the permeability seems to be a little larger than in the residual areas of the brain. Interestingly, the FET-PET images, shown in the top right of Figure 9.18, show that the supposed tumour area estimated with the MP-RAGE images is larger than the area with increased FET uptake. The blood volume maps are even more interesting (bottom left, Figure 9.18). It appears that the area with increased blood volume and the area with the higher FET uptake add to the total dark area visible in the MP-RAGE images.

Subject A2 The second patient suffering from an astrocytoma, A2, shows a clear BBB disruption (cf. Figure 9.19, top left). The strong accumulation of the FET tracer within a smaller region of the suspected tumour area (top right in Figure 9.19) overlaps very well the CA enhanced areas in the post CA MP-RAGE images. The blood volume maps complement the PET-images as already observed in patient A1.

9.7. Discussion

Previous studies [15, 131] have already demonstrated the use of DCE-MRI along with the Patlak model as this approach allows for the evaluation of the BBB permeability. Calculations

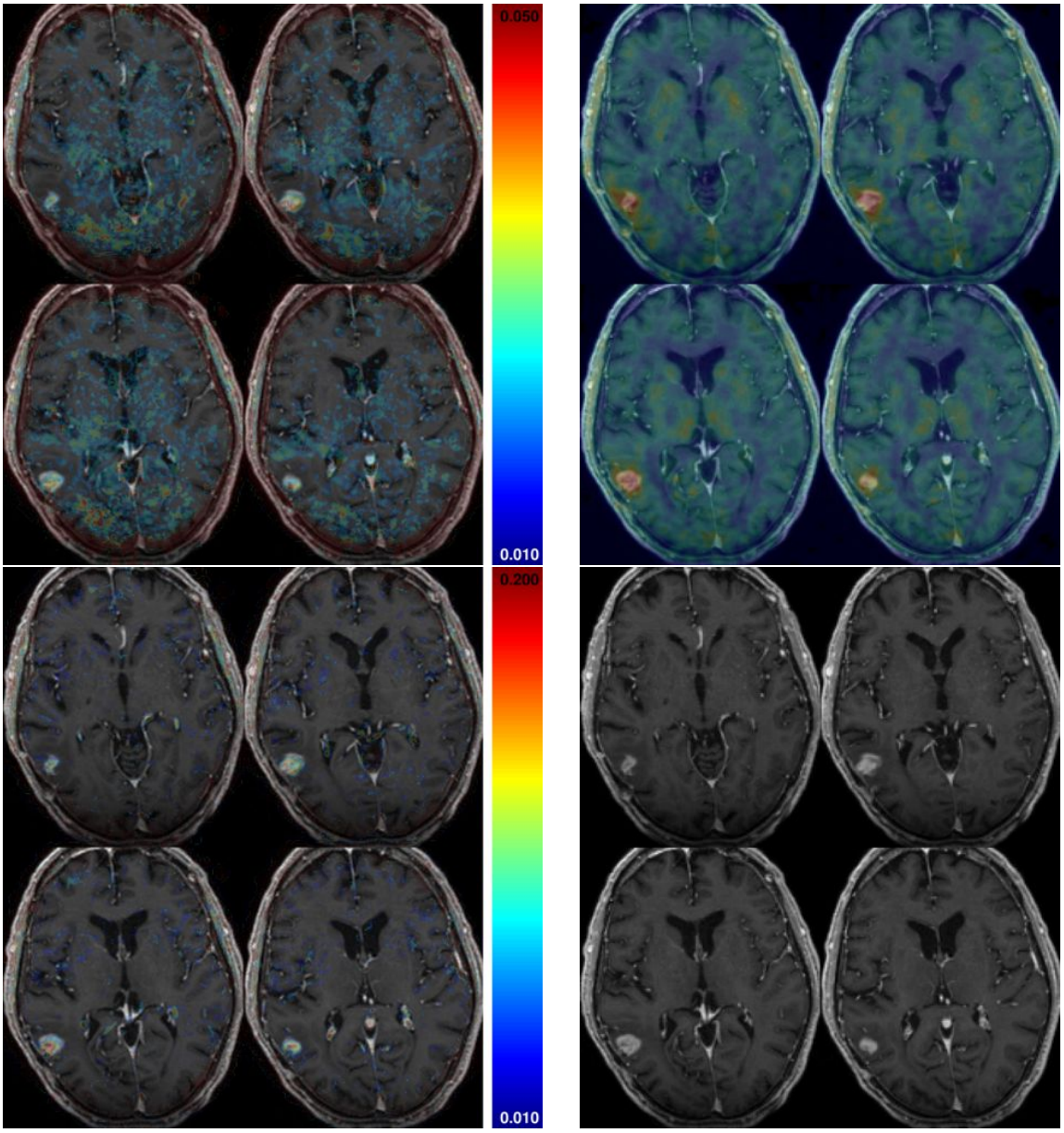

Figure 9.15: *K-map* $[^{ml}/_{g\ min}]$*, FET-PET, V-map* $[^{ml}/_{g}]$ *and MP-RAGE images of Patient G1.*
Top left to bottom right: Overlaying the permeability map on the post CA MP-RAGE images, FET-PET image over the post CA MP-RAGE image, V map on the post CA MP-RAGE and the MP-RAGE image without any overlay.

of the BBB permeability based on quantitative T_1 maps rather than on T_1-weighted images benefits from its independence of the sequence parameters and the results are not influenced by transmitter and receiver inhomogeneities. The method allows for a dense and long time course of measurements and this enables the detection of subtle abnormalities in the BBB [15]. In addition, patients benefit from a lower dose of Gd-DTPA compared to conventional DCE-MRI.

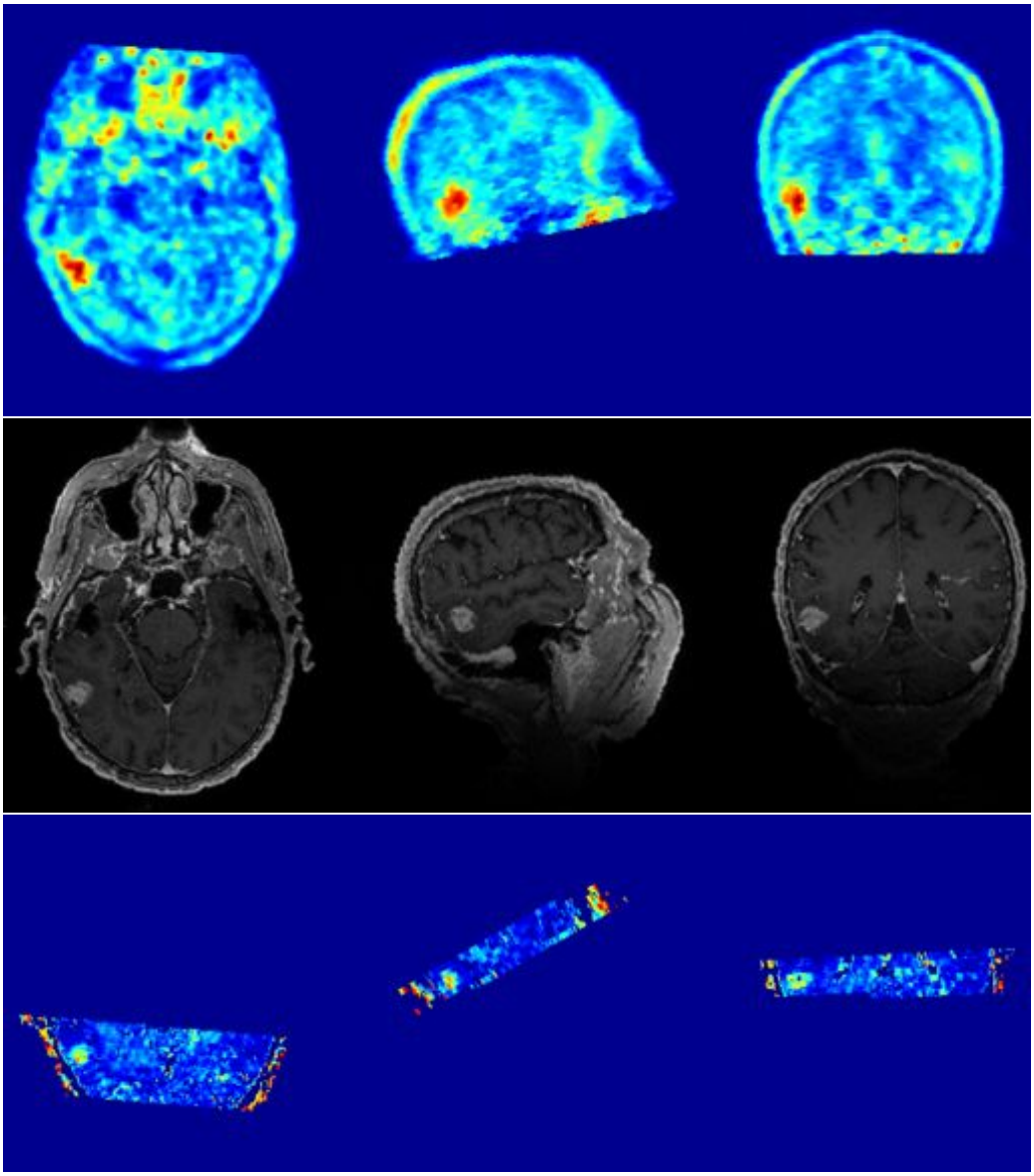

Figure 9.16: *BBB permeability measurements results from subject A. Top to bottom: FET-PET image, post CA MP-RAGE image, permeability (K) map, centred at the tumour position.*

The method presented in [15] and [131] has two weaknesses. First, *all* available data points are used for the estimation of the permeability. The Patlak method, however relies on the *linear* part of the so called Patlak plot. An additional error is introduced, if all data points are used for the fitting procedure and the consequences thereof cannot be neglected. Second, the AIF was determined from the time course of the signal change in *one pixel* containing the SSS [15]. The statistics and consequently the method will clearly improve if several voxel within the SSS are used for the estimation of the AIF.

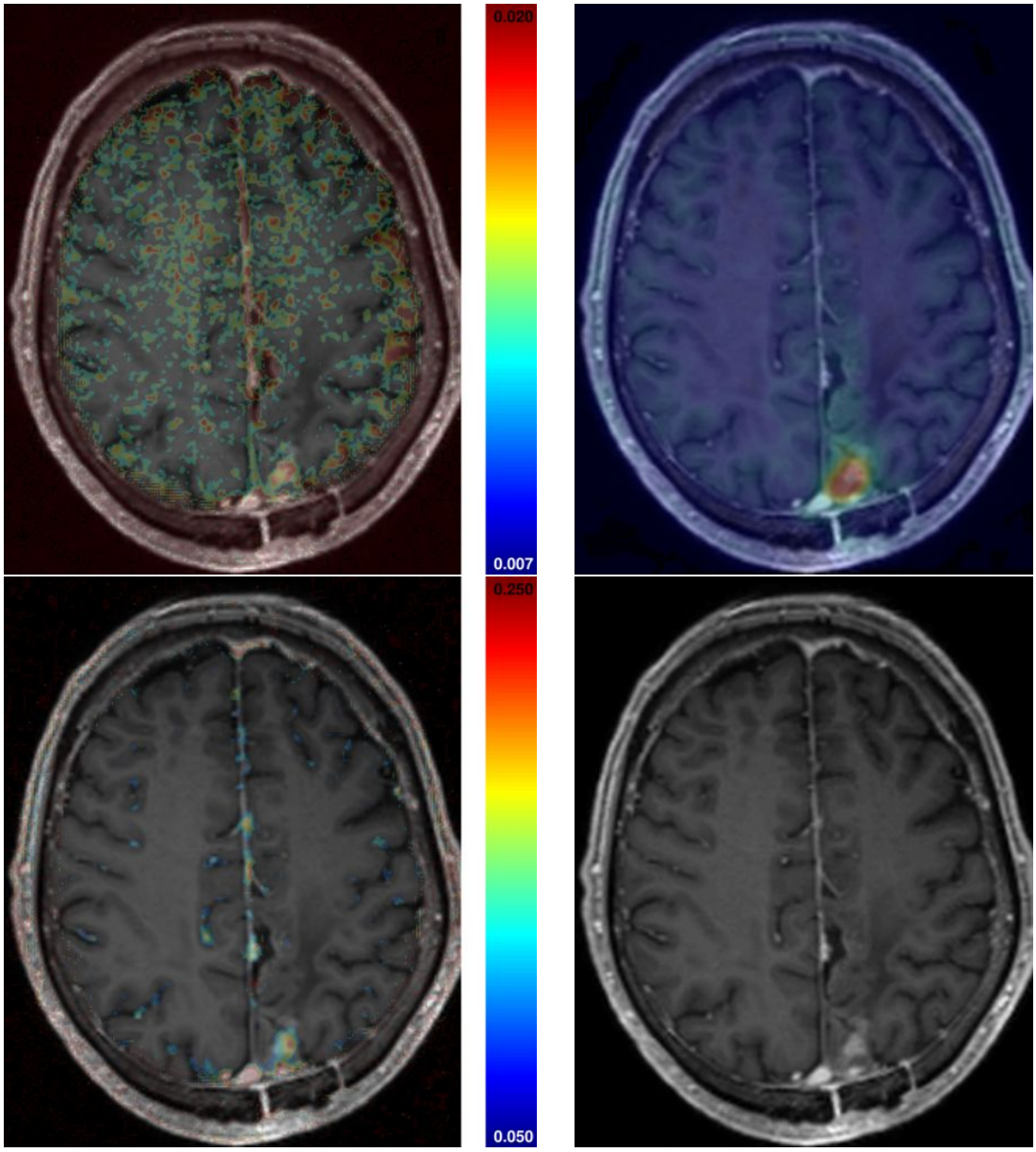

Figure 9.17: *Overlaying the Patlak results with the post CA MP-RAGE images of patient G2. Top left to bottom right: K-map* $[^{ml}/_{g\ min}]$*, FET-PET, V-map* $[^{ml}/_{g}]$ *and MP-RAGE, post CA.*

9.7.1. Optimisation of the Method

Within this study, further improvements and additional emendations were included. Optimisation of the TAPIR sequence and a careful choice of sequence parameters allows for the acquisition of 10 rather than 7 timepoints (as done in [15]). This gives a more reliable fit, in particular in the presence of noise, which is necessary for *in vivo* measurements. The single T_1 maps were acquired faster (acquisition time 1:33 min per T_1 map), this gives rise to a higher temporal res-

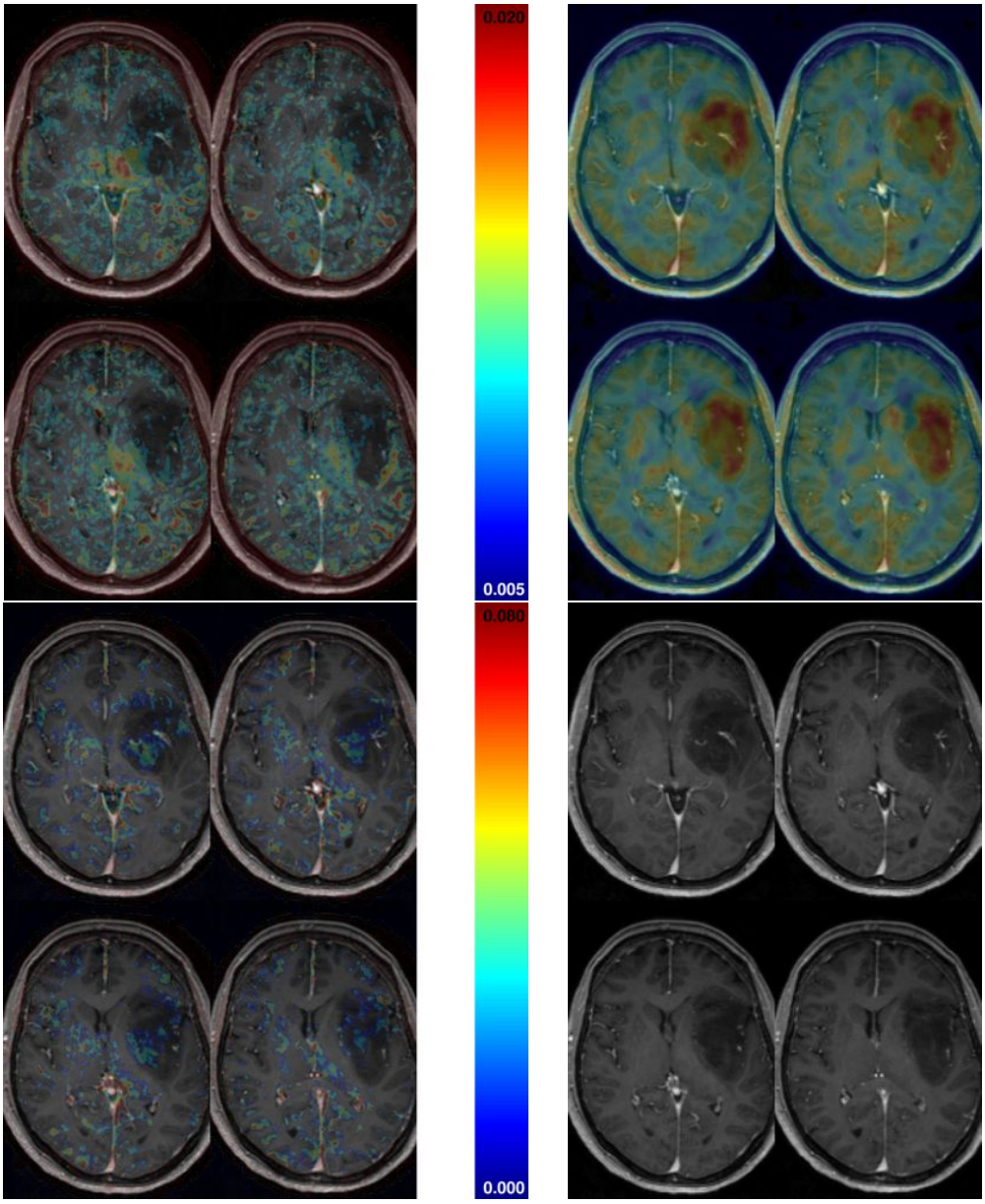

Figure 9.18: *Overlaying the Patlak results with the post CA MP-RAGE images of patient A1. Top left to bottom right: K-map [ml/g min], FET-PET, V-map [ml/g] and MP-RAGE, post CA.*

olution and thus even faster leakage rates can be assessed. Even more important, the AIF was estimated based on several voxels per timepoint (usually about 8) and fitting the AIF to the measured data gives a smooth, optimised shape of the AIF. The linear part of the Patlak plot was detected carefully by employing the correlation approach. As shown in Figures 9.5, 9.6 and 9.7, the results are qualitatively comparable but the usage of only the linear part data has a strong impact on the quantity of the K maps. Bearing in mind that the quantification relies on the assumption that tumour tissue obeys the same relaxivity as healthy tissue, white matter

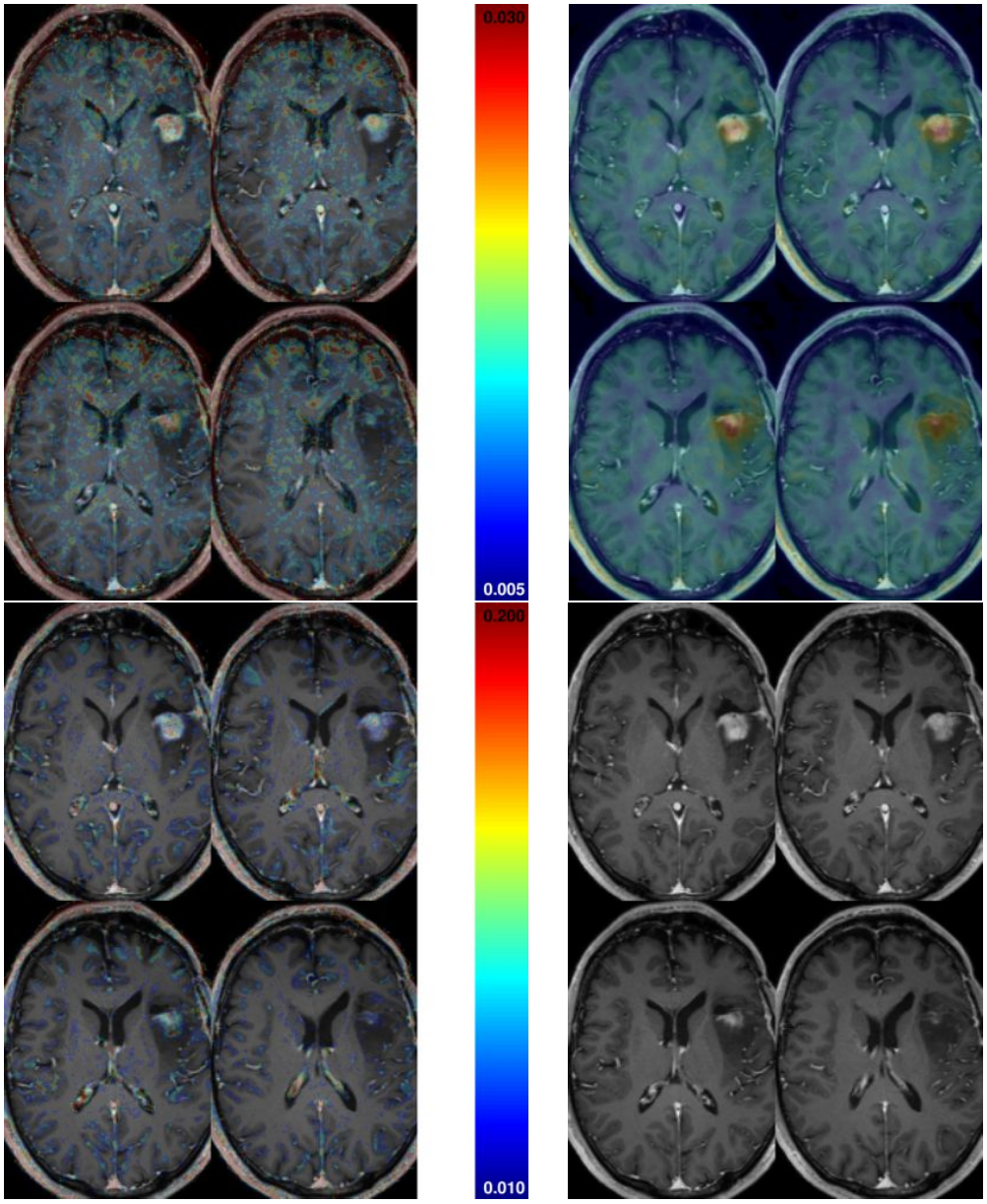

Figure 9.19: *Overlaying the Patlak results with the post CA MP-RAGE images of patient A2. Top left to bottom right: K-map [$^{ml}/_{g\ min}$], FET-PET, V-map [$^{ml}/_{g}$] and post CA MP-RAGE.*

the same as grey matter etcetera, future studied are desired to evaluate, whether this statement holds true as well as the general question whether quantitative K-maps (under consideration of the specific relaxivity) are superior to K maps based on quantitative T_1 maps but neglecting the particular relaxivity (cf. Section 9.3.1.2).

9.7.2. Measuring the Blood-Brain Barrier Permeability: Evaluation and Comparison of MRI and PET

The results presented here indicate that some tumour types might benefit from an additional measurement of the BBB permeability. In particular, the astrocytoma patients benefits from additional information arising from the TAPIR measurements. The reduced permeability within the FET accumulated astrocytoma region confirms, that the FET-accumulation within the tumour does not originate from a BBB disruption [132]. In addition, glioma patients might benefit from additional permeability measurements. Compared to the PET scans, the MR based permeability measurements allow for a higher resolution; this is of value for differential diagnosis as well as to guide stereotactic biopsy. Additional information about blood volume might as well be beneficial for therapy as well as surgery planning.

Results of the permeability measurements within GM and the outer brain regions should be evaluated with caution and with due consideration of partial volume effects.
Some drawbacks of the method have to be noted. It is quite common that tumour tissue has larger T_1 values than the surrounding (WM) brain tissue. One should be aware that the fast TAPIR method was optimised for WM/GM. Thus, the method is not as precise for T_1 values larger than 1500 ms as for the common WM values around 900 ms [74][5]. In principle, higher resolution could be achieved by paying the price of longer measurement times. This involves either longer acquisition times or the acquisition of less sampling points. Further investigations are necessary to find the optimal balance between number of sampling points, number of acquired TAPIR timepoints, resolution and the slices acquired. All these parameters influence the acquisition time and have an impact on the final result. Hence, a careful evaluation of the parameters leading to the best and most accurate results is desired.

Further investigation, in particular long-term follow-up studies of the same patient as well as larger clinical studies are desired in order to provide new insights into the general benefits of the method presented for the patients and the diagnosis.

[5] This limitation can be overcome by using larger τ values, but this prolongs the acquisition time

10. Summary, Conclusions and Outlook

A number of aspects of mapping the longitudinal relaxation time, T_1, in the presence of magnetisation transfer were analysed in this work. The presented simulation framework (jemris MT, Chapter 6) allows one to explore MT effects on any MRI sequence. The simulations were confirmed by phantom and *in vivo* measurement but also issues of MT, which are not amenable to measurements, can be investigated. Thus, jemris MT gives rise to various applications, not only for T_1 mapping but also for other quantitative and non-quantitative methods. For example, it offers the possibility to include, and thus, to understand, MT effects in other MRI methods, such as diffusion imaging or arterial spin labelling. Another application is the optimisation of protocols for MT contrast imaging. By means of simulations, changes in contrast due to MT can be evaluated in detail and one can control any single sequence as well as any sample parameter and thus, the consequences of variations thereof can be assessed.

In the first part of the thesis (Chapter 5) the problem of T_1 quantification in the presence of MT was specified. The important aspect here was the separation of two main approaches, which were both treated in this thesis (cf. Chapter 5, 7 and 8) as well as the separate issue of saturation effects. These are commonly discussed issues in the realm of the MT effect. One can conclude that the longitudinal relaxation is indeed influenced by magnetisation transfer effects. However, it depends on the sequence, its parameters and the evaluation of the data how strong the effect alters the effective T_1 values. Careful consideration of MT saturation does not change the estimated T_1 value at all. It was shown in Section 7.2 that the effects of saturation pulses on the $T_1^{observed}$ values do not affect the longitudinal recovery but instead lead to different initial conditions of the equations. If these are considered correctly, the resultant $T_1^{observed}$ value is the same with and without saturation.

For the first T_1 quantification approach, "mapping the MT relaxation times with modified signal equations", a set of signal equations, describing the behaviour of the longitudinal magnetisation component in the presence of MT was derived (cf. Section 5.2). Dependencies between the sample parameters and the longitudinal recovery are complex and non-intuitive. In the MT case, the longitudinal relaxation time is no longer monoexponential and the observed recovery rate has contributions of many different sample parameters, such as the T_1 values of the single

pool, the size of the pools and the exchange rates. The multiexponential nature of the recovery propagates to the signal equations used for T_1 quantification and the observed recovery time, $T_1^{observed}$, is shorter than the largest single pool T_1 (cf. Section 7.1). As these equations are far too complex and have too many free parameters for a potential *in vivo* application, the second approach, namely "standard T_1 mapping, neglecting the influences of MT" becomes important. The consequences for the quantification thereof were assessed (cf. Chapter 8). In particular, neglect of MT effects on the estimated T_1 values were studied (cf. Chapter 8.1) by simulations with and without the MT effect. The simulations showed that inversion recovery based methods give T_1 estimations of high accuracy (better than 2%) and precision (better than 5%), even in the presence of MT. However, this high accuracy can only be achieved if MT is considered either by biexponential fitting or - more reliably - by neglecting very short inversion times ($<$ 80ms). The choice of the inversion time is of vital importance for inversion recovery sequences. On the contrary, T_1 mapping techniques employing the spoiled gradient echo are less accurate and show worse precision than the inversion recovery methods, especially if only few sample points are considered. In fact, the precision was found to be worse than the error arising from the neglect of MT. Finally, as a good compromise between precision and acquisition time, the Look-Locker based method was evaluated. The method is well suited for *in vivo* applications and the estimated T_1 values showed a strong dependence (in the presence of MT effects) on the sequence parameters used. This parameter dependence has been analysed in detail by simulations and the results were confirmed *in vivo* (cf. Section 8.2). It was discovered that in the presence of MT, the fitted T_1 values obtained from the Look-Locker approach depend strongly on the inversion time used in the acquisition. For very short inversion times, the bound pool impairs the observed T_1 values while its influence has strongly decreased for longer inversion times. In conjunction with these simulations it was demonstrated that a controlled variation of the inversion time gives rise to a novel method of MT quantification, i.e. to estimate changes in the exchange rate as well as the T_1 values of the bound and free water pool in tissue undergoing MT. Although this new method, the TAPIR TI approach, does not quantify all MT sample parameters, this approach has the advantage of a 3-parameter fit to reveal some MT properties of the sample, instead of fitting 7 or more parameters simultaneously or successively as is the case in common MT quantification approaches. The method is based on small changes in the fitted T_1 values and hence requires a T_1 mapping method of high accuracy and precision while short acquisition times are a prerequisite for *in vivo* measurements. Thus the TAPIR method is the method of choice for this particular application. The simulation results were successfully validated by *in vivo* measurements on 10 volunteers and thus the experimental feasibility of the method was proven. However, as with every new method, careful testing of the stability, reproducibility as well as on the gain of the information achieved through by this approach is necessary. Thus,

the method should be tested first on a larger group of healthy volunteers before application in patients suffering from diseases where changes in the MT effect are pronounced, e.g. in multiple sclerosis.

The thesis closes with an application for T_1 mapping, where T_1 quantification is employed to measure the permeability of the blood-brain barrier as well as the blood volume (cf. Chapter 9). The results were compared to FET-PET data. Good agreement between the two methods was found for the tumour patients suffering from a glioma, while the results of the astrocytoma patients are diverse. It was shown that the method gives additional insight into the blood-brain barrier permeability in brain tumour patients but further investigations are needed to establish the method as a standard method for clinical diagnostics.

A. MT Presaturation on Resonance

To use on resonance presaturation pulses, *zero flip angle pulses* or *transparent pulses* are used. To understand the concept behind this, the modified Bloch equations (3.8) have to be solved. Then the effects of MT exchange on both pools during RF irradiation can be understood [61]. The exchange time constants are usually at least one order of magnitude larger than a typical RF pulse, therefore the chemical exchange process does not affect the system during excitation. Assuming $M_{xy} = 0$ as initial condition and neglecting the chemical exchange process, T_1 recovery and off resonance effects, the M_z magnetisation in the presence of a **constant amplitude continuous RF field** is given by [133]

$$M_z = M_z(0) \cdot e^{-\frac{t}{2T_2}} \cdot \left(\cosh\left(\frac{s}{2T_2}\right) + \frac{1}{s}\sinh\left(\frac{st}{2T_2}\right)\right), \tag{A.1}$$

$$s = \sqrt{1 - 4\omega_1^2 {T_2}^2}. \tag{A.2}$$

There are two different cases to discriminate: For long T_2 values (liquid protons), $s \in \mathbb{C}$ and M_z oscillates (see Figure A.1, left). For protons with short T_2 values, (macromolecules, bound protons) $s \in \mathbb{R}$ and M_z decays (see Figure A.1, right). As we are interested in saturating the bound protons ($M_z = 0$), it is possible to create an RF pulse which is transparent for the liquid protons but visible for the bulk protons. In other words, one would like to selectively saturate the bound proton pool without disturbing the liquid pool protons.

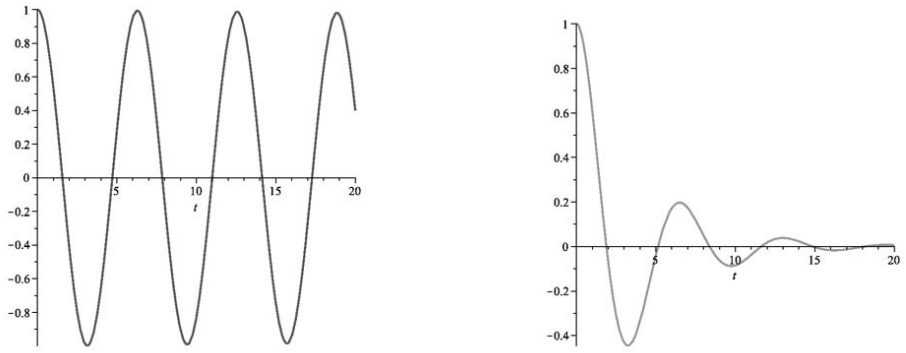

Figure A.1: ***Left:*** *$M_z(t)$ for long T_2 values.* ***Right:*** *$M_z(t)$ for short T_2 values, saturation can be achieved.*

One prerequisite for pulsed MT is to design a *transparent pulse*. The effect of such a selective

saturation pulse on the M_z magnetisation is displayed in Figure A.1. Its amplitude is chosen to be sufficient to spoil the M_z magnetisation of the bound proton pool (Figure A.1, right), while the long T_2 pool (free protons) *sees* a zero degree flip angle. One method to produce such a zero degree flip angle pulse would be to apply a 2π pulse. The drawback of this approach is, that it is very sensitive to SAR limits and B_1 inhomogeneities. So a better idea would be to use width modulated, so called 'binomial trains', denoted as e.g. $1\bar{2}1$ or $1\bar{3}3\bar{1}$. These pulses are of minimal SAR due to their constant magnitude [133]. Those binomial pulse trains are in fact the most popular presaturation pulses for MT imaging. Different variations of binomial pulses are used for example in [134, 59, 135] or [136].

B. Protocol Optimisation for the T_1 Mapping Sequences

B.1. IR-FID and IR-SE:

Sequence parameters for the inversion recovery sequences were chosen to cover a large fraction of the relaxation curve. TI values were spaced equally between 5 ms and 4010 ms. As T_1 values between 1071 and 2417 ms are expected, the relaxation curves are sufficiently sampled.

B.2. Multiple Flip Angle Approach:

Monte Carlo simulations were employed to find the optimal TR range for the T_1 values expected. 10,000 simulations were performed to obtain the mean and standard deviation of $T_1^{calculated}$ and $M_0^{calculated}$. 10 flip angles were considered, starting from 10° to 100°, equally spaced. The calculated accuracies (in %), ΔT_1 and ΔM_0 from the input values T_1 and M_0 were calculated as

$$\begin{aligned} \Delta(T_1) &= 100 - \frac{\text{mean}(T_1^{calculated}) - T_1}{T_1} \cdot 100, \\ \Delta(M_0) &= \frac{\text{mean}(M_0^{calculated}) - M_0}{M_0} \cdot 100. \end{aligned} \tag{B.1}$$

The precisions, $\sigma(T_1)$ and $\sigma(M_0)$, were calculated as:

$$\begin{aligned} \sigma(T_1) &= 100 - \frac{\text{std}(T_1^{calculated})}{T_1} \cdot 100, \\ \sigma(M_0) &= \frac{\text{std}(M_0^{calculated})}{M_0} \cdot 100. \end{aligned} \tag{B.2}$$

The results are summarised in Figure B.1 and Figure B.2.
Using only 2 flip angles decreases the precision and accuracy, as one would expect (Figure B.3 and B.4).
If MT is considered, the accuracy and precision maps look quite different - both, accuracy and precision suffer if MT in present. Figure B.5 to Figure B.8 display the results of the Monte Carlo simulations for Equation (5.19).

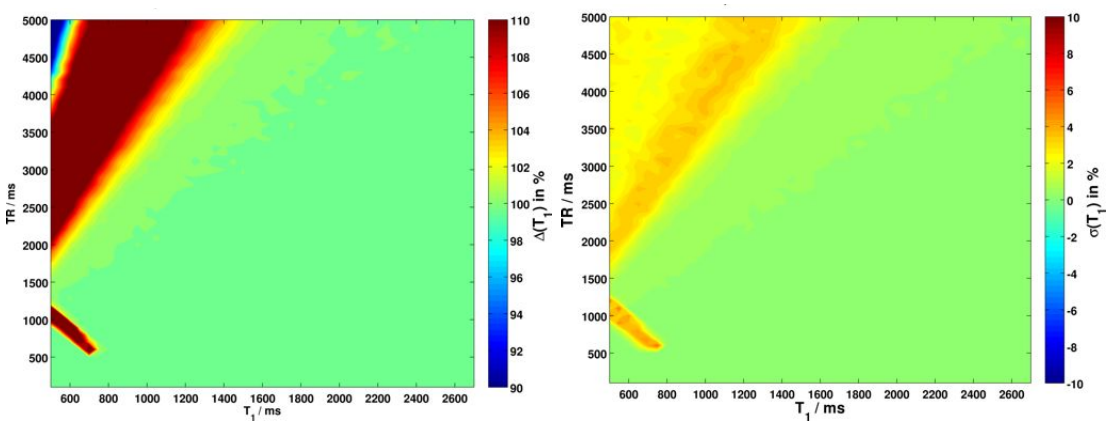

Figure B.1: *Accuracy (left) and precision (right) [%] of T_1 mapping based on gradient echo sequences with 10 different flip angles.*

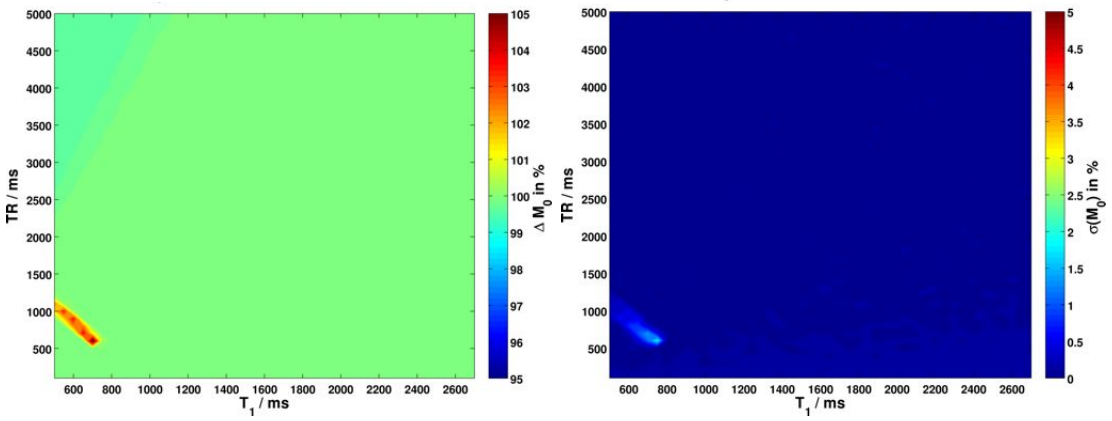

Figure B.2: *Accuracy (left) and precision (right) [%] of M_0 mapping based on gradient echo sequences with 10 different flip angles.*

B.3. Look-Locker based Method TAPIR:

TAPIR parameters were chosen based on [74]. The protocol was optimised for a T_1 value of 1744 ms, which was chosen as it represents the mean T_1 value. The optimal sequence parameters according to [74] are summarised in Table B.1. The basis set of parameters given in Table B.1 was simulated as well as other flip angles and timepoints. As there were several T_1 values, there is no single set of parameters which gives the best accuracy. Other parameter combinations were therefore simulated as well in order to examine the influences of the sequence parameter choice on the estimated T_1 values.

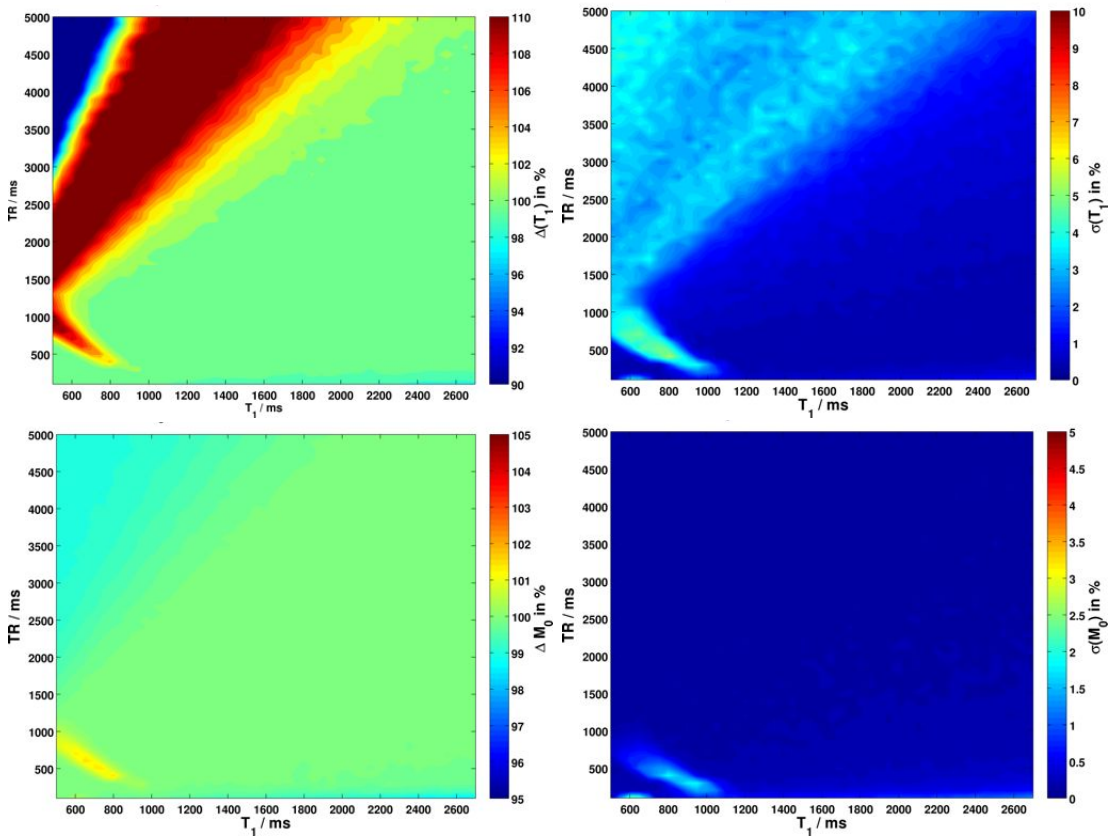

Figure B.3: *Accuracy (left) and precision (right) of T_1 (top) and M_0 (bottom) mapping based on gradient echo sequences with flip angles of 30°and 60°.*

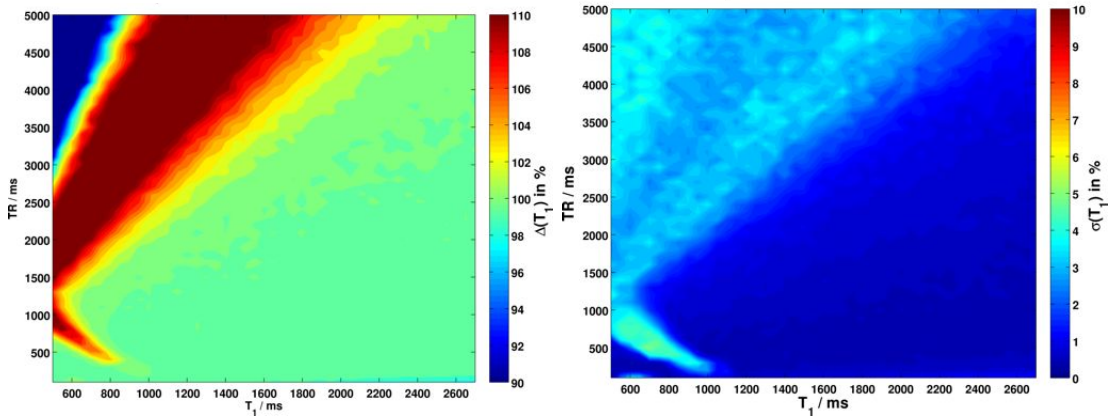

Figure B.4: *Accuracy (left) and precision (right) [%] of T_1 mapping based on gradient echo sequences with flip angles of 20°and 70°. As the accuracy and precision for M_0 mapping is good for the whole simulated range of TR and T_1, the data is not shown.*

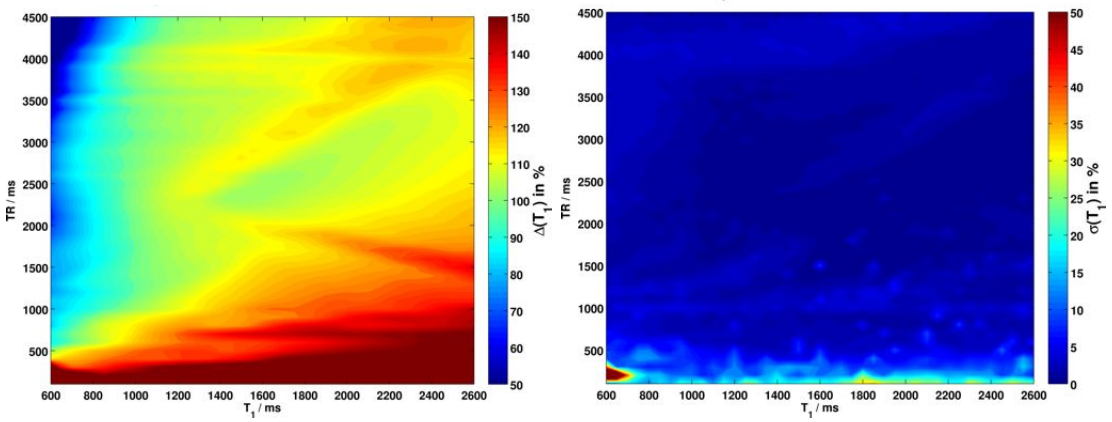

Figure B.5: *Accuracy (left) and precision (right) [%] of T_1 mapping based on gradient echo sequences with 10 different flip angles under consideration of MT effects.*

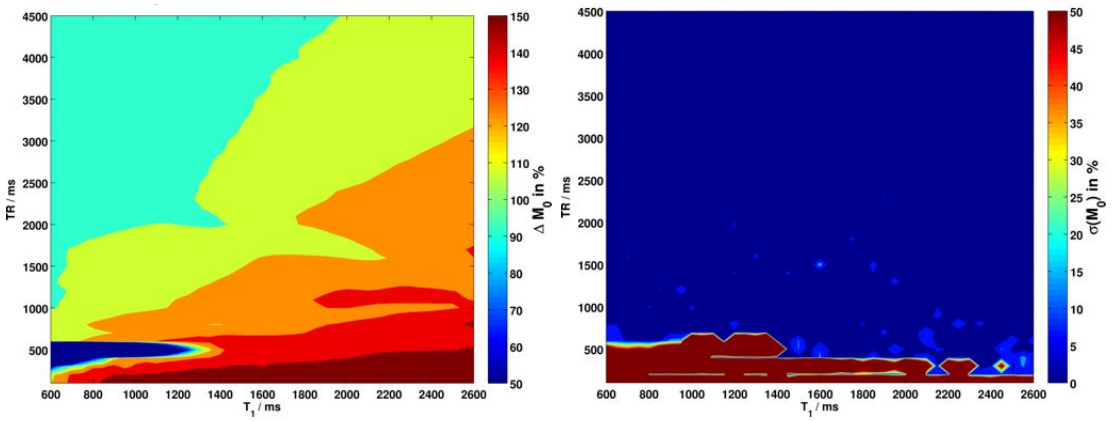

Figure B.6: *Accuracy (left) and precision (right) of M_0 mapping based on gradient echo sequences with 10 different flip angles under consideration of MT effects. Sample parameters were: $M_0 = 1, A = 0.122037, S_B = 0.2$.*

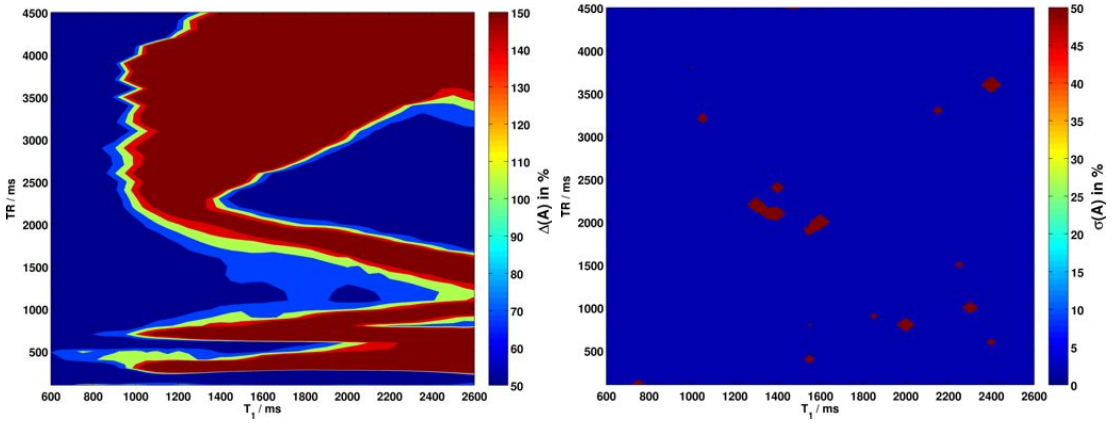

Figure B.7: *Accuracy (left) of A mapping based on gradient echo sequences with 10 different flip angles under consideration of MT effects. Sample parameters were: $M_0 = 1, A = 0.122037, S_B = 0.2$.*

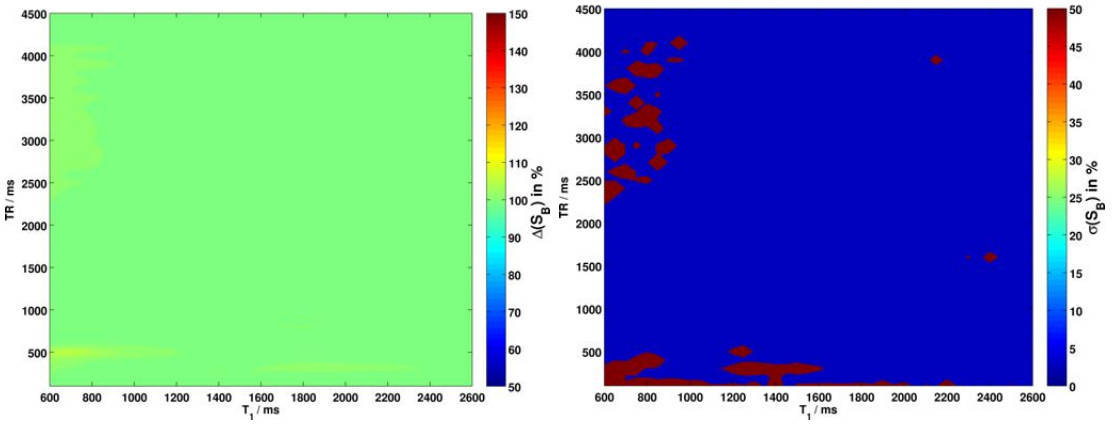

Figure B.8: *Accuracy of S_B mapping based on gradient echo sequences with 10 different flip angles under consideration of MT effects. Sample parameters were: $M_0 = 1, A = 0.122037, S_B = 0.2$.*

TAPIR Sequence Parameters	
α	40°
τ/ ms	4000
TR/ ms	175
Timepoints	45
TE/ ms	5
TI/ ms	10

Table B.1: *Basic set of TAPIR simulation parameters optimised for a T_1 of 1748 ms. The choice is based on the optimal parameters given in [74]*

C. List of Publications

Paper

T_1 Mapping by means of Look-Locker type Sequences in the Presence of Magnetisation Transfer

Miriam Rabea Kubach, Kaveh Vahedipour, Klaus Hans Manfred Möllenhoff, Tony Stöcker and N. Jon Shah

Submitted to Magnetic Resonance in Medicine

MRI Measurements of the Blood-Brain Barrier Permeability by means of the Patlak Model: Improvements and Comparison to FET-PET Data

Miriam Rabea Kubach, Christian Filss, Karl-Josef Langen, Hans Herzog and N. Jon Shah

In Preparation

Demonstrating the Influence of Magnetisation Transfer on Putative T_1 Relaxation Times in Inversion Recovery Spin Echo Sequences: a Simulation and Phantom Study

Miriam Rabea Kubach, Kaveh Vahedipour, Daniel Brenner, Tony Stöecker, A.M. Oros-Peusquens and N. Jon Shah

In Preparation

Cardiac Phase-Specific Shimming (CPSS) for SSFP MR Cine Imaging at 3 T

Miriam Rabea Kubach, Axel Bornstedt, Vinzenz Hombach, Nico Merkle, Michael Schär, G. Ulrich Nienhaus and Volker Rasche

Physics in Medicine and Biology, 54 (2009) 467-478

Conference Proceedings

2011

Oral Presentation:

On the TI_{min} Dependence of T_1 in Look-Locker like Sequences: Simulations and in vivo Results

Miriam Rabea Kubach, Kaveh Vahedipour, Tony Stöcker, N. Jon Shah

28^{th} *Annual Scientific Meeting of the European Society for Magnetic Resonance in Medicine and Biology (ESMRMB), Leipzig, Oct 2011*

Influence of Magnetisation Transfer on Established $\mathbf{T_1}$ Mapping Methods

Miriam Rabea Kubach, Kaveh Vahedipour, Tony Stöcker, N. Jon Shah

19^{th} *Scientific Meeting and Exhibition of the International Society for Magnetic Resonance in Medicine (ISMRM), Montreal, May 2011*

Mapping of Water Content in the Human Brain using TAPIR

Klaus H. M. Möllenhoff, Fabian Keil, *Miriam Rabea Kubach*, Vincent Gras, Zaheer Abbas, A.M. Oros-Peusquens, N. Jon Shah

28^{th} *Annual Scientific Meeting of the European Society for Magnetic Resonance in Medicine and Biology (ESMRMB), Leipzig, Oct 2011*

A New 3D Method for Water and Relaxation Time Mapping: Comparison with the 2D "Gold Standard"

A.M. Oros-Peusquens, Fabian Keil, Vincent Gras, Zaheer Abbas, Daniel Brenner, *Miriam Rabea Kubach*, Klaus H. Möllenhoff and N. Jon Shah

19^{th} *Scientific Meeting and Exhibition of the International Society for Magnetic Resonance in Medicine (ISMRM), Montreal, May 2011*

Quantitative Water Content Mapping at 1.5 and 3 Tesla Field Strength

Vincent Gras, Zaheer Abbas, A. M. Oros-Peusquens, Klaus H. M. Möllenhoff, Fabian Keil, *Miriam Rabea Kubach*, N. Jon Shah

19^{th} *Scientific Meeting and Exhibition of the International Society for Magnetic Resonance in Medicine (ISMRM), Montreal, May 2011*

2010

Demonstrating the Influence of Magnetisation Transfer on Putative $\mathbf{T_1}$ Relaxation Times: a Simulation Study

Miriam Rabea Kubach, Kaveh Vahedipour, A. M. Oros-Peusquens, Tony Stoecker, N. Jon Shah

18^{th} *Scientific Meeting and Exhibition of the International Society for Magnetic Resonance in Medicine (ISMRM), Stockholm, May 2010*

2009

Fast and Improved Fitting of the Magnetisation Density using Multiple Echo Gradient Echo sequences

Miriam Rabea Kubach, Fabian Keil, A.M. Oros-Peusquens, N.Jon Shah

26^{th} *Annual Scientific Meeting of the European Society for Magnetic Resonance in Medicine and Biology (ESMRMB), Antalya, Oct 2009*

Complex Simulation of MT and CEST Effects for Arbitrary MR-Sequences

Miriam Rabea Kubach, Kaveh Vahedipour, Tony Stoecker, N. Jon Shah

Wilhelm and Else Heraeus Seminar "Molecular Imaging" 442 (2009)

Phase Contrast in the Human Brain and its Field Dependence

A.M. Oros-Peusquens, *Miriam Rabea Kubach*, N.Jon Shah

17^{th} *Scientific Meeting and Exhibition of the International Society for Magnetic Resonance in Medicine (ISMRM), Honolulu, May 2009*

A Three-Field Study of Cerebral Transverse Relaxation Rates *in vivo*: Implications for Brain Iron Measurements

A.M. Oros-Peusquens, *Miriam Rabea Kubach*, M. Laurila, N.Jon Shah

17^{th} *Scientific Meeting and Exhibition of the International Society for Magnetic Resonance in Medicine (ISMRM), Honolulu, May 2009*

A High-Resolution Quantitative Method for the Study of the Post Mortem Brain

A.M. Oros-Peusquens, Fabian Keil, *Miriam Rabea Kubach*, N.Jon Shah

17^{th} *Scientific Meeting and Exhibition of the International Society for Magnetic Resonance in Medicine (ISMRM), Honolulu, May 2009*

A High-Resolution Method for Proton Density and Relaxation Time Mapping in the Human Brain

A. M. Oros-Peusquens, Fabian Keil, *Miriam Rabea Kubach*, N. Jon Shah

26^{th} *Annual Scientific Meeting of the European Society for Magnetic Resonance in Medicine and Biology (ESMRMB), Antalya, Oct 2009*

2008

Improvement of Magnetic Field Homogeneity for Cardiac MRI at 3 Tesla

Miriam Rabea Kubach, Axel Bornstedt, Michael SchÃďr, G. Ulrich Nienhaus, Volker Rasche

16^{th} *Scientific Meeting and Exhibition of the International Society for Magnetic Resonance in Medicine (ISMRM), Toronto, May 2008*

D. Bibliography

[1] Paul Tofts.
Quantitative MRI of the Brain.
John Wiley and Sons Ltd, 1 edition, 2004.
(Cited on pages 11 and 53.)

[2] P Tofts and A Kermode.
Measurement of the blood brain barrier permeability and leakage space using dynamic mr imaging. 1. fundamental concepts.
Magnetic Resonance in Medicine, Jan 1991.
(Cited on pages 11, 12, 131 and 139.)

[3] H Larsson and P S Tofts.
Measurement of blood–brain barrier permeability using dynamic gd–dtpa scanning: a comparison of methods.
Magnetic Resonance in Medicine, 1992.
(Cited on pages 11, 12, 131, 139 and 142.)

[4] Ewa E Odrobina, Toby Y J Lam, Teresa Pun, Rajiv Midha, and Greg J Stanisz.
Mr properties of excised neural tissue following experimentally induced demyelination.
NMR Biomed, 18(5):277–84, Aug 2005.
(Cited on page 11.)

[5] N Jon Shah, Heiko Neeb, Maxim Zaitsev, S Steinhoff, G Kircheis, K Amunts, D Haeussinger, and Karl Zilles.
Quantitative t1 mapping of hepatic encephalopathy using magnetic resonance imaging.
Hepatology, 38(5):1219–1226, 2003.
(Cited on pages 11 and 53.)

[6] N Jon Shah, Heiko Neeb, G Kircheis, P Engels, D Haeussinger, and Karl Zilles.
Quantitative cerebral water content mapping in hepatic encephalopathy.
Neuroimage, 23:723–731, Mar 2008.
(Cited on pages 11 and 53.)

[7] Heiko Neeb, V Ermer, Tony Stoecker, and N Jon Shah.
Fast quantitative mapping of absolute water content with full brain coverage.

Neuroimage, Jan 2008.
(Cited on pages 11, 53 and 59.)

[8] Heiko Neeb and N Jon Shah.
Enhancing the precision of quantitative water content mapping by optimizing sequence parameters.
Magnetic Resonance in Medicine, 56(1):224–229, 2006.
(Cited on page 11.)

[9] A Oros-Peusquens, M Laurila, and N Jon Shah.
Magnetic field dependence of the distribution of nmr relaxation times in the living human brain.
MAGMA, Jan 2008.
(Cited on page 11.)

[10] G Brix, L R Schad, M Deimling, and W J Lorenz.
Fast and precise t1 imaging using a tomrop sequence.
Magn Reson Imaging, Jan 1990.
(Cited on pages 11 and 114.)

[11] Sean C. L Deoni, Brian K Rutt, and Terry M Peters.
Rapid combined t1 and t2 mapping using gradient recalled acquisition in the steady state.
Magnetic Resonance in Medicine, 49(3):515–526, 2003.
(Cited on pages 11 and 92.)

[12] Gunther Helms, Henning Dathe, and Peter Dechent.
Quantitative flash mri at 3t using a rational approximation of the ernst equation.
Magnetic Resonance in Medicine, 59(3):667–72, Mar 2008.
(Cited on page 11.)

[13] Adrianus J de Langen, Vivian E M van den Boogaart, J Tim Marcus, and Mark Lubberink.
Use of h2(15)o-pet and dce-mri to measure tumor blood flow.
Oncologist, 13(6):631–44, Jun 2008.
(Cited on pages 11 and 139.)

[14] H Larsson and M Stubgaard.
Quantitation of blood–brain barrier defect by magnetic resonance imaging and gadolinium–dtpa in patients with multiple sclerosis and brain tumors.
Magnetic Resonance in Medicine, 1990.
(Cited on pages 11 and 139.)

[15] Saeid Taheri, Charles Gasparovic, and N Shah.

Quantitative measurement of blood–brain barrier permeability in human using dynamic contrast–enhanced mri with fast t1 mapping.
Magnetic Resonance in Medicine, 65(4):1036–1042, 2011.
(Cited on pages 11, 12, 53, 142, 149, 155, 156, 157 and 158.)

[16] Kai-Hsiang Chuang and Alan Koretsky.
Improved neuronal tract tracing using manganese enhanced magnetic resonance imaging with fastt1 mapping.
Magnetic Resonance in Medicine, 55(3):604–611, Mar 2006.
(Cited on page 11.)

[17] R Damadian, K Zaner, and D Hor.
Human tumors detected by nuclear magnetic resonance.
Proc Natl Acad Sci USA, Jan 1974.
(Cited on pages 11 and 53.)

[18] Takashi Katsube, Masahiro Okada, Seishi Kumano, Masatoshi Hori, Izumi Imaoka, Kazunari Ishii, Masatoshi Kudo, Hajime Kitagaki, and Takamichi Murakami.
Estimation of liver function using t1 mapping on gd–eob–dtpa–enhanced magnetic resonance imaging.
Invest Radiol, 46(4):277–283, 2011.
(Cited on page 11.)

[19] P. J Wright, O. E Mougin, J. J Totman, A M Peters, M. J Brookes, R Coxon, P. E Morris, M Clemence, S. T Francis, R. W Bowtell, and P. A Gowland.
Water proton t 1 measurements in brain tissue at 7, 3, and 1.5t using ir-epi, ir-tse, and mprage: results and optimization.
Magn Reson Mater Phy, 21(1-2):121–130, Mar 2008.
(Cited on page 12.)

[20] Sean C. L Deoni, SCR Williams, P Jezzard, J Suckling, DGM Murphy, and DK Jones.
Standardized structural magnetic resonance imaging in multicentre studies using quantitative t1 and t2 imaging at 1.5 t.
Neuroimage, 40(2):662–671, 2008.
(Cited on page 12.)

[21] M Zweckstetter and TA Holak.
An adiabatic multiple spin-echo pulse sequence: removal of systematic errors due to pulse imperfections and off-resonance effects.
Journal of Magnetic Resonance, 133(1):134–147, 1998.
(Cited on page 12.)

[22] G Parker, G Barker, and P S Tofts.
Accurate multislice gradient echo t1 measurement in the presence of non-ideal rf pulse shape and rf field nonuniformity.
Magnetic Resonance in Medicine, Jan 2001.
(Cited on page 12.)

[23] Xiawei Ou, Shu-Wei Sun, Hsiao-Fang Liang, Sheng-Kwei Song, and Daniel F Gochberg.
Quantitative magnetization transfer measured pool–size ratio reflects optic nerve myelin content in ex vivo mice.
Magnetic Resonance in Medicine, 61(2):364–371, Feb 2009.
(Cited on page 12.)

[24] Steven D Wolff and Robert S Balaban.
Magnetization transfer contrast (mtc) and tissue water proton relaxation in vivo.
Magnetic Resonance in Medicine, 10(1):135–144, 1989.
(Cited on page 12.)

[25] Xiawei Ou and Daniel F Gochberg.
Mt effects and t1 quantification in single-slice spoiled gradient echo imaging.
Magnetic Resonance in Medicine, 59(4):835–845, 2008.
(Cited on pages 12, 59, 64, 99, 105, 106 and 112.)

[26] N Bloembergen, S Shapiro, P Pershan, and J Artman.
Cross–relaxation in spin systems.
Physical Review, Jan 1959.
(Cited on page 12.)

[27] H Bagher-Ebadian, R Paudyal, and T Nagaraja.
Mri estimation of gadolinium and albumin effects on water proton.
Neuroimage, Jan 2010.
(Cited on page 12.)

[28] Andrew M Prantner, G. Larry Bretthorst, Jeffrey J Neil, Joel R Garbow, and Joseph J.H Ackerman.
Magnetization transfer induced biexponential longitudinal relaxation.
Magnetic Resonance in Medicine, 60(3):555–563, Sep 2008.
(Cited on page 12.)

[29] HM McConnell.
Reaction rates by nuclear magnetic resonance.
The Journal of Chemical Physics, 28:430, 1958.
(Cited on pages 12, 45 and 59.)

[30] Tony Stoecker, Kaveh Vahedipour, Daniel Pflugfelder, and N Jon Shah.
High-performance computing mri simulations.
Magnetic Resonance in Medicine, 64(1):186–93, Jul 2010.
(Cited on pages 12 and 67.)

[31] Clifford S Patlak.
Derivation of equations for the steady-state reaction velocity of a substance based on the use of a second substance.
J Cereb Blood, 1(1):129–31, Jan 1981.
(Cited on pages 12, 131, 132 and 134.)

[32] Clifford S Patlak, R G Blasberg, and Joseph D Fenstermacher.
Graphical evaluation of blood–to–brain transfer constants from multiple-time uptake data.
J Cereb Blood, Jan 1983.
(Cited on pages 12, 131, 132, 136 and 139.)

[33] H. Y. Carr.
Field gradients in early mri.
Physics Today, 57(7):83, 2004.
(Cited on page 13.)

[34] P.C. Lauterbur.
Image formation by induced local interactions: Examples employing nuclear magnetic resonance.
Nature, 242:190–191, 1973.
(Cited on page 13.)

[35] R.V. Damadian.
Tumor detection by nuclear magnetic resonance.
Science, 171:1151–1153, 1971.
(Cited on page 13.)

[36] Fritz Kurt Kneubuehl.
Repetitorium der Physik.
Vieweg+Teubner Verlag, 1994.
(Cited on page 14.)

[37] Arnulf Oppelt.
Imaging Systems for Medical Diagnostics.
Publicis Corporate Publishing, 2005.
(Cited on pages 14, 15, 16, 21, 22, 37, 45 and 48.)

[38] L Hanson.

Is quantum mechanics necessary for understanding magnetic resonance?
Concepts in Magnetic Resonance Part A, Jan 2008.
(Cited on page 15.)

[39] F Bloch.
Nuclear induction.
Physical Review, 70(7-8):460–474, Oct 1946.
(Cited on pages 15, 20 and 21.)

[40] Anatole Abragam.
The Principles of Nuclear Magnetism.
Oxford University Press, USA.
(Cited on page 15.)

[41] Dwight G Nishimura.
Principles of Magnetic Resonance Imaging.
Stanford Univ, 1994.
(Cited on pages 17, 19, 21, 23 and 52.)

[42] Siemens AG Erlangen.
Magnets, spins and resonances, 2003.
(Cited on pages 19, 24, 32, 34 and 39.)

[43] J Pauly and Dwight G Nishimura.
A k-space analysis of small-tip-angle excitation.
Journal of Magnetic Resonance, Jan 1989.
(Cited on page 20.)

[44] Zhi-Pei Liang and Paul C Lauterbur.
Principles of Magnetic Resonance Imaging (A Signal Processing Perspective).
Wiley-IEEE Press, 2000.
(Cited on pages 23 and 25.)

[45] X Yang, S Sammet, and P Schmalbrock.
Postprocessing correction for distortions in t2* decay caused by quadratic cross-slice b0–inhomogeneity.
Magnetic Resonance in Medicine, Jan 2010.
(Cited on page 25.)

[46] EL Hahn.
Spin echos.
Physical Review, 80:580, 1950.
(Cited on page 25.)

[47] H Carr and EM Purcell.
Effects of diffusion on free precession in nuclear magnetic resonance experiments.
Physical Review, Jan 1954.
(Cited on page 26.)

[48] E. Mark Haacke, Robert W. Brown, Michael R. Thompson, and Ramesh Venkatesan.
Magnetic Resonance Imaging, Physical Principles and Sequence Design.
Wiley-Liss, 7 edition, 1999.
(Cited on page 33.)

[49] Mark Woods, DE Woessner, and A Dean Sherry.
Paramagnetic lanthanide complexes as paracest agents for medical imaging.
Chemical Society Reviews, 35(6):500–511, 2006.
(Cited on pages 43 and 49.)

[50] Jinyuan Zhou and Peter C M VanZijl.
Chemical exchange saturation transfer imaging and spectroscopy.
Progress in Nuclear Magnetic Resonance Spectroscopy, 48:109–136, May 2006.
(Cited on page 45.)

[51] RM Henkelman, X Huang, GJ Qing-San Xiang, Joseph Stancanello, and MJ Bronskill.
Quantitative interpretation of magnetization transfer.
Magnetic Resonance in Medicine, 29(6):759–766, 1993.
(Cited on pages 45, 47, 50, 59, 71, 72, 73, 74, 78, 80, 95 and 96.)

[52] Jinyuan Zhou, David A Wilson, Phillip Zhe Sun, JA Klaus, and Peter C M VanZijl.
Quantitative description of proton exchange processes between water and endogenous and exogenous agents for wex, cest, and apt experiments.
Magnetic Resonance in Medicine, 51(5):945–952, 2004.
(Cited on pages 45 and 47.)

[53] Elena Vinogradov, Shanrong Zhang, Angelo J M Lubag, James A Balschi, A Dean Sherry, and Robert E Lenkinski.
On–resonance low b1 pulses for imaging of the effects of paracest agents.
Journal of Magnetic Resonance, 176(1):54–63, Sep 2005.
(Cited on pages 45 and 47.)

[54] Joseph C McGowan.
Magnetic resonance imaging and magnetization transfer.
Advances in Imaging and Electron Physics, 118:1–83, Oct 2001.
(Cited on pages 45 and 51.)

[55] Sture Forsen and Ragnar A Hoffman.

Exchange rates by nuclear magnetic multiple resonance. iii. exchange reactions in systems with several nonequivalent sites.
The Journal of Chemical Physics, 40:1189, 1964.
(Cited on page 45.)

[56] Alex X Li, Robert H E Hudson, John W Barrett, Craig K Jones, Stephen H Pasternak, and Robert Bartha.
Four-pool modeling of proton exchange processes in biological systems in the presence of mri-paramagnetic chemical exchange saturation transfer (paracest) agents.
Magnetic Resonance in Medicine, 60(5):1197–1206, Nov 2008.
(Cited on page 45.)

[57] Malcom H Levitt.
Spin Dynamics.
John Wiley and Sons, 2007.
(Cited on page 45.)

[58] Z Luz and S Meiboom.
Rate and mechanism of proton exchange in aqueous solutions of phosphate buffer.
J Am Chem Soc, 86(22):4764–4766, 1964.
(Cited on pages 46 and 78.)

[59] HN Yeung and Joseph Stancanello.
Transient decay of longitudinal magnetization in heterogeneous spin systems under selective saturation.
Journal of Magnetic Resonance, 99(3):466–479, 1992.
(Cited on pages 48 and 168.)

[60] R G Bryant.
The dynamics of water–protein interactions.
Annual Review of Biophysics and Biomolecular Structure, 25(1):29–53, 1996.
(Cited on page 49.)

[61] SJ Graham and RM Henkelman.
Understanding pulsed magnetization transfer.
Journal of Magnetic Resonance Imaging, 7(5):903–912, 1997.
(Cited on pages 50, 51 and 167.)

[62] E Schneider, RW Prost, and GH Glover.
Pulsed magnetization transfer versus continuous wave irradiation for tissue contrast enhancement.
Journal of Magnetic Resonance Imaging, 3(2):417–423, 1993.

(Cited on pages 50 and 52.)

[63] Joseph C McGowan, M D Schnall, and J S LeighJr.
Magnetization transfer imaging with pulsed off–resonance saturation: variation in contrast with saturation duty cycle.
Journal of Magnetic Resonance Imaging, 4(1):79–82, 1994.
(Cited on page 51.)

[64] O Bieri and K Scheffler.
Optimized balanced steady-state free precession magnetization transfer imaging.
Magnetic Resonance in Medicine, 58(3):511–518, 2007.
(Cited on page 52.)

[65] P. A Gowland, P Mansfield, and P Bullock.
Dynamic studies of gadolinium uptake in brain tumors using inversion-recovery echo-planar imaging.
Magnetic Resonance in Medicine, Jan 1992.
(Cited on pages 53, 56 and 114.)

[66] M Karlsson and B Nordell.
Phantom and in vivo study of the look–locher t1 mapping method.
Magn Reson Imaging, 17(10):1481–8, Dec 1999.
(Cited on page 53.)

[67] S A Johansson Back, P Magnusson, A Fransson, L E Olsson, A Montelius, O Holmberg, P Andreo, and S Mattsson.
Improvements in absorbed dose measurements for external radiation therapy using ferrous dosimeter gel and mr imaging (femri).
Phys Med Biol, 43(2):261–76, Feb 1998.
(Cited on page 53.)

[68] M Karlsson and B Nordell.
Analysis of the look-locker t1 mapping sequence in dynamic contrast uptake studies: simulation and in vivo validation.
Magn Reson Imaging, Jan 2000.
(Cited on page 53.)

[69] Sean C L Deoni, Brian K Rutt, and Terry M Peters.
Rapid combined t1 and t2 mapping using gradient recalled acquisition in the steady state.
Magnetic Resonance in Medicine, 49(3):515–526, Mar 2003.
(Cited on page 54.)

[70] DC Look and DR Locker.

Time saving in measurement of nmr and epr relaxation times.
Review of Scientific Instruments, 41:250, 1970.
(Cited on pages 55 and 114.)

[71] A J Freeman, P A Gowland, and P Mansfield.
Optimization of the ultrafast look locker echo planar imaging t1 mapping sequence.
Magn Reson Imaging, 16(7):765–72, Sep 1998.
(Cited on pages 56 and 114.)

[72] P Gowland and P Mansfield.
Accurate measurement of t1 in vivo in less than 3 seconds using echo-planar imaging.
Magnetic Resonance in Medicine, 30(3):351–4, Sep 1993.
(Cited on page 56.)

[73] N Jon Shah, Maxim Zaitsev, S Steinhoff, and Karl Zilles.
A new method for fast multislice t1 mapping.
Neuroimage, 14(5):1175–1185, 2001.
(Cited on pages 56, 92, 114 and 117.)

[74] M Zaitsev, S Steinhoff, and N J Shah.
Error reduction and parameter optimization of the tapir method for fast t1 mapping.
Magnetic Resonance in Medicine, 49(6):1121–1132, Jun 2003.
(Cited on pages 56, 57, 109, 114, 118, 161, 170 and 173.)

[75] S Steinhoff, Maxim Zaitsev, Karl Zilles, and N Jon Shah.
Fast t1 mapping with volume coverage.
Magnetic Resonance in Medicine, 46(1):131–140, 2001.
(Cited on pages 56 and 92.)

[76] J Brookes, T Redpath, and F Gilbert.
Accuracy of t1 measurement in dynamic contrast–enhanced breast mri using two–and three–dimensional variable flip angle fast low-angle shot.
Journal of Magnetic Resonance Imaging, Jan 1999.
(Cited on page 59.)

[77] N Bloembergen, EM Purcell, and RV Pound.
Relaxation effects in nuclear magnetic resonance absorption.
Nature Physical Reviews, 73:679, 1947.
(Cited on page 59.)

[78] I Berry, Gareth J Barker, F Barkhof, A Campi, V Dousset, JM Franconi, A Gass, W Schreiber, DH Miller, and P S Tofts.
A multicenter measurement of magnetization transfer ratio in normal white matter.

Journal of Magnetic Resonance Imaging, 9(3):441–446, 1999.
(Cited on page 59.)

[79] Robert S Balaban and TL Ceckler.
Magnetization transfer contrast in magnetic resonance imaging.
Magnetic resonance quarterly, 8(2):116, 1992.
(Cited on page 59.)

[80] R Harrison, MJ Bronskill, and RM Henkelman.
Magnetization–transfer and t–2 relaxation components in tissue.
Magnetic Resonance in Medicine, 33(4):490–496, Jan 1995.
(Cited on page 59.)

[81] G B Pike.
Pulsed magnetization transfer contrast in gradient echo imaging: a two-pool analytic description of signal response.
Magnetic Resonance in Medicine, 36(1):95–103, 1996.
(Cited on pages 59, 61, 63 and 65.)

[82] Greg J Stanisz, Ewa E Odrobina, Joseph Pun, Michael Escaravage, Simon J Graham, Michael J Bronskill, and R. Mark Henkelman.
T1, t2 relaxation and magnetization transfer in tissue at 3t.
Magnetic Resonance in Medicine, 54(3):507–512, Sep 2005.
(Cited on pages 59, 62, 95 and 96.)

[83] Gunther Helms, Henning Dathe, and Peter Dechent.
Modeling the influence of tr and excitation flip angle on the magnetization transfer ratio (mtr) in human brain obtained from 3d spoiled gradient echo mri.
Magnetic Resonance in Medicine, 64:177–185, Jul 2010.
(Cited on page 59.)

[84] Tabea Gringel, Walter Schulz-Schaeffer, Erck Elolf, A Froelich, Peter Dechent, and Gunther Helms.
Optimized high-resolution mapping of magnetization transfer (mt) at 3 tesla for direct visualization of substructures of the human thalamus in clinically feasible measurement time.
Journal of Magnetic Resonance Imaging, 29(6):1285–1292, Jun 2009.
(Cited on page 59.)

[85] J Hennig, A Nauerth, and H Friedburg.
Rare imaging: a fast imaging method for clinical mr.
Magnetic Resonance in Medicine, 3(6):823–33, Dec 1986.

(Cited on page 59.)

[86] E Purcell.
Effects of diffusion on free precession in nuclear magnetic resonance experiments.
Physical Review, Jan 1954.
(Cited on page 59.)

[87] S Meiboom.
Modified spin–echo method for measuring nuclear relaxation times.
Review of Scientific Instruments, Jan 1958.
(Cited on page 59.)

[88] Gunther Helms and Gisela E Hagberg.
In vivo quantification of the bound pool t1 in human white matter using the binary spin–bath model of progressive magnetization transfer saturation.
Phys Med Biol, Jan 2009.
(Cited on page 59.)

[89] Simon J. P Meara and Gareth J Barker.
Impact of incidental magnetization transfer effects on inversion-recovery sequences that use a fast spin-echo readout.
Magnetic Resonance in Medicine, 58(4):825–829, Jan 2007.
(Cited on page 59.)

[90] Sture Forsen and Ragnar A Hoffman.
Study of moderately rapid chemical exchange reactions by means of nuclear magnetic double resonance.
The Journal of Chemical Physics, 39:2892, 1963.
(Cited on page 61.)

[91] http://www.jemris.org.
Webpage of the JEMRIS project.
(Cited on page 67.)

[92] DE Woessner, Shanrong Zhang, ME Merritt, and A Dean Sherry.
Numerical solution of the bloch equations provides insights into the optimum design of paracest agents for mri.
Magnetic Resonance in Medicine, 53(4):790–799, 2005.
(Cited on pages 69, 71, 72, 73, 74 and 76.)

[93] N Bloembergen, EM Purcell, and R Pound.
Nuclear magnetic relaxation.
Nature, 160:475–476, 1947.

(Cited on page 78.)

[94] J Pauly, P Le Roux, D Nishimura, and A Macovski.
Parameter relations for the shinnar-le roux selective excitation pulse design algorithm [nmr imaging].
IEEE Transactions on Medical Imaging, 10(1):53–65, Jan 1991.
(Cited on page 88.)

[95] Kenner A Christensen, David M Grant, Edward M Schulman, and Cheves Walling.
Optimal determination of relaxation times of fourier transform nuclear magnetic resonance. determination of spin-lattice relaxation times in chemically polarized species.
J. Phys. Chem., 78(19):1971–1977, Sep 1974.
(Cited on page 92.)

[96] Forman S Acton.
Numerical Methods that Work.
The Mathematical Association of America.
(Cited on pages 94 and 130.)

[97] Daniel F Gochberg and John C Gore.
Quantitative imaging of magnetization transfer using an inversion recovery sequence.
Magnetic Resonance in Medicine, 49(3):501–5, Mar 2003.
(Cited on pages 95 and 112.)

[98] P A Bottomley, C J Hardy, R E Argersinger, and G Allen-Moore.
A review of 1h nuclear magnetic resonance relaxation in pathology: are t1 and t2 diagnostic?
Med Phys, 14(1):1–37, Jan 1987.
(Cited on page 96.)

[99] S Cavassila, S Deval, C Huegen, D vanOrmondt, and D Graveron-Demilly.
Cramer–rao bounds: an evaluation tool for quantitation.
NMR Biomed, 14(4):278–83, Jun 2001.
(Cited on page 109.)

[100] P Hodgkinson and P J Hore.
Sampling and the quantification of nmr data.
Advances in magnetic and optical resonance, 20:187–244, 1997.
(Cited on page 109.)

[101] J A Jones, P Hodgkingson, A L Barker, and P J Hore.
Optimal sampling strategies for the measurement of spin-spin relaxation times.
Journal of Magnetic Resonance Series B, 113:25–34, 1996.

(Cited on page 109.)

[102] Fabian Keil.
Development of methods for functional magnetic resonance imaging and relaxation time mapping.
Master's thesis, Universitaet Dortmund, 2010.
(Cited on page 111.)

[103] R Graumann, M Deimling, T Heilmann, and A Oppelt.
A new method for fast and precise t1 determination.
SMSM Book of Abstracts, pages 922–923, 1986.
(Cited on page 114.)

[104] R Deichmann, D Hahn, and A Haase.
Fast t1 mapping on a whole–body scanner.
Magnetic Resonance in Medicine, 42(1):206–9, Jul 1999.
(Cited on page 114.)

[105] P B Kingsley.
Signal intensities and t1 calculations in multiple-echo sequences with imperfect pulses.
Concepts in Magnetic Resonance Part A, 11(1):29–49, 1999.
(Cited on page 114.)

[106] P B Kingsley and W G Monahan.
Correcting for incomplete saturation and off–resonance effects in multiple-site saturation–transfer kinetic measurements.
Journal of Magnetic Resonance, 146(1):100–9, Sep 2000.
(Cited on page 114.)

[107] Daniel R Messroghli, Aleksandra Radjenovic, Sebastian Kozerke, David M Higgins, Mohan U Sivananthan, and John P Ridgway.
Modified look-locker inversion recovery (molli) for high-resolution t1 mapping of the heart.
Magnetic Resonance in Medicine, 52(1):141–6, Jul 2004.
(Cited on page 114.)

[108] D Messroghli, K Walters, and S Plein.
Myocardial t1 mapping: application to patients with acute and chronic myocardial infarction.
Magnetic Resonance in Medicine, Jan 2007.
(Cited on page 114.)

[109] P A Gowland, M O Leach, and J C Sharp.

The use of an improved inversion pulse with the spin-echo/inversion-recovery sequence to give increased accuracy and reduced imaging time for t1 measurements.
Magnetic Resonance in Medicine, 12(2):261–7, Nov 1989.
(Cited on page 114.)

[110] R Deichmann.
Fast high resolution t1 mapping of the human brain.
Magnetic Resonance in Medicine, Jan 2005.
(Cited on page 117.)

[111] Klaus Hans Manfred Moellenhoff.
Development of an optimised tapir sequence for t1 and h2o mapping using adiabatic inversion pulses and parallel imaging techniques.
Master's thesis, Universitaet Dortmund, 2010.
(Cited on page 118.)

[112] M Cercignani and Gareth J Barker.
A comparison between equations describing in vivo mt: The effects of noise and sequence parameters.
Journal of Magnetic Resonance, 191(2):171–183, 2008.
(Cited on page 130.)

[113] TL Ceckler, J Maneval, and B Melkowits.
Modeling magnetization transfer using a three-pool model and physically meaningful constraints on the fitting parameters.
Journal of Magnetic Resonance, 151(1):9–27, 2001.
(Cited on page 130.)

[114] Vasily L Yarnykh and Chun Yuan.
Cross relaxation imaging reveals detailed anatomy of white matter fiber tracts in the human brain.
Neuroimage, 23(1):409–24, Sep 2004.
(Cited on page 130.)

[115] Andrew J Farrall and Joanna M Wardlaw.
Blood–brain barrier: ageing and microvascular disease–systematic review and meta-analysis.
Neurobiology of aging, 30(3):337–52, Mar 2009.
(Cited on page 131.)

[116] B Zlokovic.
The blood–brain barrier in health and chronic neurodegenerative disorders.

Neuron, Jan 2008.
(Cited on page 131.)

[117] Rolf Dermietzel, David C. Spray, and Maiken Nedergaard.
The Blood–Brain and Other Neural Barriers: Reviews and Protocols.
Jan 2006.
(Cited on page 131.)

[118] H Larsson and F Courivaud.
Measurement of brain perfusion, blood volume, and blood–brain barrier permeability, using dynamic contrast–enhanced t1–weighted mri at 3 tesla.
Magnetic Resonance in Medicine, 2009.
(Cited on pages 131, 139, 140 and 142.)

[119] J Hearon.
Theorems on linear systems.
Annals of the New York Academy of Sciences, Jan 1963.
(Cited on page 134.)

[120] Jorg Pintaske, Petros Martirosian, Hansjorg Graf, Gunter Erb, Klaus-Peter Lodemann, Claus D Claussen, and Fritz Schick.
Relaxivity of gadopentetate dimeglumine (magnevist), gadobutrol (gadovist), and gadobenate dimeglumine (multihance) in human blood plasma at 0.2, 1.5, and 3 tesla.
Investigative Radiology, 41(3):213–21, Mar 2006.
(Cited on pages 140 and 141.)

[121] Martin Rohrer, Hans Bauer, Jan Mintorovitch, Martin Requardt, and Hanns-Joachim Weinmann.
Comparison of magnetic properties of mri contrast media solutions at different magnetic field strengths.
Investigative Radiology, 40(11):715–24, Nov 2005.
(Cited on pages 140 and 141.)

[122] William K Purves, David Sadava, Gordon H Orians, and Craig H Heller.
Life: The Science of Biology.
W. H. Freeman, 2004.
(Cited on page 140.)

[123] M Rijpkema, J H Kaanders, F B Joosten, A J van der Kogel, and A Heerschap.
Method for quantitative mapping of dynamic mri contrast agent uptake in human tumors.
Journal of Magnetic Resonance Imaging, 14(4):457–63, Oct 2001.
(Cited on pages 142 and 144.)

[124] Y Cao, S L Brown, R A Knight, J D Fenstermacher, and J R Ewing.
Effect of intravascular to extravascular water exchange on the determination of blood–to–tissue transfer constant by magnetic resonance imaging.
Magnetic Resonance in Medicine, 53(2):282–93, Feb 2005.
(Cited on page 142.)

[125] Ramesh Paudyal, Hassan Bagher-Ebadian, Tavarekere N Nagaraja, Joseph D Fenstermacher, and James R Ewing.
Modeling of look-locker estimates of the magnetic resonance imaging estimate of longitudinal relaxation rate in tissue after contrast administration.
Magnetic Resonance in Medicine, May 2011.
(Cited on page 142.)

[126] K Donahue and D Burstein.
Studies of gd dtpa relaxivity and proton exchange rates in tissue.
Magnetic resonance, Jan 1994.
(Cited on page 142.)

[127] Vaclav Smidl.
Robust detection of linear part of patlak rutland plots.
Technical report, Academy of Science of the Czech Republic, 2008.
(Cited on pages 143 and 144.)

[128] James R Ewing, R Knight, and Tavarekere N Nagaraja.
Patlak plots of gd–dtpa mri data yield blood–brain transfer constants concordant with those of 14c–sucrose in areas of blood–brain opening.
Magnetic Resonance in Medicine, Jan 2003.
(Cited on page 144.)

[129] Deirdre M McGrath, Daniel P Bradley, Jean L Tessier, Tony Lacey, Chris J Taylor, and Geoffrey J M Parker.
Comparison of model-based arterial input functions for dynamic contrast–enhanced mri in tumor bearing rats.
Magnetic Resonance in Medicine, 61(5):1173–84, May 2009.
(Cited on page 145.)

[130] W Pardridge.
Introduction to the blood–brain barrier: methodology, biology, and pathology.
Cambridge University Press, 1998.
(Cited on page 151.)

[131] S. Taheri, C. Gasparovic, B. N. Huisa, J.C. Adair, E. Edmonds, J. Prestopnik, M. Grossetete, N.J. Shah, J. Wills, C. Qualls, and G. A. Rosenberg.
Blood–brain barrier permeability abnormalities in vascular cognitive impairment.
Stroke, 42:2158–2169, 2011.
(Cited on pages 155 and 157.)

[132] D. Pauleit, G. Stoffels, A. Bachofner, F. W. Floeht, M. Sabel, H. Herzog, L. Tellmann, P. Jansen, G. Reifenberger, K. Hamacher, H. H. Coenen, and K.-J. Langen.
Comparison of f18–fet and f18–fdg pet in brain tumors.
Nuclear Medicine and Biology, 36:779–787, 2009.
(Cited on page 161.)

[133] BS Hu, SM Conolly, GA Wright, Dwight G Nishimura, and A Macovski.
Pulsed saturation transfer contrast.
Magnetic Resonance in Medicine, 26(2):231–240, 1992.
(Cited on pages 167 and 168.)

[134] Jun Hua, Craig K Jones, Jaishri O Blakeley, Seth A Smith, Peter C M VanZijl, and Jinyuan Zhou.
Quantitative description of the asymmetry in magnetization transfer effects around the water resonance in the human brain.
Magnetic Resonance in Medicine, 58(4):786–793, 2007.
(Cited on page 168.)

[135] Seth A Smith, Jonathan A D Farrell, Craig K Jones, Daniel S Reich, Peter A Calabresi, and Peter C M VanZijl.
Pulsed magnetization transfer imaging with body coil transmission at 3 tesla: feasibility and application.
Magnetic Resonance in Medicine, 56(4):866–75, Oct 2006.
(Cited on page 168.)

[136] DJ Meyerhoff.
Proton magnetization transfer of metabolites in human brain.
Magnetic Resonance in Medicine, 42(3):417–420, 1999.
(Cited on page 168.)

E. List of Figures

F. List of Tables

Lebenslauf

Persönliche Daten

Miriam Rabea Kubach

Geboren am 11. 06. 1984 in Rheinfelden
Staatsangehörigkeit: deutsch

Schulbildung

1990 – 1994	Grundschule Langenbrettach
1994 – 2000	Mittlere Reife, Realschule Neuenstadt a.K.
2000 – 2003	Abitur, Technisches Gymnasium Heilbronn, Note 1,2 Leistungskurse Mathematik und Gestalungs- und Medientechnik

Studium

10/2003 – 09/2005	Vordiplom Physik an der Universität Ulm
09/2005 – 01/2006	Auslandssemester an der University of Leeds, UK
01/2006 – 03/2007	Hauptstudium an der Universität Ulm
04/2007 – 03/2008	Diplomarbeit an der Universität Ulm, Fakultät für Biophysik in Kooperation mit der Inneren Medizin des Uniklinikums Ulm Titel der Arbeit: Vierdimensionale Minimierung von patienteninduzierten Magnetfeldinhomogenitäten für die kardiale Magnetresonanztomographie
03/2008	Physik Diplom der Universität Ulm, Gesamtnote “sehr gut”

Promotion

05/2008 – 12/2011	Promotion am Forschungszentrum Jülich, Institut für Neurowissenschaften und Medizin, Physik der Medizinischen Bildgebung und RWTH Aachen

Aachen, 03.07.2012

Acknowledgements

I would like to thank all the people who contributed to the success of this work.

First and foremost I offer my sincerest gratitude to my supervisor, Prof. Dr. N. Jon Shah for providing me with the opportunity to complete my PhD thesis in his department. He has supported me throughout my thesis with his patience and knowledge whilst allowing me the room to work in my own way. This thesis, would not have been completed or written without his encouragement and endorsement.

I would like to thank Prof. Dr. Achim Stahl for his spontaneous willingness to review my work.

Special gratitude is dedicated to Dr. Tony Stoecker. Discussions with him were always helpful, positive and profitable. My work benefits a lot by his constructive criticism. He also spent a lot of time correcting my manuscripts - thank you so much.

Furthermore, I would like to thank my fellow students, especially Fabian Keil, Daniel Brenner, Daniel Fiege and Ruediger Stirnberg. Working with you guys was a pleasure. Discussions provided always further insights and many ideas grew up during our meetings. Your critical reading of my manuscript and your helpful suggestions contributed a lot to the success of this work. Many thanks to Kaveh Vahedipour who taught me a lot about programming and especially how NOT to program. Furthermore, his technical support and uplifting when my ankle was broken and I had to work at home contributed a lot to the final version of JEMRIS MT.

I would like to thank Prof. Dr. Langen, Prof. Dr. Herzog as well as Christian Filss for their support and advice for the Patlak study.

I am indebted to all of my colleagues, the Juelich MR Group, to support me during my time there. I received a lot of support from anybody - starting from fighting the bureaucracy to scientific input and finally for the great atmosphere and the "beer and nibbles" evenings. You all made me have a great time in Juelich.

A very grateful thank you to all persons volunteering for the MRI measurements required for the preparation and completion of this thesis.

This thesis would not have been possible without the support of my parents and grandparents. Their thoroughly supported my studies and my thesis not only monetary but more importantly by motivating me and finding the the right words in (the few) times of stagnation. Thank you so much!